Additively Manufactured Materials Allowables for Critical Applications

Phoebe Eleanor May
(BEng Hons.)

Submitted to Swansea University in fulfilment of the requirements for the Degree of Philosophy

Swansea University
December 2025

Declaration

This work has not previously been accepted in substance for any degree and is not being concurrently submitted in candidature for any degree.

Signed ....[redacted]....................... (candidate)

Date ....8th December 2025...................

This thesis is the result of my own investigations, except where otherwise stated. Other sources are acknowledged by footnotes giving explicit references. A bibliography is appended.

Signed ....[redacted]....................... (candidate)

Date ....8th December 2025...................

I hereby give consent for my thesis, if accepted, to be available for electronic sharing

Signed ....[redacted]....................... (candidate)

Date ....8th December 2025...................

The University's ethical procedures have been followed and, where appropriate, that ethical approval has been granted.

Signed ....[redacted]....................... (candidate)

Date ....8th December 2025...................

Abstract

Laser powder bed fusion, an additive manufacturing technique, brings significant opportunities for manufacturing in terms of new structural designs, higher performance, and a reduction in weight and material required. Among the various high-performance alloys adapted for laser powder bed fusion, Inconel 718, a precipitation-strengthened nickel-based superalloy renowned for its exceptional mechanical strength and thermal stability, has generated significant interest for aerospace and nuclear applications. However, for this potential to be unlocked, industry requires the creation of high calibre datasets to enable design and product certification. This requires a deep understanding and evaluation of the effect of defects, appropriate adoption of test methods, and relating the process of creating additive manufactured material to the microstructure and lifing of a component in-service.

Investigation into the mechanical and microstructural performance of laser powder bed fused Inconel 718 against conventionally wrought material, with emphasis on evaluation of the influence of varying post-processing heat treatment routes on powder bed fused Inconel 718, was conducted. Variants for laser powder bed fusion included a non-heat treated variant, and two heat treated variants to improve varying mechanical properties (fatigue and creep).

Microstructural analysis via advanced electron microscopy showed grain characteristics and phase variation between the additive variants and a contrast to the wrought Inconel 718. The different microstructures directly related to the mechanical properties, which were evaluated via room and elevated temperature: tensile, strain control low cycle fatigue, constant load creep testing, alongside hardness testing and small scale techniques – small punch tensile and small punch creep.

Overall, the additively manufactured variants, particularly the heat treated variants, exhibited mechanical superiority compared to the wrought Inconel 718. However, the heat treatment implemented did not typically show the intended desired properties. Additionally, small scale test techniques showed general trends could be gathered but direct correlations to uniaxial tests were not accurate. Consequently, conclusions advise the need for further research into AM specific HTs and the use of small-scale testing.

Table of Contents

List of Figures

List of Tables

List of Equations

Paris' Law	$\frac{da}{dN} = C\Delta K^{m}$	(1)
k$_{sp}$ method	$F/\sigma_c = 3.33k_{sp}R^{-0.2}r^{1.2}h_o$	(2)
UTS prediction	$\sigma_{UTS} = \beta_1\left(\frac{F_{MAX}}{t * d_m}\right) + \beta_2$	(3)
YS prediction	$\sigma_y = \alpha_1\left(\frac{F_e}{t^2}\right) + \alpha_2$	(4)

List of Abbreviations

Acronym	Meaning
AM	additive manufacture
AM CoE	Additive Manufacturing Center of Excellence
APT	atom probe tomography
AR	as-received
ASTM	American Society for Testing and Materials
BED	backscatter electron
BJT	binder jetting
CAD	computer aided design
CDRX	continuous dynamic recrystallisation
DDRX	discontinuous dynamic recrystallisation
DED	directed energy deposition
DEM	discrete element method
DfAM	design for additive manufacture
DLD	directed laser deposition
DMD	direct metal deposition
DRX	dynamic recrystallisation
DSA	dynamic strain aging
EBM	electron beam melting
EBSD	electron backscatter diffraction
EDM	electrical discharge machining
EDX	energy dispersive x-ray spectroscopy
EPSRC	Engineering and Physical Sciences
ESR	electroslag remelting
ET	elevated temperature
FCC	face-centred cubic
FDM	fuse deposition modelling
FEG-SEM	field emission gun-scanning electron microscope
FEM	finite element method
GOS	grain orientation spread

H or 0°	horizontal
HAGBs	high angle grain boundaries
HCF	high cycle fatigue
HIP	hot isostatic pressing
HT	heat treatment
HT1	heat treatment 1
HT2	heat treatment 2
IDSA	inverse dynamic strain aging
IN625	Inconel 625
IN718	Inconel 718
IPF	inverse pole figure
ISM	Institute of Structural Materials
LAGBs	low angle grain boundaries
LCF	low cycle fatigue
LENS	laser engineered net shaping
LM	laser melting
LoF	lack of fusion
LS	laser sintering
LVDT	linear variable displacement transducer
M	metal ion
M	metal ion
MAM	metal additive manufacturing
MEX	material extrusion
MJT	material jetting
MUD	multiple of uniform density
NDE	non-destructive evaluation
NDSA	normal dynamic strain aging
PBF	powder bed fusion
PBF-EB	electron beam powder bed fusion
PBF-LB	laser bed powder bed fusion
PIP	profilometry-based indentation plastometry
PLC	Portevin-Le Chatelier
PREP	plasma rotating electrode process

PS	proof stress
PSD	powder size distribution
PSP	process-structure-property
REP	rotating electrode process
RT	room temperature
Rx	recrystallisation
SEM	scanning electron microscope
SEM	secondary electron
SHL	sheet lamination
ShPT	Shear punch tensile
SL	stereolithography
SLM	selective laser melting
SMaRT	Swansea Materials Research & Testing Ltd
S-N	stress-life
SP	small punch
SPC	small punch creep
SPT	small punch tensile
STL	Standard Tessellation Language
TCP	topologically close-packed
UKAS	United Kingdom Accreditation Service
UTS	ultimate tensile strength
UV	ultraviolet
V or 90°	vertical
VAR	vacuum arc remelting
VIM	vacuum induction melting
VPP	vat photopolymerization
YS	yield strength
1^y	primary creep
2^y	secondary creep
3^y	tertiary creep
Σ3s	annealing twins
µCT	micro X-ray computed tomography

List of Symbols

Symbol	Meaning	Unit
a	crack length	mm
C	constant	
d_b	deflection at break	mm
d_m	deflection at F_{MAX}	mm
F	force	N
F_e	SPT yield	N
F_{MAX}	maximum force	N
G	temperature gradient	
h_o	disc thickness	mm
k	initial stiffness	N/mm
k_{sp}	correlation factor	
m	constant	
N	number of cycles, life	
Nf	number of cycles to failure	
P-h	load-depth	
$P_{II\text{-}III}$	transition load from section II to section III	N
$P_{III\text{-}IV}$	transition load point between section III and section IV	N
P_{max}	maximum load	N
P_y	yield load	N
R	stress ratio	
R	radius of receiving hole	mm
r	radius of punch	mm
R_g	growth rate	
S_a	arithmetic mean height	µm
S-N	stress-life	
S_v	maximum pit height	µm
t	thickness	mm
T_m	melting temperature	°C/F
U	strain energy	J
α_1	constant	

α_2	constant	
β_1	constant	
β_2	constant	
γ	gamma	
γ'	gamma prime	
γ''	gamma double prime	
δ	delta	
δ^*	specimen deflection at fracture	mm
ΔK	variation of stress intensity factor K	
δ_m	deflection at maximum load	mm
$\Delta\sigma$	stress range	MPa
ε	strain	%
ε-N	strain-life	
σ_a	stress amplitude	MPa
σ_c	equivalent uniaxial creep stress	MPa
σ_m	mean stress	MPa
σ_{max}	maximum stress	MPa
σ_{min}	minimum stress	MPa
σ_r	stress range	MPa
σ_s	sigma phase	
σ_{UTS}	predicted ultimate tensile stress	MPa
σ_y	predicted yield strength	MPa

Acknowledgements

This research was supported by funding under Engineering and Physical Sciences Research Council (EPSRC) Industrial Case Award EP/T517987/1 and American Society for Testing and Materials (ASTM) International Additive Manufacturing Center of Excellence (AM CoE) whose contributions were essential in facilitating the completion of this project.

I would like to extend my greatest appreciation to my academic supervisor, Prof Robert Lancaster, for their guidance, critical insight, and support throughout the course of this work. Their expertise and feedback have played a significant role in shaping the direction and outcomes of this thesis. Also, I would also like to acknowledge the contributions of my industrial supervisors and supporting team: Dr Martin White, Dr Alberto Bordin, Dr Richard Huff, and Dr Lauren Ednie, for their ongoing support, technical guidance, and provision of relevant materials throughout the course of this project.

Thanks are also due to the staff and peers within Swansea University, particularly within the Institute of Structural Materials (ISM) for their constructive discussions and collaborative engagement over the duration of this programme. Additional thanks extend to Swansea Materials Research & Testing Ltd (SMaRT) for completion and support of mechanical testing.

Lastly, I would like to acknowledge the support of my family and friends. Their patience, and encouragement throughout this process have been greatly appreciated. While not directly involved in the research, their understanding and willingness to provide support played an important role in sustaining my focus and motivation throughout the PhD process.

1 Introduction

Additive manufacturing (AM), often referred to as 3D printing, is a manufacturing technology with the ability to revolutionise traditional manufacturing across various industries, including: aerospace, medical, automotive, and nuclear [1,2]. By enabling the layer-by-layer fabrication of components from digital models, AM allows for the production of custom and complex geometries whilst reducing material waste and energy usage. Particularly, laser bed powder bed fusion (PBF-LB) has gained significant attention for the production of high-performance metallic components due to its precision and design flexibility [3]. The PBF-LB process involves producing near-fully dense components from a bed of metallic powder, with a high-powered laser consolidating each layer. One alloy that has been heavily adopted for PBF-LB use is Inconel 718 (IN718), a nickel-based superalloy, which is known for its excellent mechanical strength and corrosion resistance, even at elevated temperatures (ET) [4,5]. However, the unique thermal histories associated with the PBF-LB technique of IN718 can lead to microstructural features and residual stresses that are not typically associated with conventionally manufactured counterparts. Consequently, the implementation of post-process heat treatment (HT) is essential to tailor the microstructure and optimise the mechanical properties of PBF-LB IN718 for demanding in-service conditions.

IN718 was originally developed for use in high-temperature applications such as turbine engines [5,6], where it exhibits superior resistance to creep, fatigue, and oxidation. These properties arise from a microstructure consisting of a primary γ matrix strengthened by coherent γ’ and γ’’ precipitates, alongside other stable phases such as δ and carbides [7]. However, the thermal cycles and rapid, directional solidification associated with PBF-LB can result in a microstructure consisting of high dislocation densities, segregation of alloying elements, and anisotropy in the form of a columnar grain structure parallel to the build direction [8,9]. To mitigate these effects and enable the precipitation of strengthening phases, HTs such as hot isostatic pressing (HIP), solution annealing, and aging, are implemented post-build. These HTs aim to reduce residual stress, homogenise the microstructure, and precipitate phases with the required morphology, quantity, and location, to enhance the desired mechanical properties [10,11].

The influence of HTs on PBF-LB IN718 is still being heavily researched, as post-processing conditions must be optimised to balance defect mitigation, phase stability, and microstructural refinement [12–15]. For instance, solution annealing treatments promote recrystallisation and dissolution of undesired phases, but may lead to grain growth and loss of fine microstructural features. Aging treatments, typically in two stages, are essential for γ’ and γ’’ precipitation, whilst controlling the formation of phases such as δ, Laves, and carbides. Additionally, the role of HIP, effectively eliminates internal porosity and can reduce anisotropy. Overall, the influence of post-processing on the mechanical behaviour of PBF-LB IN718 is complex and demands a detailed understanding of the process-structure-property (PSP) relationship.

As mentioned, the mechanical properties of PBF-LB IN718 are linked to the resulting post-HT microstructure. Standard mechanical tests such as uniaxial tensile, creep, and low cycle fatigue (LCF), are used to assess the material behaviour under service-relevant conditions by providing insight into the strength, ductility, time-dependent deformation, and cyclic-life of a component [16]. However, conventional, full-sized mechanical test methods can often be constrained by the size and geometry of the fabricated parts and cost (particularly for ET) testing, which is reported less in literature, as it requires more energy and specialised equipment. Consequently, small-scale testing such as small punch tensile (SPT) and small punch creep (SPC), offer an alternate approach to assess material properties using miniature specimens. These methods have shown promise in correlating well with conventional tests, allowing for the assessment of tensile and creep behaviour [17,18].

Overall, despite all the promising advantages of AM and various modes of analysis, a significant barrier to its widespread industrial adoption remains: the absence of comprehensive standards and robust, high-quality datasets required for the qualification and certification of AM parts [19–21]. This is especially critical for safety-sensitive industries where components must meet stringent performance and reliability criteria. Traditional manufacturing processes with decades of empirical data and well-established quality assurance protocols are a contrast to AM technologies (like PBF-LB) that lack universally accepted guidelines for material processing, defect tolerance, and in-service behaviour. The intrinsic variability from AM builds – from machine parameters, powder characteristics, and post-processing conditions – further complicate the establishment of qualification frameworks. Additionally, the limited availability of high-calibre datasets, particularly under long-term, high temperature, or cyclic conditions, impedes industrial confidence in the deployment of AM parts for both critical and non-critical applications. Consequently, this underscores the need for systematic studies that not only explore the influence of processing and HT on material properties, but also contribute to a growing body of reliable data that supports standardisation and qualification efforts.

Therefore, this thesis aims to investigate how different HT routes influence the microstructure and mechanical properties of PBF-LB manufactured IN718. With particular focus on characterising microstructural features including: grain morphology, phase composition, precipitate distribution, and defect evaluation, through the use of various electron microscopy techniques. Additionally, mechanical behaviour is assessed via tensile, creep, and LCF, providing both room temperature (RT) and ET results (where possible), as well as small-scale techniques including SPT and SPC testing, at RT and ET (where possible). By integrating microstructural analysis with mechanical assessment, this work will provide a comprehensive understanding of the PSP link, alongside high-calibre data that will support data generation for standardisation and product certification and qualification.

2 Literature Review

2.1 Additive Manufacturing

The term AM is used for fabrication methods where 3D components are built by consolidating 2D discrete layers, and there are various techniques that fall under the AM category. Initial usage of AM was for rapid prototyping but it has now developed to produce near-net shaped engineering components of near-full density. Utilisation of this unconventional method has been adopted by many industries such as, aerospace, automotive, and medical, due to its multiple advantages: production of custom, complex, near-net shape components, with reduced lead time, material usage and artisan. Albeit there are many advantages, AM does pose some limitations: high cost entry, low production volumes, and unpredictability in regards to microstructure and mechanical performance. Nonetheless, AM continues to grow in popularity, and consequently, so does the materials science research for this increasingly prevalent manufacturing method.

2.1.1 Additive Manufacturing Processes

AM may be referred to as: additive fabrication, direct digital manufacturing, freeform fabrication, layer manufacturing, rapid prototyping and 3D printing [22,23]. AM technologies are grouped based on their feedstock material type and energy source [22,24,25] and most AM processes, except for cold spray, fit into one of the seven categories defined by ISO/ASTM 52900 [26,27]. The process categories are: binder jetting (BJT), directed energy deposition (DED), material extrusion (MEX), material jetting (MJT), powder bed fusion (PBF), sheet lamination (SHL), and vat photopolymerization (VPP) [26]. All of these categories are depicted in Figure 1 [28].

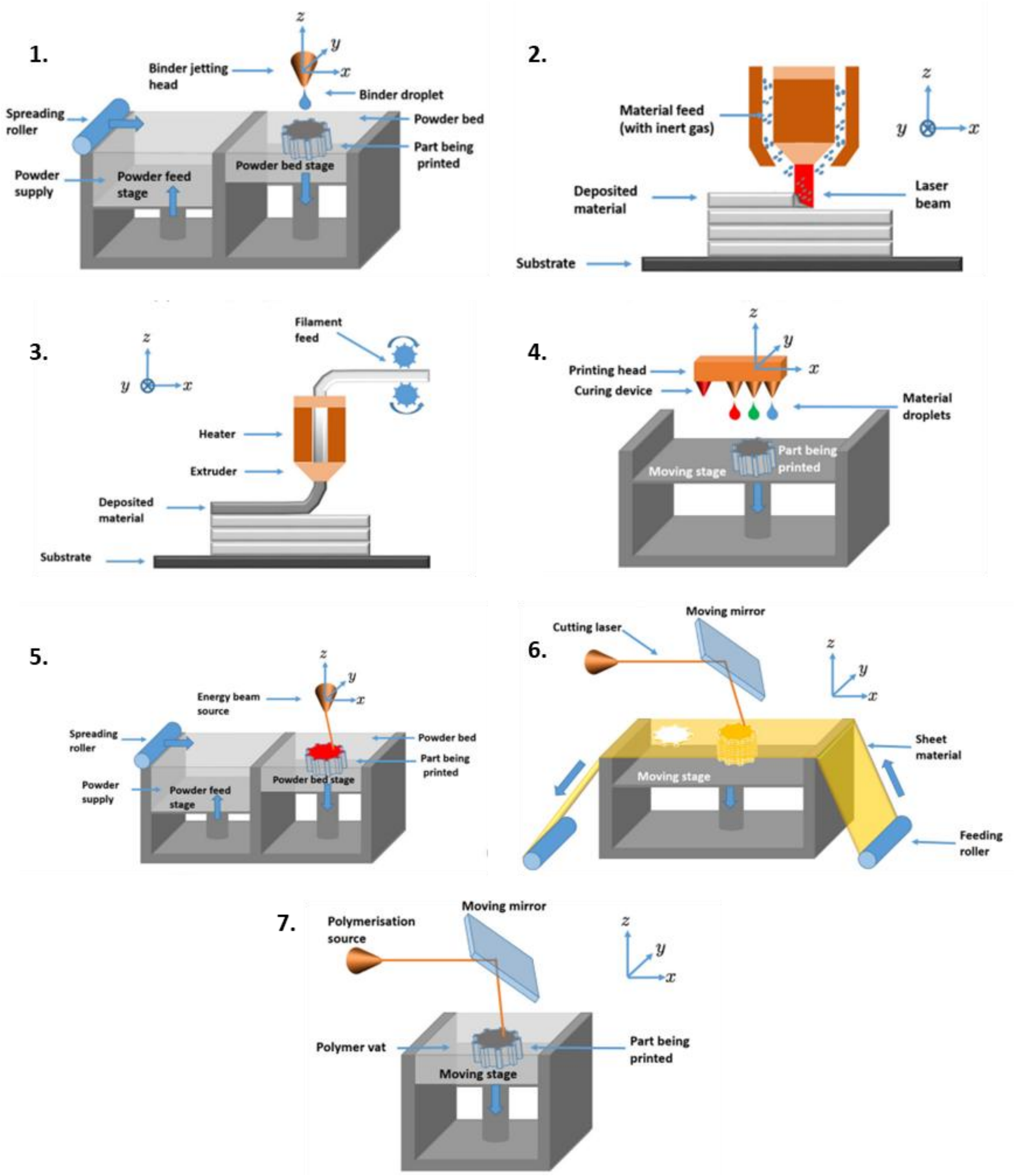

Figure 1: *Schematic of the seven AM categories: 1) BJT, 2) DED, 3) MEX, 4) MJT, 5) PBF, 6) SHL, 7) VPP. Reproduced from* [28].

2.1.2 Advantages of Additive Manufacturing

One of the key benefits of AM is the ability to produce more elaborate components, with reduced post-processing, compared to traditional manufacturing [29]. Layer-by-layer construction using a precise heat source allows for accurate 2D layers to be produced, enabling complex internal features. Engineers are able to implement design for AM (DfAM) to reduce weight and material consumption whilst still maintaining required, if not improved, mechanical properties. For example, a fuel injector component for missile application is designed via AM to include internal chambers and an assembly of two parts [30]. This saves material waste, eliminates the need for complex assembly and welding, and can provide energy savings whilst the component is in service.

Flexibility to produce customisable, small batches through the ability to design a component in CAD and manufacture it without the need of large financial investment such as purchasing new casting moulds, tools, and other equipment, like a conventional route would require, is another advantage to AM [24]. For this reason, healthcare industries such as dentistry and osteopathy, are able to use data from medical forms and radiology scans to produce personalised implants [31].

Furthermore, near-net shape manufacturing that is possible with AM can reduce lead times by decreasing the number of manufacturing stages including steps such as assembly and post-processing, like machining.

2.1.3 Limitations of Additive Manufacturing

Although there are many advantages, AM still poses some limitations, with the main downfall considered to be the presence of microstructural and mechanical integrities from the manufacturing process, which reduces quality, reliability and the predictability of mechanical properties [24]. Anisotropy, which is created from the exposure to large thermal gradients from the scan strategies during the layer-by-layer build, is undesirable in AM parts. Alongside this, the rapid melting and solidifying cycles can induce residual stress within the component being manufactured. High residual stress can lead to delamination from the build plate, as well as cracking on the macro and micro scale [32]. In addition, the manufacturing process can give rise to defects such as lack of fusion (LoF) and gas porosity [33]. All of these undesirable microstructural and mechanical properties have to be controlled via the use of optimum process parameters and post-processing techniques.

Although mentioned previously that AM reduces financial investment for customisable batches, the initial set-up for AM can be expensive to employ for companies wanting to start working with AM. There can also be issues surrounding AM when it comes to possible component build size; size limitations for AM is due to the dimensional restrictions from the build chamber. Consequently, AM is predominantly considered for one-off builds or batches of smaller components, making it inefficient to scale-up operations to produce high volumes of components [34]. Overall, AM can only be considered cost-effective when the component produced via AM adds value that cannot be achieved via conventional manufacturing.

Environmentally, AM production is not considered sustainable. Specifically, AM processes such as PBF, where build rates are slow and use of lasers is not energy efficient. Conventional processes such as injection moulding are usually more energy efficient than AM, with machining consuming approximately one-tenth of the energy usually utilised by AM methodologies [35]. Also, time consuming build rates can be contradictory to reduced lead time, where AM deposition rates are deemed slow in order to achieve high quality [34].

Even though these disadvantages within AM exist, companies are still keen to utilise AM as a method to produce complex near-net shaped components. However, these drawbacks are the major reason industries are reluctant to adopt AM for critical components [36,37]. Consequently, research into AM is still needed to overcome this.

2.1.4 Powder Bed Fusion

PBF is an AM technique that has been readily developed and employed by industry for commercial use. PBF has two main processes, laser powder bed fusion PBF-LB and electron beam powder bed fusion (PBF-EB) [38] (see Figure 1 for a generic illustration of the AM powder bed processes). Both techniques are described and analysed but PBF-LB is the focus of this review.

For both PBF-LB and PBF-EB the manufacturing process is very similar. 2D 'slices' of a 3D model are created using a heat source scan path that is calculated to define the boundaries and contours of the model, and each slice is bonded on top of each other to build a whole component. The heat source to bond each layer is an energy beam (either a laser or electron beam). After each layer is consolidated, powder is re-spread, ready for the next layer to be completed [26]. The powder is redistributed with a roller or blade and each layer is typically 25 – 100µm thick. Prior to the initial layer being deposited, the build platform is preheated. This is performed to reduce residual stress and prevent a fine microstructure being located towards the bottom of the component builds, as an un-preheated build plate would act as a heat sink for the component [32]. Park et al. [39] demonstrated that increasing the temperature of the build plate from 50°C to 150°C can lower the residual stress by nearly 22%.

Even though the main concept of PBF is the same for laser beam and electron beam PBF, there are some differences. PBF-EB uses an electron beam as the main energy source and is performed under vacuum. The use of an electron beam causes pre-sintering of the powder, as the electrons charge the powder bed and cause particles to disperse. Albeit, pre-sintering means additional post-processing to remove the final part from out of the powder cake and improve surface roughness, the powder cake formed from the pre-sintering can acts as a support, therefore (possibly) removing the need for support structures to stabilise the build part [40]. For PBF-EB, post processing may include: removal of any sacrificial supports, breaking the part out of the powder cake, finishing (polishing etc.) and heat treatment(s) [41].

On the other hand, PBF-LB, also termed selective laser melting (SLM), direct laser metal sintering, laser metal fusion etc. [32] uses a laser as the main source of energy for layer consolidation. It is used in an inert gas atmosphere e.g. argon or under vacuum. The production part often requires supports for stabilisation of overhangs and to help with thermal control. Any unused powder during the printing process can be reused but it can degrade over time due to oxidation [40,42]. Once the part is fully consolidated, post processing techniques will be performed. These include: removal of loose powder, heat treatment to relieve stresses, removal from the build plate using wire electrical discharge machining (EDM) or band saw, finishing machining to smooth surfaces and HIP, chemical milling, grit blasting, deburring etc. may also be performed [40,41].

The geometry of the layer recoating spreader has a large influence over the efficiency of redepositing the powder layer. Powder density, homogeneity and force exerted onto the solid section can be affected by the respreading process, which overall contributes to build speed, geometric accuracy and part quality [43]. Producing simulations via discrete element method (DEM), Wang et al. [43] implied that a round blade deposited the largest amount of powder compared to the other shaped spreaders, whilst also performing best for spreading efficiency and powder layer homogeneity. However, the round blade showed the largest force on the underlying part. Conclusions from their research showed that the roller spread had the most inhomogeneous powder layers and exerted a small load on the underlying part, with occasional extreme load, at higher force than the round blade. Round and roller blades were compared with vertical, declined, inclined and wide blades.

The main advantages of use of PBF compared to conventional processes are explained previously in detail in section 2.1.2. One particular example where the limitations of conventional manufacturing are overcome through the use of AM is the aerospike rocket engine designed by LEAP 71 and manufactured by Aconity3D. Using DfAM, the complex part was printed using an advanced copper alloy (CuCrZr) via PBF-LB, followed by cleaning of copper powder by Solukon, and heat treatment by Fraunhofer Institute for Laser Technology. The aerospike was successfully tested in December 2024 and is shown in Figure 2.

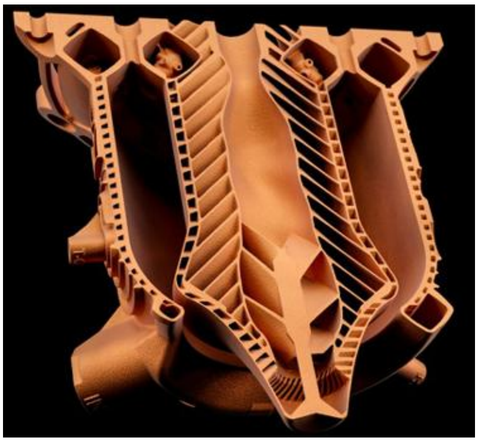

Figure 2: *Image of PBF-LB aerospike nozzle designed by LEAP 71 [44].*

2.1.5 Powder Feedstock

For AM, the control and quality of the feedstock is important. The feedstock is the raw material that is used to create the final component and is typically particle based (sometimes referred to as powder) [22].

Powder feedstock is typically made through atomisation [45]. The atomisation process, in general, is the breakup of a molten liquid into fine solid particles. For metallic atomisation, there are many methods such as plasma atomisation and centrifugal atomisation [46,47].

Plasma atomisation allows for the production of fine particle distributions, with low oxygen content, and high spherical geometry (sphericity), for reactive metals and alloys. For this process, the material is initially in the form of a metal wire. This feedstock is fed into plasma torches, where the wire melts and disperses into droplets, where it solidifies to form metallic powder. This method typically produces a particle size distribution of nanometres to 250µm [48].

An alternative method is centrifugal atomisation, which consists of using centrifugal forces to disperse molten metal. It has two types which are the most popular. Firstly, rotating electrode process (REP). This is where an electrode is rotated at high velocity, roughly 15,000rpm, whilst it is melted with an arc between the metal electrode and the tungsten electrode. The molten metal is then spun out centrifugally as molten metal droplets, which solidify. On the other hand, if a plasma arc is used, this is referred to as plasma rotating electrode process (PREP), the second common centrifugal atomisation process. Although PREP tends to produce higher quality powder compared to processes such as gas atomisation, the final quality of the built component is dictated by the optimised processing parameters of the AM method [49].

However, the most widely used processes are water and gas atomisation, where the gas used is typically air or argon. For both water and gas atomisation, the initial step is to pour molten feed from an induction furnace into a crucible above atomising jets. This material is then released as a molten stream into the chamber where the water or gas jets segregate the stream into powder droplets, which solidify rapidly into powder particles. The particles produced are collected at the bottom as a water/powder slurry, which is then processed via a de-watering module. These powders can then be sorted depending on size requirements. Comparison between these two processes shows water atomisation is a cheaper process but it does produce irregular shaped particles, from the higher cooling rates, when compared to gas atomisation [46]. Alternatively, gas atomisation is the most common process for producing metal powder for AM, giving spherical shape, good cleanliness, fine, and homogenous microstructure. When building AM components correctly, without any processing defects like keyholing, there can still be low levels of porosity detected in completed components. This porosity is from the transference of trapped inert gas in gas-atomised powder that has not been allowed to escape due to slow melting times [50].

Powder feedstock has characteristics such as particle size, particle size distribution, particle morphology, and purity, as well as bulk powder properties such as flowability and spreadability; all of which impact the quality of final AM components [24,50]. Defect and quality issues that can arise due to low quality powder feedstock include: poor packing density leading to internal voids, contaminants that give rise to porosity and impurities, poor surface topography and defects which affect mechanical performance [32,45]. Figure 3 shows the relationship between powder properties and the end influence on part property through different researchers.

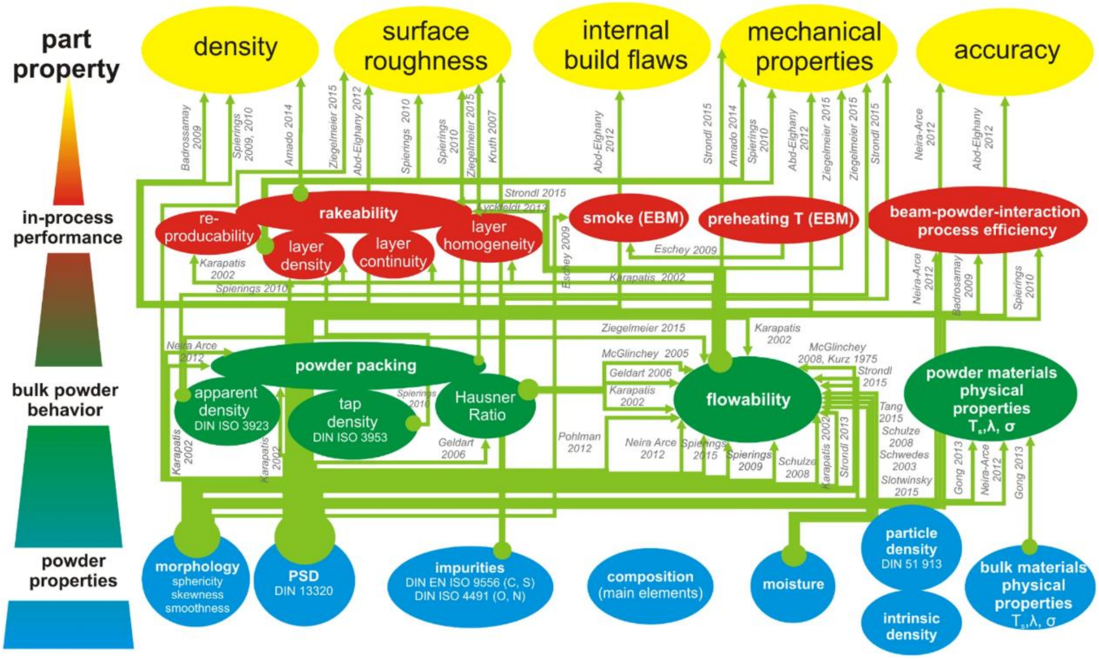

Figure 3: *Diagram illustrating the relationship between powder properties, bulk powder behaviour, in-process performance and built part property by different researchers. Reproduced from* [51].

One of the most important characteristics of metallic powder is the powder size distribution (PSD), which varies from alloy to alloy, as well as within batches. This makes PSD a variable that must be controlled and assessed regularly to ensure quality. When assessing PSD it can be presented in tabular or graphical format, recording particle size and volume. This is usually measured and recorded via laser diffraction methods or, more traditionally, via sieve analysis [46]. Theoretically, for good flow and prevented segregation, a narrow PSD is required [51].

Variation in particle morphology is due to particle size and manufacturing technique. Particle morphology has a large effect on flowability, layer density, and defect formation. There are lots of descriptions when it comes to particle morphology, which accounts for shape and surface features, but some of the well-known definitions would include: sphericity, circularity, aspect ratio and shape factor. Particles with higher sphericity are deemed to have better flowability, except for when the particles are very fine (smaller than 10μm [46]). The flowability of the powder is an important powder property as it governs layer thickness and packing density, which has an overall effect on the build quality; poor flowability gives inadequate spreading which can lead to streaking, varying layer thicknesses and defects such as porosity. In AM, powder flow occurs vertically (in the hopper) and horizontally (across the build plate), and currently there is not a universal technique that can fully characterise powder flowability. In turn, a variety of tests that match the AM conditions that the powder would be exposed to, would be carried out e.g. ASTM B213 (Hall Flow Test) [52] and ASTM B527 (Tap Density) [53].

2.1.6 Powder Feedstock Recycling

When discussing metal powder for AM, it is important to understand powder reuse and powder recycling [54]. Powder reuse relates to the repetitive use of a single powder batch, originally virgin, during multiple cycles in AM machines. Whereas, powder recycling relates to a powder or scrap material being remelted or ground to form new atomisation feedstock. The interest in powder recycling and reusing is driven by aerospace and orthopaedic industries, as metallic powders are a large cost in AM. In addition, awareness of the relevant environmental impacts and energy costs associated with the feedstock process is important for producer and user to understand. In theory, powder feedstock can be reused until depleted, but in practice, each reuse cycle impacts the feedstock properties such as, chemistry, morphology, and flowability [55].

Yi et al. [56] demonstrated with gas-atomised pre-alloyed IN718 that after fourteen reuses, there was no effect to chemistry, an increase in particle size, similar microstructure between virgin and reused powder, little effect on mechanical properties and an improvement in reducing the porosity volume and pore sphericity.

Soltani-Tehrani et el. [57] employed tensile testing to study the effect of powder reuse on tensile behaviour, including details on powder characteristics. Using the “top-up” method, the IN718 powder was reused eighteen times. Analysis of the results showed that the tensile behaviour of the different fabrication batches, produced with different recycle counts, did not influence the ultimate tensile strength (UTS) or yield strength (YS). This is because the powder reuse did not manipulate the microstructure. Variation in ductility was observed between the different PBF-LB parts. Explanation was owed to the correlation between defect content and the number of powder reuse times due to changes in powder flowability.

Further research by Paccou et al. [58] demonstrated that recycling powder up to 50 times for IN718 AM fabrication had slightly increased oxygen content and significantly increased powder flowability but saw no influence on the porosity in different powder recycling levels. Different powder recycling rates showed no variation in the solidification process, and resulting microstructure, and non-recycled compared to recycled had a similar average residual stress of approximately 60 MPa. It was reported that the recycled powder produced components with a slight reduction in fatigue life but the average fatigue life was considered to be of the same order than the result scattering for one given load and kind of samples.

2.1.7 Current Alloys in Additive Manufacturing

Development of alloys for metal additive manufacturing (MAM) has been of interest to many industrial users and researchers [59], as the number of alloys for use in AM is much lower than for conventional processes. However, as the demand for AM increases, the availability of metallic alloys for AM also increases. It is common to chemically alter conventional alloys that would not work for AM, to allow use within AM.

Some examples of commercially available AM alloys include: iron-based alloys, cobalt-based alloys, aluminium-based alloys, titanium-based alloys and nickel-based superalloys. Inconel, a nickel-based superalloy, has been at the forefront of research for AM use due to its good weldability, specifically Inconel 625 (IN625) and IN718 [60], as depicted in Figure 4 [61,62].

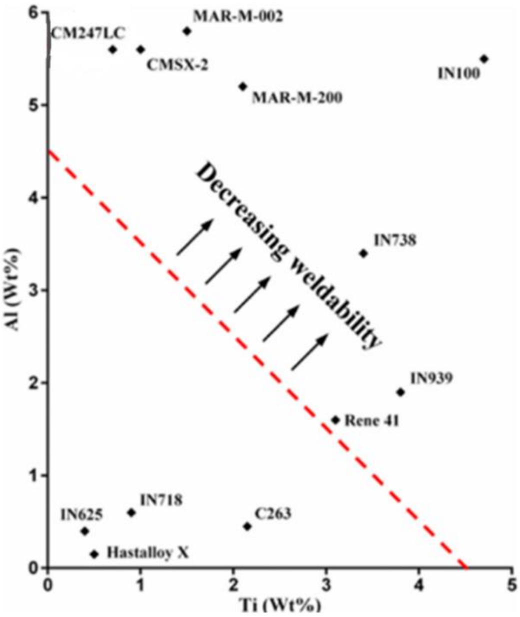

Figure 4: *'Weldability' diagram of various nickel based superalloys with respect to Ti and Al content. Poor weldability is considered above the red dotted line. Amended from* [62].

2.2 Nickel-based Superalloys

Superalloys are a class of metallic materials that can be used in elevated ET applications, typically in excess of $0.7T_{\mathrm{m}}$ (where T_m is melting temperature) [55,63]. They are classified based on the predominant metallic element in the alloy, of which there are three groups: iron-nickel, nickel and cobalt. Alloying elements typically include: aluminium, niobium, molybdenum, chromium and titanium. Figure 5 depicts the typical alloying elements in nickel based superalloys. Superalloys are key materials for industries such as aerospace and nuclear due to their excellent creep and oxidation resistance, which is maintained when operating at high temperatures [63,64]. Nickel-based superalloys are best suited for elevated temperature applications, and will be the focus of this report, specifically Inconel 718. The characteristics presented by nickel-based superalloys can be manipulated in order to optimise properties by altering the alloying elements' composition and modifying the process parameters.

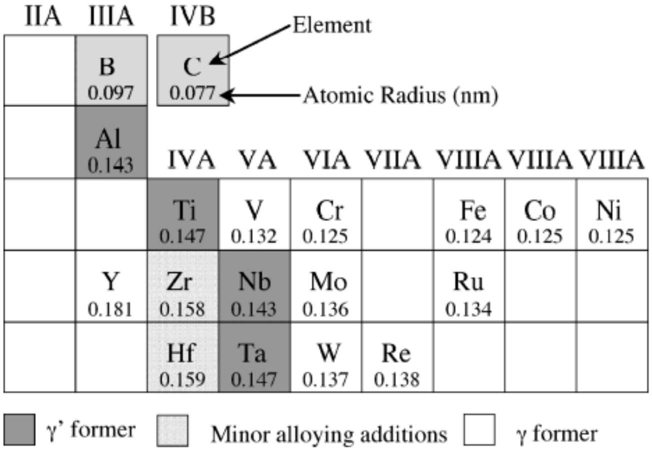

Figure 5: *Alloying elements present in nickel-based superalloys. Reproduced from* [65].

2.2.1 Microstructure of Nickel-based Superalloys

Nickel based superalloys consist of a two-phase equilibrium microstructure consisting of a primary γ matrix and secondary γ’ precipitate phase. Additionally, an important tertiary phase, recognised as carbides, are present at several locations within the microstructure. [63].

The γ matrix is a face-centred cubic (FCC) solid solution of nickel with other elements such as Co, Cr and Mo, in a random distribution. All elements that readily dissolve are considered solid solution formers and are illustrated in Figure 5 as ‘γ formers’ [65]. Solid solution strengthening is why nickel superalloys are much stronger compared to the parent nickel and have improved creep strength of the matrix. This is because the solid solution increases the resistance to the movement of dislocations due to the distortions and shear modulus changes in the lattice [66].

The γ’ precipitate phase is an intermetallic compound that has a primitive cubic lattice where the nickel atoms are at the face-centres and the aluminium or titanium atoms are at the cube corners. This L12 ordered structure is very robust, even at temperatures up to the material’s melting point (1385°C) [65]. Schematics of the crystal structures for γ and γ’ are shown in Figure 6. The γ’ phase develops coherently with the matrix and has a general formula of A_3B, where A represents Ni (electronegative) and B represents elements such as Al, Ti, Nb (electropositive) [63]; typically $Ni_3(Al,Ti)$. The formed precipitates further strengthen the alloy by increasing the resistance of dislocation motion and can act to pin grain boundaries, therefore, dislocations must either bow around the precipitates or cut through them [66].

However, there can be a degree of mismatch, which is relative to the proportions of the γ' forming elements, and when a high mismatch is present it can make the precipitates thermally unstable [63]. Figure 7 shows the microstructural comparison between γ and γ'.

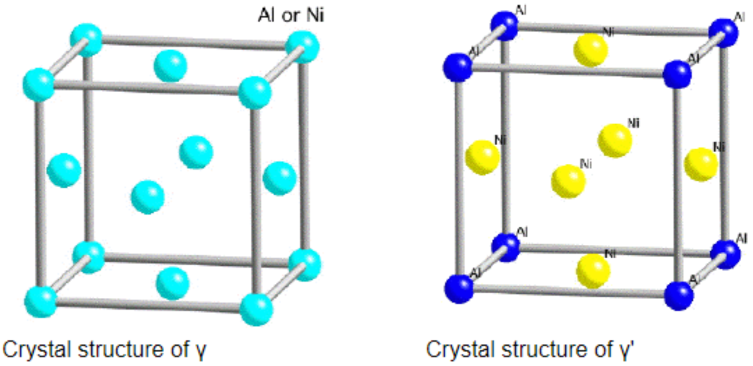

Figure 6: *Schematic diagram to show unit cell for γ and γ'. Reproduced from* [63].

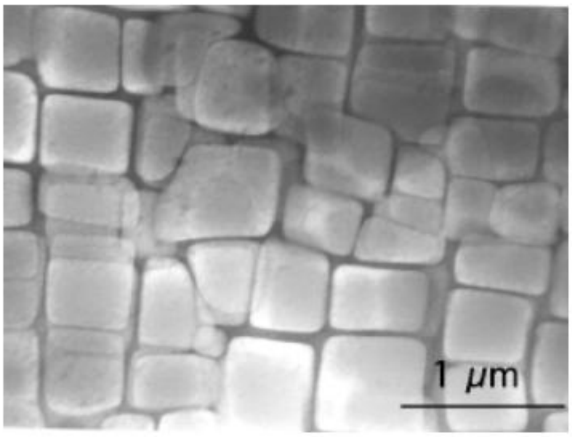

Figure 7: *Transmission electron micrograph showing a large fraction of cuboidal γ' particles in a γ matrix. Ni-9.7Al-1.7Ti-17.1Cr-6.3Co-2.3W at%. Reproduced from* [63].

Carbides have a significant influence on grain structure control and mechanical properties that are strongly influenced by grain boundaries, by restricting grain boundary sliding i.e. creep rupture [65]. There are several forms of carbides that can be present within the microstructure: MC, $M_{23}C_6$, and M_6C, where M represents the metal ion [65,66]. MC has an FCC structure, typically with a coarse cubic morphology, and forms just below the freezing temperature. $M_{23}C_6$ tends to occur at grain boundaries as a block-like particle, which typically forms during lower temperature heat treatment and after service exposure from the degeneration of MC carbides. M_6C presents a complex cubic structure and can develop at grain boundaries, and they form at higher temperatures when the presence of refractory alloying elements is high.

Although there are various phases that are considered beneficial to the microstructural characteristics of Ni-based superalloys, there are a number of undesirable phases [67] that can be present within the microstructure, including topologically close-packed (TCP) phases such as: hexagonal Laves, orthorhombic δ, and tetragonal σ_s, which typically occur at grain boundaries [24].

It is also important to consider 'oxide formers' when discussing the microstructure of nickel based superalloys. Elements considered as oxide formers are Cr and Al. Oxide formers provide an adherent diffusion resistant oxide layer to protect the alloy. In addition, surface oxidation at elevated temperature operations can suppress crack initiation and assist in the closure of microstructurally short cracks [68].

Some Ni-based superalloys, such as IN718 and IN625, have a γ'' precipitate phase with a D022 crystal structure present within the microstructure [69]. This precipitate is a predominant phase for strengthening in these alloys. However, γ'' is a thermodynamically unstable precipitate at relatively high temperatures. For IN718, the γ'' precipitate is only stable up to ~650°C. This is because at prolonged exposure above 650°C, the metastable γ'' precipitate transforms to δ phase with an orthorhombic structure, which results in the deterioration of strength and service life of the alloy [69].

2.2.2 Inconel 718

Introduced in early 1959 by the Huntington Alloy Production Division of INCO (now Special Metals Co.), IN718 was quickly adopted by companies such as General Electric for aerospace engine components [70]. Typical uses of IN718 for the aerospace industry include, but are not limited to: shafts, blades, discs, pressure vessels and supporting structures. Other applications include: rings and pressure vessels in rocket engines, sub-sea valves for the oil and gas industry, and containers used at cryogenic temperatures.

IN718 is a niobium-modified precipitation hardened nickel-based superalloy with the nominal composition shown in Table 1. Its microstructure consists of an FCC matrix of γ (Al) with a high amount of strengthening carbide and intermetallic phases:

FCC γ' $Ni_3(Al,Ti,Nb)$ (L12), ordered tetragonal γ'' Ni_3Nb (D022), and FCC MX (Nb,Ti)(C,N) (B1). The microstructure may also include undesirable TCP phases, such as: hexagonal Laves $(Ni,Fe,Cr)_2(Nb,Mo,Ti)$ (C14), orthorhombic δ $Ni_3(Nb,Ti)$ (D0a), and tetragonal σ_s CrFe (D8b) [24].

Table 1 *- Nominal composition of IN718. Amended from* [24].

Element (wt.%)	**Ni**	**Cr**	**Nb**	**Mo**	**Ti**	**Co**	**Al**	**Fe**
IN718	50-55	17-21	4.8-5.5	2.8-3	0.65-1.15	1	0.2-0.8	Bal.

2.2.3 Properties of Inconel 718

IN718 is designed for strength, creep resistance, and fatigue resistance, at high temperatures of up to ~650°C [71]. Elevated temperature application is more abundant for IN718, but the alloy can be used for some cryogenic applications [72].

The mechanical properties exhibited by wrought IN718 at ambient temperature and elevated temperature are reported in Table 2.

Table 2 *- Mechanical properties of IN718 at ambient and elevated temperature. Amended from* [73].

	Ultimate Tensile Strength (MPa)	**Yield Tensile Strength (MPa)**	**Elongation (%)**
Ambient Temperature (23°C)	1375	1100	25
Elevated Temperature (650°C)	1100	980	18

The dominant strengthening mechanism of IN718 is due to the metastable γ'' and γ' phases, which are coherent with the γ FCC matrix and heat treatments are typically employed to optimise the precipitation of these phases. The strength of IN718 can be optimised by precipitating γ''(Ni_3Nb) and γ'($Ni_3(Al,Ti)$) phases in the γ matrix to a volume fraction of 16% and 4%, respectively, via heat treatments [24,71]. However, over aging during heat treatment can transform γ'' to incoherent δ precipitates, causing a decrease in the material's strength [24]. The δ phase is detailed more in section 2.2.11 with supporting micrographs.

Good weldability is another admirable characteristic of IN718, which is due to its relatively slow precipitation kinetics. However, high refractory element segregation e.g. Nb or Mo, from the solidification process during casting or welding can lead to the formation of Laves phases $(Ni,Fe,Cr)_2(Nb,Mo,Ti)$ at the interdendritic regions. Laves phase are detrimental to the material's strength, ductility, fatigue, and creep rupture properties, by offering easier crack initiation and propagation, and depleting the main elements needed for precipitation strengthening [71]. The Laves phase is discussed in more detail in section 2.2.5.

2.2.4 Inconel 718 for Industry

Given the exceptional properties of IN718 discussed previously, companies widely utilise IN718 for industrial components. The combination of mechanical properties with good manufacturability, as well as relatively low cost, has meant for wide application for hot-section component application e.g. for industrial gas turbines and many aerospace engine components [70,74]. It is suggested that 30% of the total finished component weight of a modern aircraft engine is comprised of IN718 [24,71].

Many of the mentioned in-service applications require operating across a large temperature range. IN718 offers a maximum operating temperature of up to approximately 650°C [69], therefore has the ability to be used for such applications. Consequently, research of the materials microstructural changes at maximum operating temperature, and the influence on the mechanical properties is necessary for industry.

2.2.5 Traditional Manufacturing of Inconel 718

With high industrial demand of IN718 components, manufacturing of nickel-based superalloys, such as IN718, is undertaken worldwide across multiple production facilities performing a range of methods. One method typically used for some gas turbine rotating parts includes a complex triple melt process that requires extremely low purity levels. The triple melt process typically involves a combination of vacuum induction melting (VIM), electroslag remelting (ESR) and vacuum arc remelting (VAR) [75]. Following the melt process, the molten metal can be processed to various mill forms such as plate, sheet, bar and wire. However, conventionally casting ingots after the melt process is typically more popular [75]. After the ingot is produced, there may be a final melt process, before producing the final part.

After melting, traditionally, the IN718 component is either cast, forged, or welded (or joined via another joining method). The method used from the list mentioned prior, is dictated by the geometric and mechanical needs for the component being made.

Due to the challenges with machining IN718, investment casting is a favoured option for producing accurate parts that are near-net shape. There is still need for some final machining once the part is produced but this process is cost effective for complex parts that are needed in high volumes. Vacuum investment casting is the most popular casting process for IN718, as it eliminates porosity issues that are prevalent in non-vacuum casting processes. For vacuum investment casting, a mould is made the same way as for normal investment casting. The mould is made by coating a wax pattern with a ceramic slurry, which once dried, is put through a thermal cycle to remove the wax core, leaving a ceramic shell with the desired component shape. Before filling with molten metal, the air is pumped out of the mould cavity. This whole process typically takes place within a vacuum induction melting machine, where the ceramic investment shell is placed in a lower chamber, below a melt crucible. Once in place the molten metal is poured in to fill the mould. Once full, the metal is left to solidify. After, the ceramic mould is then removed to reveal the cast part. Cast IN718 has a microstructure consisting of two main compositions, that are heavily segregated: dendritic regions are rich in Fe, Cr, and Ni, whereas the interdendritic regions are high in Nb, Mo and Ti [76]. The segregation is controlled by the rate of cooling; the faster the cooling, the less segregated. This variation is demonstrated in Figure 8. Consequently, post thermal processing is a necessity. Although conventional casting has its advantages, it also poses challenges regarding manufacturing of complex IN718 components, such as turbine blades with internal cooling nozzles or numerous tiny nozzles of liquid rocket engine injectors [24].

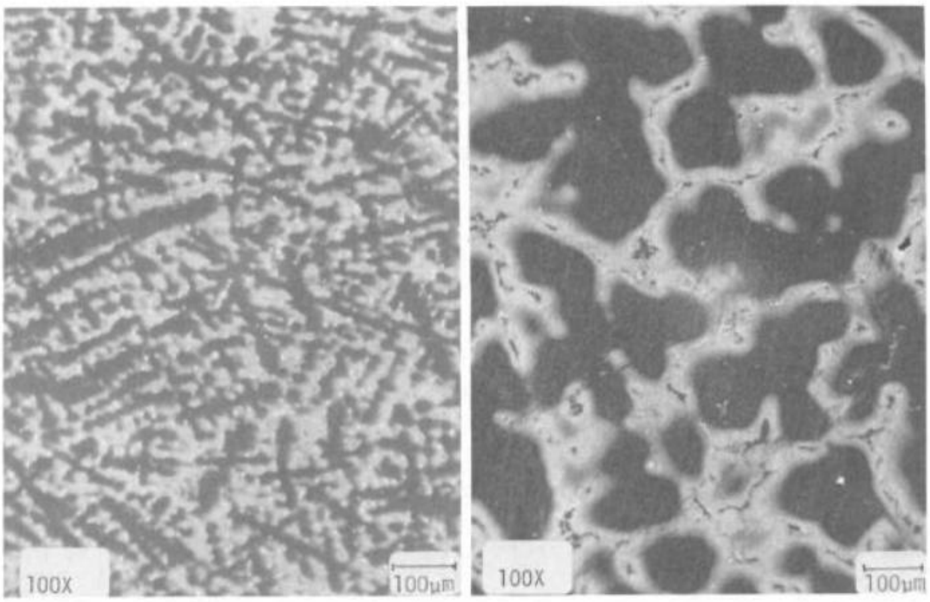

Figure 8: *Typical IN718 microstructures. Micrograph on the left shows fine grain as-cast IN718 and the micrograph on the right shows large grain as-cast IN718. Reproduced from* [76].

Alternatively, wrought IN718 can be produced by forming the material into a desired shape by using methods such as forging, rolling, hammering, and extruding etc. but typical processing involves some kind of 'heat and beat' method [76]. These processes induce plastic work into the material and achieves geometries such as bar or sheet. With the use of heat and deformation, microstructural control during the process can improve material quality as larger inclusions can be broken down into smaller ones whilst also encouraging grain refinement via recrystallisation [77]. Consequently, this is why some critical applications such as disks are only accepted in the wrought state. The associated microstructure for wrought IN718 is displayed in Figure 9.

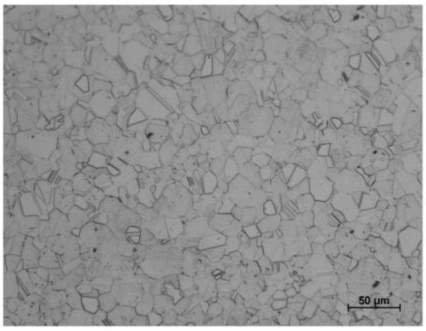

Figure 9: *Micrograph of IN718 in cold-rolled sheet, heat-treated (in accordance with AMS 5596) condition. Reproduced from* [78].

There are various heat treatments that can be adopted for IN718, but they are typically split into three main sections: homogenisation, solution annealing, and aging [79]. For homogenisation, temperatures typically exceed ~1060°C, causing partial homogenisation of Nb and Ti, without causing δ growth but encouraging recrystallisation and grain growth. Solution annealing typically occurs between ~850°C and ~1060°C in order to contribute to δ growth, rather than Nb and Ti homogenisation, and typically inhibits recrystallisation and grain growth. Aging tends to occur between ~620°C and ~760°C and promotes γ', γ'' (and sometimes δ) growth. Facilities used for these processes are usually low-dew-point argon or vacuum furnaces. Implementation of varying combinations of homogenisation, solution annealing, and aging, allow for manipulation of the IN718 microstructure, in order to provide desired mechanical properties [80–84].

Prior to heat treatment, components with high porosity typically undergo a HIP process. HIP involves compressing the finished component by applying elevated temperature and high isostatic pressure. The pressure medium is usually argon. The process is conducted to decrease porosity, improve density, homogenise the alloy, and overall, improve the creep and fatigue properties of the alloy, making this process essential for safety critical components. For IN718, HIP treatment normally occurs for three hours at 120MPa and a temperature of 1200°C [85]. Early research by Schirra et al. [86] reported on the influence of HIP on Laves phase in wrought and cast IN718. They demonstrated that Laves phase could be minimised through the use of a homogenisation heat treatment, as demonstrated by Figure 10. This control was proposed as Laves phase can have a deleterious effect on properties of IN718.

been quick to adopt and research new manufacturing technologies, such as AM, that reduce, if not remove, the need for post-build machining.

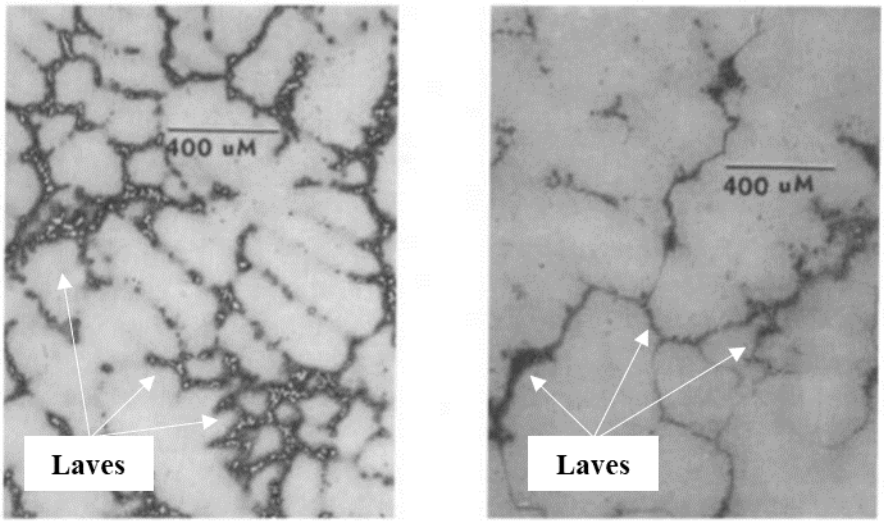

Figure 10: *Cast IN718 at 2°C/minute from 1371° to 1177°C, and then processing through the following thermal cycles: (left image) 1107°C/2 hours HIP, and (right image) 1135°C/8 hours + 1149°C/16 hours pre-HIP heat treat + 1191°C/4 hours HIP. Amended from [86].*

Although HIP improves microstructural and mechanical features of the component, surface features such as surface pores or microcracks will need to be relieved via post-processing methods such as machining.

Machining of IN718 components is a difficult process due to the alloy's low thermal conductivity, work hardening, and tendency to adhere to cutting tools [87]. During machining, the heat generated between the tool-chip interface causes poor tool life, low dimensional stability of the workpiece and inferior surface finish [87]. It also causes excessive tool wear and low material removal rates, making machining costly and time consuming. Research to improve conventional machining and tooling methodologies for IN718 has and is being carried out [88–90]. However, industry has

2.2.6 Additive Manufacturing of Inconel 718

Limitations of traditional manufacturing of IN718 can be overcome through the use of AM, as it has the potential to improve component performance, design flexibility, weight, rapid prototyping capability and reduce manufacturing cost [55]. However, the adoption and utilisation of AM in industry is influenced by the overall properties of a component designed and printed via AM. The resultant properties are heavily dictated by the manufacturing process and resulting microstructure.

2.2.7 Process-Structure-Property

Utilisation of AM to support or replace traditional manufacturing techniques requires a deeper level of understanding between the manufacturing process, how the process affects the microstructure, and how the microstructure influences the mechanical properties of the printed component. This ‘link’ is also sometimes referred to as PSP.

The ‘process’ section of PSP refers to parameters involved in the manufacturing plan, whether this be powder based (e.g. chemistry, particle morphology, particle size distribution), process parameter based (e.g. build orientation, laser power, layer thickness) or post-processed based (e.g. heat treatment route, use of hot-isostatic pressing).

For the ‘structure’ section of PSP, this relates to the variation in microstructure from the different manufacturing processes. For example, the microstructure of AM IN718 is presented as a supersaturated solid solution with inter-dendritic micro-segregation, compared to the cast microstructure of IN718, which typically consists of macro-segregation of Nb and Mo. In addition, grain growth of AM IN718 is heavily influenced by the direction of heat, giving rise to grains directed in one of the <001> directions.

Finally, the ‘property’ section of PSP refers to the resulting mechanical performance of the printed component, which is linked heavily to the microstructure of the AM part. Following the example used for the ‘structure’ section of PSP, the presence of directional, columnar grains, gives rise to mechanical anisotropy.

2.2.8 Process Parameters for Laser Powder Bed Fusion

Process parameters are a set of “operating parameters and system settings that are used during a build cycle” [26]. For laser powder bed systems there are a number of process parameters that can arise and need to be controlled. These parameters can be classed as either machine input parameters (also known as primary parameters), or input parameters that can arise from the characteristics of the material being used. Both types of process parameters influence the microstructural and mechanical features of the component produced via AM. Hence, these parameters have, and still are, heavily researched to find ultimate optimisation for a given material. Machine input parameters are those that relate to laser speed and power, point distance, exposure time, and hatch spacing. In addition, layer thickness and scan patterns are considered machine parameters. Some of these parameters are depicted in Figure 11. Material input parameters include thermal characteristics (e.g. melting temperature and thermal conductivity), powder characteristics (e.g. particle size, roughness and morphology), and metallurgical characteristics (e.g. alloy composition and diffusion coefficient). To produce high quality, fully dense, components, optimum process parameters must be identified and utilised.

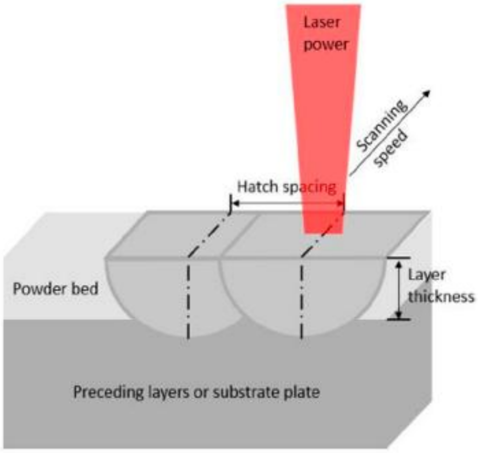

Figure 11: *PBF-LB process parameters: hatch spacing, laser power, layer thickness and scanning speed. Reproduced from* [91].

As PBF-LB is a layer-by-layer process, it is fundamental to understand the single tracks that compose each layer. When a laser beam passes over the powder bed, the energy heats the powder particles, causing them to melt and form a melt pool. Once the laser beam has passed over the area, the melt pool then begins to cool and solidify. Therefore, controlling a stable melt pool by using optimum process parameters is important during PBF-LB. The sequential heating and cooling, and layer-by-layer process, causes a fine microstructure with anisotropic properties, when compared to conventional processes [32,92]. The type of microstructure present once the melt pool is solidified is dictated by the thermal gradient, G, and growth rate, R_g – Figure 12 – which is similar to the basic principles of welding. For alloys such as austenitic steels, aluminium alloys, and nickel-based alloys produced via PBF-LB, it is typical to observe epitaxial nucleation and cellular or cellular/dendritic crystallisation [32]. When considering the gradient G, if it is steep, then the material will crystallise in a directional cellular mode, whereas if the gradient is sloping mildly, then directionally solidified dendrites with well-developed arms will form [32]. The latter microstructure is more prevalent in DED.

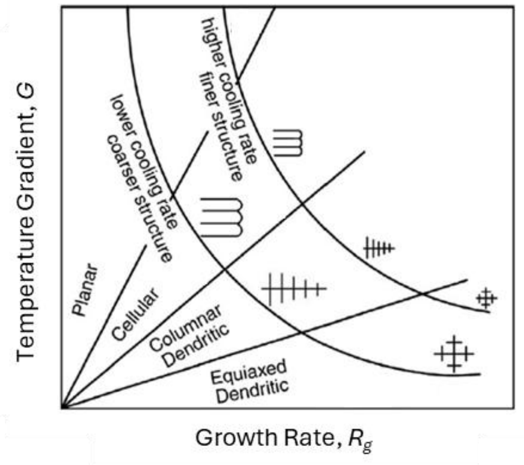

Figure 12: *Morphology of microstructure influenced by temperature gradient, G, and growth rate,* R_g*. Amended from [32].*

Understanding the machine input parameters and their definitions is essential, as varying these parameters has a significant effect on the quality of the build component. For laser power, this is the total energy emitted by the laser per unit time, and when discussing laser speed, this is defined by the point distance divided by exposure time. Point distance is the distance between the laser spots and exposure time is the duration of which the laser source heats one spot. Focusing on the laser speed and power: 1) Low laser power and low scanning speed causes an insufficient energy density to melt and bind the powder particles together. Consequently, partial melting in the final component can be present as defects such as lack of fusion (LoF). 2) High laser power and low scan speed melts the powder layer sufficiently, giving better densification, but can form irregularities such as keyholes. 3) High laser power and high scan speed can lead to an unstable melt pool which can lead to balling. Given these scenarios with various laser power and laser speed parameters, it suggests that there should be an optimal process parameter region where there is little to no defects produced, as depicted in Figure 13. The optimum process parameter region on Figure 13 shows where the right combination of laser power and laser speed creates a stable melt pool of the required size, with sufficient depth to bond with the layer below, without re-melting excessively.

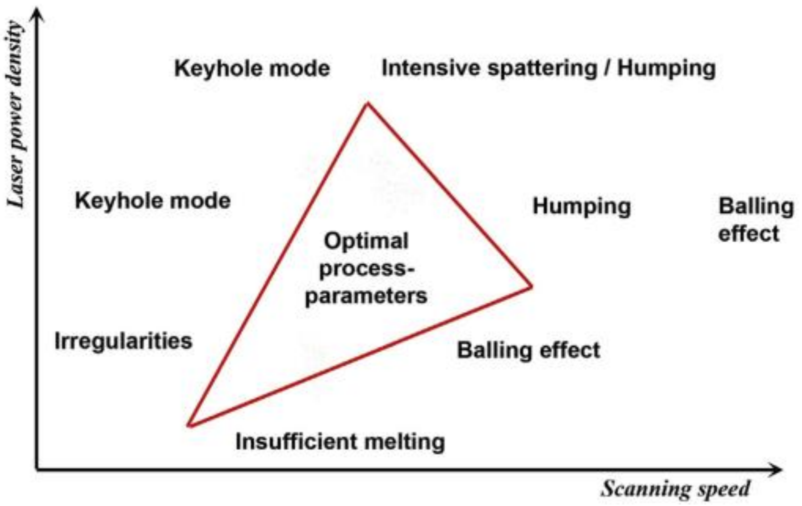

***Figure 13:** Diagram to represent the optimum process parameters for laser power and laser speed. Reproduced from* [32].

Another machine parameter is the hatch spacing; this is the distance between the adjacent paths of the laser beam, allowing for beam overlap. When setting hatch parameters for a build, layer strategy and layer rotation will also be set. Layer strategy is the pattern that the laser will follow within a layer and the layer rotation is the rotation of the layer between each layer. Regarding hatch distance (otherwise known as hatch spacing), setting the distance too close can cause excess energy input and setting the distance too far can cause lack of contact between molten regions. In addition, layer thickness can affect the quality of the build component. Thin layers are preferred for reduced scan times and successful PBF-LB built parts. However, thinner layers require more time than thicker layers. On the other hand, having thicker layers with a specified laser power can cause inadequate energy to be absorbed per unit volume, leading to balling [91]. The final machine input to discuss is the scan strategy, this can include the scanning direction and the order of the scan sequence. Scan strategies are important as they influence the cooling time of the single layers, affecting the overall microstructure of the component. Research by Al-Lami et al. [93] compared microstructural features and tensile responses of horizontal PBF-LB IN718 fabricated using different scan strategies: B0, a bidirectional strategy with 0° interlayer rotation, and CB67, a chessboard strategy with 67° interlayer rotation. The research conducted showed that the B0 strategy created an ordered structure with coarse grains separated by finer grain clusters. Consequently, under tensile loading deformation was uneven due to plastic strain localisation, making B0 unsuitable for high-performance applications despite its higher tensile strength. In contrast, the CB67 strategy introduced layer rotation, producing a more randomized texture and dislocation distribution, reducing anisotropy, and enabling more uniform deformation – making it the preferred choice for improved mechanical performance in AM Inconel 718.

2.2.9 Microstructure of Additive Manufactured Inconel 718

Typical AM parameters for IN718 will give an expected microstructure consisting of a columnar structure in the X and Y planes (parallel to the build direction) and an equiaxial structure in the Z plane (where the Z plane is the scanning surface, perpendicular to the build direction), as demonstrated by Figure 14. The columnar structure is present throughout several layers due to epitaxial growth from partial re-melting and heterogenous nucleation of γ dendrites [24]. In comparison, the layers closer to the build platform appear less columnar and more equiaxed due to the larger cooling rate from the direct contact to the build platform. The lower cooling rate seen further away from the build platform promotes micro-segregation, causing a higher percentage of Laves phase, with some presence of large, continuous Laves networks.

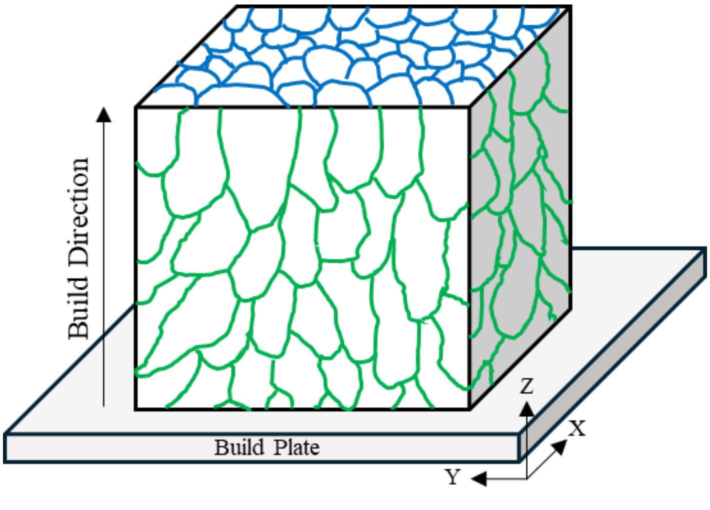

Figure 14: *Schematic of epitaxial growth with respect to build direction.*

The usual IN718 AM microstructure is exhibited and compared to investment cast IN718 by Pereira et al [94], in the as-built/as-cast and heat-treated conditions (TT0 is standard heat treatment, TT1 is a modified HT, and TT2 is direct aging), all shown in Figure 15. For the as-built condition, the Y-axis and Z-axis exhibit a fine cellular microstructure from the rapid solidification and high cooling rates from the PBF-LB process. The variation in microstructure on each direction indicates anisotropy.

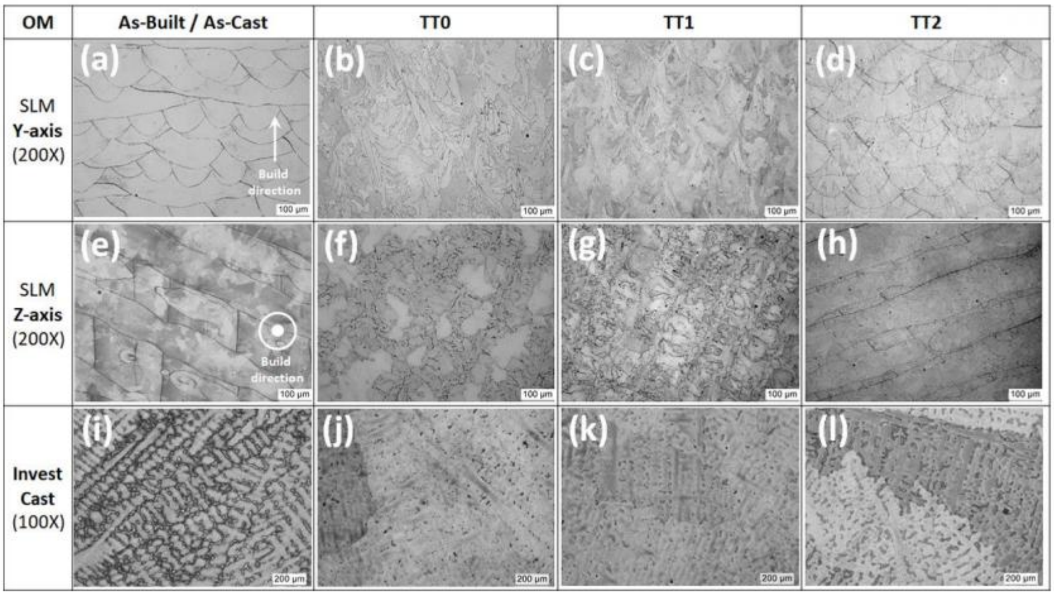

Figure 15: *Optical micrographs for IN718 in as-built/as-cast and heat-treated conditions. (a-d) PBF-LB samples in Y-axis, (e-h) PBF-LB samples in Z-axis, and (i-l) investment casting samples. Reproduced from* [94].

Crystallographic texture of IN718 manufactured via PBF-LB is dependent on the direction of heat flow and dominant growth of grains in one of the six <001> directions, which typically occurs parallel to the build direction. Various textures can be present, depending on the process parameters used, and control of the final texture can be beneficial when designing a component with specific properties e.g. elevated temperature fatigue properties. Gokcekaya et al. [95] demonstrated that varying laser speed and laser power had influence on the microstructure, crystallographic orientation, and mechanical properties of IN718. Variation of laser speed and power affected the thermal gradient and solidification rate, giving either a single-crystal-like microstructure, crystallographic lamellar microstructure, or a polycrystalline microstructure. Popovich et al. [96] investigated varying laser power on PBF-LB IN718. Laser powers of 250W and 900W were employed and showed that the microstructure for the higher laser power (950W) had a coarser microstructure when compared to the lower laser power. It was also noted that the porosity measured for the 950W areas showed nearly three times more porosity (~ 0.27%) than for the 250W areas (~ 0.11%). In addition, Thanumoorthy et al. [97] demonstrated that varying infill strategies with DED heavily influenced the texture. Utilisation of inverse pole figures (IPF) demonstrated that material produced with a 0° infill showed strong texture with a multiple of uniform density (MUD) value of 11.095, whereas a sample with 67° infill rotation showed weak texture with a MUD value of 3.984.

Anisotropic microstructures presented by AM components is of key interest to researchers, particularly the effects of mechanical loading direction or component build direction [98–101]. This is needed for the design of AM components that require mechanical properties in a given direction.

Ghorbanpour et el. [98] studied the relationship between microstructural anisotropy and fatigue crack growth behaviour of functionally graded and non-functionally graded IN718 fabricated via PBF-LB. A comparison to wrought material and hardness testing was also investigated. Different microstructures were induced in the AM samples by varying the laser power (250W and 950W) and laser speed (700mm/s and 320mm/s). For the various parameter controls, it was optimised to give approximately the same volume energy density for each build. The different builds consisted of vertical and horizontally fabricated samples, where the predicted crack path was aligned with the sample's vertical symmetry axis. The horizontal samples with the higher laser power were highly affected by the build parameters, showing strong <100> texture with elongated grains in the build direction. Analysis of the fatigue crack growth at a low stress ratio (R=0.1) on the non-graded IN718 material concluded that the 250W samples were the only samples to exhibit fatigue behaviour comparable to the wrought heat treated material. Hardness values across the non-graded PBF-LB IN718 was lower than that of the wrought material, due to the finer grains and strengthening precipitates present in the wrought material.

Alongside anisotropy, residual stress can form during the manufacturing of AM parts. Understanding the development and the subsequent effect of residual stress on mechanical performance and developing the procedures to remove residual stress is necessary, as the presence of residual stress can detrimentally affect AM components by causing cracking in the alloy [102]. Consequently, heat treatment and post-processing is utilised to remove stresses or cracking.

Overall, for industries to fully accept AM, a strong understanding between the AM process, the microstructure of the component, the properties of the component, and the overall performance of the component, is essential. The link between the process and presence of defects has been studied e.g. LoF can arise when the scan speed is too fast and there is too little power, and keyholes occur when there is too much power for a chosen speed [32,103].

2.2.10 Mechanical Behaviour of Additive Manufactured Inconel 718

An extensive review of the mechanical behaviour of IN718 components produced via various AM techniques was conducted by Hosseini et al. [24] who showed tensile results on different variants of IN718. Figure 16 and Figure 17 report the room temperature tensile data for as-built and heat treated AM IN718 samples, with a comparison to the wrought and cast counterparts. Data from the figures shows that the strength of the as-built IN718 AM samples is lower, and the ductility is lower, when compared to the heat treated samples. It was concluded that this was due to the absence of the primary strengthening mechanism in the as-built alloy; precipitation hardening of γ' and γ''. In addition, it was noted for both the heat treated and as-built samples that the reported strength values for AM IN718 was between that of the cast and wrought samples. Superior strength of AM IN718 compared to its cast counterpart was linked to the fine microstructure produced in AM. For any inferior properties observed, porosity was identified as the main attributer. Furthermore, a comparison between the PBF-LB and EBM data conducted by Hosseini et al. revealed higher strength for the as-built EBM samples. This was owing to the higher processing temperature, that possibly led to in-situ precipitation hardening of the alloy during fabrication via EBM [104].

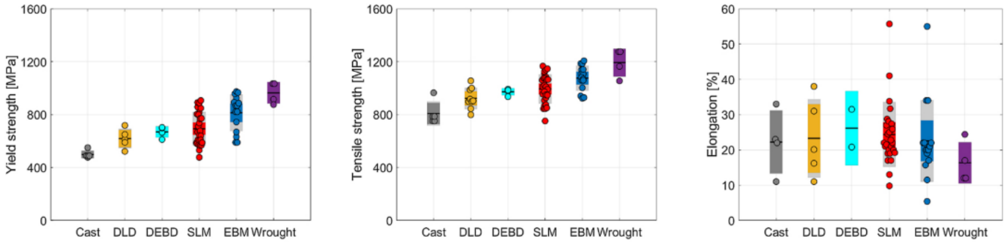

(a) (b) (c)

Figure 16: *Tensile properties of cast, wrought and as-built AM IN718 a) yield strength, b) ultimate tensile strength and c) elongation. The graphs show standard deviation and standard error. Reproduced from* [24].

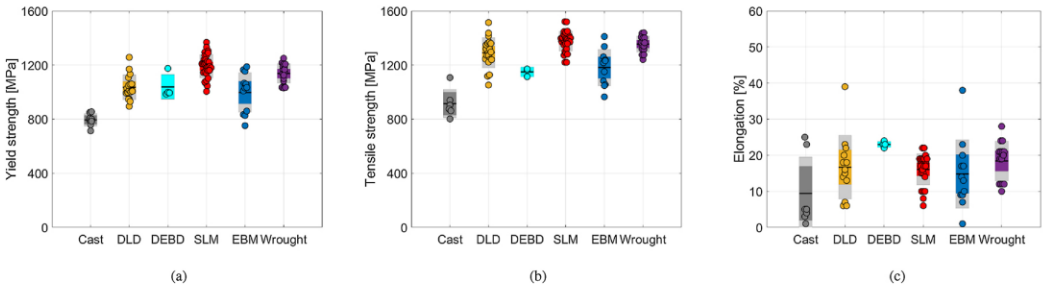

Figure 17: *Tensile properties of cast, wrought and fully heat treated AM IN718 a) yield strength, b) ultimate tensile strength and c) elongation. The graphs show standard deviation and standard error. Reproduced from* [24].

Hosseini et al also collated data to demonstrate anisotropy effects in AM IN718, as shown in Figure 18. They found higher ductility, lower yield strength and elastic modulus in samples built parallel to the build direction, which was attributed to the common <001> texture and columnar grain morphology, as opposed to those built perpendicular or diagonally.

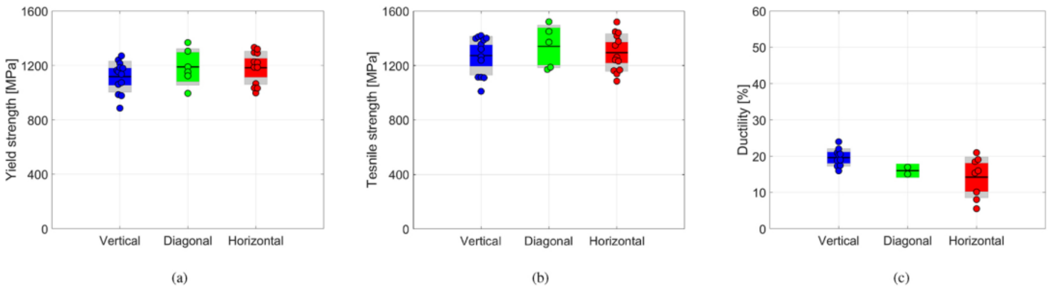

Figure 18: *Anisotropy of reviewed tensile test data for AM samples printed in the vertical, diagonal (45°) and horizontal orientations. The graphs show standard deviation and standard error. Reproduced from* [24].

Alternate work by Popovich et al. [96] showed that the texture of IN718 is heavily influenced the Young's modulus. The lowest elastic modulus (~113GPa) was seen in regions of coarser grains with {100} texture.

To reduce the microstructural effect on the mechanical properties of AM components, it is typical to conduct post-processing.

2.2.11 Post-processing of Additive Manufactured Inconel 718

After consolidation of the alloy to form the as-built structure, subsequent post-processing is typically required to meet the required microstructural and mechanical properties of the final component. For IN718, typical post-processes include stress relieving to reduce residual stresses in the component, HIP to remove flaws and porosity, solution and homogenisation steps to control δ and the Laves phase, final aging steps to form strengthening phases, and machining to remove any surface discontinuities.

Reducing residual stress, prior to removal of the AM built components from the build plate, is a key post-processing technique to reduce the negative effect of cracking, delamination or distortion. In a recent study, Gruber et al. [105] demonstrated that the standard stress relieving procedure for IN718 (1065°C for 1.5 hours) reduced the macro-residual stress within as-built components, whereas elevated temperature stress relieving (1150°C for 6 hours) reduced macro-residual stress and micro-residual stress. The elevated temperature stress relieving generated an isotropic, recrystallised microstructure, whereas the standard stress relieving treatment left the microstructure non-recrystallised.

HIP is commonly used for castings [106] but has also been considered to eradicate intrinsic defects in metallic AM parts such as cracks and pores. This process is necessary when wanting to achieve near 100% density. Research into reduced fatigue strength of IN718 due to porosity in PBF-LB components was undertaken by Tillmann et al. [107], who discussed the reduction in porosity achieved by varying HIP parameters. Use of micro X-ray computed tomography (µCT) and a scanning electron microscope (SEM) enabled Tillmann et al. to conclude that the use of HIP could improve the relative density of the components fabricated via PBF-LB. Varying the HIP parameters showed that process temperature had a greater effect on the densification than process pressure. Furthermore, it was noted that the HIP process caused grain enlargement, reducing the characteristic structure associated with PBF-LB. However, final conclusions showed that it would be unlikely to achieve 100% dense parts due to argon entrapment.

Although HIP shows many benefits in improving the microstructural and mechanical properties of as-built components, it can be time consuming and costly. Current research for conventional manufacturing by Bernal et al. [108] considers integration of HIP with the typical heat treatment process for modified Ti-Nb-Mo alloys, into one single route. This could be something that future AM incorporates to reduce post-processing times.

Due to the large variation in microstructure of AM and conventionally manufactured IN718, common heat treatments have been developed specifically for AM materials. Evolution of an as-built microstructure to a post-heat treatment microstructure has been assessed in various literary sources [109–112]. This includes Tajyar et al. [113], where research into the effects of various heat treatments on the microstructural and mechanical properties of AM IN718 was presented. Comparison of as-built IN718 against two different heat treatments, modified solution heat treatment – heated to 1160°C for 4 hours, and modified annealed heat treatment (heated to 1160°C for 4 hours, followed by two-step aging heat treatment consisting of two thermal routes at 720°C for 8 hours, furnace cooling to 620°C for 8 hours, and a final air-cooling stage), was conducted. Microscopy showed the as-built samples had a fine cellular and columnar structure, attributed to the thermal gradient during fabrication. Whereas, the microscopy for the modified solution heat treatment samples showed a more uniform structure with coarser grains, likely due to the ET being above the solvus temperature of the δ phase and Laves phase. However, the modified solution heat treatment samples did show larger carbides present in the microstructure, which was attributed to the increased diffusion rate. Modified annealed HT samples showed a similar microstructure to modified solution HT, but with an even more homogenous distribution of γ”. The change in microstructure subsequently influenced the hardness properties; hardness decreased after modified solution heat treatment and increased after modified annealed HT.

Further research by Heo et al. [114] considered the influence of build orientation (vertical (V) and horizontal (H)) and post-process heat treatment (as-built, homogenization + solution + aging, homogenization + aging, and solution + aging) on the microstructure and primary strengthening phases in IN718 produced via PBF-LB. The detailed heat treatments with respective field emission gun-scanning electron microscope (FEG-SEM) images are shown in Figure 19. Linking the microstructure of the different heat treatments to their respective tensile tests showed the significant role of δ phase distribution and Laves phases in determining tensile strength. Excess or insufficient δ phase and the presence of Laves phases negatively impacted tensile properties. The solution + aging heat treatment offers the best tensile strength, attributed to optimal δ and γ″ phase precipitation and fine microstructure.

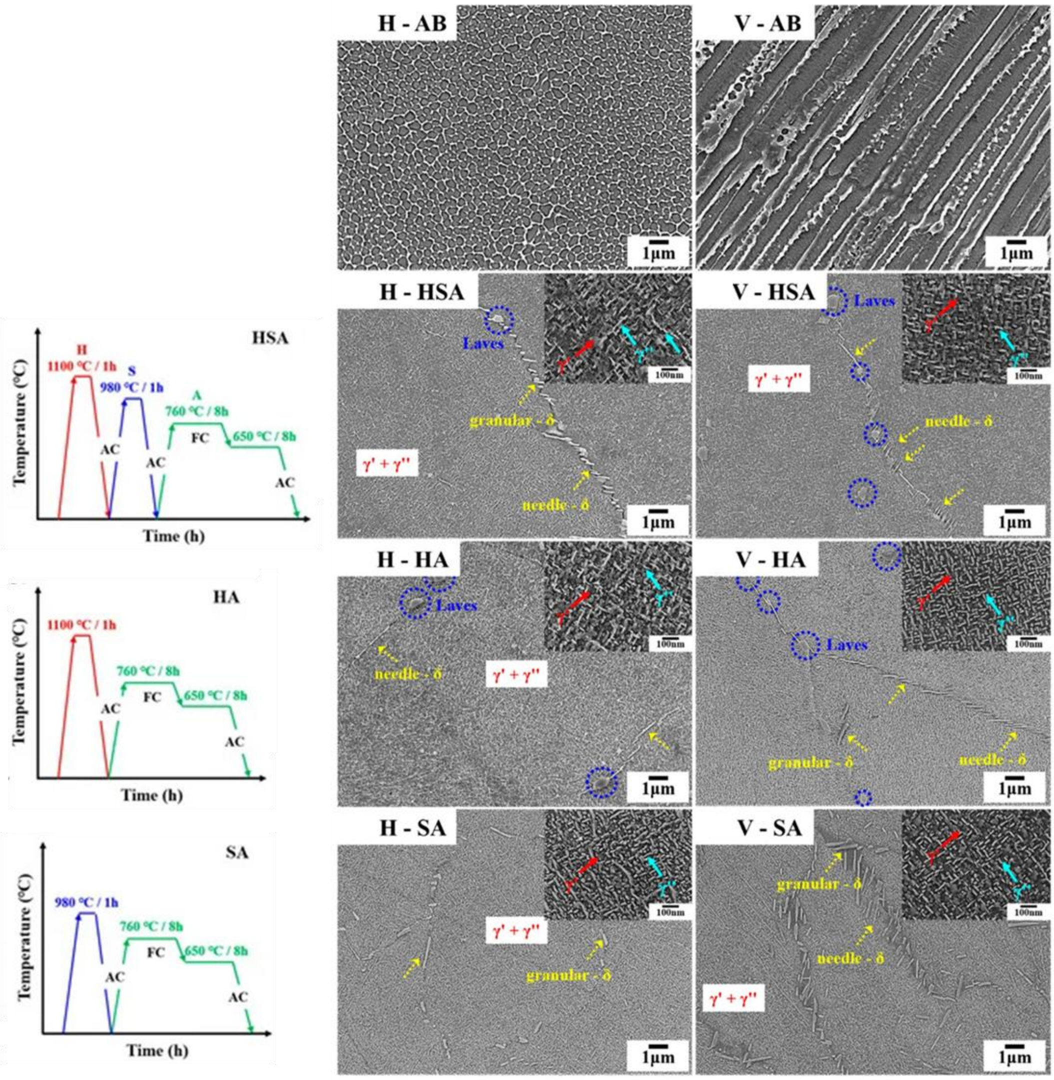

Figure 19: *Heat treatment routes with respective FEG-SEM images of aligned δ precipitates and Laves phase in the building direction with higher magnification images of γ' and γ" phases for varying build orientation and heat treatment (as labelled). Amended from [114].*

Li et al. [115] conducted high temperature (650°C) tensile testing on PBF-LB IN718 with varying heat treatments. The as-built samples showed moderate strength at room temperature and 650 °C due to few precipitates. Solution treatment yielded similar strength and ductility, as the effect of fine δ particles was offset by grain growth. Both as-built and solution-treated samples fell below AMS tensile requirements. However, solution treatment followed by double aging greatly improved properties, reaching 1394 MPa and 18.6% elongation at room temperature, and 1124 MPa and 12.3% elongation at 650 °C, due to finely dispersed γ' and γ'' nanoprecipitates, comparable to wrought alloys.

After completing the relevant thermal cycles, it is typical to machine and finish components to ensure any surface flaws are removed, since surface condition has a large influence on the fatigue properties of IN718. Lee at al. [116] investigated the effect of five surface treatments on the surface topography of IN718 produced via PBF-LB. The five treatments were: sand-blasting, drag-finishing, turning, grinding, and grinding + drag-finishing. The investigation concluded that the finishing techniques that removed the most material (turning, grinding, and grinding + drag-finishing), produced samples with a more improved surface condition and fatigue performance, when compared to the less aggressive techniques (sand-blasting and drag-finishing). It was also discussed that the machining marks from the finishing processes, acted as stress raisers that could initiate cracks from the surface.

2.2.12 Defects in Additive Manufactured Inconel 718

For AM production it is important to consider structural integrity. Structural integrity can be affected by flaws, anomalies, defects, and rogue defects, and is highly dependent on their distribution within the material. When discussing flaws this is a general term that covers all imperfections that are potential stress raisers that initiate, grow, and fracture from cracks developing under cyclic and steady loads. More specifically, an anomaly is a flaw that is likely to be present within the material, meaning if present, it could still be integrally sound for use. Whereas, a defect is a flaw that is less likely to be present and if found in a part will not be accepted for use due to the detrimental impact it has on service life. Also, a rogue defect is a very rare defect that has an even larger detrimental impact on part service life. Consequently, the presence of defects in AM components can be detrimental and concerns surrounding defects present within AM parts is the main reason that AM has not been widely accepted for use in safety-critical parts or as an alternative method to traditional manufacturing. The generation of defects within AM components is typically linked to the process parameters [103], which were discussed in the previous section, and are depicted in Figure 20.

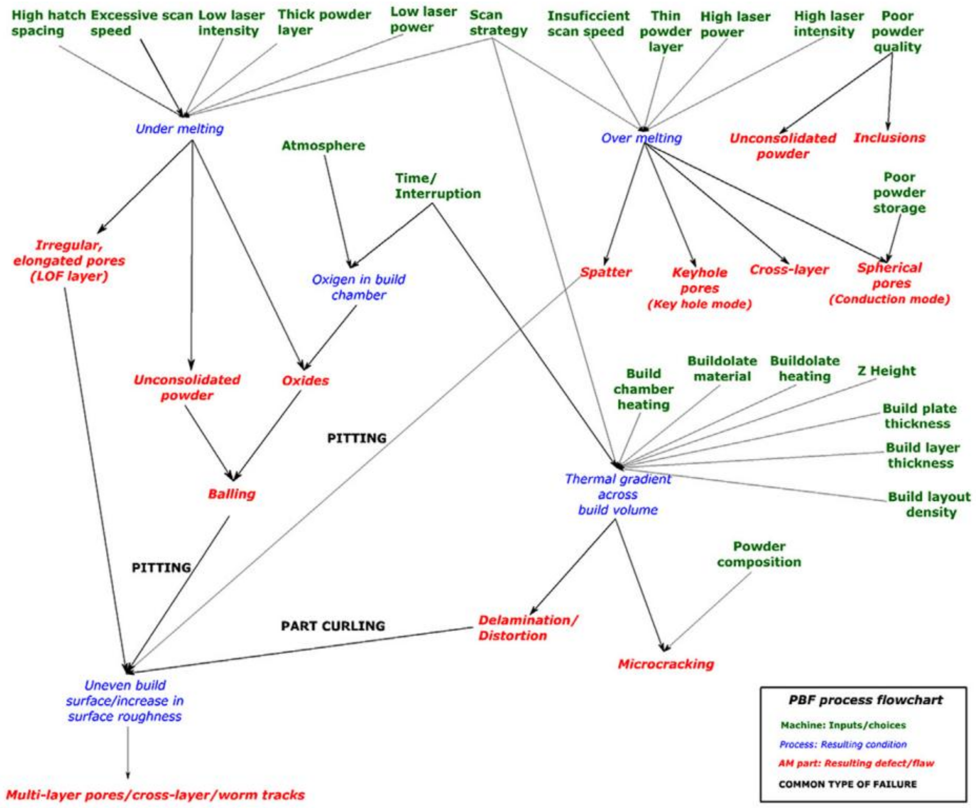

Figure 20: *Flowchart to show defect generation in powder bed fusion process. Reproduced from* [103,117].

Porosity is a typical feature seen in AM IN718 and is an important defect when considering part density. There are various forms of porosity within AM built components: gas porosity, LoF and keyhole collapse. All types of pores described, if present, can act as stress raisers and be detrimental to service life. However, if not surface connected, can be removed via post processing e.g. HIP.

Round circular pores tend to be due to the entrapment of gas, and are referred to as gas pores. It can be possible for gas pores to also form via supersaturation of dissolved gasses or a chemical reaction that produces a gas within the molten pool. Gas pores formed via a powder bed process are typically 5 to 20µm in size [33]. Irregular shaped porosity is referred to as LoF, which occurs when powder is not fully molten and fused during the PBF-LB process [24]. Specifically, LoF are defects of irregular shape that range from 50µm to several millimetres in size and it is common to find unmelted powder particles in the LoF region [33]. Keyhole porosity forms when keyholes become unstable and repeatedly form and collapse, entrapping vapor to form a void; typically measuring 10 to 50µm in size [33].

Xu et al. [118] confirmed the influence of volumetric energy density of the laser on the relative density of the components produced via PBF-LB. Analysis showed that a volume energy density of 80 – 110J/mm^3 achieved optimum relative density of more than 99%. At lower laser energy densities there was insufficient energy, which led to poor fluidity and insufficient filling, causing LoF. Whereas, at higher laser energy densities, excessive energy caused high thermal stress and evaporation of elements, leading to the formation of gas pores. Presence of gas pores in the above-optimum laser volume energy density resulted in a reduction of the microhardness.

Density of the final AM component can also be affected by cracks within the structure. Cracks can occur in two ways: either 1) hot cracking, which is formed from the deformation in the solid structure from part solidification or insufficient convection in the liquid region or 2) cold cracking, which is linked to residual stresses, from rapid expansion and contraction from the thermal cycles.

Most AM parts produced are subject to poor surface roughness, which typically arises from non-optimal conditions such as wide layer thickness, large powder size, the stair-casing effect and increased amount of balling. As the main advantage with AM is the production of near-net shaped components without post-processing, the poor surface roughness is a hinderance. Increased surface roughness provides a high stress intensity factor, therefore, increasing the likeliness of crack initiation at the surface and subsequently, reducing fatigue life. Commonly, poor surface roughness is overcome by final polishing.

The effect of surface roughness on the mechanical behaviour of PBF-LB IN718 was investigated by Gockel et al. [119], where links between AM process parameters and surface roughness were analysed and linked with fatigue life. Using various surface roughness measurement techniques, it was linked that *Sa* (arithmetic mean height) decreases with an increase in laser power. Also, it was concluded that *Sv* (maximum pit height) decreases with increasing laser power and increases with an increasing speed. Further correlation between surface roughness measurements and fatigue life showed that an increase in *Sv* causes a reduction in fatigue life. Also, fractography indicated that high roughness and maximum notch values caused large notches due to a lack of adhesion between layers, creating initiation sites. Whereas, when there was adequate adhesion between layers, notches were smaller, so failures were more influenced by factors such as inclusions or subsurface porosity.

2.3 Mechanical Behaviour of Additive Manufactured Materials

For alloys that are used in components with possible exposure to elevated temperature, such as IN718, service life is a key consideration, with vulnerability to various damage mechanisms. The ability to design the component, with known mechanical properties, so it does not excessively deform and cause ultimate failure is therefore of high importance. These mechanical properties are obtained by conducting various laboratory based experiments that replicate the environment of the in-service component. This testing is of interest to many parties in order to acquire standards for AM and fully understand the mode of damage experienced by the component. Mechanical characterisation should be conducted on AM components to understand the impact of varying processes on the microstructural and mechanical properties of the material. Also, it is an important procedure to complete in order to provide data to support the use of AM components compared to non-AM components.

2.3.1 Tensile

A tensile test, sometimes referred to as a tension test, is a destructive testing technique that provides information and data on the strength and ductility of a material whilst subjected to uniaxial tensile stresses. The data collected from this test can be useful for materials comparison, development of alloys, and quality control [120]. Even though tensile testing can provide insight for the mechanical properties of the material being tested, it does not fully represent the whole component. This is because the specimens used for tensile testing are standardised machined dimensions that are from a selected region of the whole part. In addition, tensile testing does not reflect the true behaviour of the in-service component that would be subjected to a different environment to the atmosphere stated in the tensile testing standard, ASTM E8/E8M [120].

To conduct a tensile experiment, initially the material being analysed is machined to standard dimensions [120]. It is then placed into the grips of the apparatus (consisting of a load frame and load cell) and pulled in tension at a constant rate, until complete failure of the material. In addition, an extensometer can be used to measure the elongation of the sample more accurately than the elongation given by the apparatus. These pieces of equipment are each calibrated to a standard. The tensile data collected can then be used to link the microstructure produced from a given process with the mechanical properties presented.

This conventional method of tensile testing can be valuable for AM components when assessing, compared to conventional components or characteristics such as anisotropy, and effect of heat treatment or HIP [121–123].

Research conducted by Kim et al. [121] on the effects of specimen orientation and heat treatment on the mechanical properties of IN718 are displayed in Figure 21. The study concluded that the yield strength and tensile strength of the horizontally (Type II) as-built PBF-LB (As-SLM) specimens was higher than for the vertically (Type I) built specimens, whereas elongation was reversed. Following heat treatment (heated), the yield strength and tensile strength increased in the horizontally and vertically built specimens. This was linked to the formation of fine and evenly distributed γ'' precipitates, which impeded dislocation movement through the matrix during tensile strain. In addition, anisotropy was still observed after heat treatment. This was because the effect of the heat treatment adopted was negligible on the grain size and shape of the PBF-LB samples.

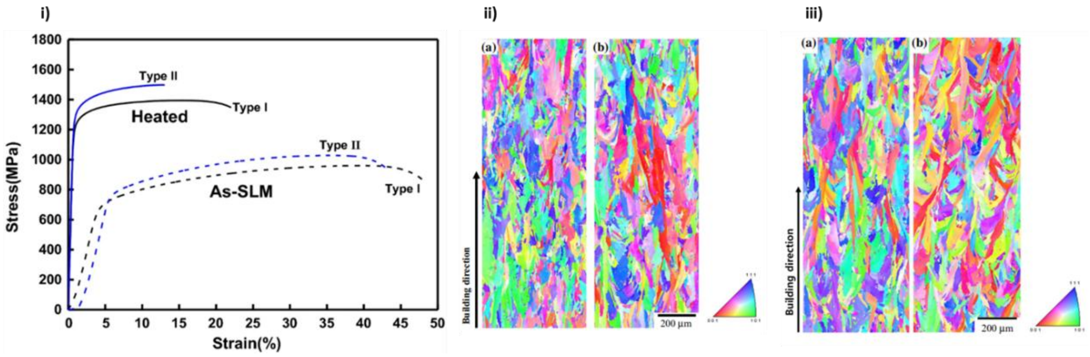

Figure 21: *i) Tensile stress strain curves of as-built and heat treated specimens with different build directions at room temperature. ii) Electron backscatter diffraction (EBSD) mapping on Type 1 (a) and Type 2 (b) in as-built condition. iii) EBSD mapping on Type 1 (a) and Type 2 (b) after heat treatment. Reproduced from* [121].

Further research performed by Sun et al. [122] touched upon the comparison of wrought, PBF-EB IN718 and HIPed PBF-EB IN718. Tensile data at 650°C showed that the PBF-EB samples had comparable elongation against the wrought and HIPed samples but had lower strength. This trend was linked to the larger grain size observed in the PBF-EB samples.

However, conventional tensile testing cannot truly capture the inhomogeneous structure presented by AM components. Therefore, researchers sometimes prefer employment of miniaturised uniaxial tensile testing to characterise local properties in complex-shaped AM parts. This method also reduces expenses in terms of time and resources.

Preliminary work of miniaturised tensile testing by Dzugan et al. [124] evaluated the location-dependent and orientation-dependent properties in various AM samples. Miniature tensile specimens were 8mm in length, 0.5mm thick, width of 1.5mm and active part length of 3mm. Overall conclusions for the as-built PBF-LB IN718 turbine blade showed that miniaturised tensile testing specimens taken from the bulk parts can exhibit similar tensile properties to bulk printed specimens, with exclusion of elongation values, as this is dependent on gauge length. Additionally, it was noted that caution on miniaturised tensile testing use should be taken to ensure at least 10 grains are present across the specimen cross-section, in order to represent true polycrystalline behaviour. The miniaturised tensile testing also showed that the IN718 blade exhibited location-dependent and orientation-dependent properties in the various regions of the blade (attachment, transition and blade regions), as shown in Figure 22. This was linked to anisotropies from different microstructural scales and differences in defects induced from the process.

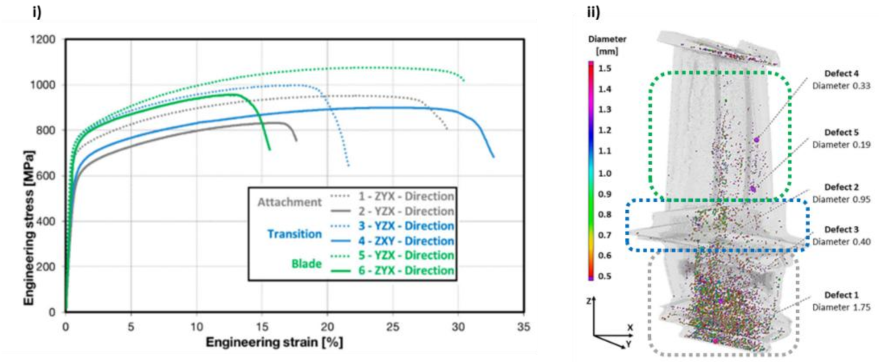

Figure 22: *i) Engineering stress-strain curves for M-TT specimens at various locations and orientations for IN718 blade ii) X-ray μCT of IN718 blade (grey region is attachment, blue region is transition, green region is blade) showing clear regions of higher pore density. Amended from* [124].

Overall, interest and research into miniaturised tensile testing is invested by industry, as it is a time and cost effective method. It is also driven by scientific researchers that are keen to explore mechanical testing techniques specifically for AM, instead of utilising mechanical testing techniques that were originally developed for conventional materials. However, implementation of miniaturised tensile testing is still in the early stage, alongside other small scale testing methodologies.

2.3.2 Fatigue

Fatigue is a cyclic mode of damage where failure occurs at stresses lower than the tensile or yield strength of a material when subjected to dynamic and fluctuating stresses, e.g. aircraft or bridge components. Stresses exerted on in-service components can be 1) tension and/or compression, known as axial 2) bending, referred to as flexural and 3) twisting, which is torsional. It is also possible to have a combination of these different fluctuating stresses. Fatigue failures account for most failures of metallic materials, approximately 90% of all failures [64], so it is paramount to understand the mechanisms for this mode of failure.

Fatigue failure occurs due to the formation and propagation of cracks. It is a three-stage process. Stage I, crack formation, tends to occur at a free surface or a stress concentration feature such as an inclusion or a defect. Stage II crack propagation then follows, where the crack grows incrementally with each stress cycle. The rate of crack propagation can be described using Paris' Law (1), which can be expressed as:

$$\frac{da}{dN} = C\Delta K^m \tag{1}$$

where a stands for the crack length, N is number of cycles, ΔK is the variation of stress intensity factor K, and C and m are constants. Stage III then coincides as the stage of final fracture, which occurs rapidly once the crack has grown to a critical size. These three stages can be represented graphically in Figure 23. Typically, fatigue failure is exhibited as brittle-like, even for more ductile associated materials. This is because there is little, to no, plastic deformation linked with the failure. Post-fatigue, components have a fracture surface that is usually perpendicular to the applied stress.

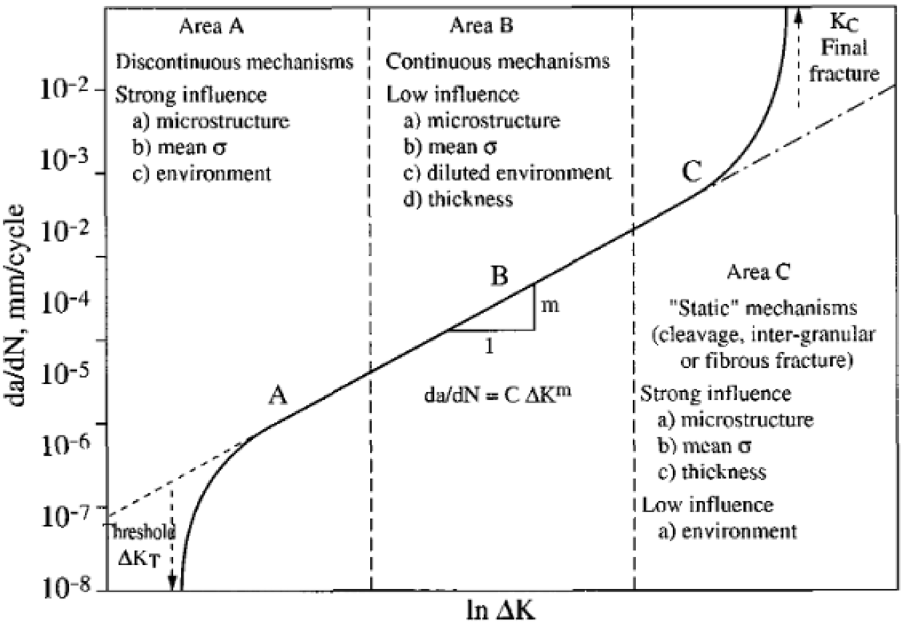

Figure 23: *Graphical representation of the propagation rate of a crack, da/dN, as a function of the strain intensity factor, ΔK. Region A shows low cracking rate (Stage I), region B shows intermediate regime (Stage II) and region C shows high cracking rate (Stage III). Reproduced from* [125].

Fatigue can be divided into two different regimes: LCF and high cycle fatigue (HCF). For LCF, this is defined as repeated plastic deformation in each cycle leading to failures prior to 10^5 cycles, whereas HCF is defined as predominantly elastic deformation in each cycle leading to failures post 10^5 cycles.

Further to the various types of fatigue, there are different fatigue loading conditions to consider. Two approaches that can be performed include the stress-life (S-N) approach or the strain-life (ε-N) approach. For S-N, a constant stress amplitude is utilised with a chosen waveform such as sinusoidal, triangular or trapezoidal. The sinusoidal waveform can be seen in Figure 24, where σ_a is the stress amplitude, σ_m is the mean stress, σ_{max} is the maximum stress, σ_{min} is the minimum stress and $\Delta\sigma$ or σ_r is the stress range. The terms are explained by the relevant equations in Figure 24. The stress ratio (R) is determined by dividing σ_{min} by σ_{max}. The most common stress ratios are R = -1 and R = 0.

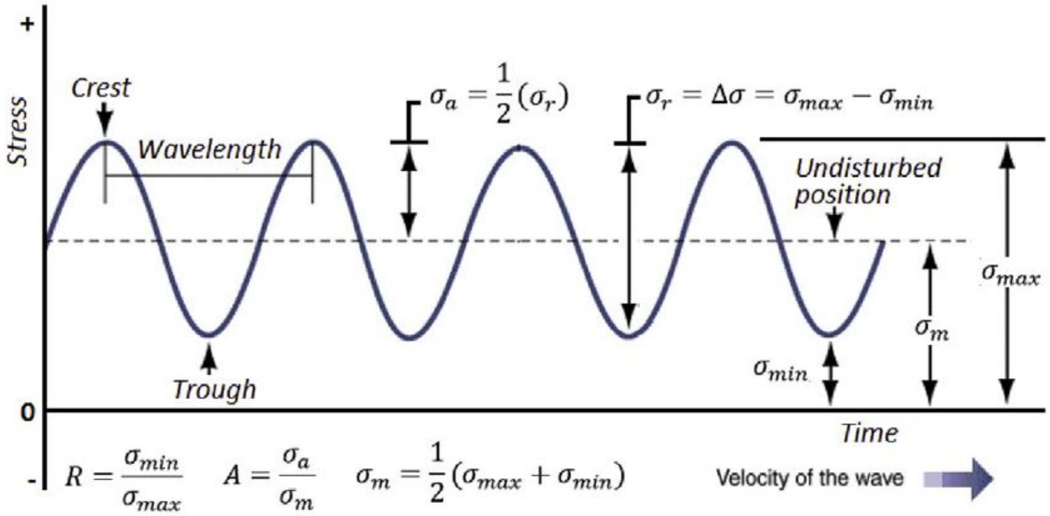

Figure 24: *Fully reversed (R=-1) sinusoidal fatigue waveform with constant stress amplitude. Reproduced from* [126].

Konečná et al. [127] collated and compared fatigue crack growth rate of conventional and PBF-LB IN718 samples, as shown in Figure 25. In high ΔK regions PBF-LB samples and conventional samples exhibited similar crack growth resistance. However, in the intermediate ΔK region the PBF-LB samples had a faster fatigue crack growth rate, when compared to the conventional samples. Poor fatigue resistance was seen in the PBF-LB samples, showing a threshold intensity factor of roughly 1×10^{-7} mm/cycle, which is much lower than for the conventional samples. The differences in the fatigue crack growth behaviour between the conventional and PBF-LB material were attributed to the lower boron content, finer microstructure, and residual stresses found in the PBF-LB samples.

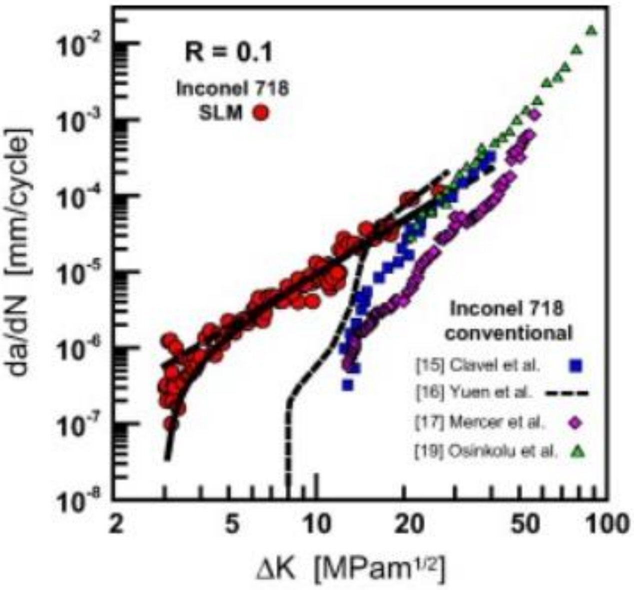

***Figure 25:** Fatigue crack growth for PBF-LB and conventional IN718 samples. Reproduced from* [127].

2.3.3 Creep

Creep is a damage mechanism that causes time-dependent deformation at elevated temperatures under a constant load (stress). The mechanism of creep can be observed in three distinct stages: primary creep (1^y), secondary creep (2^y) and tertiary creep (3^y), prior to failure via creep or stress-rupture. Firstly, the primary creep stage has a decreasing creep rate and is governed mainly by dislocation generation and movement within the grains. Secondly, the secondary creep stage is steady-state creep, where the creep remains unchanged and is shown graphically as a straight line. This stage is mainly due to the strain accumulation. Finally, the tertiary creep stage is accelerating creep, where the creep rate increases quickly until failure. This is due to the development of grain boundary cavities enhancing deformation. The variation in creep rate through the different stages is seen graphically in

Figure 26. Testing methods for creep analysis can be time-consuming, therefore, lifing models can be used for creep and for creep at different conditions i.e. various temperatures or applied stresses.

Research of creep properties of AM components have previously shown that nickel based superalloys produced via AM have inferior creep properties when compared to traditionally manufactured counterparts [128,129]. Trends seen were correlated to AM-related features, such as: porosity, fine columnar grain structure and micro-segregation. For example, the formation of Laves phase at grain boundaries or inter-dendritic sites due to micro-segregation leads to cavity nucleation sites located in adjacent sites. Consequently, rapid formation of cavities occurs, leading to a reduced cross-sectional area which causes an increased stress and accelerated creep rate. Therefore, cavitation formation in AM built components is a main factor that influences creep rate. The comparison of creep rate and creep life between AM and conventional samples is displayed in

Figure ***26***, where the initial microstructure for AM alloys gives faster cavity kinetics, inducing a higher initial creep rate and shorter creep lifetime when compared to the conventional counterparts.

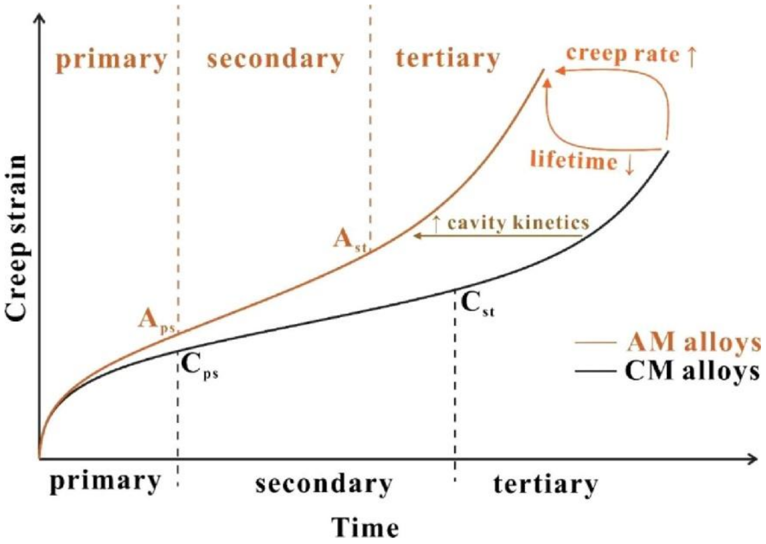

Figure 26: *Schematic to demonstrate the three stages of creep for additive manufactured (AM) and conventionally manufactured (CM) alloys. Zones between primary/secondary stages and secondary/tertiary stages for AM and CM alloys are denoted Aps, Ast, Cps and Cst, respectively. Reproduced from* [130].

Additionally, creep mechanisms in IN718 such as diffusion creep, dislocation creep, grain boundary sliding and precipitation effects should be considered. At high temperatures, diffusion of atoms through the lattice (Nabarro–Herring) or along grain boundaries (Coble) enables time-dependent deformation. Fine-grained materials favour Coble creep, whereas coarse grains promote lattice diffusion. PBF-LB IN718, with directionally solidified columnar grains, exhibits different diffusion creep behaviour compared to wrought IN718. At intermediate temperatures (600‑700° C), deformation occurs by dislocation glide and climb through the γ matrix. The γ' and γ'' precipitates act as obstacles, forcing dislocations to bow or cut through particles. The effectiveness of γ'' strengthening is critical; incomplete precipitation in the as-built state results in inferior creep resistance. Grain boundary sliding contributes significantly under low stress or high temperature. The δ-phase, often present after PBF-LB due to reheating, can either inhibit sliding (when finely distributed) or embrittle grain boundaries (when continuous), reducing creep ductility. The stability of γ'' determines long-term performance. Coarsening, dissolution, or over aging reduces strength. AM-specific segregation patterns influence γ'' precipitation kinetics, making heat-treatment selection essential. Therefore, it is particularly important to understand for AM IN718, where columnar grains exhibit reduced grain boundary sliding but possible enhanced slip along <001> , Laves can act as nucleation sites and residual stress may accelerate tertiary creep.

2.3.4 Small Scale Testing

Comprehensive understanding of the mechanical performance of alloys produced via more novel methods, such as AM, is essential to the development process before using full size service components. Even though there are globally recognised and well established standardised uniaxial testing methods, there are scenarios where smaller scale testing would be considered to be more beneficial. For example: 1) The development of new alloys for metal additive manufacturing, where material volume can be low, and the production of traditional test samples can be unattainable and expensive [131]. 2) Reducing testing time and costs when quantifying mechanical effects of radiation damage in reactor materials [132]. 3) Analysis of mechanical properties across a component where heterogeneous characteristics may be present and small scale testing allows for the extraction of samples from the final components to provide localised characterisation of properties of AM parts, compared to conventional testing, where test samples are built to a dissimilar geometry. For these reasons, there is increased research and use of small scale testing such as: SPT, shear punch tensile (ShPT), small ring, SPC, nanoindentation and profilometry-based indentation plastometry (PIP).

SPT testing is a technique that has seen a rapid uptake in the last few decades, with increased application and interest from industries such as the energy sector, where nuclear power plants are approaching end of life and need mechanical assessment. SPT is used in alignment with BS EN 10371 [133] or ASTM E3205 [134] and the method is considered non-destructive as it uses samples from in-service components without impacting the mechanical integrity of the part. The SPT test uses a small, thin test disc that is subjected to bending and stretching; an upper die and lower die hold the coupon and punch it with a spherical ball (or head) to create contact and deform the specimen. The data collected is then represented as a force-displacement curve, with five distinct regions, as shown in Figure 27. Section I is elastic bending, section II is plastic bending, section III is membrane stretching, section IV is plastic instability and section V is the tail end of section IV showing the failure of the sample. The typical inflection and deflection points can be used to equate SPT results with conventional stress-strain results: k is the initial stiffness, δ_m is the deflection at maximum load, δ^* is the specimen deflection at fracture, U is the strain energy, P_y is the yield load, $P_{II\text{-}III}$ is the transition load from section II to section III, $P_{III\text{-}IV}$ is the transition load point between section III and section IV, and P_{max} is the maximum load.

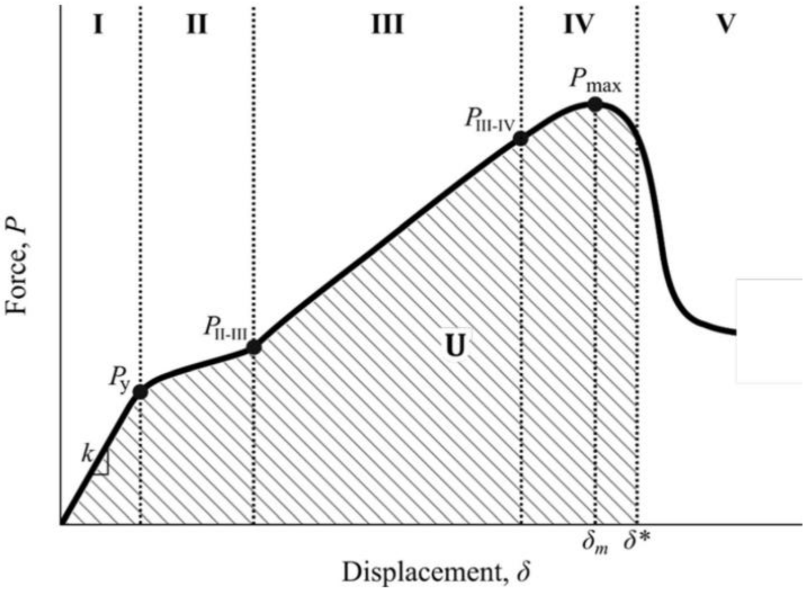

Figure 27: *Typical SPT load-displacement curve with denoted inflection and correlation points. Reproduced from* [135].

SPT has the ability to predict the anisotropy of as-manufactured AM materials, especially those produced via PBF-LB, where literature has shown that fracture morphology is highly dependent on the build orientation [136]. Research by Rezaei et al. [17] concluded that SPT on PBF-LB IN718 was suitable to predict the level of anisotropy present. Fractography of room temperature samples showed that the sample parallel to build direction displayed a fracture mode that was ductile, whereas the sample perpendicular to the build direction showed a brittle fracture.

Furthermore, use of inflection points in the force-displacement data to equate values for mechanical properties was reviewed by Torres et al. [135]. Analysis of data from various literary sources showed that there was strong correlation between UTS and $P_{max}/\delta_m t$ (where t is the specimen thickness), as shown in Figure 28. However, there are several points that are outside of the majority of the data that belong to the AM class of materials, including DLD C263, direct metal laser sintering (DMLS) GP1, and SLM 625, which are outlined in Figure 28. This is attributed to the unique characteristics of AM materials and their high dependency on processing and post-processing parameters. It is noted that the other DLD C263 and SLM 718 data fits well within the data, suggesting that significant research is still needed to strengthen this relationship.

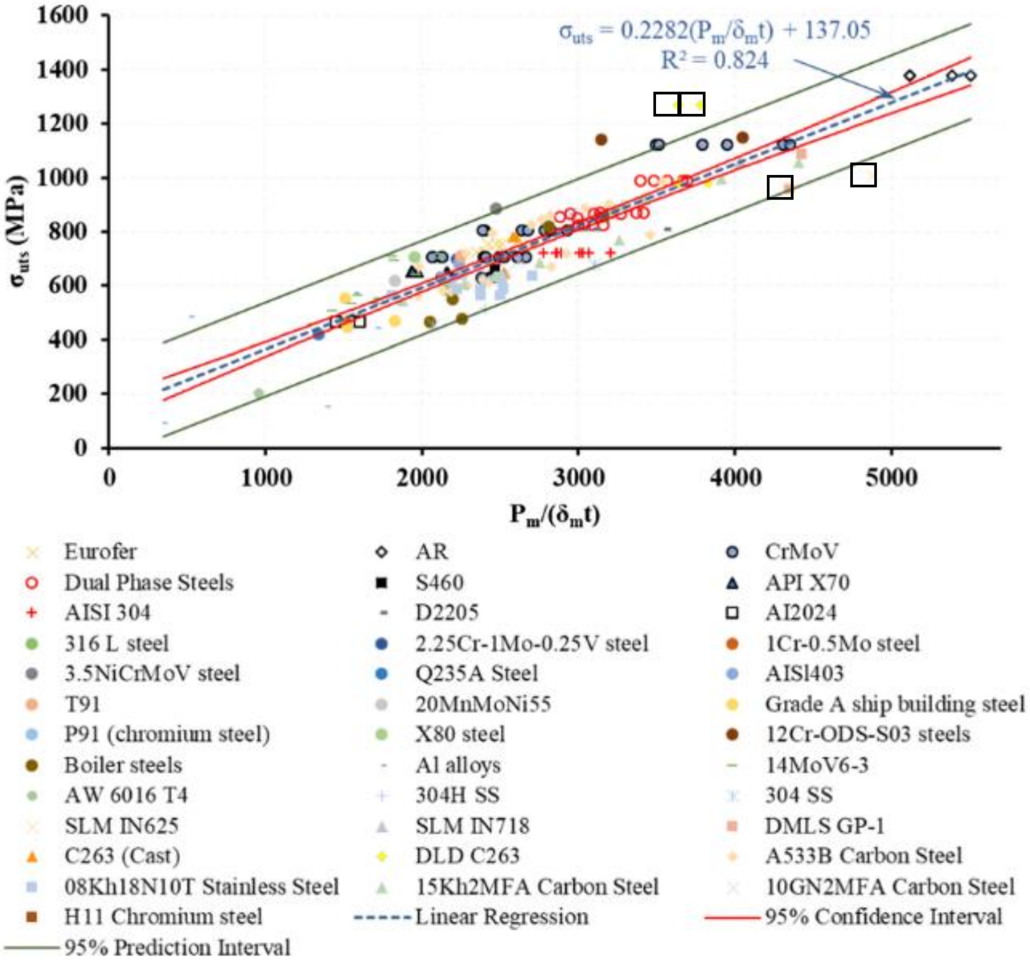

Figure 28: *Corelation of tensile and SPT tensile strength data compiled from various sources of experimental data.* σ_{uts} *is ultimate tensile strength and* $P_{max}/\delta_m t$ *is maximum load divided by deflection at maximum load, multiplied by original specimen thickness. Reproduced from* [135].

ShPT testing is a form of SPT that follows BS EN 10371 [133] or ASTM E3205 [134] and is employed to determine shear properties, which uses a flat punch rather than a round ended punch. This set up allows for the primary deformation mode in the sample to be shearing along the edges of the punch [135]. The shear stress, τ, is then calculated from the load-displacement data. Currently, there is only data for wrought material in research, which is reported successfully. For example, SPT, ShPT, and uniaxial tensile testing, presented by Lancaster et al. [137] on various wrought materials (including copper, aluminium, stainless steel, IN718 and Ti-6Al-4V) proved linear relationships between the data sets. In addition, unity plots showed high levels of correlation for ultimate tensile stress and proof stress between experimental uniaxial results and empirically derived SP and ShPT predicted properties. From the current research on wrought samples, ShPT should be considered for research by materials engineers as a viable small scale testing method for AM components.

Small ring testing is a novel small scale method for creep testing that has recently been extended for determination of tensile material properties. Initially developed in 2009 by Hyde and Sun [138], small ring testing allows for accurate creep strain data to be obtained. This technique is advantageous to conventional testing as the samples are simple to manufacture, has high sensitivity (due to large equivalent gauge length) and is self-aligning. However, this specimen type cannot obtain tertiary creep data. Further development of the technique by Kazakeviciute et al. [139] has enabled the evaluation of tensile properties for isotropic materials.

Work conducted by Rouse et al. [140] investigated the use of small ring testing to characterise Ti-6Al-4V processed via PBF-LB. Use of test data and analytical models showed successful estimation of varying AM mechanical properties across build volume and build plane. However, it was suggested that further work was necessary to validate the method for PBF-LB materials and varying build conditions.

Further to small ring testing, SPC testing is another small-scale test that provides data on the creep behaviour of the tested material. SPC testing follows BS EN 10371 [133] or ASTM E3205 [134]. Similarly to SPT, a thin test coupon is held between an upper and lower die and perforated with a punch head via a ‘dead’ load at a desired temperature. After rupture, the collected data typically produces a time-displacement (or deflection) curve which shows the usual stages of creep (1^y, 2^y and 3^y) that would be seen in a conventional creep test. However, the mechanism of deformation during SPC testing is very different to the deformation during uniaxial creep testing where typical coupons elongate over time when under an applied load. For SPC, the primary stage is dictated by the amount of elastic bending in the thin test coupon. Following this, the extended secondary phase is indicative of the plastic deformation and membrane stretching caused by the biaxial stress state. After continued deformation and necking due to thinning of the coupon, the tertiary phase is met where failure occurs. Although there is a variation in deformation modes between uniaxial creep and SPC, researchers and industrial sectors can use SPC to correlate behaviours using various methods. Some methods to correlate SPC and uniaxial creep include Chakrabarty membrane stretch model, k_{sp} method, Monkman-Grant model, Larson-Miller, Wilshire equation, and Norton creep equation [141–143].

Focussing on the k_{sp} method, which is derived from Chakrabarty's membrane stretch model, the empirical relation is shown in Equation (2) where: F is SPC force, σ_c is equivalent uniaxial creep stress, R is radius of the receiving hole, r is radius of punch, h_o is the disc thickness, and k_{sp} is the correlation factor.

$$F/\sigma_c = 3.33 k_{sp} R^{-0.2} r^{1.2} h_o \tag{2}$$

The correlation factor, k_{sp}, depends on material and test temperature. Consequently, a CEN code of practice recommends to calculate k_{sp} for a given test temperature and disc material [144,145].

Research provided by Williams et al [143] compared different methods to accurately convert SPC loads into equivalent uniaxial stresses for Waspaloy. The methods for comparison were k_{sp}, Mokman-Grant, and Wilshire. Assessment of the uniaxial creep and SPC data suggested that utilisation of the Mokman-Grant model and Wilshire equations was more accurate for a Ni-based superalloy than the k_{sp} method.

Peng et al. [146] researched and discussed the effects of aging and solution heat treatments on the creep properties of PBF-LB IN718 samples and rolled IN718 by conducting SPC testing. In addition, this research implemented the Larson-Miller method to predict creep life and compared it to tested SPC life. It was found that the majority of the predicted creep lifetimes were within a 1.5 times error zone, as displayed by Figure 29, suggesting that the Larson-Miller method can be suitable for prediction of creep life.

Additionally, Davies et al. [147] used SPC testing along with an adapted Wilshire empirical model to examine the impact of heat treatment on the creep properties of PBF-LB nickel-based superalloy C263. Two heat treatment regimes were compared: a standard heat treatment and a higher temperature solution heat treatment. SPC testing revealed that the higher temperature solution heat treatment promoted recrystallisation and reduced grain anisotropy, consequently improving creep performance and performing closely to that of cast C263. This study highlights SPC testing as an effective method to assess and optimise heat treatment strategies for PBF-LB materials.

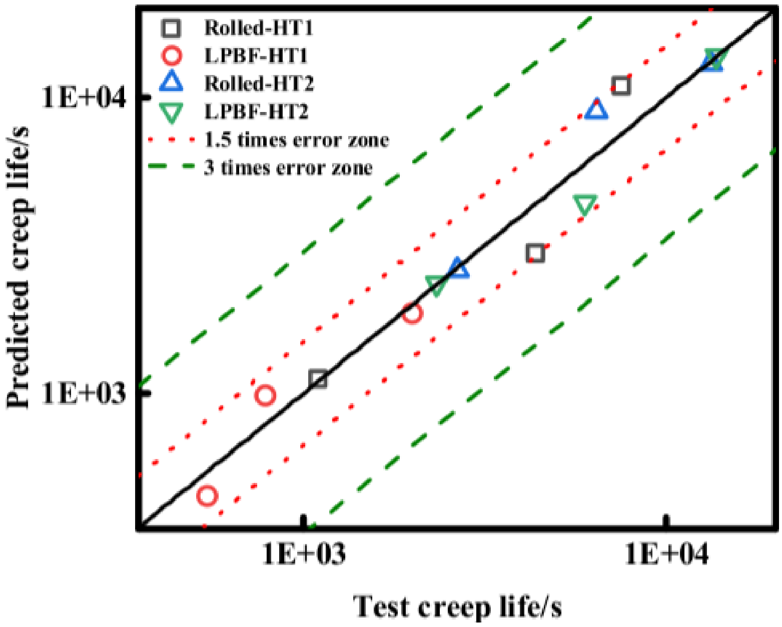

Figure 29: *Comparison between predicted creep life via Larson-Miller method and tested creep life. Reproduced from [146].*

Additional small scale test approaches includes indentation methods such as nanoindentation and PIP.

The nanoindentation process that follows ISO 14577 [148] or ASTM E2546 [149] and consists of two primary stages: loading, where the indenter presses into the material, and unloading, during which the material's elastic recovery is measured. Applying a controlled load to an indenter while recording the corresponding penetration depth, generates indentation load-depth (P-h) curves as demonstrated in Figure 30. By analysing these curves, key mechanical properties such as stiffness, strength and fracture resistance are derived [150–152].

Nanoindentation offers several advantages, including high spatial resolution, the ability to test small material volumes, and minimal sample preparation. Additionally, it enables mechanical property mapping across heterogeneous materials. However, nanoindentation has limitations [153]. For instance, it is highly sensitive to surface roughness and material anisotropy, which can affect measurement accuracy. The technique may also exhibit size effects, where mechanical properties vary with indentation depth, complicating data interpretation [154]. Furthermore, in certain materials, pile-up or sink-in effects can distort contact area measurements, impacting hardness and modulus calculations.

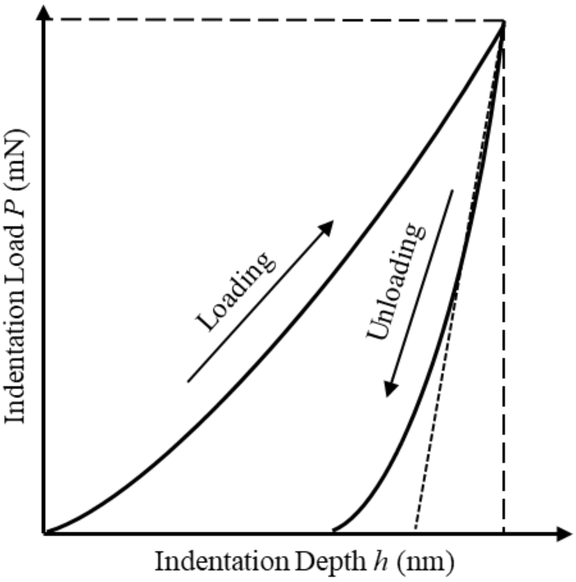

Figure 30: *Schematic of nanoindentation P-h curve.*

PIP is an advanced technique that obtains stress-strain curves from indentation test data using an inverted finite element method (FEM), unlike nanoindentation, which relies on *P-h* curves. This testing technique is being considered as an alternative means to tensile testing [155–157] for the determination of key mechanical properties, including yield strength, hardening behaviour, and ultimate tensile strength. To obtain a tensile stress-strain curve using an indentation test, several steps are completed: 1) With a known force a spherical indenter is pushed into the surface of the sample material, which has been previously mounted and polished to at least 2500 grit. 2) Indents made are then profiled using a stylus with a depth resolution of approximately 1μm. 3) FEM simulation of the test results against plasticity parameter values are compared to find a best fit. 4) Followed by use of the resultant true stress-strain relationship in the FEM simulation.

The PIP method is useful for testing metals and other plastically deforming materials. It is non-destructive, requires minimal sample preparation, and can be applied to a wide range of material types. Additionally, because it does not rely on direct force-displacement measurements, it avoids some of the limitations associated with conventional indentation techniques, such as instrument compliance and tip blunting. However, PIP has certain drawbacks. The accuracy of extracted mechanical properties depends on the quality of profilometry measurements and the assumptions used in finite element modelling. Surface roughness and material anisotropy can also affect the precision of the indentation profile, potentially leading to deviations in property calculations.

A comparison experiment between tensile testing and PIP methodology was conducted by Tang et al. [155] on AM ABD-850AM alloy (a Ni-based superalloy) with a strong directional structure. Testing along the horizontal sections provided higher stiffness, yield stress, and UTS values, when compared to the vertical direction. Using the PIP methodology on the horizontal sections showed a nominal stress-strain curve that was closer to the curve obtained experimentally, compared to the vertical sections. Overall, it was concluded that this method showed consistent measurements that reflected anisotropy.

Overall, the utilisation of small scale testing can be beneficial for the many reasons mentioned previously and consequently, there is a drive to develop protocols for small scale testing which can consistently determine mechanical properties of AM components. Achieving this will reduce testing time, cost, and material volume, and still provide similar information as conventional testing. Consequently, manufacturing time and production costs will be lowered, making AM a more competitive manufacturing technique when compared to conventional routes [132].

2.4 Standards

A standard is a document developed and published that is formatted with rules, definitions, methods, vocabularies, or codes of practices, to describe technical specifications or a list of guidelines [158]. Standards are used across various sectors to ensure best practices, conformity and formalised procedures. Adoption of this practice and standard certification increases quality and can be greatly beneficial to improve productivity and reliability, and enables international trade and competitiveness.

2.4.1 Overview of Standards for Additive Manufacturing

Currently, the major challenge within AM is the lack of standards and certification for industry, which has been caused by the rapid growth of AM over the last decade. The standards required will need to be unified across industries to ensure repeatability, reliability, and quality, of safety-critical and non-safety-critical AM components [36]. Ideally the production of standards will increase the adoption of AM within industry. The gap in AM standardisation has been approached collaboratively between standards development organisations (ASTM International standards as an ISO international standard, and vice versa) to accelerate the adoption process. ASTM International and the ISO agreed to a Partner Standards Developing Organization (PSDO) to cooperate with the current AM standard work: ASTM International Committee F42 for Additive Manufacturing Technologies and ISO Technical Committee 261 for Additive Manufacturing.

Although standards have been published for AM such as ISO/ASTM 52900 (General Principles – Fundamentals and Vocabulary), ISO/ASTM 52910 (Guidelines for Design for AM) and ISO/ASTM 52901 (Additive Manufacturing – General Principles – Requirements for Purchased AM Parts), there are a lack of standards for more challenging areas for AM. For instance, the variation in mechanical properties of components across the build plate of a given PBF-LB machine [159] or variation in dimensional accuracy between different PBF-LB machines [160]. Recent roadmaps produced by Additive Manufacturing Standardization Collaborative (AMSC) in July 2023 revealed 141 standard gaps across topics including: design and precursor materials, process control and post-processing, finished material properties, qualification and certification, non-destructive evaluation (NDE) and maintenance, data and digital works [161].

Fundamentally, the creation of standards for AM through research of various manufacturing processes, materials, post-processing etc., to generate high calibre datasets, will ensure process reliability with confidence of fabrication predictability. With deeper understanding of current challenges facing AM, such as variation in machine and process parameters, feedstock variation, post-processing routes etc., the standards produced can remove stigma associated with variability caused by the manufacturing technique [20,162].

2.4.2 Industrial Consideration

Production of standards for AM utilisation also needs to consider industrial applicability in terms of different build set ups and varying post-processing techniques. Taking this into consideration means performance based approaches are preferred, as it enables established processes to meet performance requirements, whilst not requiring part or supplier-specific allowables. Implementing a performance based approach does require previous knowledge of PSP of AM parts, which poses another ‘gap’ in respect to high calibre data set creation. However, adoption of this approach will enable equivalency for companies/industries where different build set ups, machines, input paraments, etc., are used.

2.5 Summary of Literature Review

IN718 is a precipitation-hardened nickel-based superalloy used for its high-temperature strength and corrosion resistance, particularly in aerospace, nuclear, and energy applications. The PBF-LB process enables near-net-shape manufacturing and complex geometries, but also introduces challenges such as residual stress, porosity, and anisotropic microstructures. Foundational studies [163–166] have outlined the unique thermal conditions and rapid solidification mechanisms in PBF-LB, which directly influence microstructural and mechanical behaviour.

These unique process conditions give rise to fine cellular dendrites, elongated columnar grains, and segregation of elements like Nb and Mo, often forming Laves and δ phases. Microstructure heterogeneity is a well-documented outcome, with EBSD and SEM revealing a strong build-direction texture. However, variability in etching techniques, sample preparation, and grain size analysis can complicate cross-study comparisons.

Since microstructure influences performance, post-processing becomes essential. However, applying conventional heat treatments developed for wrought IN718 often yields suboptimal results in LPBF parts due to differences in residual stress profiles and micro segregation. Modified heat treatment routes and HIP have been proposed to develop microstructures for improved mechanical properties [167–169], underscoring the need for HT strategies that are specifically tailored to PBF-LB parts.

Mechanical performance, particularly under service-relevant conditions, is intricately linked to both processing and post-processing histories. While RT properties are relatively well-documented, high-temperature performance (including creep, fatigue, and tensile strength) remains inconsistent and lacking across literature [170,171]. Additionally, variables such as build orientation, surface condition, and microstructure complicate efforts to standardise data.

Given the challenges of large-scale mechanical testing, especially for expensive or limited PBF-LB components, small-scale tests such as SPT and SPC are gaining attention. These techniques offer minimal material usage while enabling localised property assessments. Empirical correlations with uniaxial tests have been proposed [137,172,173], yet for PBF-LB materials, these methods are not yet fully validated due to microstructural variation and possible localised defects from alternate manufacturing routes and material chemistries.

One persistent limitation, across all themes, is the absence of standardised, high calibre datasets. Studies frequently omit critical data such as powder characteristics, scan strategies, or post-processing details, impeding reproducibility and comparisons between research. The adoption of Findable, Accessible, Interoperable, and Reusable (FAIR) data principles is starting to gain momentum within the AM sector [174,175]. However, most PBF-LB IN718 datasets remain underreported, or formatted inconsistently, hindering the development of predictive models and qualification standards.

Despite considerable progress in understanding PBF-LB IN718, a number of gaps still remain within the AM landscape. The intent of this thesis it to raise awareness and bridge some of the aforementioned gaps.

2.6 Aims and Objectives

This thesis aims to advance the understanding and optimisation of PBF-LB IN718, a nickel-based superalloy widely valued for its high-temperature strength and corrosion resistance, by addressing key knowledge gaps that currently limit its industrial application.

While the room temperature properties of PBF-LB IN718 are well documented, the mechanical performance under service-relevant elevated temperatures (650 °C) remains poorly understood. This thesis investigates tensile, LCF, and creep responses to generate high-quality, application-relevant datasets, and compares them with wrought IN718 to assess the suitability of AM components for high-temperature applications.

Standard heat treatments derived from wrought IN718 may not fully optimise the unique microstructure of PBF-LB components. This work examines how alternative post-processing routes affect microstructural evolution and mechanical performance, providing insight into tailored heat treatments specifically for AM IN718.

HIP is widely used to reduce porosity and enhance mechanical properties, but its cost, environmental impact, and potential microstructural alterations raise questions about its universal applicability. By quantifying defects and assessing mechanical performance of non-HIP samples, this research seeks to evaluate whether optimised PBF-LB process parameters could mitigate the need for HIP, enabling more efficient and sustainable manufacturing strategies.

Conventional testing methods can be resource-intensive and challenging for complex geometries. This thesis investigates the reliability of small-scale techniques, such as the SPT and SPC, by correlating them with standard tests, assessing whether these methods can provide rapid, accurate insights for AM component qualification.

Recognising the importance of reproducibility and comparability, this research emphasises the generation of high-calibre datasets and explores strategies for data standardisation, contributing to a robust framework for consistent evaluation of PBF-LB IN718 across both academic and industrial settings.

Collectively, these objectives aim to fill critical gaps in understanding, provide evidence-based guidelines for processing and post-processing, and support the reliable deployment of PBF-LB IN718 in industrial applications. This thesis contributes to both scientific knowledge and practical industrial practice by integrating fundamental materials understanding with the requirements of real-world applications.

3 Experimental Procedures

3.1 Material

The mechanical behaviour of PBF-LB IN718 with varying build orientations and post-processing techniques was assessed. Variants included vertical (90°) and horizontal (0°) build directions, where each variant underwent a different heat treatment route. Some samples were left in the as-received (AR) state, others were heat treated to improve fatigue performance (heat treatment 1 – HT1) in alignment with AMS2774 [176] and AMS5664 [177], and the remaining samples were heat treated to improve creep performance (heat treatment 2 – HT2) in alignment with AMS2774 [176] and AMS5662 [178]. For comparison, wrought IN718 was assessed to provide a baseline for the PBF-LB IN718 samples.

3.1.1 Wrought IN718

Wrought material was sourced from a third party (Goodfellow Cambridge Ltd.) with the following composition, provided by the third party, listed in Table 3. The wrought material was solution annealed at 965°C for one hour, followed by rapid air cool.

Table 3 *- Chemical composition of wrought IN718 (in wt.%).*

Element	**C**	**Si**	**Mn**	**P**	**S**	**Cr**	**Mo**	**Ni**
Wrought	0.024	0.07	0.09	0.008	0.0003	17.61	2.97	Bal.
Element	**Cu**	**Co**	**Ti**	**Al**	**Nb**	**B**	**Fe**	**N**
Wrought	0.06	0.35	0.95	0.53	5.12	0.0031	18.15	0.005
Element	**Pb**	**Ta**	**O**	**Ca**	**Mg**	**Sn**	**Se**	**Ag**
Wrought	<0.0003	<0.02	<0.0003	<0.0003	0.0015	0.0012	<0.003	<0.0001

3.1.2 Laser Powder Bed Fused IN718

The following section provides details regarding the fabrication and post-processing of the PBF-LB IN718 samples. Fabrication was completed at AddUp Inc. facilities with AS9001 and ISO13485 quality management systems.

3.1.3 Feedstock Material

PBF-LB IN718 was fabricated using Praxair IN718 powder recycled 23 times and produced via inert-gas atomisation in pure argon (gas grade HiQ Argon 5.0). The chemical composition, that was provided by the manufacturer, is stated in Table 4 (chemistry grade AMS5662 and UNS-N-07718). The PSD was measured by the manufacturer using a Microtrac S3500 in accordance to ASTM B822 [179], showing that d_{10} was 5.2µm, d_{50} was 10.63µm and d_{90} was 17.25µm. In addition, the provider reported the tap density as 4.80g/cm^3 as per ASTM B527 [180] and apparent density as 2.88 g/cm^3 as per ASTM B417 [181]. Additionally, SEM images of the powder morphology were provided by the manufacturer and are reported in Figure 31.

Table 4 - *Chemical composition of IN718 powder (in wt.%).*

Element	**C**	**Si**	**Mn**	**P**	**S**	**Cr**	**Mo**	**Ni**
Powder	0.03	0.10	0.06	<0.005	0.002	19.29	2.96	Bal.
Element	**Cu**	**Co**	**Ti**	**Al**	**Nb**	**Nb (Cb) + Ta**	**B**	**Fe**
Powder	0.03	0.17	1.00	0.61	5.13	5.14	0.0020	17.53
Element	**N**	**Pb**	**Ta**	**O**	**Ca**	**Mg**	**Se**	
Powder	0.011	<0.0005	0.01	0.031	0.00	0.00	<0.0003	

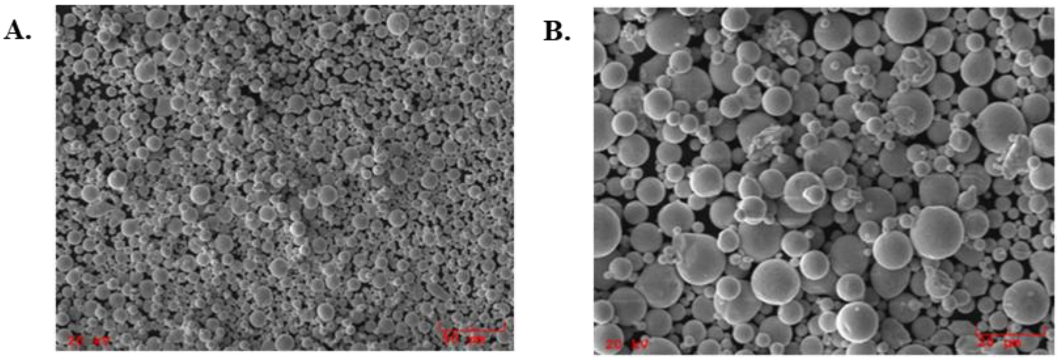

Figure 31: *SEM images of IN718 powder at A) 750x magnification and B) 2,000x magnification, produced and provided by manufacturer.*

3.1.4 Material Fabrication

PBF-LB IN718 samples for this study were fabricated on a FormUp 350, with a build capacity of ~43L, in an inert argon gas atmosphere and maximum oxygen levels of 10,000ppm. Powder was recoated using a 1.2312 tool steel roller at a speed of 0.2m/s, providing a layer thickness of 40µm (for fill and contour).

Process controls were set by the manufacturer, including a hatch and contour chessboard scan strategy with a hatch spacing of 75µm, hatch rotation of 225°, and contour spacing of 60µm. The volumetric energy density used during production was 44.44J/mm^3, with a laser power of 160W (for fill and contour), laser spot size of 80µm (for fill and contour), and laser speed of 1.2m/s for fill and 1200m/s for contour.

Samples were produced as cylinders in the vertical (90°) and horizontal (0°) directions, as shown by Figure 32, and machined to the required dimensions. Prior to machining the samples underwent various heat treatments as previously described.

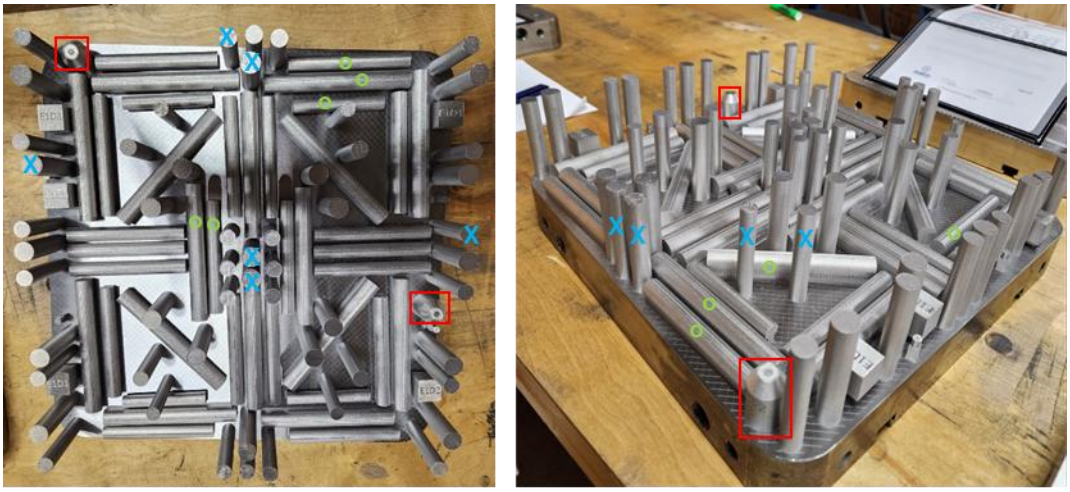

Key: powder capsules = red squares, vertical samples = blue crosses, horizontal samples = green circles

Figure 32: *Images of PBF-LB IN718 specimens build post fabrication on FormUp 350. Powder capsules and some vertical and horizontal samples denoted using key.*

3.1.5 Heat Treatment

Once the samples were removed from the build plate, various heat treatments were performed. Some samples were left in the AR condition (no heat treatment), some underwent heat treatment to improve fatigue performance (HT1) and some underwent heat treatment to improve creep performance (HT2). Details of each heat treatment are listed in Table 5 and Table 6, respectively. Alongside the tabulated heat treatments, a schematic of HT1 and HT2 is illustrated in Figure 33. Furthermore, Table 7 states the sample IDs and the relevant heat treatment that was undertook.

Table 5 *- Thermal route for HT1.*

Heat Treatment Stage	Atmosphere	Soaking Time	Soaking Temperature	Cooling Conditions	Heating Rate
					Cooling Rate
Solution Annealing	Vacuum	1 hour ±5 min	1065°C ± 8°C	Target Temp: Below 537°C Cooling Media: 2 Bar Argon Quenching	14°C/min
					42°C/min
Ageing 1st Stage	Vacuum	10 hour ±5 min	760°C ± 8°C	Target Temp: 650°C ± 15°C Cooling Media: Vacuum Cooling	10°C/min
					2°C/min
Ageing 2nd Stage	Vacuum	10 hour ±5 min	650°C ± 8°C	Target Temp: Room Temp Cooling Media: 2 Bar Argon Quenching	-
					22°C/min

Table 6 *- Thermal route for HT2.*

Heat Treatment Stage	Atmosphere	Soaking Time	Soaking Temperature	Cooling Conditions	Heating Rate
					Cooling Rate
Solution Annealing	Vacuum	1 hour ±5 min	955°C ± 8°C	Target Temp: Below 537°C Cooling Media: 2 Bar Argon Quenching	10°C/min
					42°C/min
Ageing 1st Stage	Vacuum	8 hour ±5 min	730°C ± 8°C	Target Temp: 635°C ± 15°C Cooling Media: Vacuum Cooling	10°C/min
					2°C/min
Ageing 2nd Stage	Vacuum	10 hour ±5 min	635°C ± 8°C	Target Temp: Room Temp Cooling Media: 2 Bar Argon Quenching	-
					22°C/min

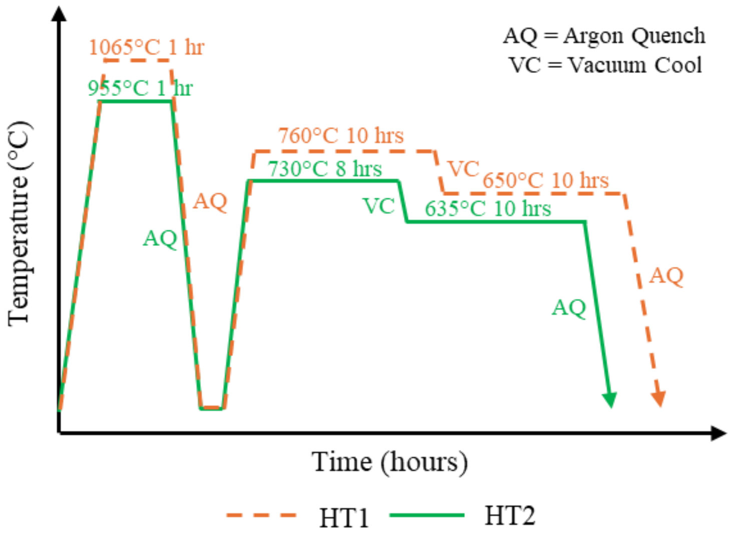

Figure 33: *Schematic to show HT1 and HT2.*

Table 7 - *Sample ID for respective heat treatment.*

	Sample IDs for As-received	Sample IDs for HT1	Sample IDs for HT2
Tensile (vertical)	A-UZ-07, A-UZ-08	A-TZ-14, A-TZ-15	A-TZ-05, A-TZ-08
Fatigue (vertical)	A-FZ-05, A-FZ-10, A-UZ-21, A-UZ-22, A-UZ-23, A-UZ-24	A-FZ-09, A-FZ-11, A-FZ-13, A-FZ-21, A-UZ-17, A-UZ-18, A-UZ-19, A-UZ-20,	A-FZ-02, A-FZ-03, A-FZ-07, A-FZ-15, A-FZ-17, A-FZ-18, A-UZ-15, A-UZ-16
Creep (vertical)	A-CZ-01	A-CZ-04	A-CZ-02
Small-scale (vertical)	A-UZ-09	A-TZ-16	A-TZ-12
Small-scale (horizontal)	A-TY-06	A-TY-09	A-TY-03

3.2 Powder Characterisation

To validate the PSD data provided by the manufacturer, powder analysis was conducted on two powder lots (A-PC-01 and A-PC-02), that were encapsulated during the fabrication process, using a Malvern Mastersizer 3000. Parameters for the Malvern Mastersizer 300 were as followed: deionised water for the particle dispersant, a particle refractive index of 1.958, particle density of 8.17g/cm^3, and particle absorption index of 0.5. For each powder lot, ten readings were taken during testing to create an average.

3.3 Material Characterisation

Microstructure of the wrought and PBF-LB IN718 samples was analysed to understand the influence of the material characteristics on the mechanical properties. For additive samples, vertical and horizontal specimens were assessed in the XZ and XY plane, as demonstrated in Figure 34. Several advanced microscopy techniques were utilised, which are discussed in this section.

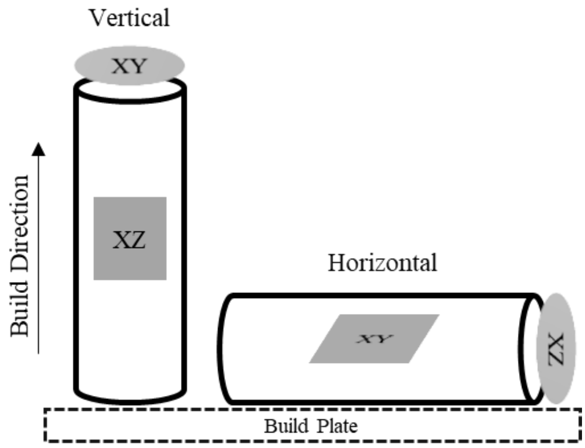

Figure 34: *Diagram to illustrate XZ and XY planes in vertical and horizontal specimens.*

3.3.1 Metallographic Preparation

Prior to microstructural analysis, material was sectioned in two orientations and then mounted in conductive Bakelite to form 32mm diameter specimens for polishing. A grinding and polishing procedure was conducted on a Struers auto-polisher using the defined route in Table 8.

Table 8 - *Metallographic preparation route for IN718 material.*

	Step 1	**Step 2**	**Step 3**	**Step 4**
Base	Piano-220	Largo	Dac	MD-Chem
Media	Water	9µm Diamond Suspension	3µm Diamond Suspension	0.4µm OPUS Colloidial Silica
Force (N)	25	25	25	20
Speed (rpm)	300	150	150	150
Time (minutes)	0.25	8	5	12
Cleaning	Water rinse and air dry	Water rinse and air dry	Water rinse and air dry	Water rinse thoroughly and air dry

3.3.2 Optical Microscopy Imaging for Porosity Analysis and Laves Quantification

To assess porosity within the material, polished specimens as described in section 3.3.1 were analysed on a Zeiss Axio Observer Inverted Light Microscope. A full image was captured at 100x magnification using bright field. The full image was produced by stitching several images together using the Zeiss software. After gathering the full micrograph, ImageJ software was employed to calculate the porosity. This was achieved by setting the image type to an 16-bit image to create a binary colour image. Following this, the threshold tool was used to decipher the regions of porosity. The slider bars were set to zero and then the lower bar was gradually increased until all the regions of porosity appeared red. The chosen threshold was then applied and porosity regions were analysed in the software to produce a percentage area. This process was repeated for three fields for each sample.

The same approach, with a different threshold, was implemented to micrographs of the as-received microstructure to quantify Laves volume fraction.

3.3.3 Optical Microscopy Imaging for Microstructural Analysis

Analysis of the respective additive and wrought microstructures were completed by etching freshly polished samples using Kalling's No.2 Reagent to reveal grain boundaries and phases including δ, carbides and Laves. To achieve the best etch possible, prior to etching (but post polishing) the sample was wash, dried with acetone, and heated with a heat gun for 20-30seconds. After etching, assessment of microstructural features was conducted on a Zeiss Axio Observer Inverted Light Microscope.

3.3.4 Electron Backscatter Diffraction (EBSD) for Microstructural Analysis

To assess the microstructural variation across the different heat treatments in the AM samples and how this compared to wrought material, electron backscatter diffraction (EBSD) was utilised. This was achieved by using an EBSD detector fitted to a Hitachi SU3500 SEM. Consistency across the EBSD scans was achieved by maintaining parameters: use of aperture 1, magnification of 100x, working distance of 20mm, accelerating voltage of 20kV, spot size of 100.0, step size of 0.31μm, and a

4x4 EBSD camera binning mode. Scans were set to detect ‘Ni Superalloy’. Once the scan completed, the data was processed through HKL Tango Channel 5 software, where noise reduction was conducted to reduce zero solutions. Settings used for data processing were defined as: 10 pixels per grain minimum as per ISO 13067 [182] and critical mis-orientation set as greater than 10° with allowed completion to 2°. Assessment of annealing twins (Σ3s) was also completed on HKL Tango Channel 5 software by utilising ‘special boundaries’ based on the known axis-angle of 60° or larger for twin boundaries.

3.3.5 Field Emission Gun-Scanning Electron Microscope (FEG-SEM) Analysis for Precipitate Characterisation

For examination of the precipitates present within the microstructure a JEOL 7800F FEG-SEM was utilised. Various methods were implemented to fully understand the precipitates present. Firstly, unetched samples were imaged to assess δ phase and carbides. Then samples etched via Kalling’s No. 2 Reagent were analysed to assess phases including δ, carbides and Laves. Lastly samples were electro-etched with 10% phosphoric acid to identify γ’ and γ’’ phases. Electro-etching was successfully implemented by ensuring the sample was freshly polished prior to etching. Electrical settings used were 3.00V and 0.80mA.

Alongside microscopy, which was used to understand phase morphology and distribution, Energy Dispersive X-Ray Spectroscopy (EDX) was completed using the attached Oxford Instruments SMax 50 to understand elemental distribution.

3.3.6 Fractography

Fractures surfaces of the mechanically tested samples were analysed on a macro and micro scale using a Hitachi SU3500 SEM. SEM images were presented using secondary electron (SE) or backscatter electron (BED). Prior to fractographic analysis, samples were cleaned with acetone in an ultrasonic bath.

3.4 Mechanical Testing

Material properties, specifically mechanical characterisation, is detailed in the following section. All mechanical testing was conducted at a United Kingdom

Accreditation Service (UKAS) accredited mechanical testing laboratory, SMaRT, within the ISM at Swansea University.

3.4.1 Microhardness

Vickers hardness testing was completed on a Struers Duramin-40 M3/A3/AC3 low load hardness tester with a Vickers hardness indenter. 25 indents were obtained per specimen in a 5 by 5 grid according to Figure 35. All tests were completed with a 1kg load and dwell time of 10 seconds. All indents were measured automatically but assessed manually to ensure accuracy in measurement. Testing was completed to ASTM E92-17, ensuring that the spacing between each indent was greater than three times the indent size [183].

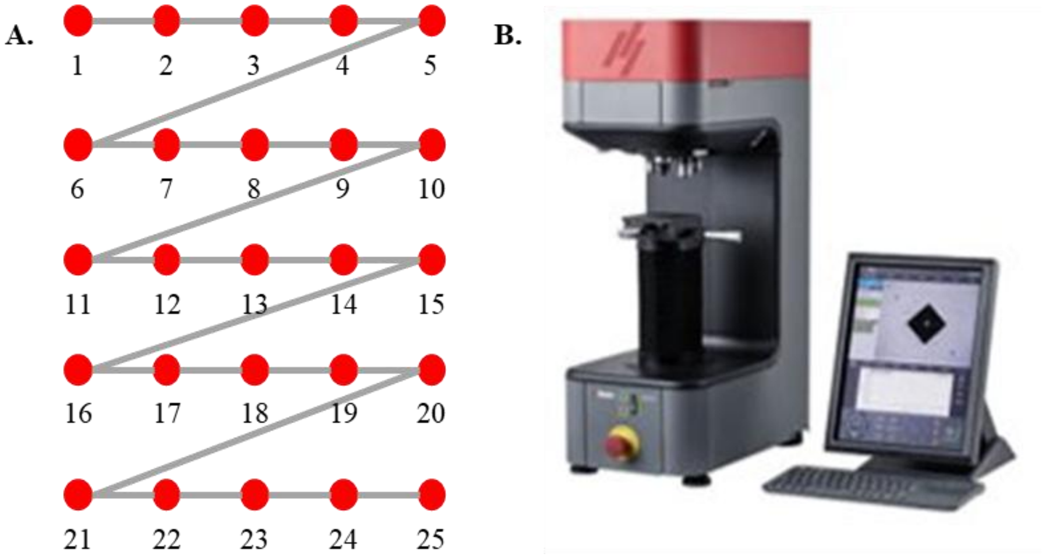

Figure 35: *A) 5 x 5 test pattern and B) Struers Duramin - M3/A3/AC3 Hardness machine.*

3.4.2 Tensile Testing

Tensile testing was conducted to ASTM E8/E8M [120] (for RT testing, 20°C) and ASTM E21 [184] (for ET testing, 650°C) on an electromechanical test system. A digitally controlled furnace and two Type N thermocouples were used to apply heat for the elevated temperature testing and maintain a tolerance of ±4°C. Testing was completed in strain control at $0.00033s^{-1}$ (0.5mm/min) until just after yield was reached, after this point, testing was conducted under load control using a rate of 5mm/min. Sample dimensions were as shown in Figure 36 and in accordance with

ASTM E8M, Specimen 3 [120]. Machined samples were finished with a longitudinal polish or circumferential polish. All AM tensile samples were fabricated in the vertical direction (0°).

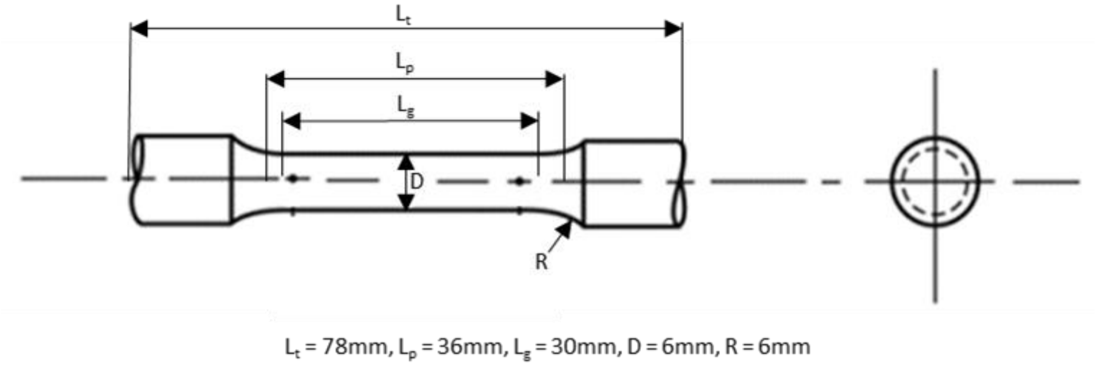

Figure 36: *Schematic of tensile sample dimensions as per ASTM E8M, Specimen 3.*

3.4.3 Strain Control Low Cycle Fatigue Testing

Strain control LCF tests were completed following BS EN 7270 [185] (for RT testing) and ISO 12106 [186] (for ET testing) on a servo-hydraulic mechanical test machine. A standard radiant furnace and two Type N thermocouples were used to apply heat for the elevated temperature testing and maintain a tolerance of ±3°C. Fatigue specimens were machined to the dimensions shown in Figure 37, finished with a longitudinal polish. Testing was conducted at 0.5Hz, with a triangular wave form, and R ratio of -1, at RT (20°C) and ET (650°C). Maximum strain (ε_{max}) values ranging from 0.3% to 0.8% were employed to investigate the influence of different loading conditions on PBF-LB IN718 with varying heat treatments, and for comparison of PBF-LB IN718 to wrought IN718. All AM fatigue samples tested were manufactured in the vertical (90°) direction. During analysis, failure is defined as the point where maximum force decreases by approximately 50% (N_f *(50%)*) as per ASTM E606/E606M [187].

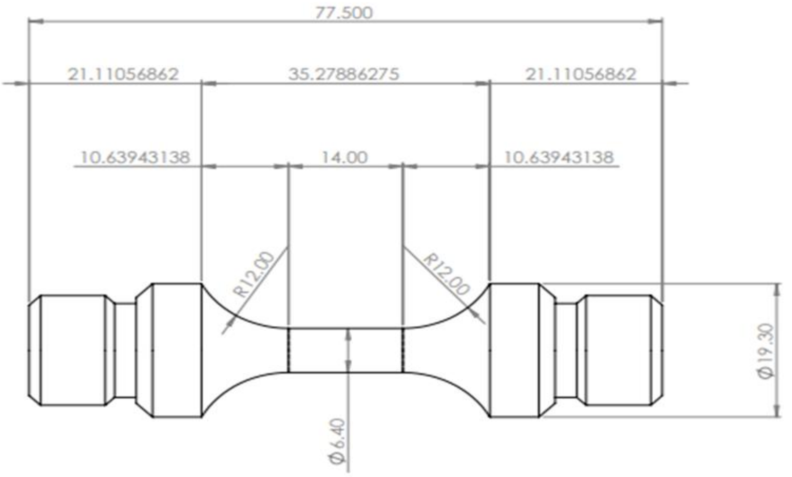

Figure 37: *Schematic of low cycle fatigue sample dimensions, in mm.*

3.4.4 Constant Load Creep Testing

Constant load creep testing was performed in accordance with ASTM E139 [188], with specimens machined to dimensions demonstrated in Figure 38. A digitally controlled furnace and two Type R thermocouples were used to apply heat for the tests and maintain a tolerance of ±4°C. Samples were machined and finished with a longitudinal polish or circumferential finish. Testing was completed on vertically built PBF-LB IN718 and wrought IN718 using a temperature range of 625°C – 675°C and stress range of 625MPa – 690MPa.

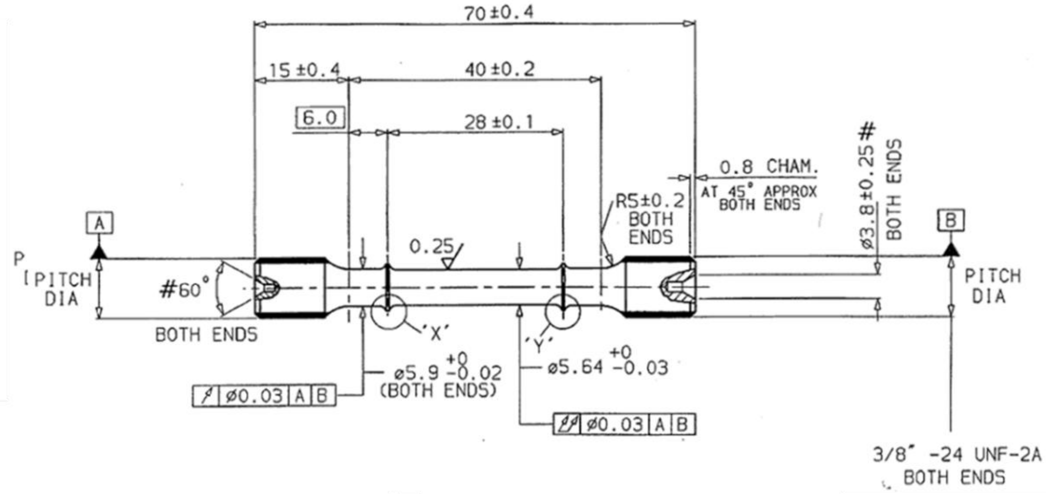

Figure 38: *Schematic of constant load creep sample dimensions, in mm.*

3.4.5 Small Punch Tensile

SPT testing was conducted on a bespoke in-house designed jig assembly, as shown in Figure 39A. The jig, which fits into a 5kN electric screw test machine, consists of an upper and lower die configured to clamp the small punch disc. Each die has a 4mm diameter receiving hole. The lower die is equipped with a 0.2mm chamfer above the 4mm receiving hole, and it has an initial die entrance of 8mm diameter to prevent interference with the punch geometry. Upon contact with the test frame cross-head with the flat surface of the push collar, a compressive displacement is initiated, applying force to the disc specimen through the punch head. Residual deflection measurements are registered using a modified transducer rod that links the centre of the underside of the specimen to a linear variable displacement transducer (LVDT). This configuration allows for deflection measurements directly from the specimen, complementing the displacement behaviour recorded from the crosshead movement.

All tests adhered to BS EN 10371 for small punch (SP) testing [133], employing a crosshead displacement rate of $0.5\text{mm}\cdot\text{min}^{-1}$. The experiments were conducted at ambient RT in a controlled laboratory environment (21°C) or at an ET of 650°C. For the elevated temperature testing a standard radiant box furnace was used to heat the sample and two Type K thermocouples were used to maintain a tolerance of ±3°C. Additionally, the 8mm diameter specimens for this testing technique were polished to a thickness of 0.5±0.005mm, following a sequential route: grind with 80 grit until 0.7mm thickness, grind with 600 grit until 0.6mm thickness, and grind with 1200 grit until 0.5mm thickness. Specimen thickness was measured at five different locations using a calibrated micrometre.

Overall, SPT was completed on wrought alongside vertical and horizontally built AM samples for AR, HT1, and HT2. Both vertical and horizontal samples for each AM variant were assessed to understand which correlation to vertical uniaxial samples would be the most feasible and accurate, as demonstrated by Figure 40. Vertical samples were tested from the ‘top’, along with one sample from the ‘bottom’, to eliminate and confirm no build height variation as shown in Figure 39B.

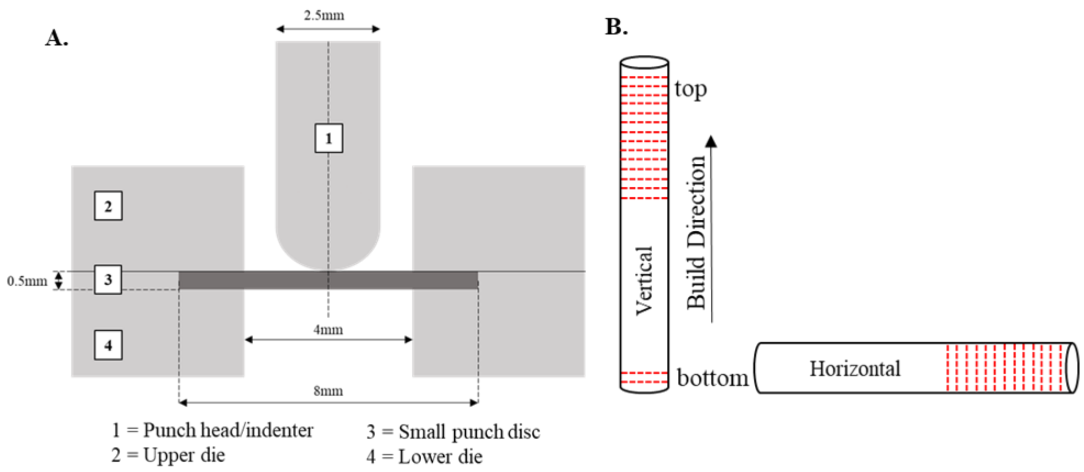

Figure 39: *Schematic of SPT A) assembly jig and B) sample locations.*

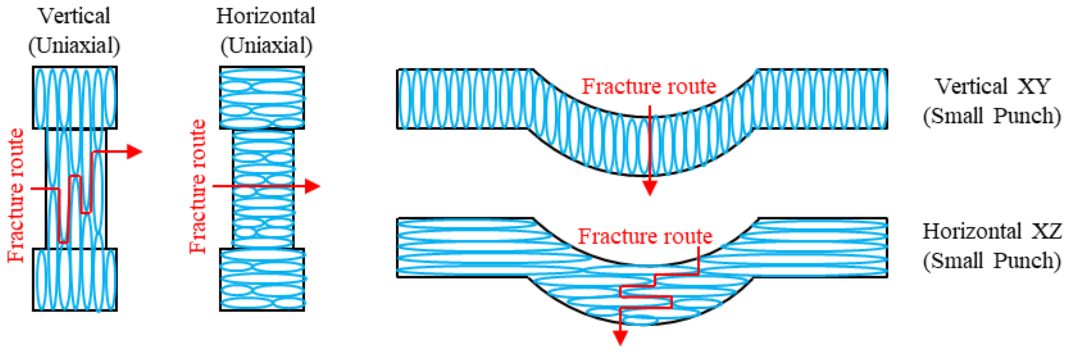

Figure 40: *Schematic to demonstrate comparison between uniaxial and small punch tensile fracture routes in relation to grain morphology.*

3.4.6 Small Punch Creep

Small punch creep tests were carried out using a specialised high-temperature SPC frame. All tests were conducted on the same frame, specifically SP-7, as shown in Figure 41. Loading predominantly occurred along the central axis of the apparatus through an upper load pan configuration. This load was directly applied to a miniature disc sample using a Nimonic 90 punch with a hemispherical end. The disc was securely clamped between upper and lower dies to prevent any residual flexing motion. Dimensions of the punch and receiving hole for the SPC frame was the same as the dimensions for the SPT frame, as per Figure 39A.

The specimen was centrally placed within a furnace and enclosed by a ceramic tube to enable an inert argon atmosphere, effectively eliminating potential oxidation effects. Cooling jackets, fitted with PTFE seals, were installed at both ends to prevent argon leakage. These seals enhanced the retention of frictional contact between the jacket and the tube, ensuring a hermetic seal for the argon. Heat was administered using a digitally controlled furnace, with constant monitoring facilitated by two Type K thermocouples positioned in a drilled hole in the upper die, near the surface of the disc.

All test were performed as per BS EN 10371 standard for SP testing [133], at a controlled temperature of 650±3°C with a load range of 450-350N. Specimen dimensions and preparation for SPC were the same as for SPT, as described in the previous section.

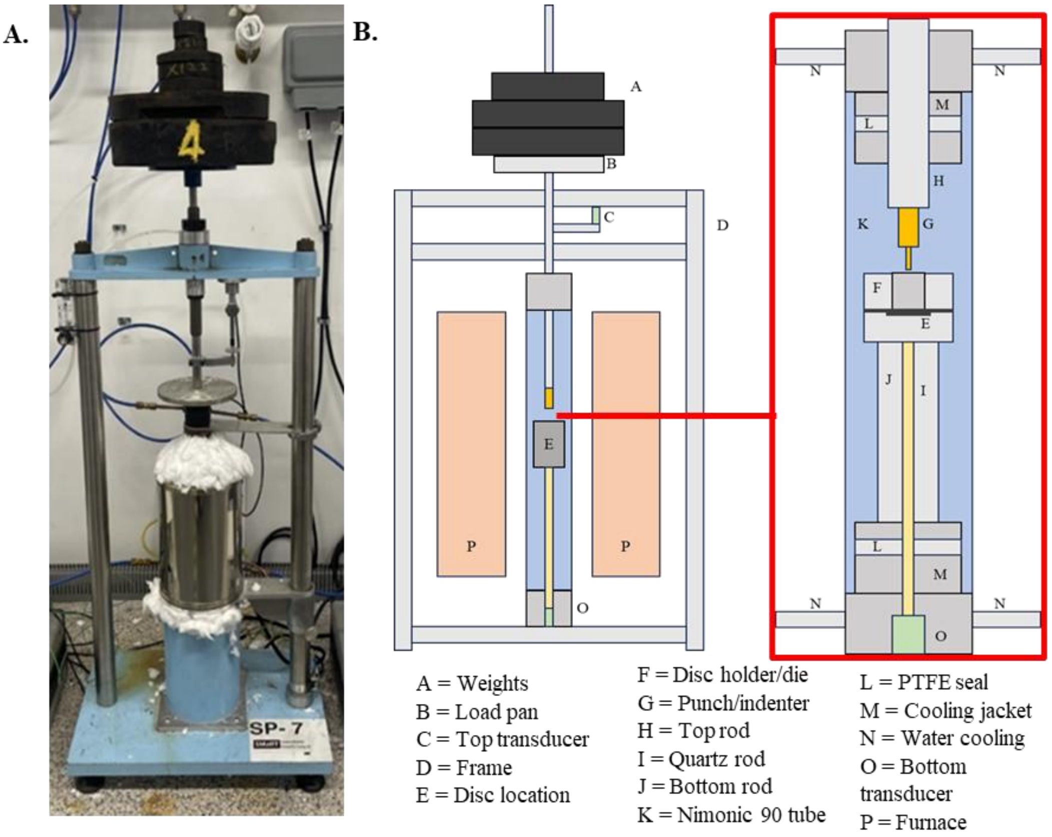

Figure 41: *A) Small punch creep frame, SP-7 with B) illustrated schematic.*

4 Results – Microstructure

4.1 Powder Characterisation

Assessment of the PSD via utilisation of a Malvern Mastersizer 300 is demonstrated in Table 9, where the distribution and average powder size of both powder lots reflects the data provided by the manufacturer (as per section 3.1.3).

Table 9 - *Powder Size Data from Malvern Mastersizer 3000.*

Record Number	**A-PC-01**			**A-PC-02**		
	d_{10} (µm)	**d_{50} (µm)**	**d_{90} (µm)**	**d_{10} (µm)**	**d_{50} (µm)**	**d_{90} (µm)**
1	5.42	10.5	18.4	5.35	10.4	18.8
2	5.43	10.6	18.5	5.35	10.4	18.9
3	5.44	10.6	18.5	5.34	10.4	18.9
4	5.46	10.6	18.6	5.34	10.4	18.9
5	5.47	10.6	18.6	5.34	10.4	18.9
6	5.48	10.7	18.5	5.35	10.5	19
7	5.49	10.7	18.6	5.34	10.5	19
8	5.51	10.7	18.6	5.35	10.5	19.1
9	5.52	10.7	18.6	5.34	10.5	19.1
10	5.52	10.8	18.7	5.34	10.5	19.1

Mean	5.47	10.7	18.5	5.35	10.5	19
Standard Deviation	0.0358	0.0752	0.0905	0.00284	0.0151	0.0892

4.2 Porosity

Following the metallographic procedure and porosity assessment of the AM samples, the following data concluded that samples were near-full density of 99.8% or over, as demonstrated by Table 10. An example micrograph and ImageJ analysis for porosity calculation, following the procedure stated in section 3.3.2, is shown in Figure 42. Wrought specimens are assumed to be fully dense, from manufacturing certificates and visual analysis from micrographs in section 4.3.1.

Table 10 - *Average porosity for PBF-LB IN718 materials.*

Sample	**Porosity (% area)**			
	Vertical		**Horizontal**	
	XY	**XZ**	**XY**	**XZ**
As-received	0.122 ±0.002	0.065 ±0.003	0.099 ±0.013	0.084 ±0.006
Heat Treatment 1	0.118 ±0.016	0.118 ±0.001	0.076 ±0.006	0.071 ±0.021
Heat Treatment 2	0.183 ±0.008	0.108 ±0.002	0.097 ±0.031	0.087 ±0.027

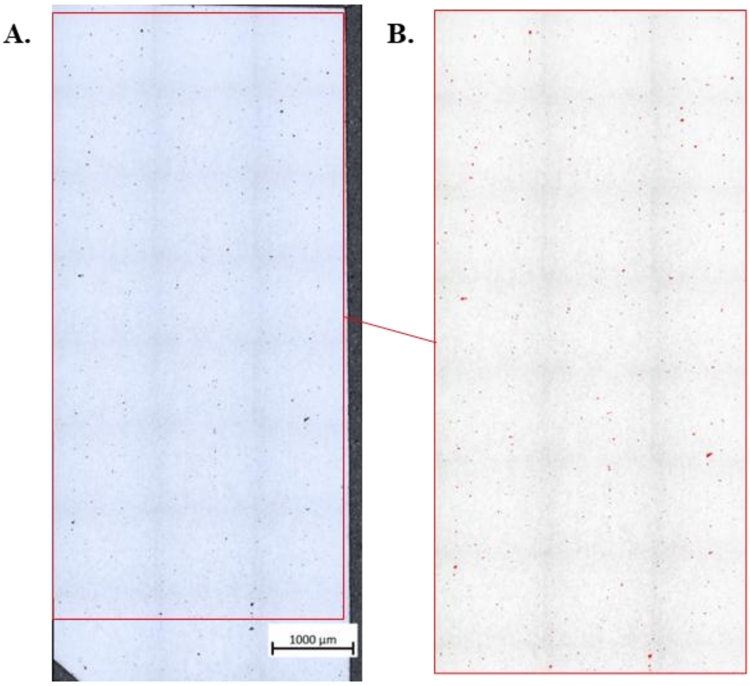

Figure 42: *Example porosity analysis via ImageJ for vertical HT1 XZ. A) 100x stitched optical micrograph. B) ImageJ processed image, where red highlights porosity features.*

4.3 Microstructural Characterisation

Microstructural characterisation was completed to understand how microstructure between wrought and PBF-LB IN718 varied. In addition, the variation of microstructures between the different heat treatments can be analysed. Understanding the microstructure is important in order to recognise how it directly influences the mechanical properties.

4.3.1 Optical

Optical analysis of wrought IN718 revealed an equiaxed microstructure with a high presence of annealing twins and large, blocky carbides, which is demonstrated in

Figure 43. Conformation of the composition of the carbides is displayed in section 4.3.3.

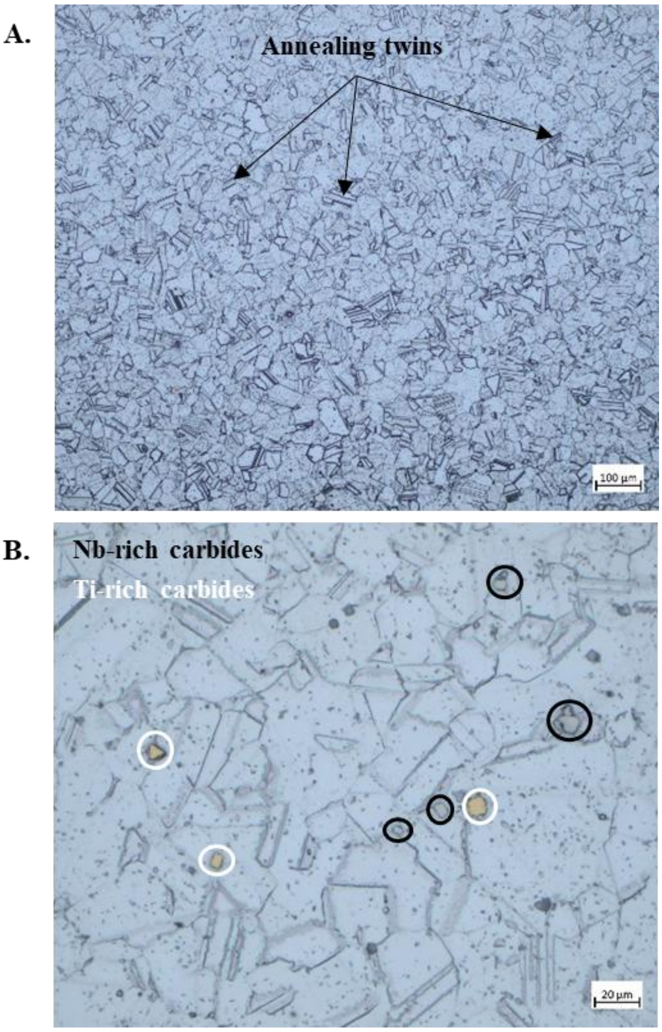

Figure 43: *Optical micrographs of wrought IN718 at A) 100x magnification and B) 500x magnification, after metallographic preparation and etching with Kalling's No.2.*

Similarly, optical micrographs of the XY and XZ planes for vertical PBF-LB samples are shown in Figure 44. The etched microstructure of AR material shows melt pool lines and anisotropy, typically associated with the fabrication process, with coloumnar grains present in the XZ plane and more equiaxed grains in the XY plane. HT1 shows a more uniform, equiaxed morphology with a larger grain structure in the XY and XZ planes, with no presence of melt pool lines. Additionally, there is an increased presence of annealing twins in both planes. On the other hand, HT2 shows a similar microstructure to AR, but without the presence of the melt pool lines. A general comparison between the different microstructures can be made but due to the fine microstructure, implementation of EBSD was performed.

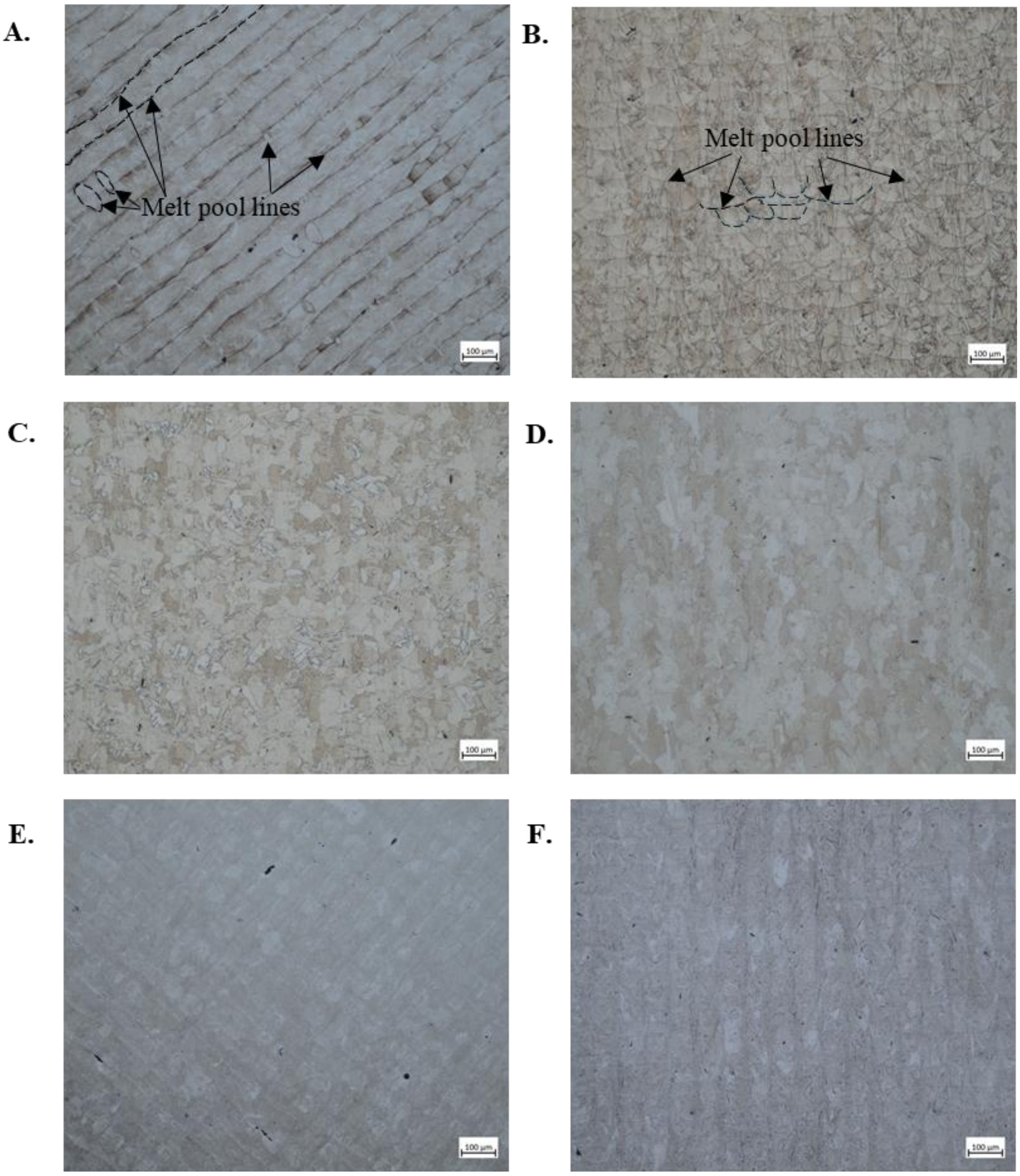

Figure 44: *Optical micrographs at 100x magnification of vertical PBF-LB after metallographic preparation and etching with Kalling's No.2.. A, C, and E, represent XY plane for AR, HT1, and HT2, respectively. B, D, and F, represent XZ plane for AR, HT1, and HT2, respectively.*

Optical micrographs of the XY and XZ planes for horizontal PBF-LB samples are shown in Figure 45. Observations for the horizontal samples are the same as the vertical samples discussed in the previous section.

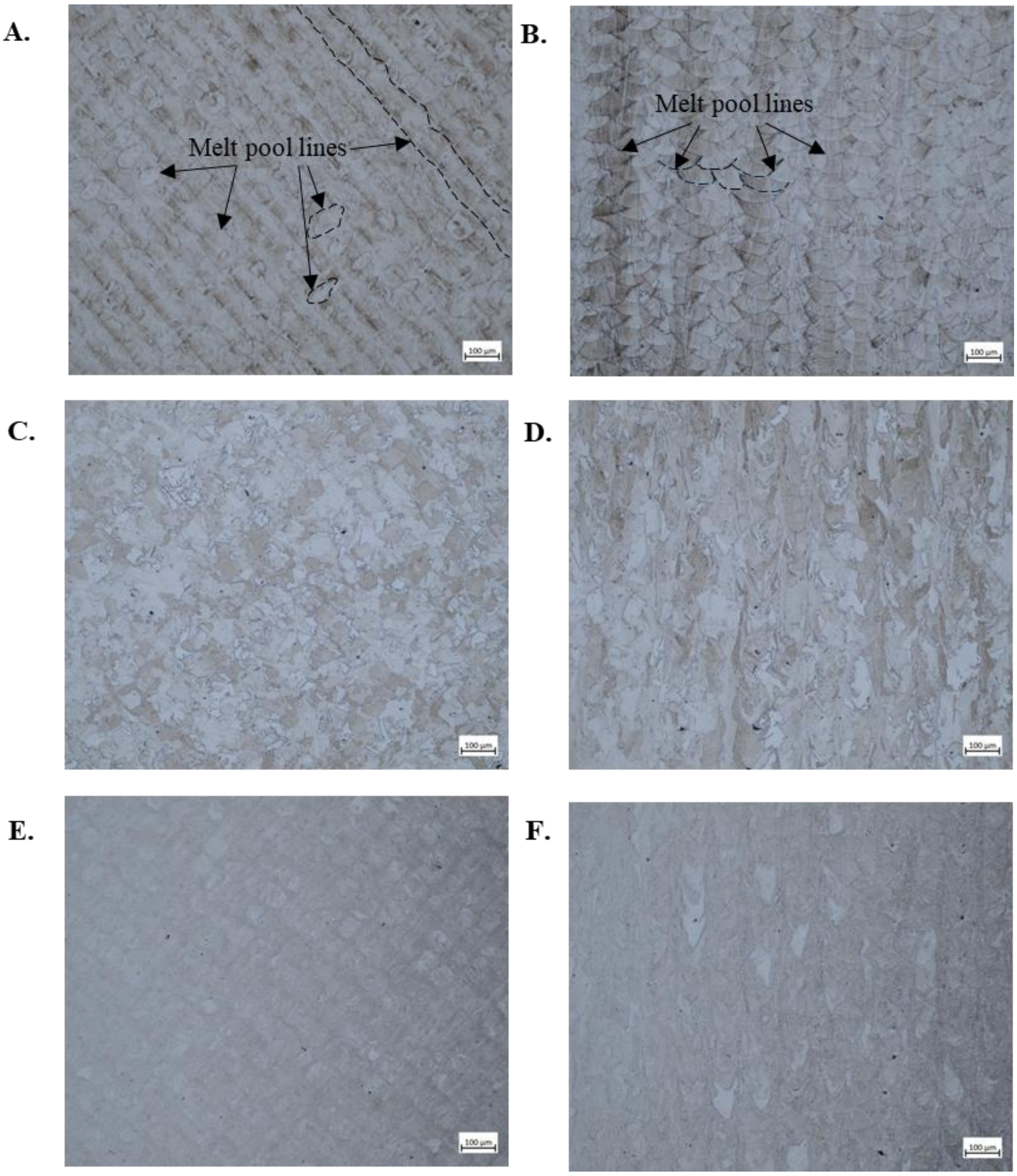

***Figure 45:** Optical micrographs at 100x magnification of horizontal PBF-LB after metallographic preparation and etching with Kalling's No.2. A, C, and E, represent XY plane for AR, HT1, and HT2, respectively. B, D, and F, represent XZ plane for AR, HT1, and HT2, respectively.*

4.3.2 EBSD

Due to the fine microstructure of the AR and HT1 samples, etching and assessing optically was not deemed sufficient, therefore EBSD has been implemented to assess microstructural features.

Utilising EBSD, an inverse pole figure (IPF) map, IPFs, and band contrast map for wrought IN718 was created, as shown in Figure 46. The IPF map and IPFs demonstrate an equiaxed microstructure with no presence of texture, as demonstrated by the low MUD value of 1.20. In addition, the band contrast map highlights grain boundaries in black and Σ3s in red as per map C in Figure 46. Quantitative data processed from the IPF map and band contrast map shows grain area, grain diameter, and aspect ratio (calculated from the major and minor axis od an ellipse fitted into the grains), alongside twin density when assessing grains with and without the inclusion of twin boundaries, as per Table 11. Additionally, a recrystallisation (Rx) value of 97.9% was calculated based on grain orientation spread (GOS) ≤ 2°.

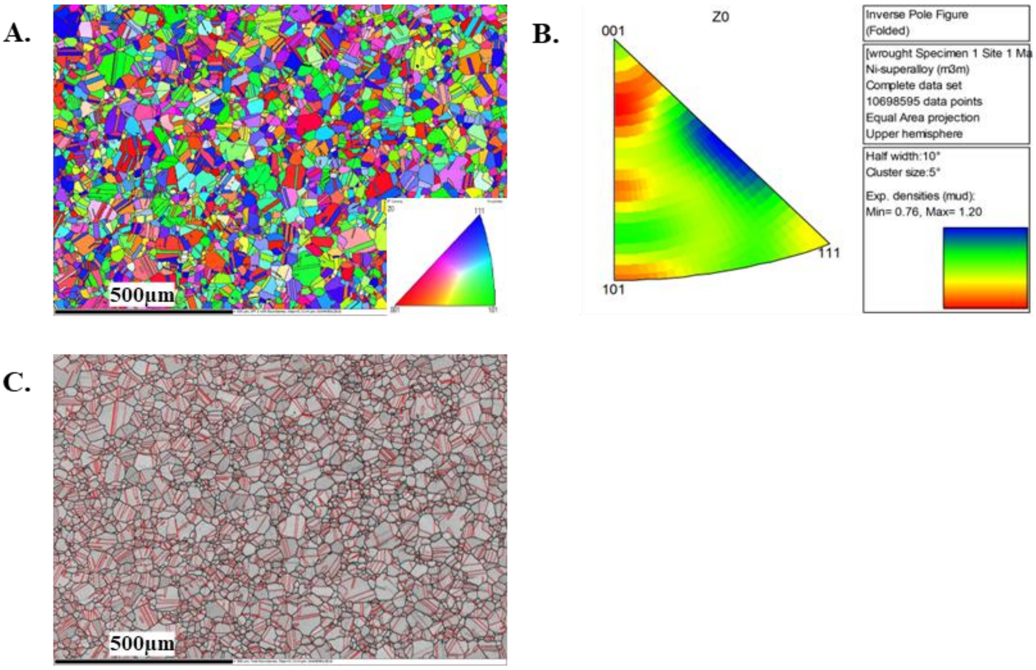

Figure 46: *A) IPF map, B) IPFs, C) and band contrast map where red indicates Σ3s, for wrought IN718 sample.*

Table 11 - *Data from IPF map for wrought IN718 sample*

Sample ID	**Without Twins**			**With Twins**			**Twin Density (%)**
	Grain Area (µm²)	**Grain Diameter (µm)**	**Aspect Ratio**	**Grain Area (µm²)**	**Grain Diameter (µm)**	**Aspect Ratio**	
Wrought	590	22	0.67	193	12.5	0.49	51.4

Likewise, EBSD was implemented for vertical PBF-LB samples in the XY and XZ plane, following the same set up parameters used for wrought IN718. The EBSD maps are shown in Figure 47, alongside the corresponding IPFs in Figure 48.

Assessment of the IPF data suggests that there is preferred growth in the (001) plane but MUD values do not exceed 2.39, suggesting there is no texture in any of the samples. In addition, band contrast maps, as shown in Figure 49, show grain boundaries outlined in black and Σ3s outlined in red.

Data formulated through the Channel 5 software is displayed in Table 12 and supports general claims made in the optical analysis, where HT1 has larger and more equiaxed grains with a higher amount of annealing twins when compared to HT2 and AR samples. Furthermore, the EBSD data confirms that AR and HT1 have very similar microstructures, where longer and more columnar grains are present in the XZ plane and smaller equiaxed grains are present in the XY plane, suggesting strong anisotropy is still present. Also, there is very little twinning present in both the AR and HT1 samples.

Additionally, Rx values of 29.7%, 77.1%, and 34.0%, were calculated for AR, HT1, and HT2, respectively. This was based on a GOS ≤ 2°. Therefore, comparing the AM samples to the wrought sample shows that the AM samples have lower grain area, grain diameter, twin density, and Rx percentage.

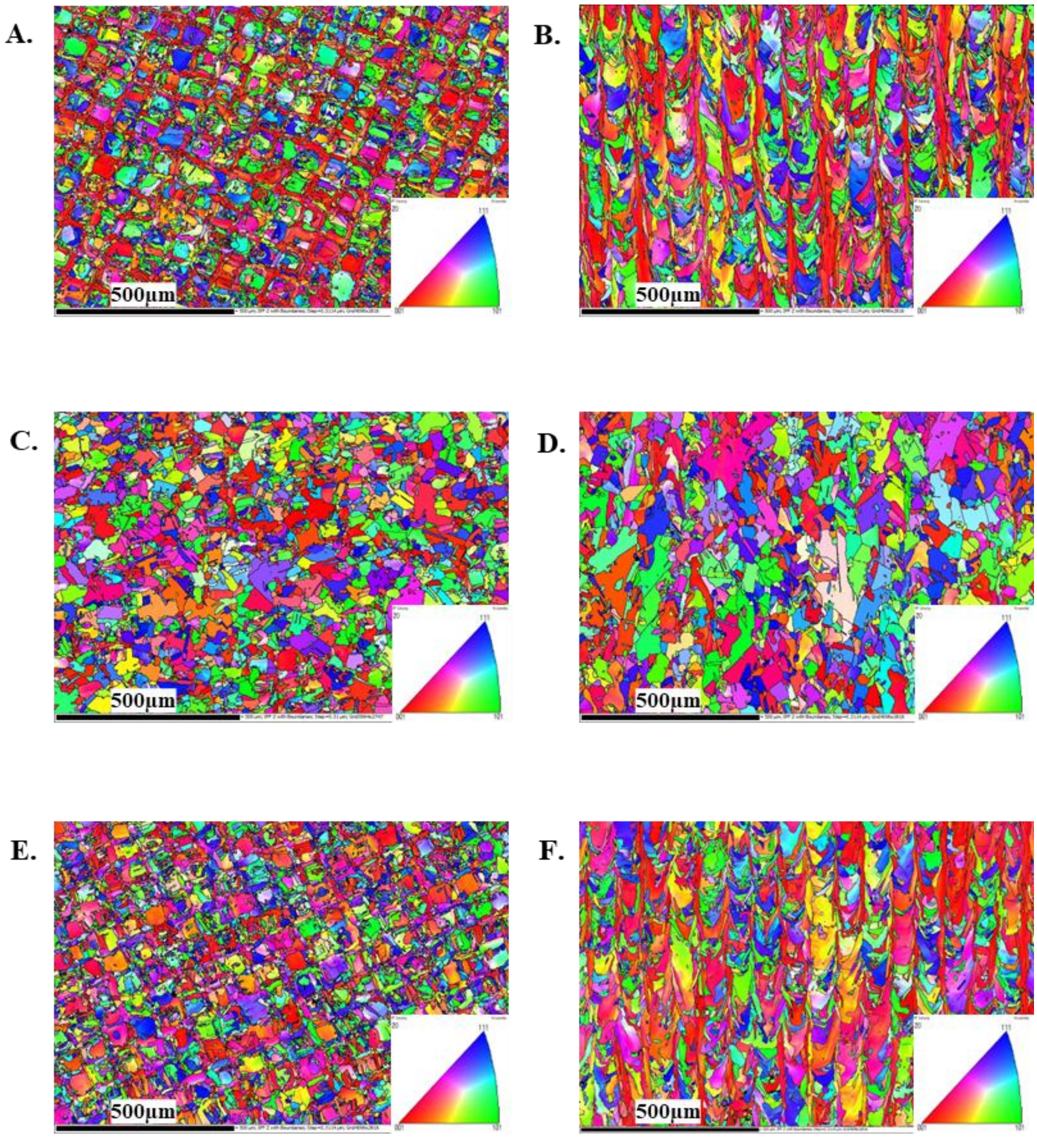

Figure 47: *IPF maps of vertical PBF-LB samples. A, C, and E, represent XY plane for AR, HT1, and HT2, respectively. B, D, and F, represent XZ plane for AR, HT1, and HT2, respectively.*

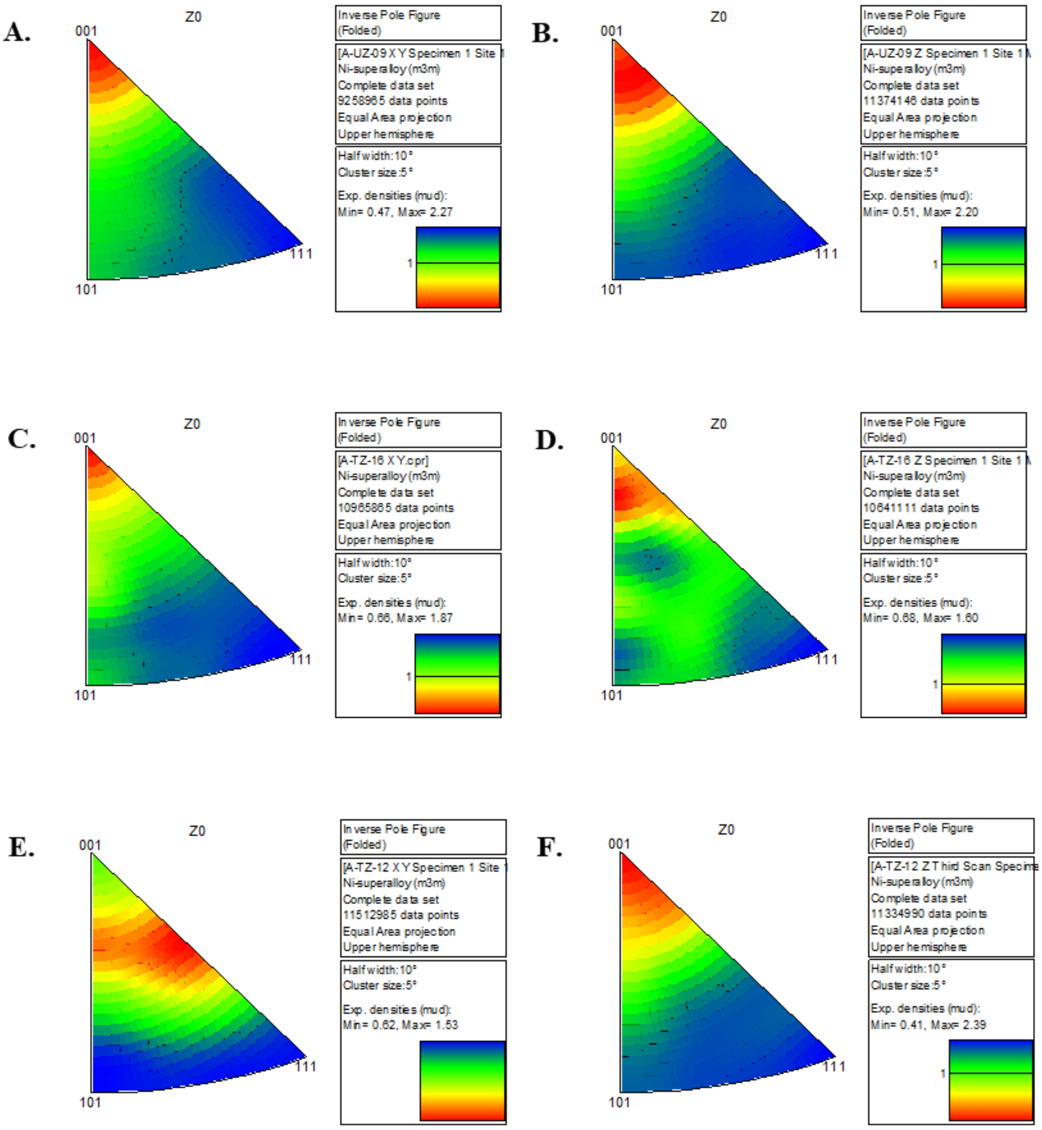

Figure 48: *IPFs of vertical PBF-LB samples. A, C, and E, represent XY plane for AR, HT1, and HT2, respectively. B, D, and F, represent XZ plane for AR, HT1, and HT2, respectively.*

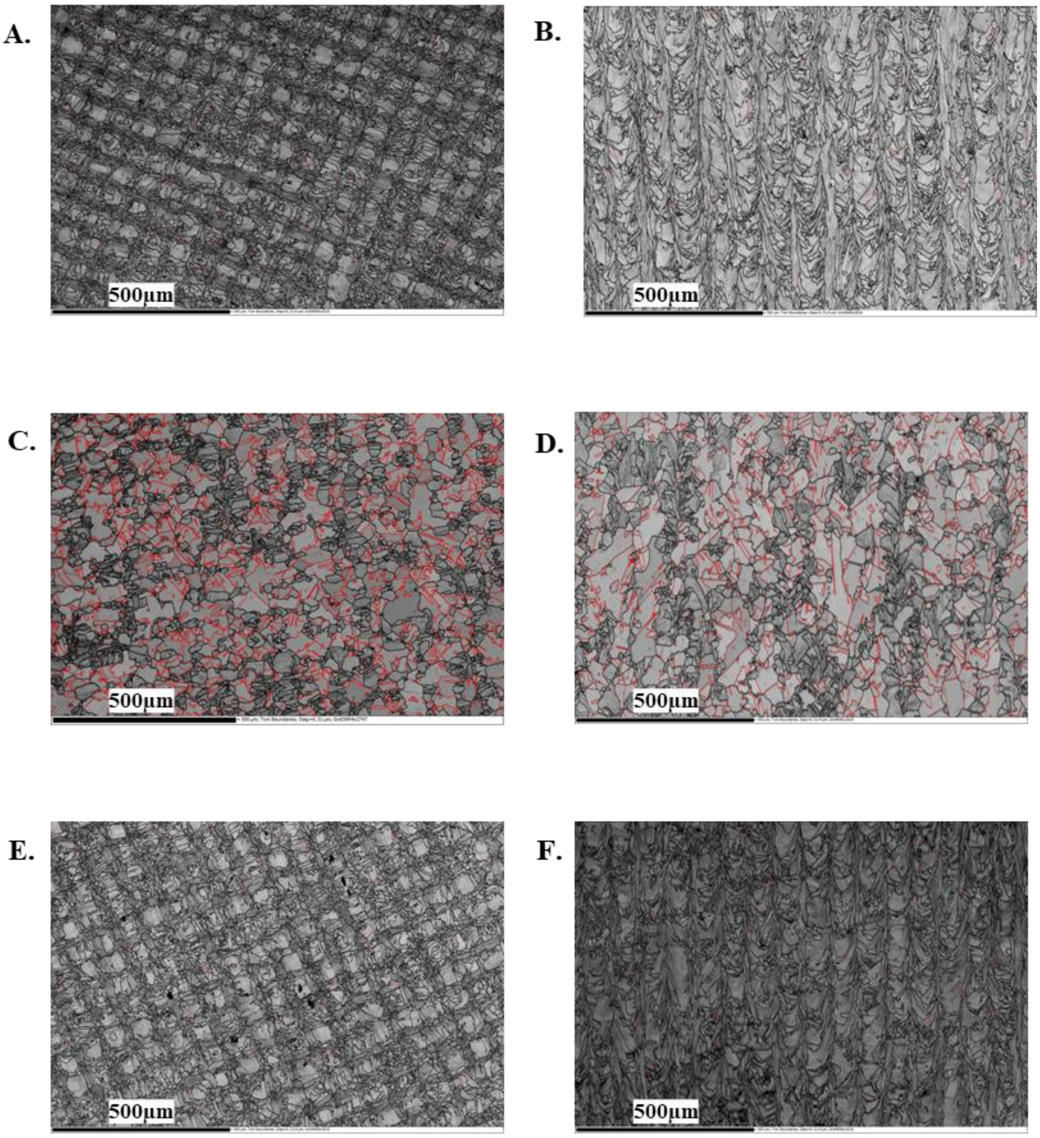

Figure 49: *Band contrast maps, where red indicates Σ3s, of vertical PBF-LB samples. A, C, and E, represent XY plane for AR, HT1, and HT2, respectively. B, D, and F, represent XZ plane for AR, HT1, and HT2, respectively.*

Table 12 *- Data from EBSD IPF maps for vertical PBF-LB.*

Sample ID	**Without Twins**			**With Twins**			**Twin Density (%)**
	Grain Area (μm^2)	**Grain Diameter (μm)**	**Aspect Ratio**	**Grain Area (μm$^{2)}$**	**Grain Diameter (μm)**	**Aspect Ratio**	
AR XZ	196	10.4	0.42	195	10.4	0.42	0.5
AR XY	91	7.6	0.55	89	7.6	0.55	0.5
HT1 XZ	465	14.5	0.49	293	13.3	0.47	25.3
HT1 XY	252	11.4	0.56	166	10.4	0.52	17.6
HT2 XZ	176	9.8	0.43	174	9.8	0.43	0.3
HT2 XY	102	8.0	0.54	101	8.0	0.54	0.4

For horizontal PBF-LB samples the same process was carried out. The relevant EBSD IPF maps are shown in Figure 50, the IPFs are shown in Figure 51, and band contrast maps with grain boundaries outlined in black and Σ3s outlined in red are shown in Figure 52, alongside data from the EBSD and band contrast maps shown in Table 13. Overall, the EBSD IPF maps, IPFs, and band contrast maps, with the relevant data, draw the same conclusions as made in the previous section for the vertical PBF-LB. Therefore, this confirms that the heat treatments behaved the same on different build orientations and that fabrication did not affect the microstructure of different build orientations.

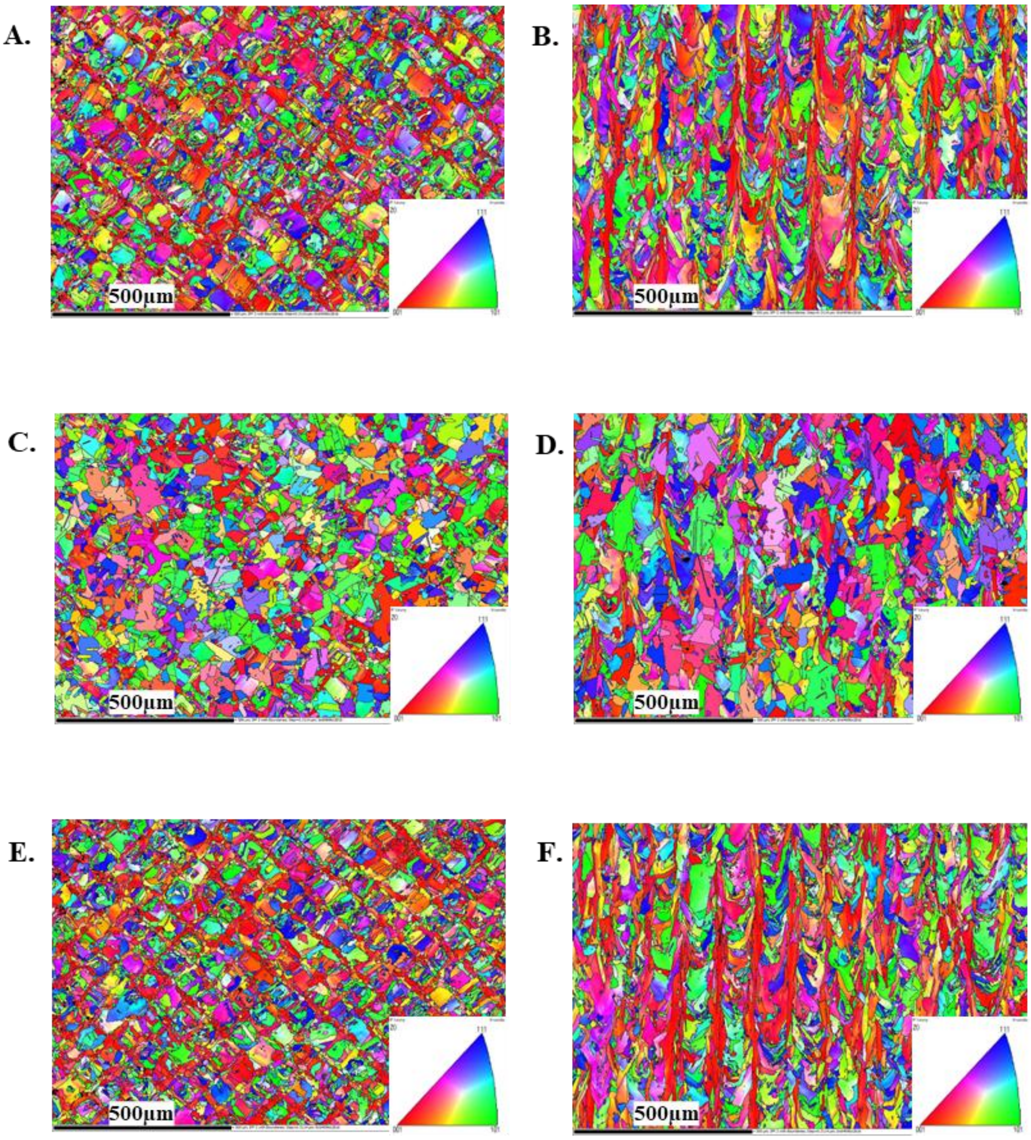

Figure 50: *EBSD IPF maps of horizontal PBF-LB samples. A, C, and E, represent XY plane for AR, HT1, and HT2, respectively. B, D, and F, represent XZ plane for AR, HT1, and HT2, respectively.*

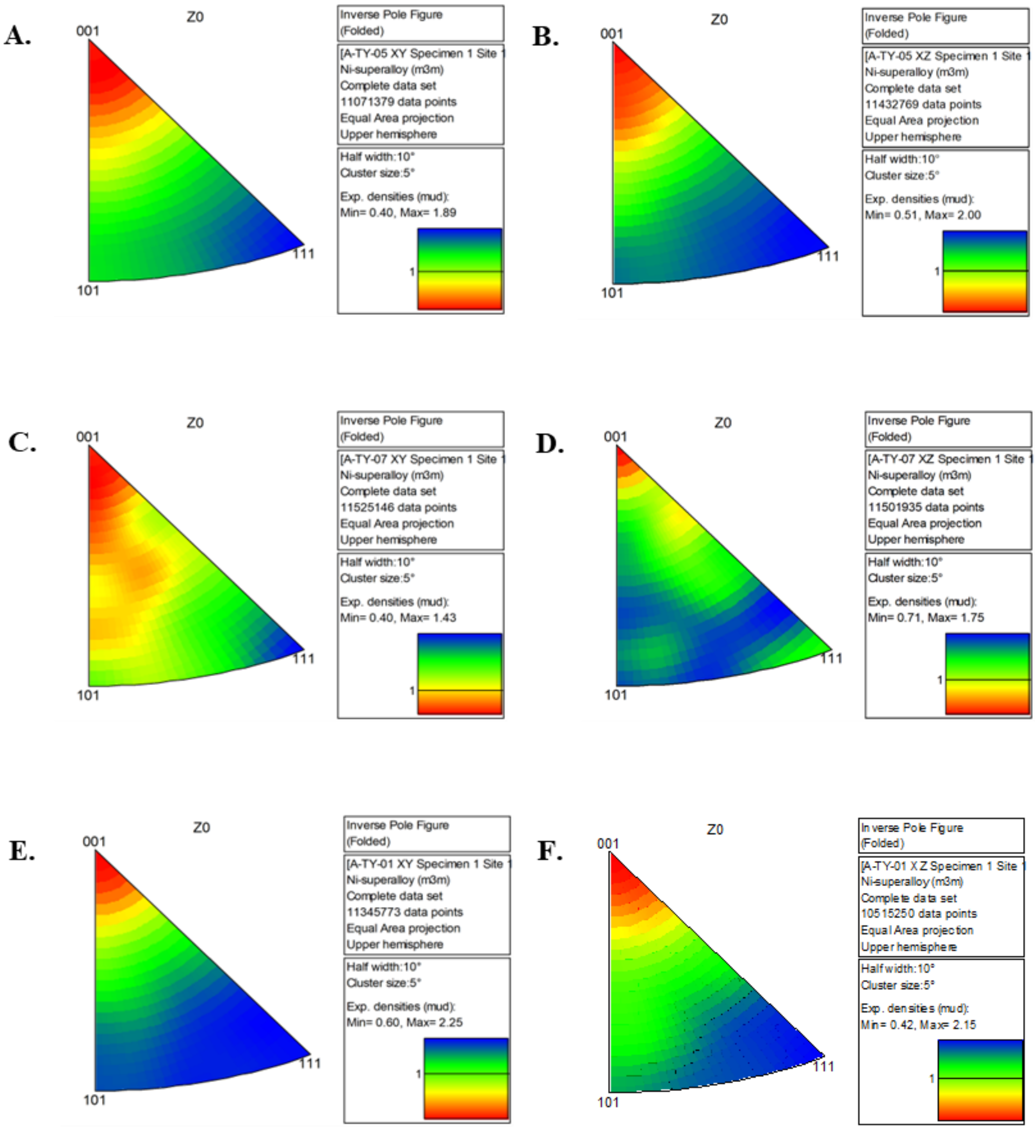

Figure 51: *IPFs of horizontal PBF-LB samples. A, C, and E, represent XY plane for AR, HT1, and HT2, respectively. B, D, and F, represent XZ plane for AR, HT1, and HT2, respectively.*

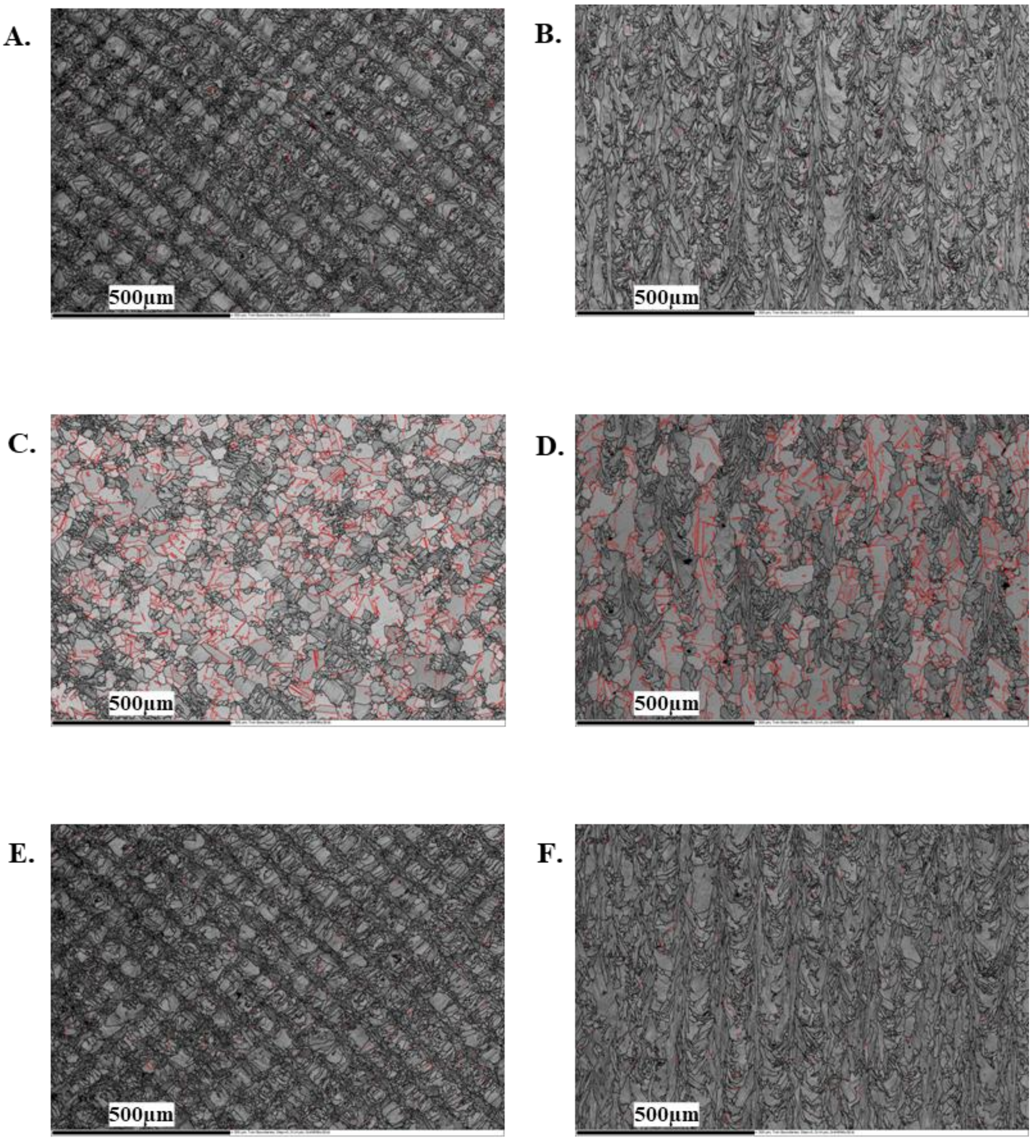

Figure 52: *Band contrast maps, where red indicates Σ3s, of horizontal PBF-LB samples. A, C, and E, represent XY plane for AR, HT1, and HT2, respectively. B, D, and F, represent XZ plane for AR, HT1, and HT2, respectively.*

Table 13 *- Data from IPF map for horizontal PBF-LB.*

Sample ID	**Without Twins**			**With Twins**			**Twin Density (%)**
	Grain Area (µm^2)	**Grain Diameter (µm)**	**Aspect Ratio**	**Grain Area (µm$^{2)}$**	**Grain Diameter (µm)**	**Aspect Ratio**	
AR XZ	152	9.5	0.43	150	9.4	0.43	0.5
AR XY	111	8.8	0.57	110	8.7	0.57	0.6
HT1 XZ	287	11.9	0.47	198	10.8	0.46	19.0
HT1 XY	231	11.1	0.56	161	10.2	0.52	21.5
HT2 XZ	158	9.3	0.43	156	9.3	0.43	0.4
HT2 XY	93	8.1	0.55	92	8.0	0.55	0.6

4.3.3 FEG-SEM

Utilisation of various different etching techniques followed by analysis on the FEG-SEM has allowed for characterisation of the phases present within each sample variant. The assessments support the link and influence of microstructure on the mechanical properties exhibited by the different samples types.

Observations of the phases present in the wrought sample are displayed in Figure 53. Both BED, Figure 53A, and SE, Figure 53B, micrographs shows large blocky carbides (black carbides are TiC, white carbides are NbC, in Figure 53A) with δ phase dispersed (white flecks/specs) throughout the microstructure on the grains and along grain boundaries. The different phases present is supported by EDX analysis shown in Table 14.

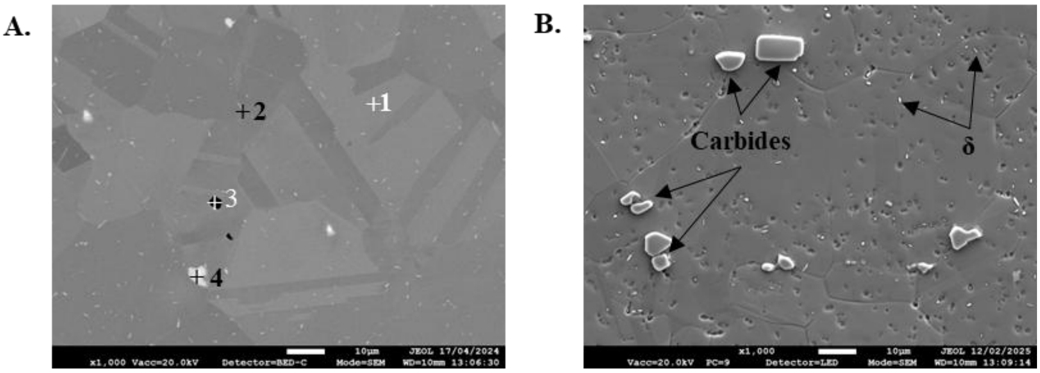

Figure 53: *A) BED FEG-SEM unetched micrograph and B) SE FEG-SEM Kalling's No.2 etched micrograph of wrought IN718.*

Table 14 - *Chemical composition of regions annotated in Figure 53A.*

Region		Chemical Composition (wt.%)							
		Ni	**Cr**	**Fe**	**C**	**Nb**	**Ti**	**Al**	**Other**
1	**Matrix**	48.79	19.11	16.61	9.23	4.52	0.88	0.39	Bal.
2	**δ**	51.78	11.71	10.03	9.30	13.09	1.63	0.34	Bal.
3	**TiC Carbide**	1.82	1.50	0.83	7.04	7.18	61.37	-	Bal
4	**NbC Carbide**	1.28	0.48	0.34	28.76	64.18	4.96	-	Bal

BED FEG-SEM assessment of as-polished vertical PBF-LB samples is depicted in Figure 54 to Figure 56 for AR, HT1, and HT2, respectively. From the BED micrographs it suggests that AR has only a large cellular Laves network with a columnar morphology. For HT1, there appears to be regions with heavy elements suggesting small carbides (blocky) and δ (needle-like) dispersed within the grains and along grain boundaries. There is also some evidence of partial regions of Laves. HT2 shows heavier elements, suggesting δ and carbides, at a much higher quantity, particularly at the grain boundaries, with additional δ within grains. BED micrographs of HT2 also suggests that there are regions of Laves still present within the microstructure.

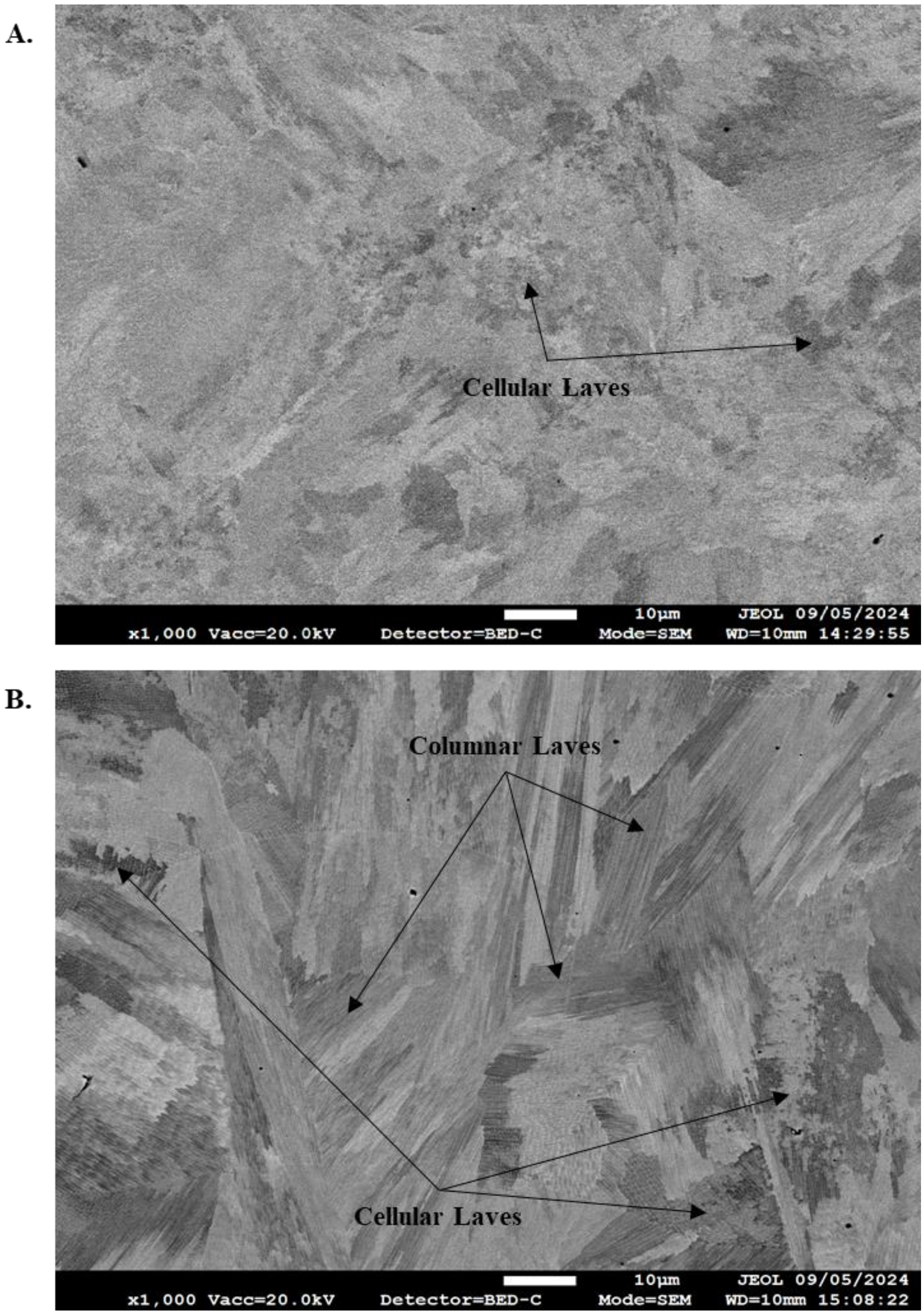

Figure 54: *BED FEG-SEM micrographs of unetched vertical AR PBF-LB samples in A) XY plane and B) XZ plane.*

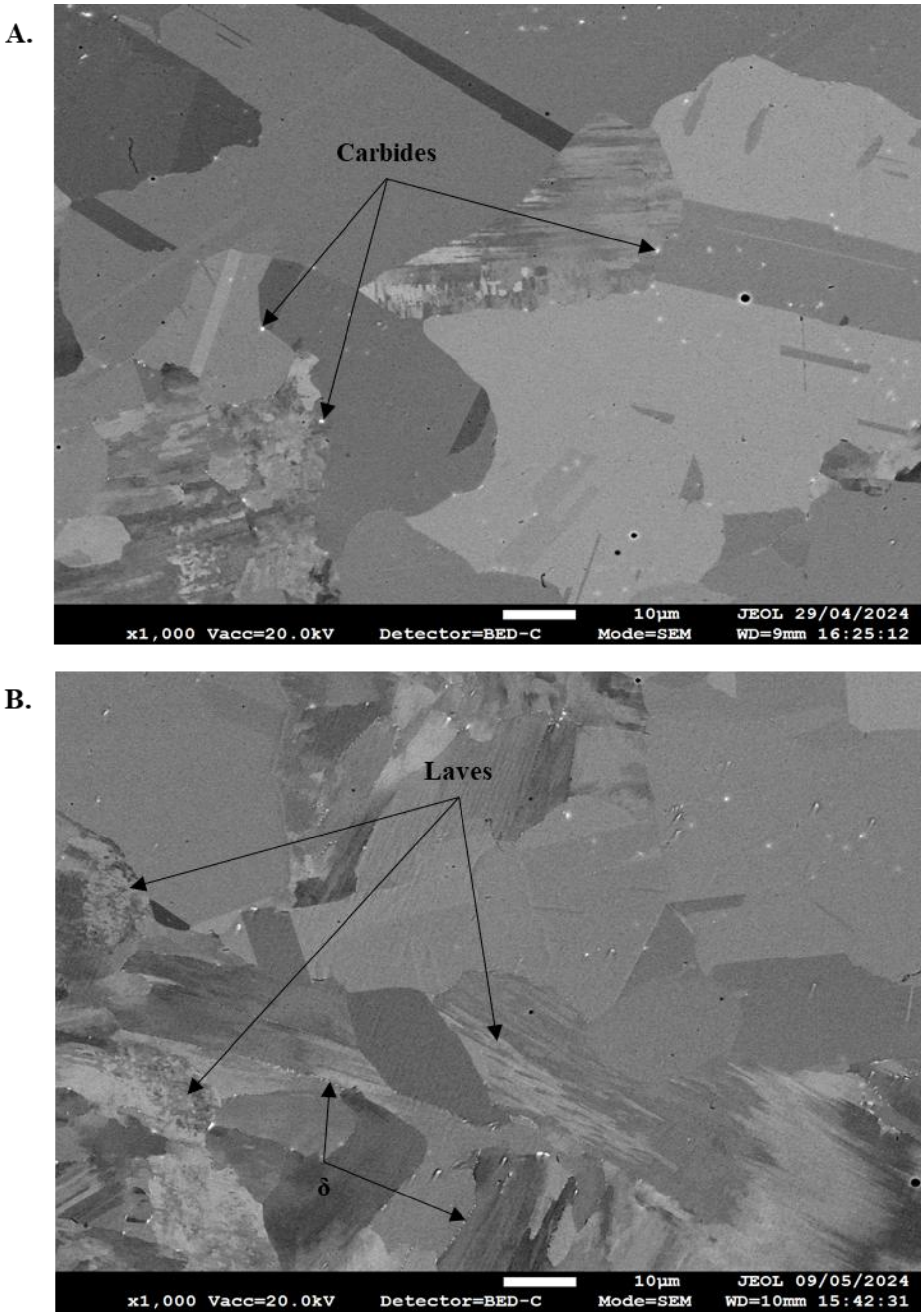

Figure 55: *BED FEG-SEM micrographs of unetched vertical HT1 PBF-LB samples in A) XY plane and B) XZ plane.*

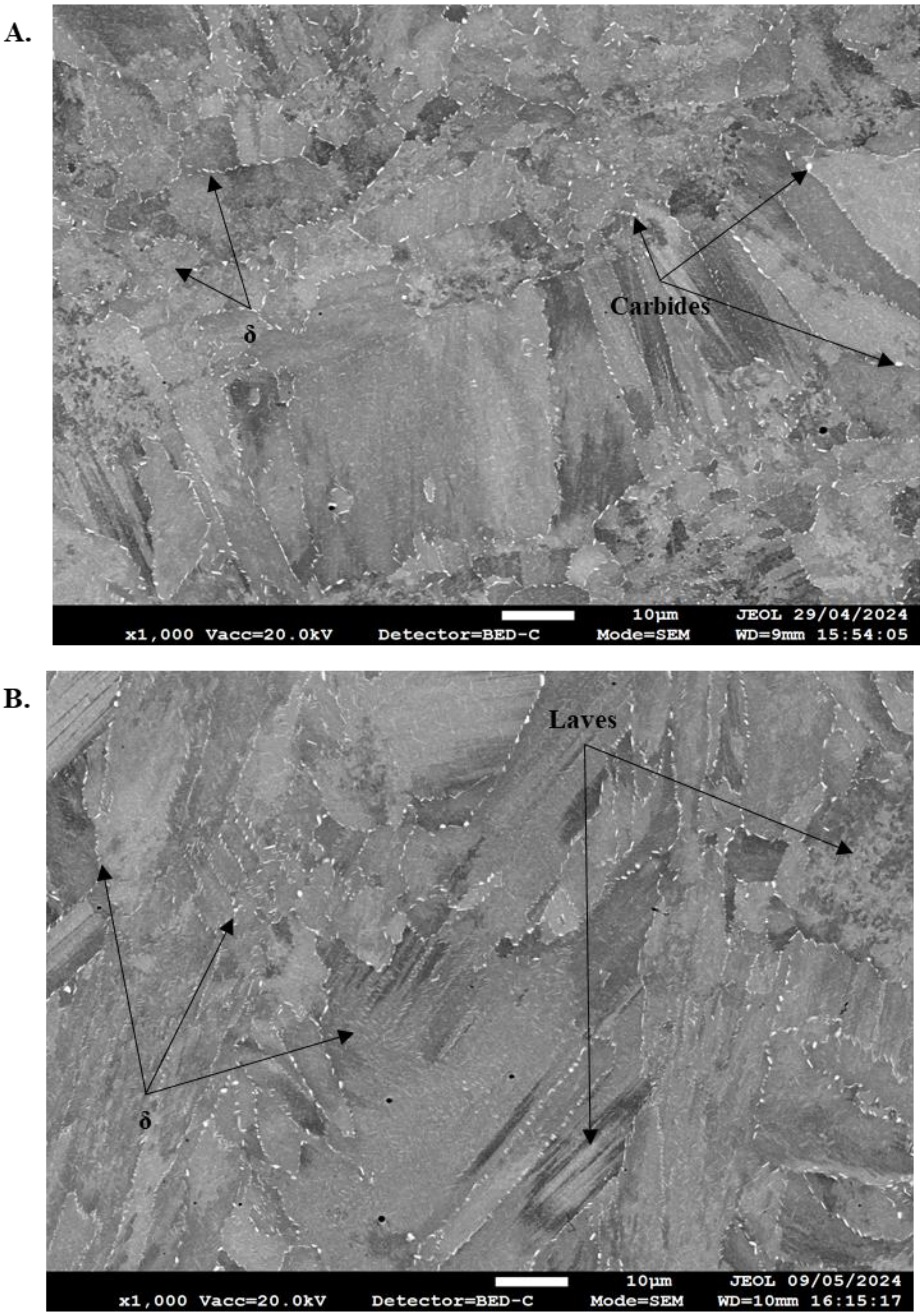

Figure 56: *BED FEG-SEM micrographs of unetched vertical HT2 PBF-LB samples in A) XY plane and B) XZ plane.*

The same procedure was replicated for the horizontal AM samples. Micrographs shown in Figure 57 reflect the same trends discussed previously for the vertical samples. Again, this confirms that build orientation during fabrication did not affect variation of phases presence and their quantities.

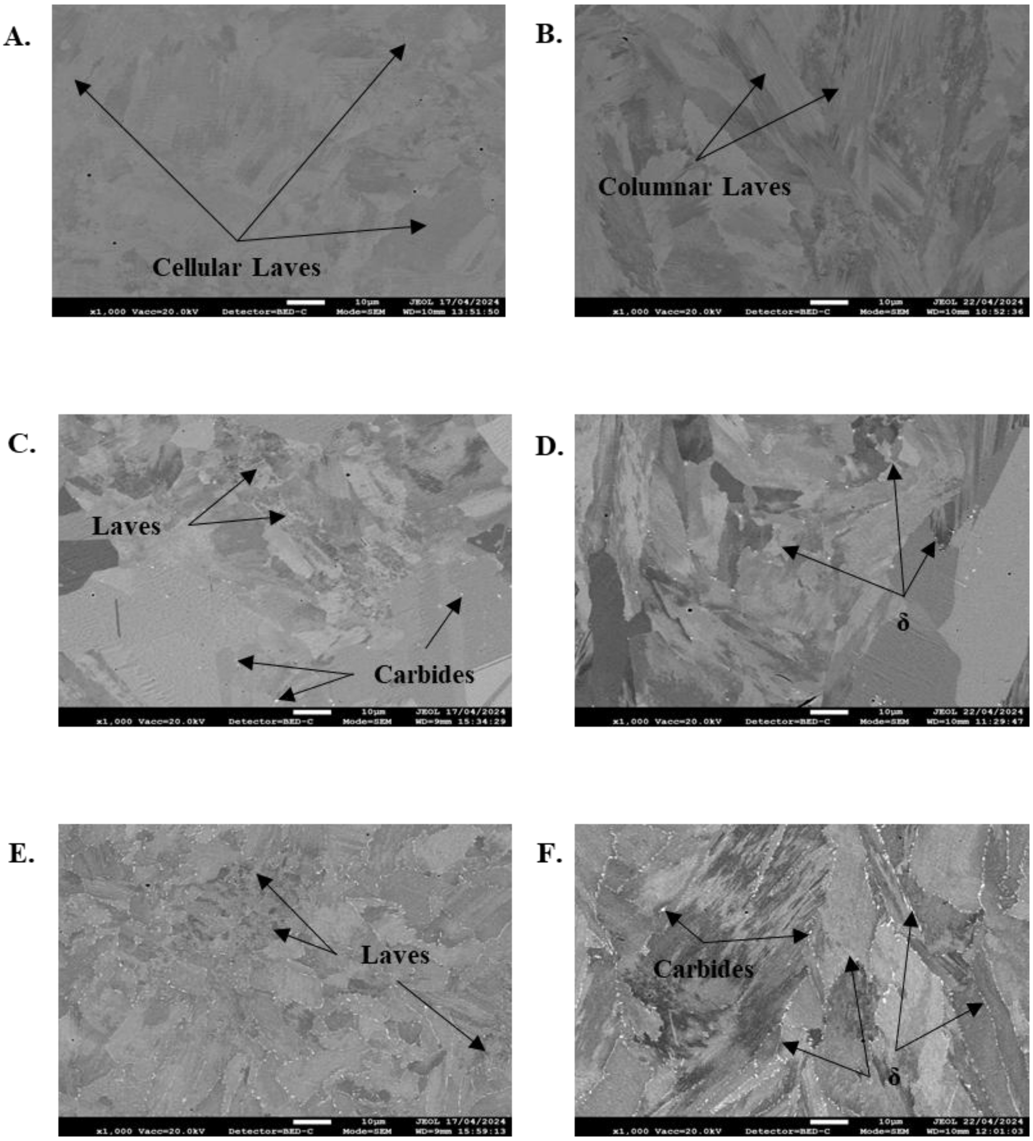

Figure 57: *BED FEG-SEM micrographs of unetched horizontal PBF-LB samples. A, C, and E, represent XY plane for AR, HT1, and HT2, respectively. B, D, and F, represent XZ plane for AR, HT1, and HT2, respectively.*

Additional higher magnification BED micrographs of unetched PBF-LB IN718 shows presence of Al/Ti oxides. These micrographs are reported in Figure 58 with respective EDX data reported in Table 15 for each micrograph. It appears that the location, volume and type of oxides appear consistent across all AM variants. Oxides were not observed in the wrought IN718.

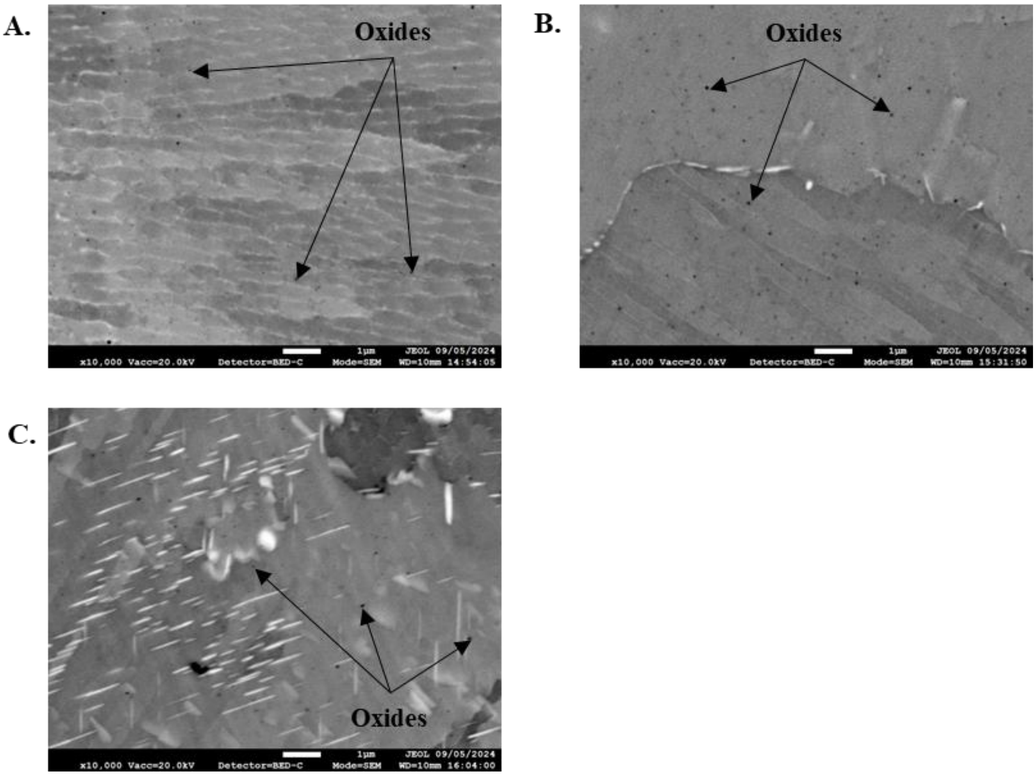

Figure 58: *BED FEG-SEM micrographs at 10,000x magnification of unetched vertical XZ PBF-LB samples. A, B, and C, are AR, HT1, and HT2, respectively.*

Table 15 - *Chemical composition of oxides from Figure 58.*

Region from Figure 58	**Chemical Composition (wt.%)**								
	Ni	**Cr**	**Fe**	**C**	**Nb**	**Ti**	**Al**	**O**	**Other**
A	36.71	14.66	12.98	5.87	3.69	1.19	10.21	11.51	Bal.
B	18.79	10.43	7.72	5.36	3.17	6.81	18.04	27.60	Bal.
C	38.06	15.92	13.48	5.59	2.82	1.33	10.31	10.67	Bal.

To fully understand the presence of the phases within the PBF-LB samples, further SE FEG-SEM analysis was conducted on the same samples but instead of being unetched the samples were etched with Kalling's No. 2 Reagent. Given that the phases are consistent across build orientation and plane, vertical XZ micrographs for AR, HT1, and HT2, are reported in Figure 59 to Figure 61, respectively. Respective EDX chemistry for regions 1 – 7 across Figure 59 to Figure 61 are reported in Table 16.

Assessment of the AR etched micrographs in Figure 59 and respective EDX data for region 1 in Table 16 shows that the AR samples exhibit columnar (Figure 59B) and cellular (Figure 59C) long-chained Laves network. ImageJ analysis of the Laves network revealed that the vertical and horizontal, XZ and XY, samples had an average Laves volume fraction of 4.39 ±0.92%.

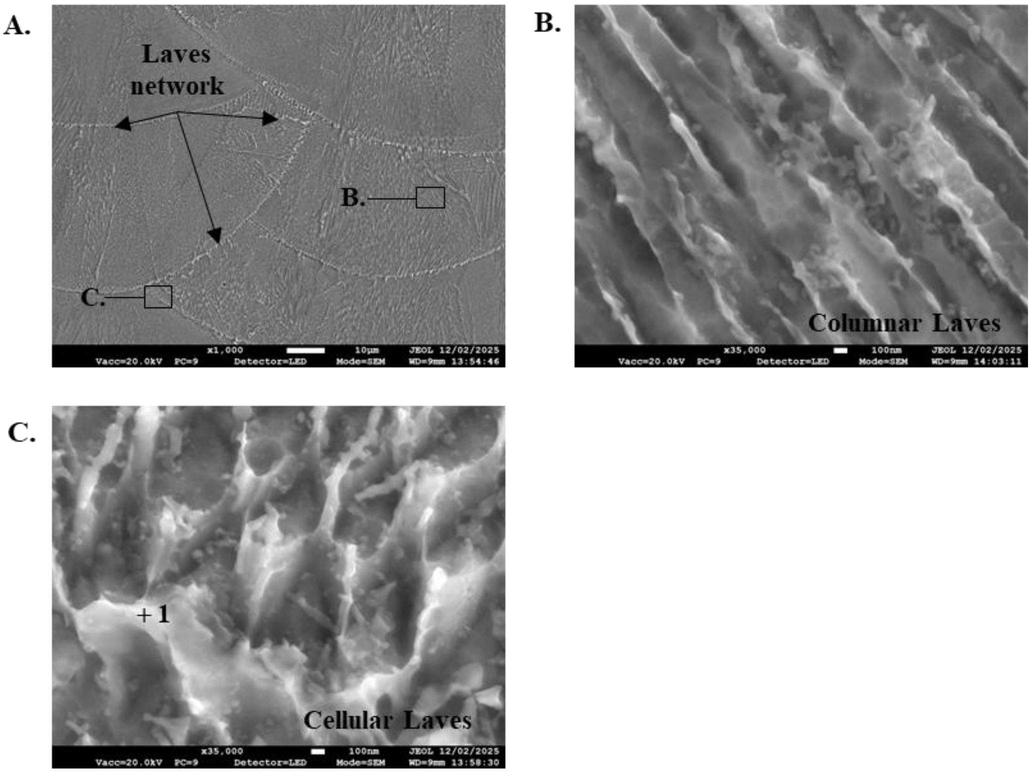

Figure 59: *SE FEG-SEM A) lower magnification micrograph and B-C) higher magnification micrographs of Kalling's No.2 etched vertical XZ AR.*

This network is not seen in HT1 and HT2. Alternatively, for HT1 the presence of carbides (Figure 60D) and δ (Figure 60B), primarily at grain boundaries, alongside discontinuous Laves (Figure 60C) predominantly within grains is seen, as per Figure 60. Identification of δ (region 2), Laves (region 3), and carbides (region 4), is supported by EDX analysis reported in Table 16

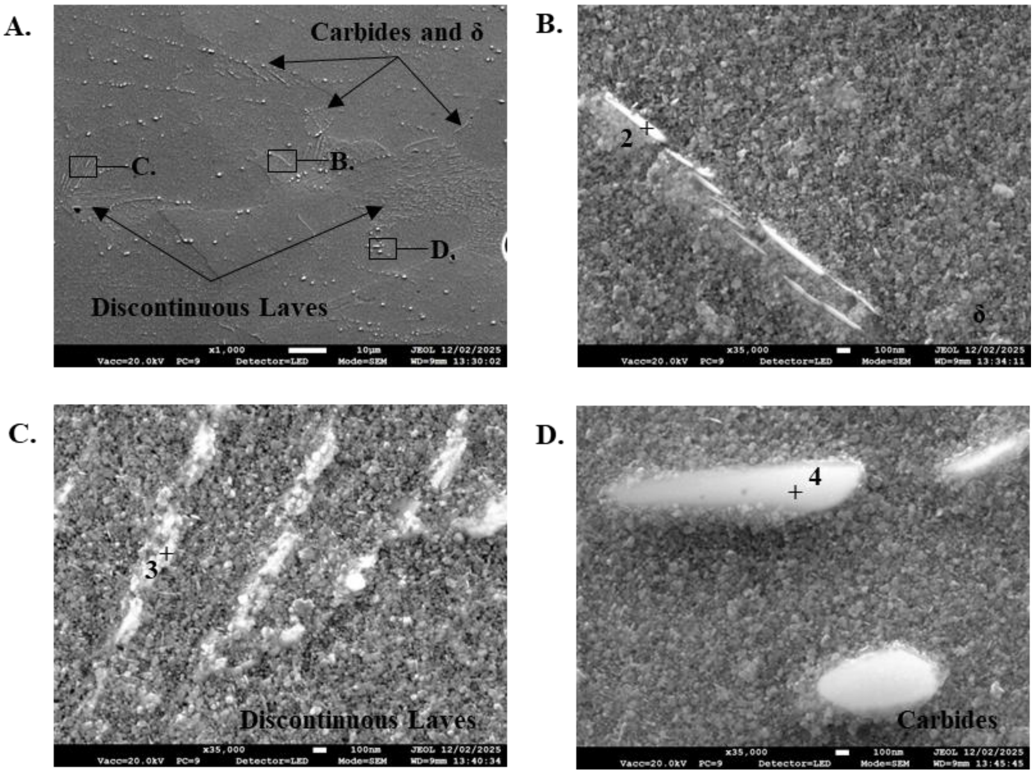

Figure 60: *SE FEG-SEM A) lower magnification micrograph and B-D) higher magnification micrographs of Kalling's No.2 etched vertical XZ HT1.*

HT2 shows discrete Laves, δ, and carbides, concentrated at grain boundaries, with some δ within the grains, as depicted by Figure 61A. The phases present in HT2 are similar to HT1 however, the quantities and distribution differ, with HT2 displaying a higher amount of δ (Figure 61B, region 6), Laves (Figure 61B, region 5) and carbides (Figure 61C, region 7) predominantly near grain boundaries.

It is noted that comparative phases for EDX from Table 14 and Table 16 for wrought, AR, HT1, and HT2, differ. This is due to the limitations of EDX and conclusions of phases based on EDX are formed on chemical increases/decreases of elements in phases within a sample (rather than across samples and exact chemistries) and previous published research (as cited later in the discussion).

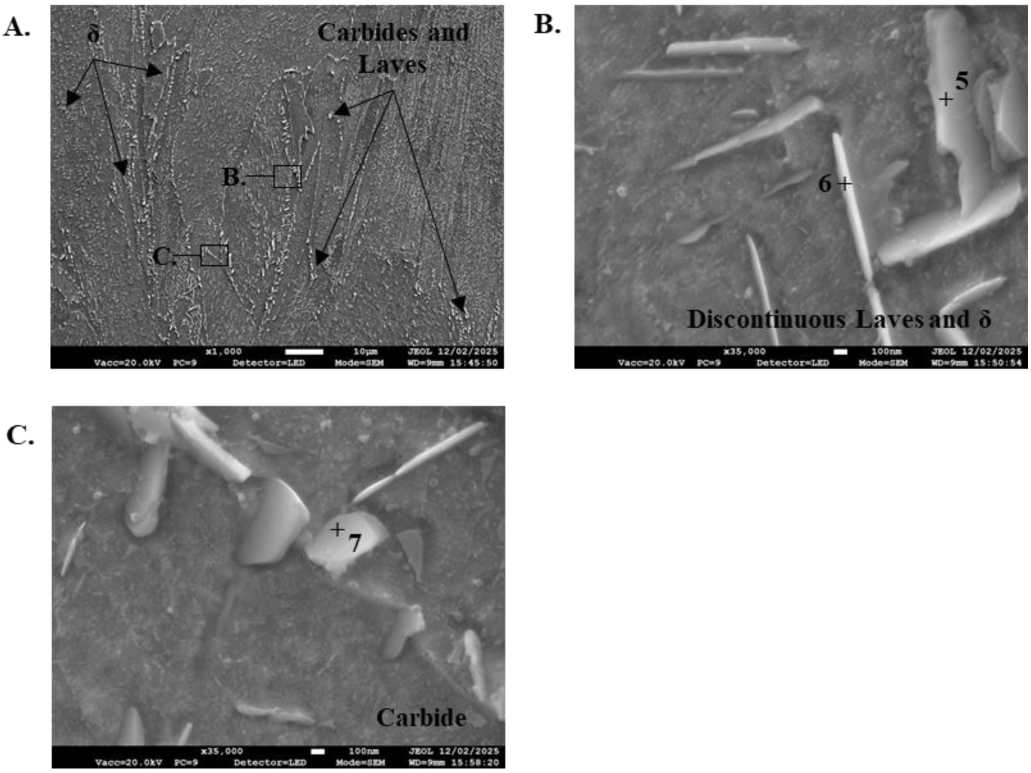

Figure 61: *SE FEG-SEM A) lower magnification micrograph and B-C) higher magnification micrographs of Kalling's No.2 etched vertical XZ HT2.*

Table 16 - *Chemical composition of regions annotated in Figure 59 to Figure 61.*

Region		Chemical Composition (wt.%)							
		Ni	**Cr**	**Fe**	**C**	**Nb**	**Ti**	**Al**	**Other**
1 (AR)	**Laves**	42.01	15.73	15.28	12.51	6.11	0.93	0.75	Bal.
2 (HT1)	**δ**	47.73	16.17	14.49	10.24	7.25	1.08	0.41	Bal.
3 (HT1)	**Laves**	48.42	17.47	15.78	9.48	4.46	1.12	0.61	Bal.
4 (HT1)	**NbC Carbide**	29.23	12.35	10.73	16.78	26.56	4.08	0.28	Bal.
5 (HT2)	**Laves**	48.46	16.54	15.45	10.25	5.36	1.15	0.55	Bal.
6 (HT2)	**δ**	51.53	10.96	9.76	12.51	11.25	1.65	0.42	Bal
7 (HT2)	**NbC Carbide**	47.63	10.03	8.84	16.09	13.56	1.54	0.53	Bal.

Further analysis of IN718 samples was carried out via electro-etching with 10% phosphoric acid, which helped to reveal the γ’ (round morphology) and γ’’ (plate-like morphology) precipitates in the HT1 and HT2 samples. This is shown by the higher magnification FEG-SEM micrographs in Figure 62. HT1 (Figure 62A) shows a presence of γ’ and γ’’ compared to HT2 (Figure 62B) which shows only γ’.

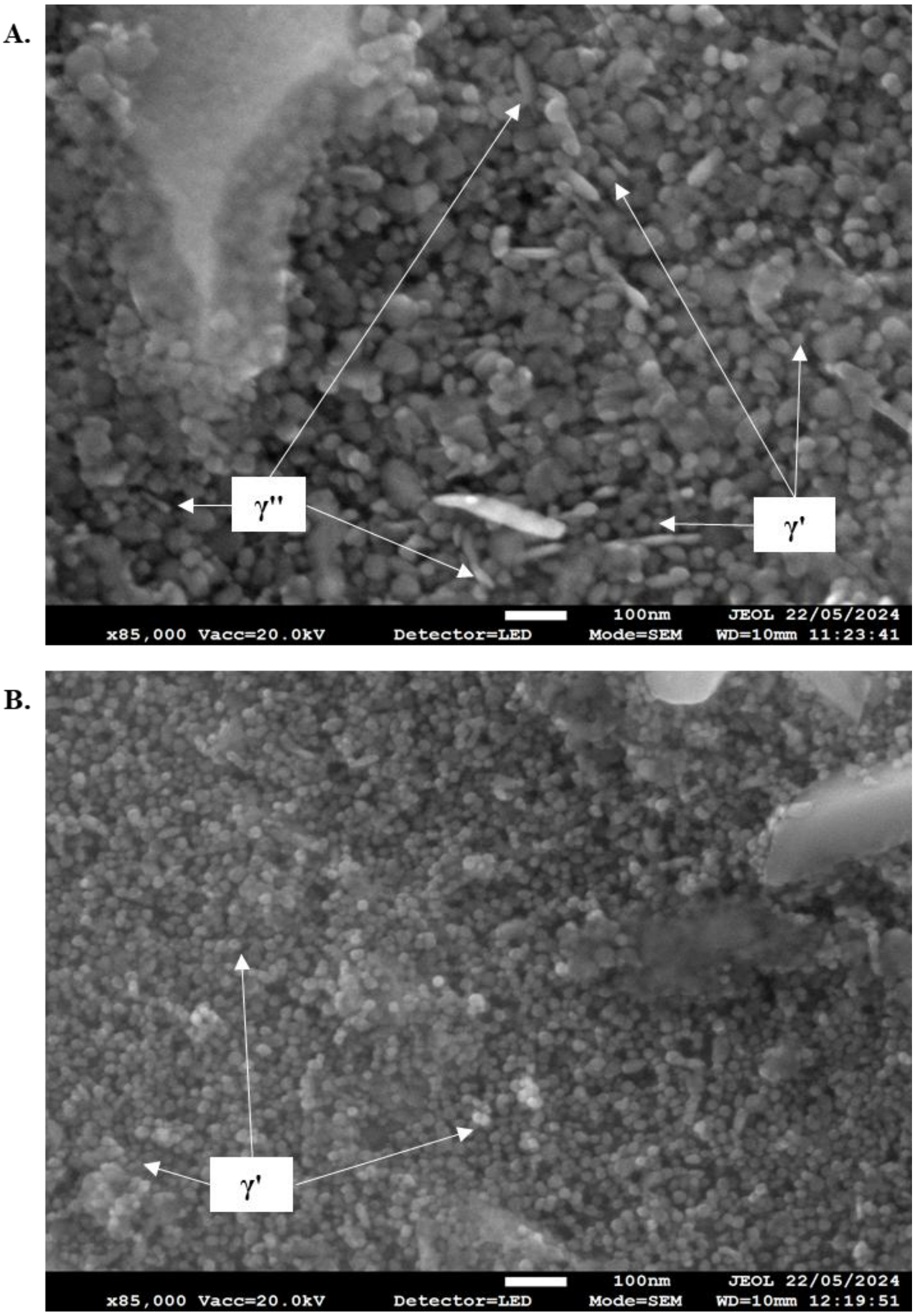

Figure 62: *SE FEG-SEM micrographs of electro-etched PBF-LB samples where A and B represent HT1 and HT2, respectively.*

4.4 Microhardness

Following the experimental procedure for Vickers hardness testing, results are shown in Table 17 and depicted graphically, as per Figure 63 and Figure 64, for vertical and horizontal samples, respectively. Data from the graphs shows that the wrought material exhibits the lowest hardness, followed by the AR samples, then HT1, and finally HT2, which is marginally higher than HT1. There is very little difference between the vertical and horizontal samples.

***Table 17 -** Vickers hardness results.*

Sample	**Average Hardness (HV/1)**			
	Vertical		**Horizontal**	
	XY	**XZ**	**XY**	**XZ**
As-received	326 ±5	333 ±8	321 ±6	337 ±4
Heat Treatment 1	469 ±14	475 ±8	475 ±9	474 ±6
Heat Treatment 2	480 ±11	485 ±12	485 ±12	485 ±8

	Average Hardness (HV/1)	
	XY	**XZ**
Wrought	213 ±6	222 ±6

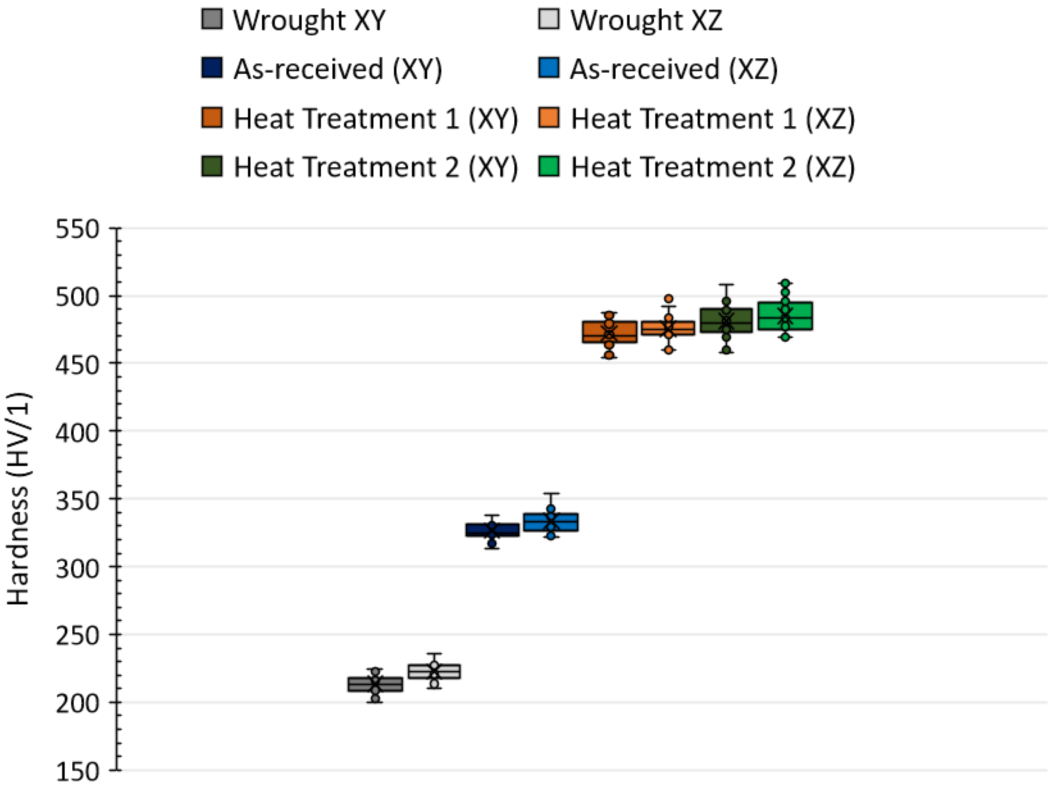

***Figure 63:** Graph to show Vickers hardness data for vertical PBF-LB IN718 samples.*

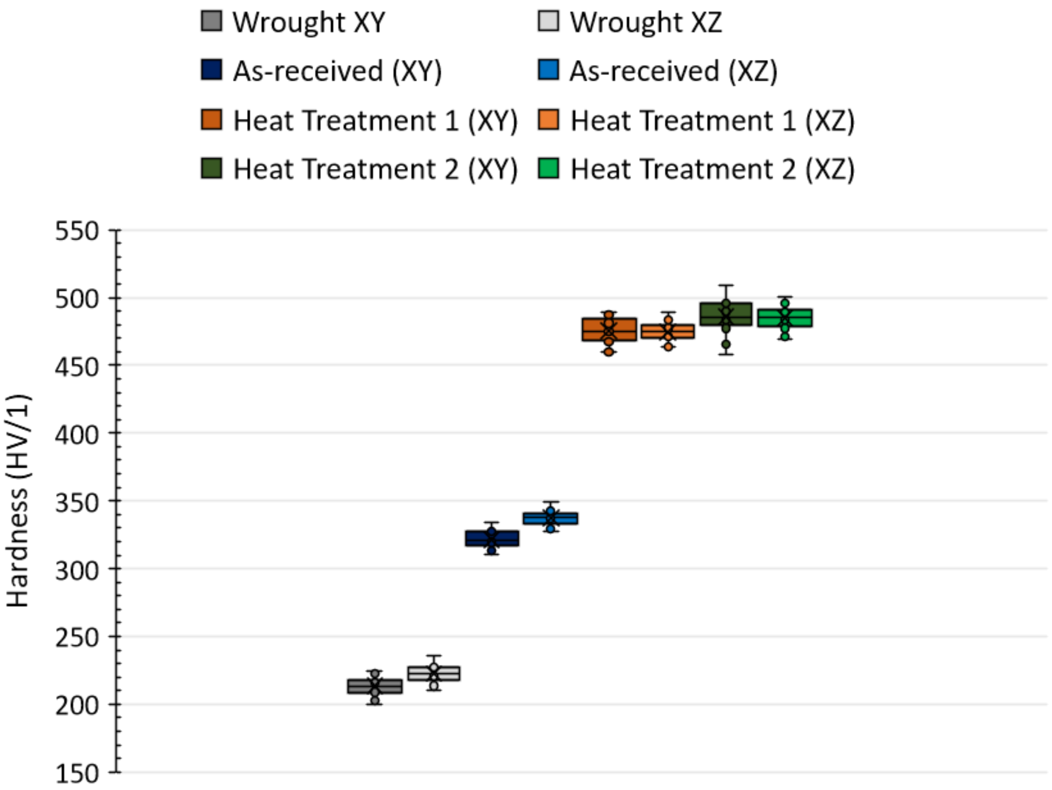

***Figure 64:** Graph to show Vickers hardness data for horizontal PBF-LB IN718 samples.*

5 Results – Tensile

5.1 Tensile

Graphical results from RT tensile testing are shown in Figure 65 and ET (650°C) tensile testing results are shown in Figure 66. Calculated tensile properties for RT and ET tests are shown in Table 18 and Table 19, respectively. Modulus is not reported in the tables as it is consistent between samples (±5%): 180GPa at RT and 150GPa at ET.

From interpreting the graphs and tables of tensile properties it is evident that the PBF-LB samples exhibit a higher UTS, 0.2% proof stress (PS), and YS but reduced strain to failure when compared to the wrought samples.

Assessment of the ET data shows an overall decrease in UTS and Young’s modulus when compared to the corresponding samples tested at room temperature. In addition, when testing at elevated temperature the 0.2% PS and YS increases for wrought and AR samples but decreases for HT1 and HT2 samples. Furthermore, as test temperature increases the strain to failure appears consistent for the wrought variant but decreases for PBF-LB variants.

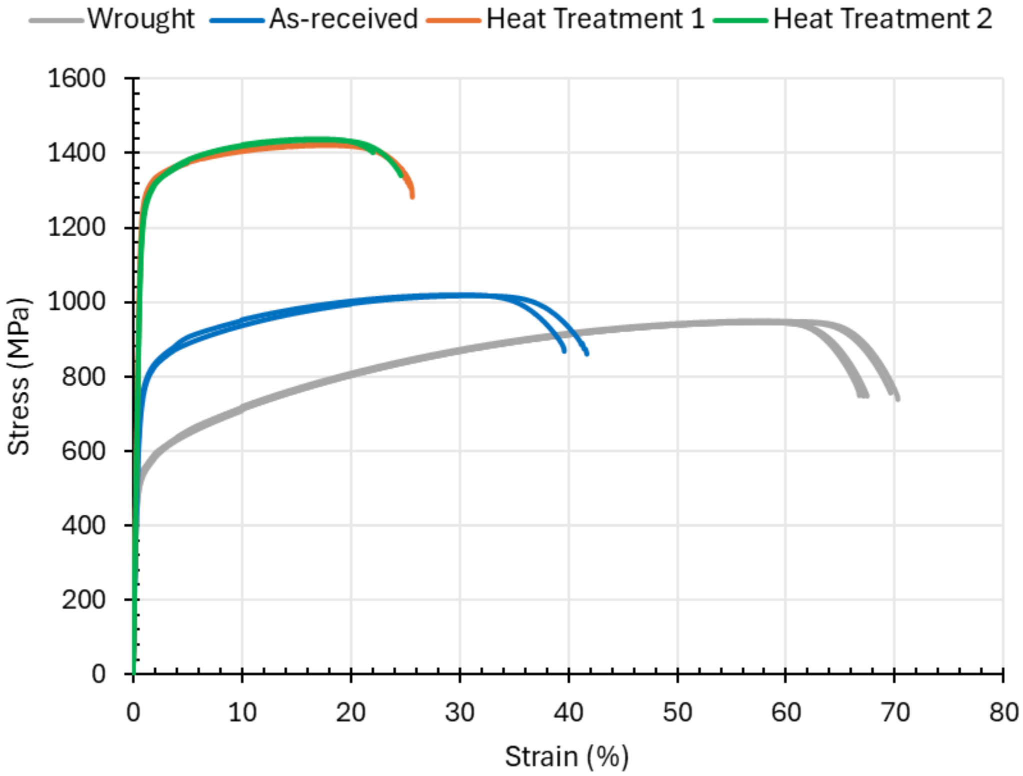

Figure 65: *Graph to show RT tensile results.*

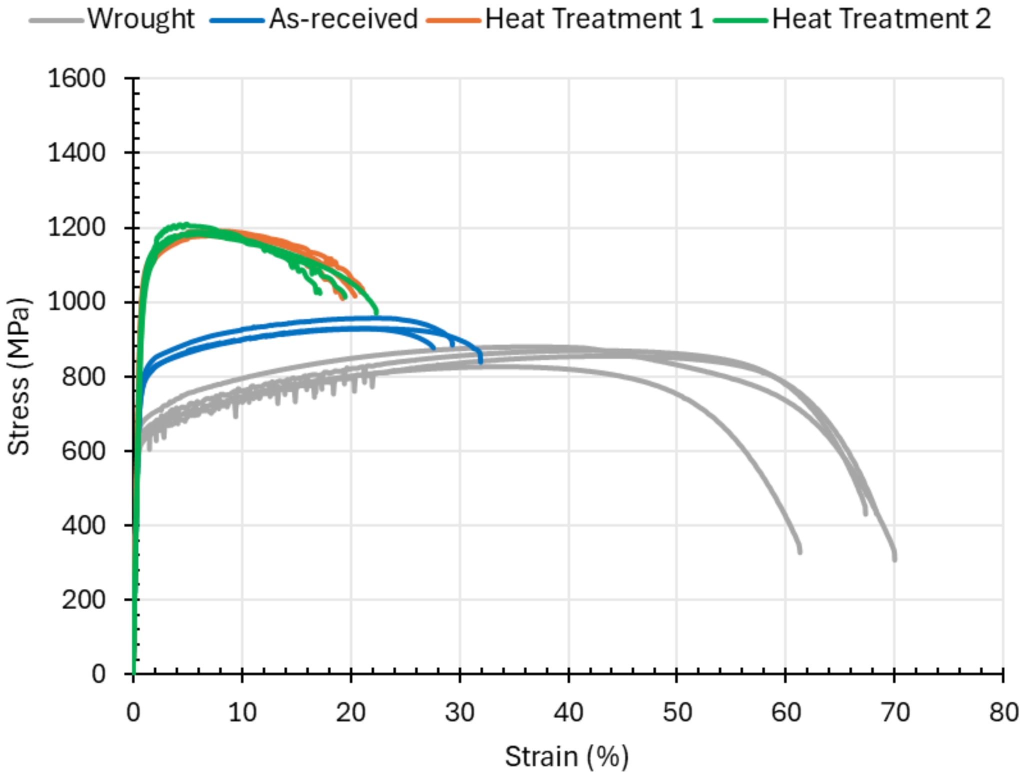

Figure 66: *Graph to show ET tensile results.*

***Table 18** - RT tensile properties.*

Sample	UTS (MPa)	0.2 PS (MPa)	YS (MPa)	Strain to Failure (%)
Wrought	947 ±1.5	504 ±18.3	514 ±10.1	68 ±1.4
As-received	1018 ±1.0	688 ±1.5	650 ±18.0	41 ±1.0
Heat Treatment 1	1422 ±1.5	1233 ±13.0	1178 ±1.5	26 ±0.1
Heat Treatment 2	1437 ±1.5	1213 ±8.5	1130 ±13.5	23 ±1.2

***Table 19** - ET tensile properties.*

Sample	UTS (MPa)	0.2 PS (MPa)	YS (MPa)	Strain to Failure (%)
Wrought	858 ±19.9	632 ±21.9	629 ±14.6	66 ±3.3
As-received	938 ±13.1	759 ±14.1	726 ±5.1	29 ±1.7
Heat Treatment 1	1186 ±5.7	1034 ±6.5	968 ±16.1	20 ±0.8
Heat Treatment 2	1193 ±11.7	1012 ±13.8	911 ±14.4	19 ±2.1

Further interpretation of the ET stress-strain curves in Figure 66 shows that all samples undergo dynamic strain aging (DSA) but the type and magnitude of DSA varies. Individual stress-strain graphs with adjusted axes are displayed in Figure 67 and show DSA regions for each variant. From this it is clear that the wrought variant undergoes the most significant DSA, mainly exhibiting types B and C, compared to the PBF-LB variants that display less prominent types D and E DSA.

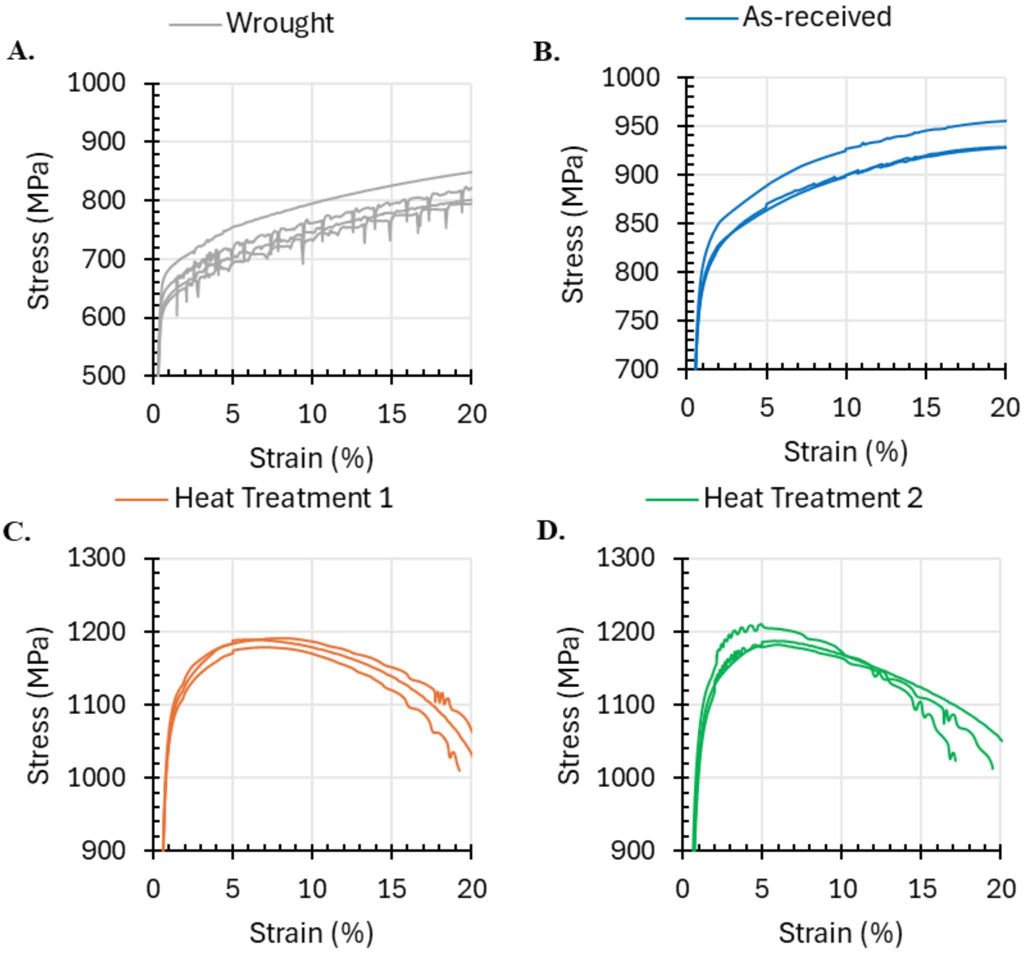

Figure 67: *Graphs to show DSA in ET tensile tests. A, B, C, and D, represent wrought, AR, HT1, and HT2, respectively.*

5.2 Tensile Fractography

Post-test fractographic analysis was conducted on the tensile samples to understand the varying modes of failure. An overall, low magnification image was captured for each sample type at each test temperature condition and are shown in Figure 68. Overall the wrought material exhibits the most ductile fracture with clear necking from a reduced cross-sectional area and micro voids on the surface. The additive material also exhibits some ductility but appears more brittle due to the flatter regions. To further support the low magnification fractographs, higher magnification images were taken on the SEM and are presented in Figure 69. The higher magnification images show micro voids in all samples but the amount varies between each sample – wrought at room and elevated temperature shows the most and HT2 at elevated temperature shows the least. Wrought also exhibits dimpling, whereas the PBF-LB samples exhibits flatter regions, further supporting the increased ductility of the wrought variant and more brittle nature of the PBF-LB variants.

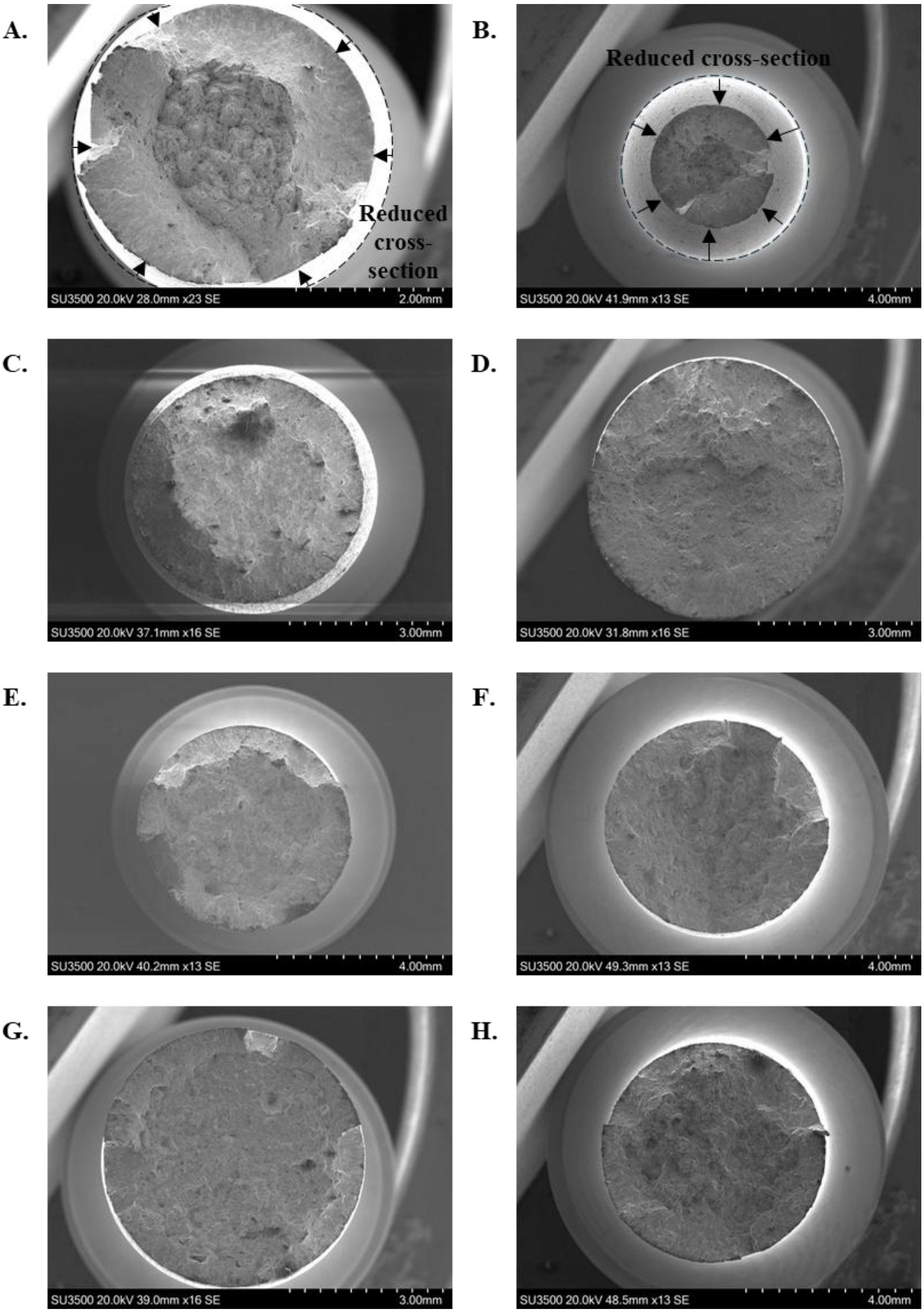

Figure 68: *Low magnification SEM images of tensile fracture surfaces. Left column are RT tests and right column are ET tests. A and B are wrought. C and D are AR. E and F are HT1. G and H are HT2.*

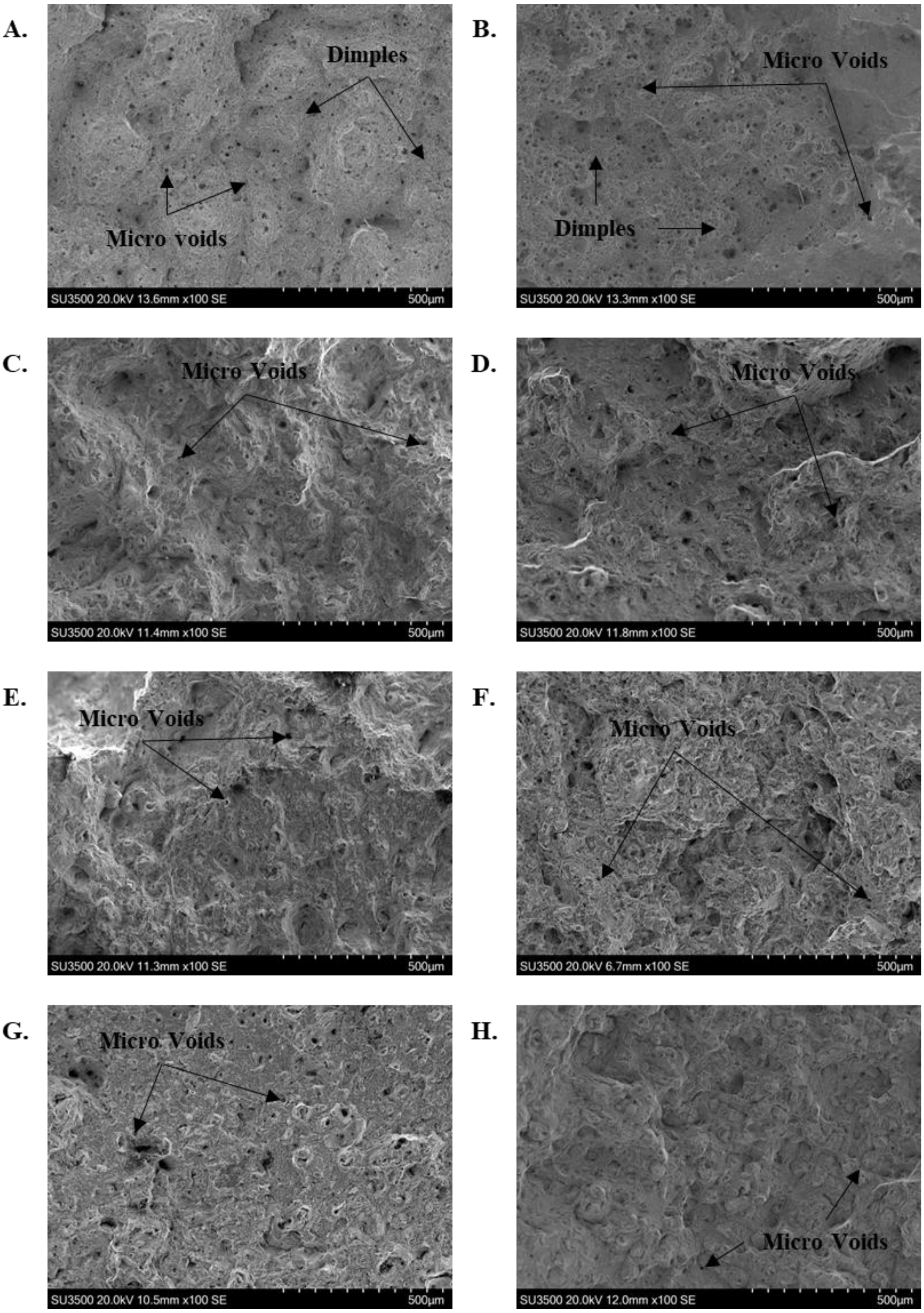

Figure 69: *Higher magnification SEM images of tensile fracture surfaces at low magnification. Left column are RT tests and right column are ET tests. A and B are wrought. C and D are AR. E and F are HT1. G and H are HT2.*

5.3 Small Punch Tensile

To validate the reliability of the SPT test, four tests at RT and four tests at ET (650°C) were conducted on wrought IN718 to assess test variation. This data is presented in Figure 70. Based on the standard deviations for the wrought variant presented in Table 20 (RT) and Table 21 (ET) it is suggested that the SPT test is reliable and repeatable for homogeneous IN718. It is also noted that the force drops seen on all of the elevated temperature wrought tests are linked to DSA. This is shown more clearly in Figure 71 where the DSA present in the ET tests on wrought material reflects regular, controlled drops in force.

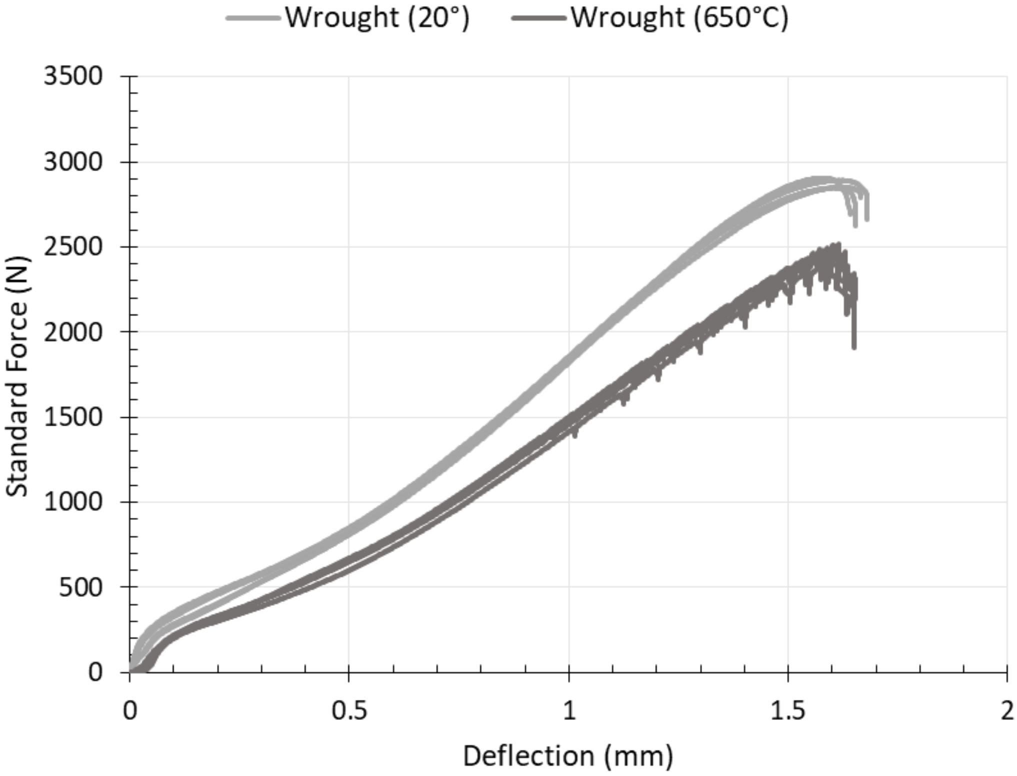

Figure 70: *Graph to show standard force against deflection for RT and ET SPT repeats on wrought IN718.*

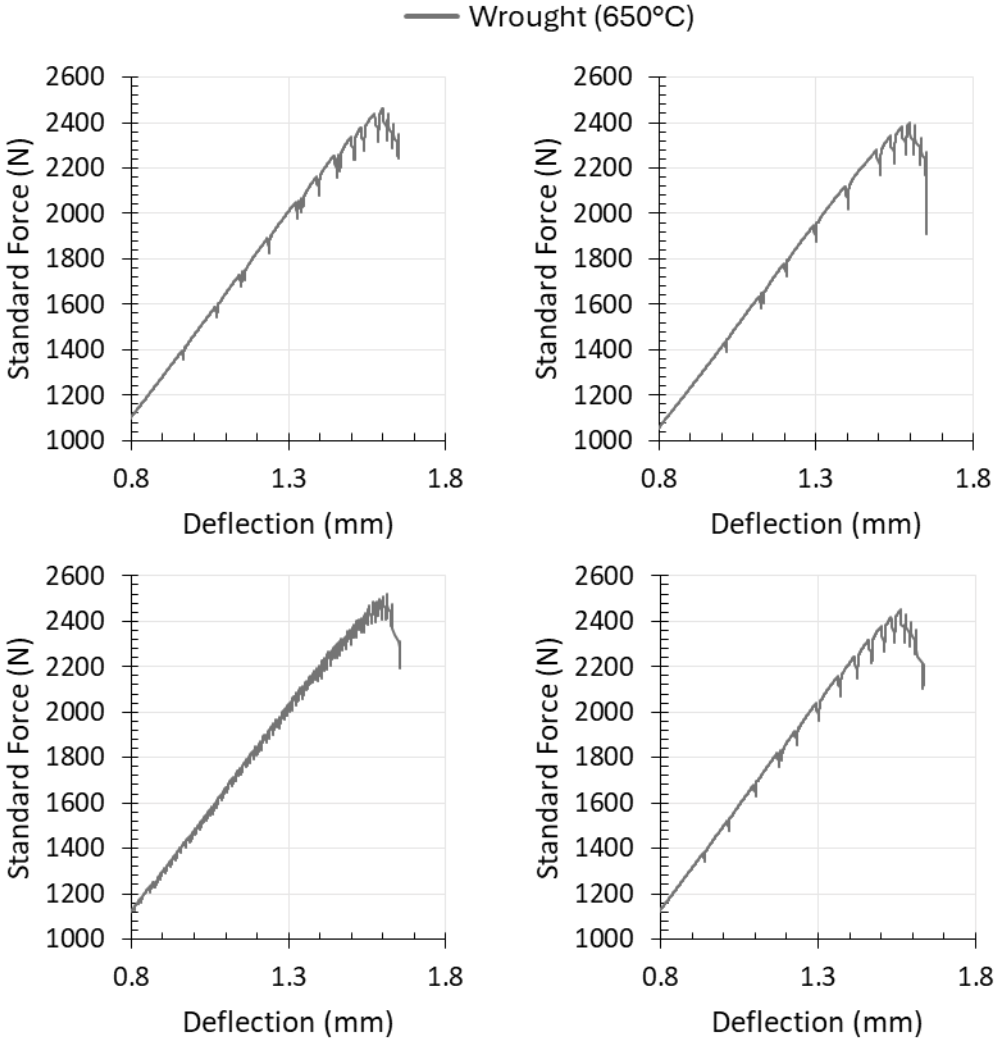

Figure 71: *Graphs to show DSA for ET SPT tests on wrought IN718.*

The maximum force against deflection at break graphs, Figure 72 and Figure 73, show plots of standard force against deflection for a representative sample of each material variant (wrought and PBF-LB) at RT and ET, respectively. These graphs show a comparison between the PBF-AM vertical and horizontal samples, the effect of the heat treatment, and the comparison of wrought to AM material, that support previous SPT figures and tables. However, assessment of Figure 73 shows DSA is present in all samples when tested at ET. This is further supported by Figure 74 where the adjusted axes clearly shows the drops in yield associated with DSA for the PBF-LB samples. The DSA present in the PBF-LB samples differs to what is seen for wrought (Figure 71) as the PBF-LB samples exhibit more irregular drops in force.

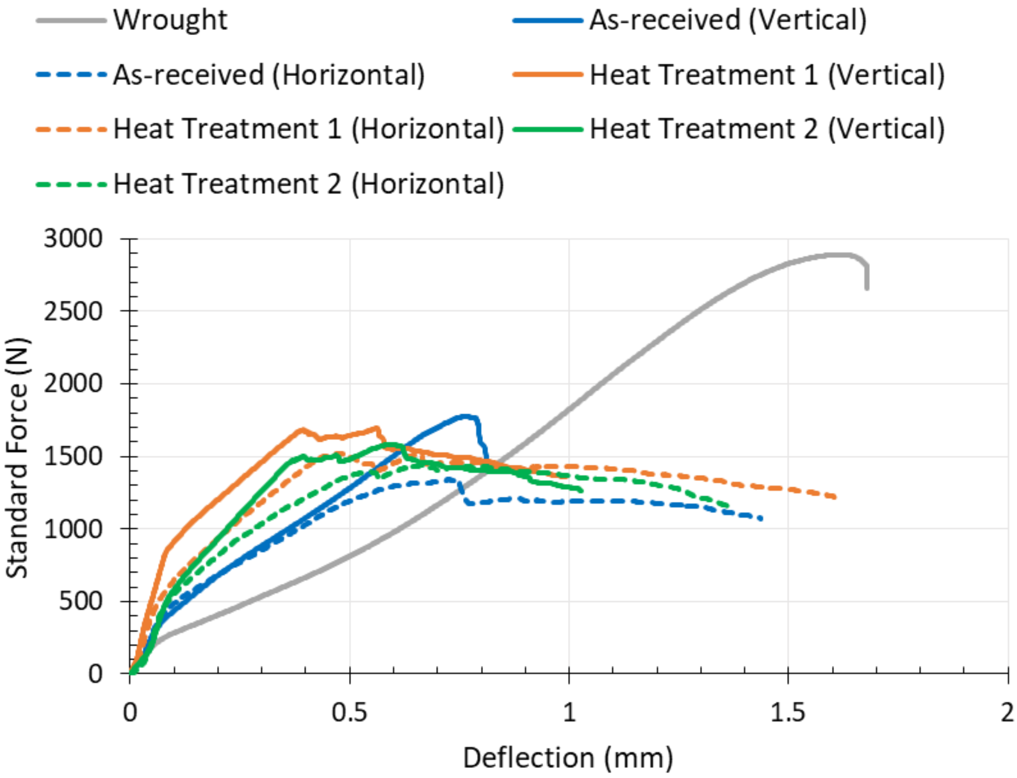

Figure 72: *Graph to show standard force against deflection for RT SPT tests.*

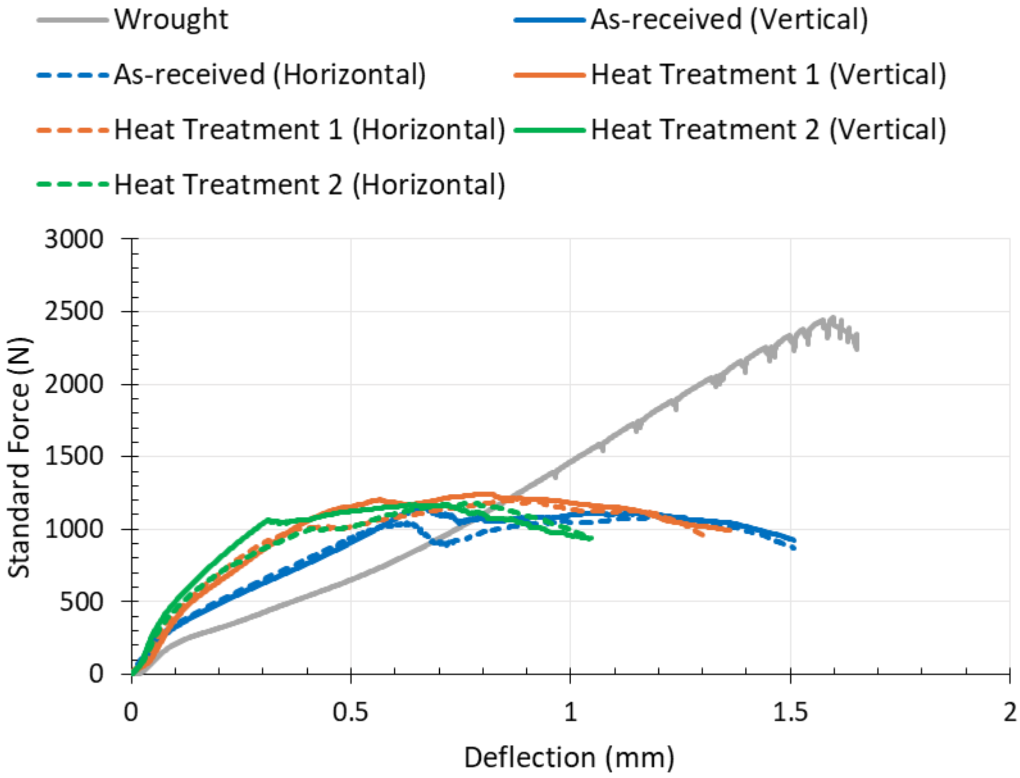

Figure 73: *Graph to show standard force against deflection for ETS PT tests.*

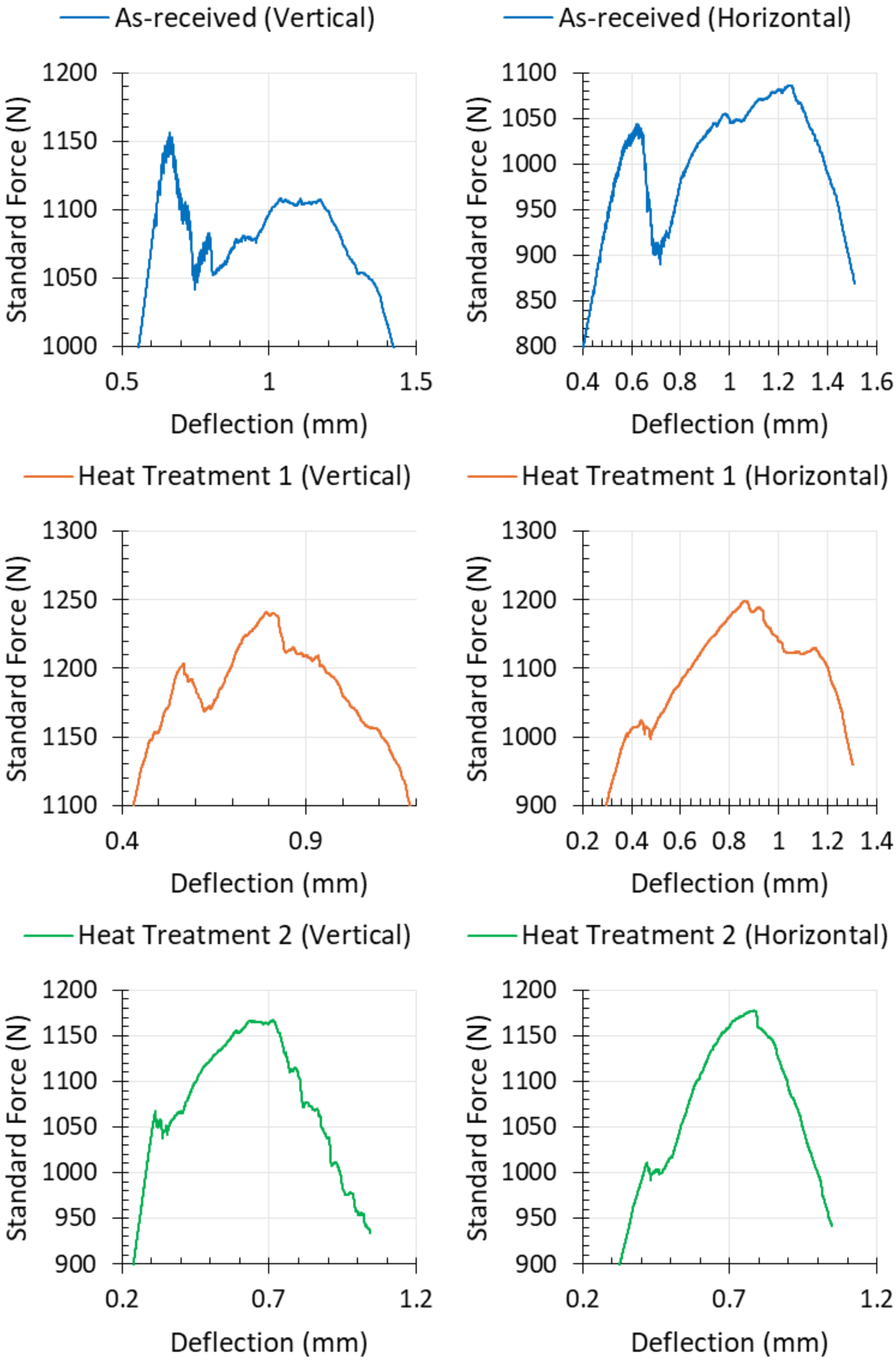

Figure 74: *Graphs to show DSA for ET SPT tests on PBF-LB IN718 variants.*

Tabulated SPT data is reported in Table 20 and Table 21 for RT and ET, respectively. The symbols/acronyms in Table 20 and Table 21 are as follows: F_{MAX} is maximum force, d_m is deflection at F_{MAX}, F_e is SPT yield, and d_b is deflection at break.

F_e was calculated via the bilinear method from the graphical plots for each test as per BS EN 10371 [133].

Table 20 *- RT SPT data.*

	F_{MAX} (N)	d_m (mm)	F_e (N)	d_b (mm)
Wrought	2873 ±25	1.60 ±0.01	272 ±14	1.66 ±0.01
AR (Vertical)	1714 ±44	0.73 ±0.06	406 ±44	0.82 ±0.05
AR (Horizontal)	1335 ±5	0.73 ±0.01	406 ±33	1.49 ±0.04
HT1 (Vertical)	1652 ±33	0.51 ±0.06	622 ±100	1.05 ±0.05
HT1 (Horizontal)	1616 ±46	0.72 ±0.09	666 ±68	1.37 ±0.07
HT2 (Vertical)	1552 ±43	0.63 ±0.04	590 ±31	1.06 ±0.05
HT2 (Horizontal)	1408 ±25	0.64 ±0.02	660 ±28	1.37 ±0.08

Table 21 *– ET SPT data.*

	F_{MAX} (N)	d_m (mm)	F_e (N)	d_b (mm)
Wrought	2458 ±43	1.59 ±0.02	235 ±5	1.64 ±0.01
AR (Vertical)	1218 ±44	0.65 ±0.02	283 ±38	1.44 ±0.04
AR (Horizontal)	1120 ±33	1.09 ±0.14	243 ±12	1.47 ±0.05
HT1 (Vertical)	1290 ±41	0.78 ±0.05	395 ±21	1.24 ±0.08
HT1 (Horizontal)	1242 ±31	0.87 ±0.07	386 ±24	1.21 ±0.06
HT2 (Vertical)	1186 ±15	0.76 ±0.09	430 ±29	1.06 ±0.05
HT2 (Horizontal)	1192 ±20	0.79 ±0.03	416 ±60	1.03 ±0.01

Additionally, SPT data for wrought and PBF-LB IN718 at RT and ET is shown graphically in Figure 75 and Figure 76, respectively. For the RT results there is a larger difference between the vertical and horizontal samples for a given variant, which is not seen as dramatically when assessing the ET results. AR at RT shows the highest variation in properties when comparing vertical and horizontal tests.

At RT and ET the wrought material has the highest maximum force and deflection at break but overall, increasing test temperature causes the maximum force to decrease for all samples. However, there is varying effect on deflection at break with increasing temperature.

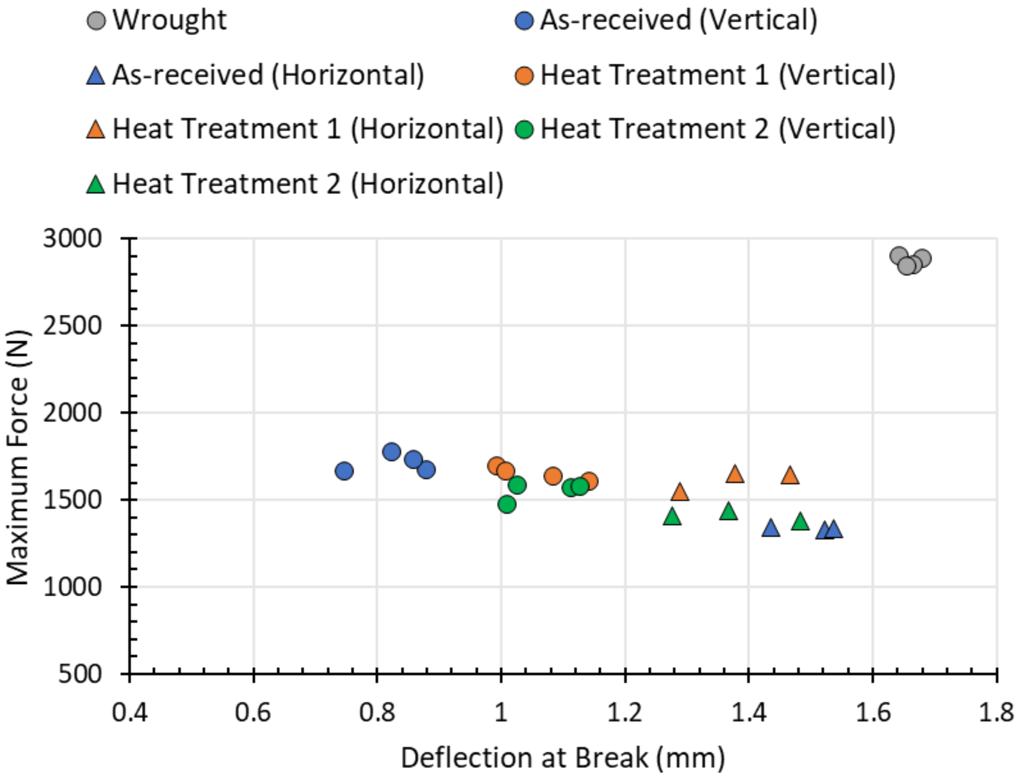

Figure 75: *Graph to show maximum force against deflection at break at RT.*

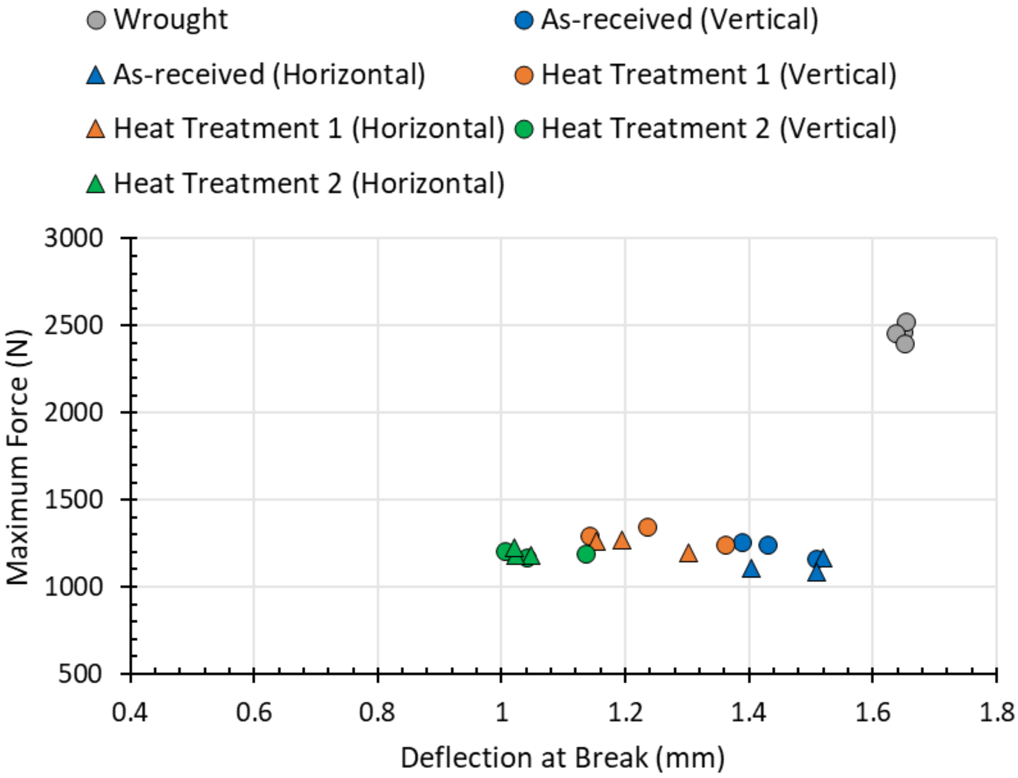

Figure 76: *Graph to show maximum force against deflection at break at ET.*

5.4 Small Punch Tensile Fractography

Following data capture, fractographic analysis was conducted on the SPT samples and is shown in Figure 77 and Figure 78 for RT and ET tests, respectively. The fractographs gathered show that the wrought specimens appear the most ductile due to the lack of secondary cracking emanating from the centre of the specimen. Alternatively, AM samples show more secondary cracking (denoted by black arrows), particularly HT2, indicating reduced ductility.

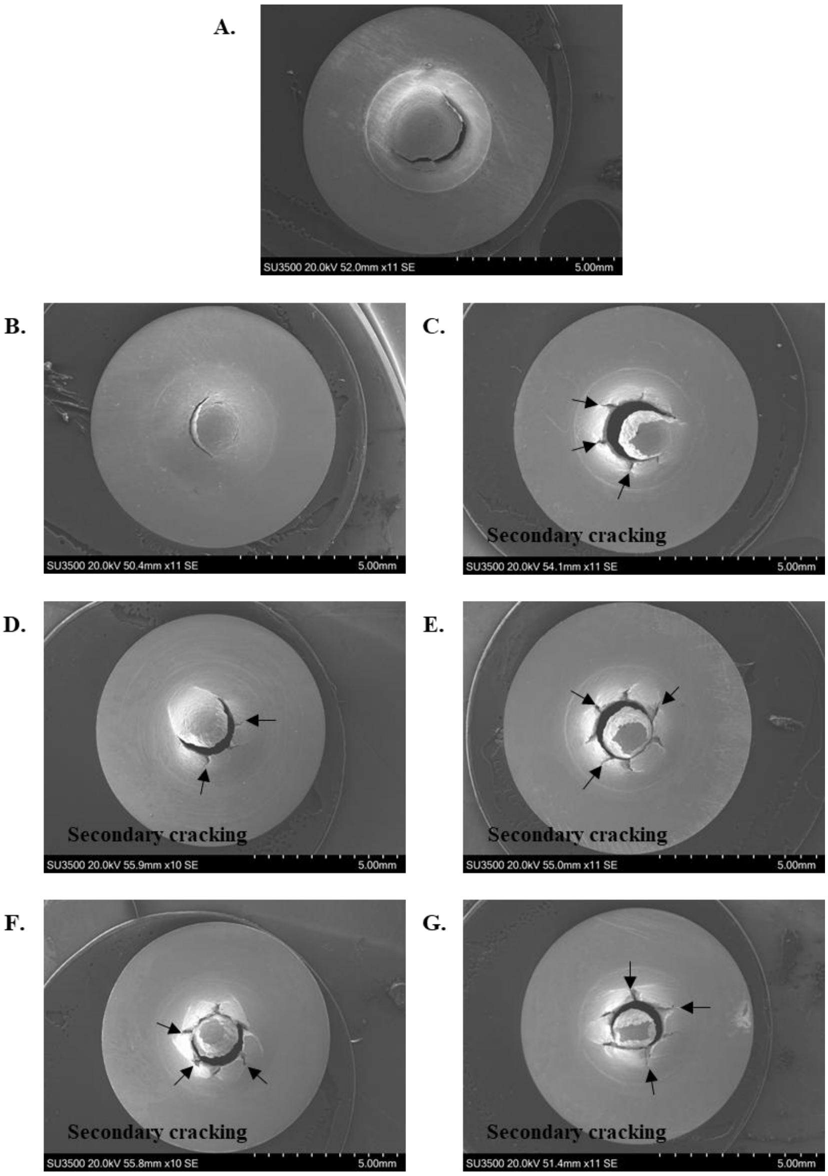

Figure 77: *Low magnification SEM images of RT SPT fracture surfaces. Black arrows denote secondary cracking. A is wrought. B and C is AR. D and E is HT1. F and G is HT2. Vertical additive samples are B, D, and F, and horizontal samples are C, E, and G.*

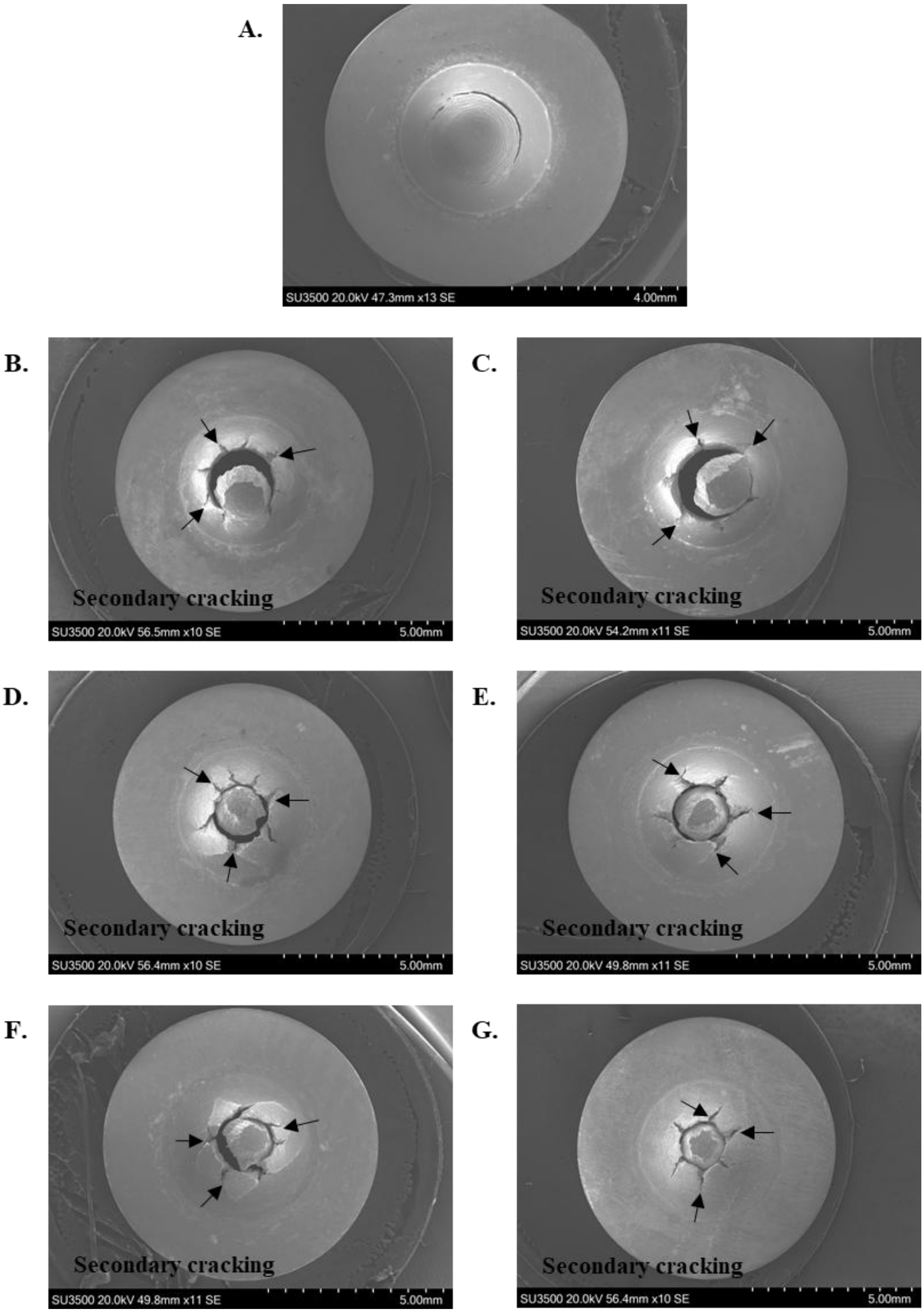

Figure 78: *Low magnification SEM images of ET SPT fracture surfaces. Black arrows denote secondary cracking. A is wrought. B and C is AR. D and E is HT1. F and G is HT2. Vertical additive samples are B, D, and F, and horizontal samples are C, E, and G.*

5.5 Correlation of Tensile and Small Punch Tensile

Evaluation of the SPT data can be completed by correlating predicted UTS and YS values from SPT tests to UTS and YS values from the equivalent uniaxial tensile tests. The equation and defined terms for UTS prediction (σ_{UTS}) are derived from [135] and shown in Equation (3) where F_{MAX} is maximum force, t is thickness, d_m is deflection at F_{MAX} and β_1 and β_2 are constants with values of 0.2282 and 137.05, respectively. The constants were previously derived from a series of experiments on alternative metallic materials with ranging ductility behaviours, which included stainless steel 316L, aluminium alloys, and IN718 [135].

The equation and defined terms for YS prediction (σ_y) are derived from [172] and are shown in Equation (4) where F_e is SPT yield, t is specimen thickness and α_1 and α_2 are constants with values of 0.416 and -5.202, respectively.

$$\sigma_{UTS} = \beta_1 \left(\frac{F_{MAX}}{t * d_m} \right) + \beta_2 \qquad (3)$$

$$\sigma_y = \alpha_1 \left(\frac{F_e}{t^2} \right) + \alpha_2 \qquad (4)$$

Utilisation of the predictive UTS and YS equations allows for calculation of percentage difference compared to uniaxial tensile results in order to establish if SPT is a feasible method for mechanical property predictions. Predicted values for vertical SPT at RT and ET against vertical uniaxial tensile are shown in Table 22 and Table 23, respectively. Graphical formats are also shown in Figure 79. From this data it can be seen that the SPT predicted YS shows the same trend as the uniaxial tensile behaviour. However, the trend does not align exactly, with a maximum percentage difference of 38.6%. Alternatively, for SPT predicted UTS, the overall trend does not follow the UTS trend seen for uniaxial tensile, especially for HT1 and HT2.

Table 22 *- Vertical SPT predicted UTS and YS at RT.*

	Wrought		**As-received**		**Heat Treatment 1**		**Heat Treatment 2**	
	Predicted (MPa)	**Difference to Uniaxial (%)**	**Predicted (MPa)**	**Difference to Uniaxial (%)**	**Predicted (MPa)**	**Difference to Uniaxial (%)**	**Predicted (MPa)**	**Difference to Uniaxial (%)**
UTS (MPa)	950	0.3	1215	19.3	1621	13.9	1257	12.4
YS (MPa)	444	13.6	674	3.7	1019	13.5	976	13.6

Table 23 *- Vertical SPT predicted UTS and YS at ET.*

	Wrought		**As-received**		**Heat Treatment 1**		**Heat Treatment 2**	
	Predicted (MPa)	**Difference to Uniaxial (%)**	**Predicted (MPa)**	**Difference to Uniaxial (%)**	**Predicted (MPa)**	**Difference to Uniaxial (%)**	**Predicted (MPa)**	**Difference to Uniaxial (%)**
UTS (MPa)	841	1.9	975	4.0	883	25.4	856	28.2
YS (MPa)	386	38.6	460	36.5	646	33.1	707	22.3

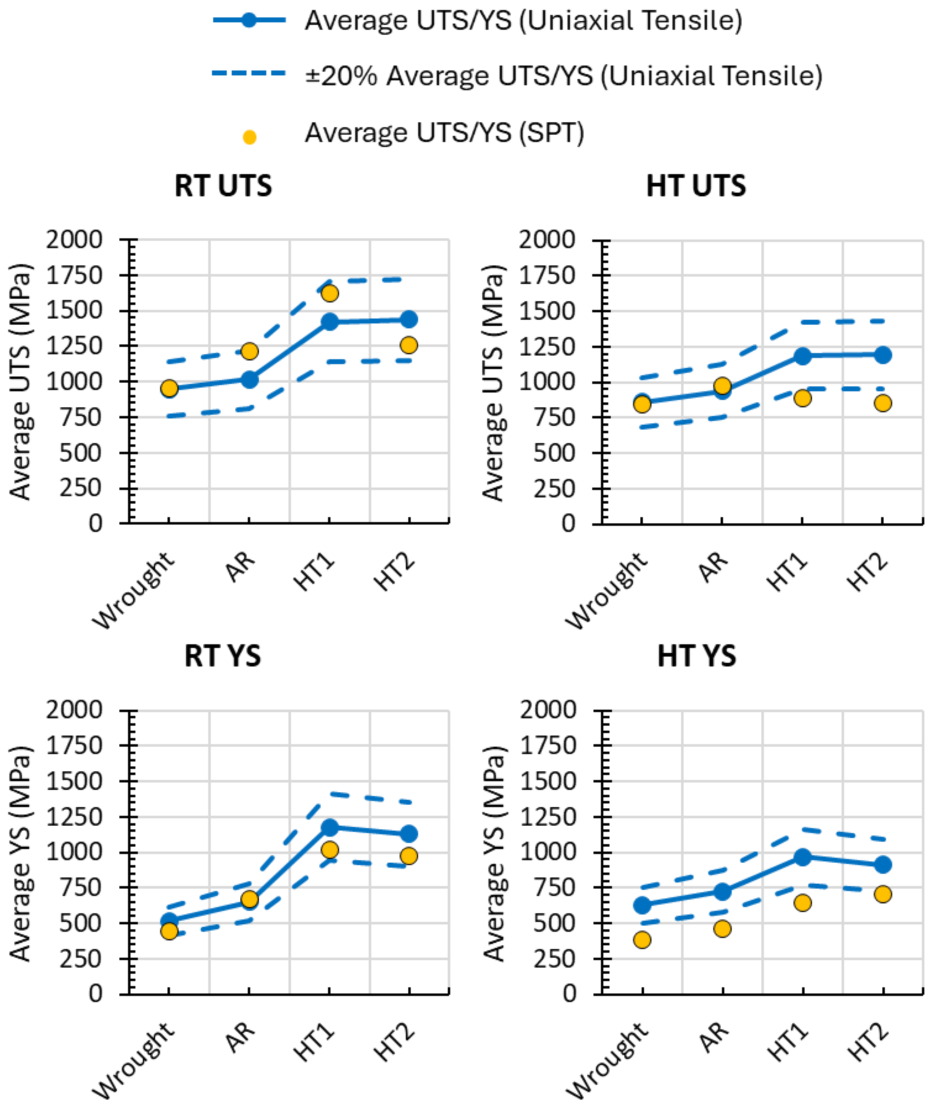

__Figure 79:__ Graphical representation of vertical SPT predicted properties.

Further correlations were completed by comparing vertical uniaxial tensile to horizontal SPT predicted UTS and YS values. This was applied to assess the reliance of directional growth on resulting SPT properties, as demonstrated previously in Figure 40. Results from the vertical uniaxial and horizontal SPT are shown in Table 24 for RT and Table 25 for ET. The respective graphical formats for Table 24 and Table 25 are shown in Figure 80.

Similarly to the SPT vertical results compared to the uniaxial vertical data, the SPT horizontal compared to uniaxial vertical shows good general trend profiles for SPT predicted YS, particularly for RT. Also, the UTS can be successfully predicted for some samples (wrought at RT and ET and AR at RT), but does not produce as effective trends that reflect the behaviours seen in the uniaxial tensile test results. The comparison of horizontal SPT predictions to uniaxial tensile appears to be slightly more accurate than comparing SPT vertical to uniaxial vertical results.

Table 24 *- Horizontal SPT predicted UTS and YS at RT*

	Wrought		**As-received**		**Heat Treatment 1**		**Heat Treatment 2**	
	Predicted (MPa)	**Difference to Uniaxial (%)**	**Predicted (MPa)**	**Difference to Uniaxial (%)**	**Predicted (MPa)**	**Difference to Uniaxial (%)**	**Predicted (MPa)**	**Difference to Uniaxial (%)**
UTS (MPa)	950	0.3	958	5.8	1169	17.7	1129	21
YS (MPa)	444	13.6	666	2.5	1092	7.3	1082	4.2

Table 25 *- Horizontal SPT predicted UTS and YS at ET*

	Wrought		**As-received**		**Heat Treatment 1**		**Heat Treatment 2**	
	Predicted (MPa)	**Difference to Uniaxial (%)**	**Predicted (MPa)**	**Difference to Uniaxial (%)**	**Predicted (MPa)**	**Difference to Uniaxial (%)**	**Predicted (MPa)**	**Difference to Uniaxial (%)**
UTS (MPa)	841	1.9	614	34.4	792	33.1	815	31.6
YS (MPa)	386	38.6	395	45.5	643	33.5	679	25.3

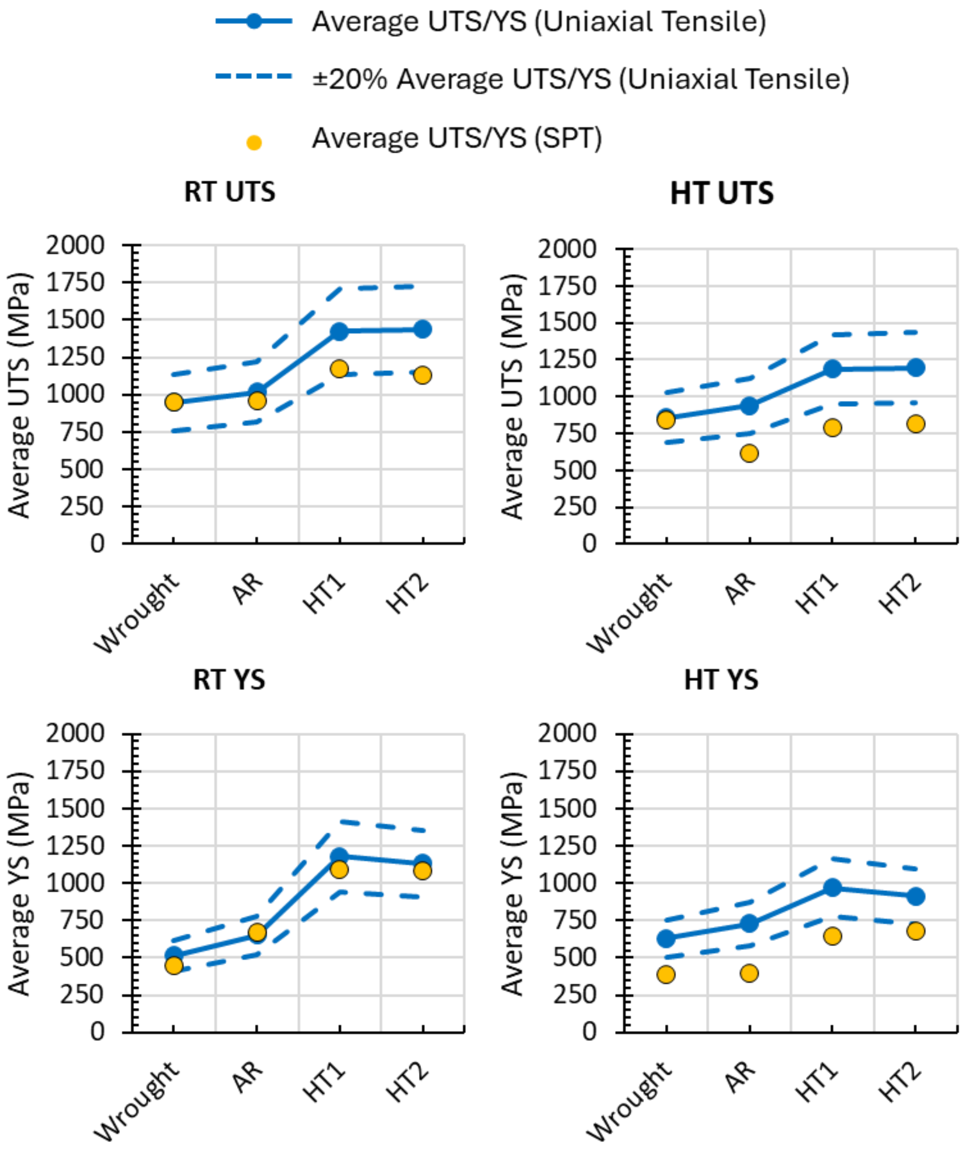

Figure 80: *Graphical representation of horizontal SPT predicted properties.*

6 Results – Constant Load Creep

6.1 Constant Load Creep

Results from constant load creep testing of three wrought IN718 samples under a fixed stress of 650MPa across three different temperatures (625°C, 650°C and 675°C) are illustrated in Figure 81. The graph shows that 650°C is the upper working temperature for IN718, given the significantly reduced creep life seen at a temperature of 675°C. In addition, Figure 82 shows the rupture life of the wrought and PBF-LB samples at varying stresses at 650°C. Trends from Figure 82 suggest that wrought and HT1 are the superior material types when considering creep resistance. Whereas, AR and HT2 appear similar in performance and inferior to wrought and HT1.

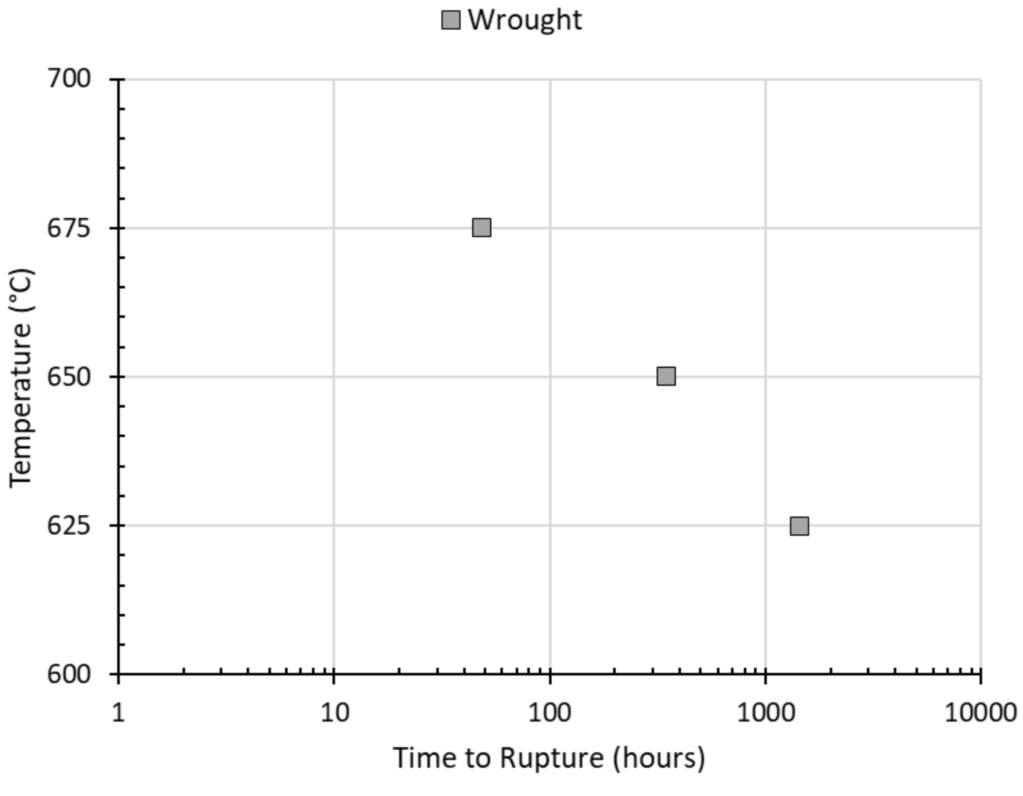

Figure 81: *Graph to show creep rupture time for wrought IN718 at 650MPa with varying temperature .*

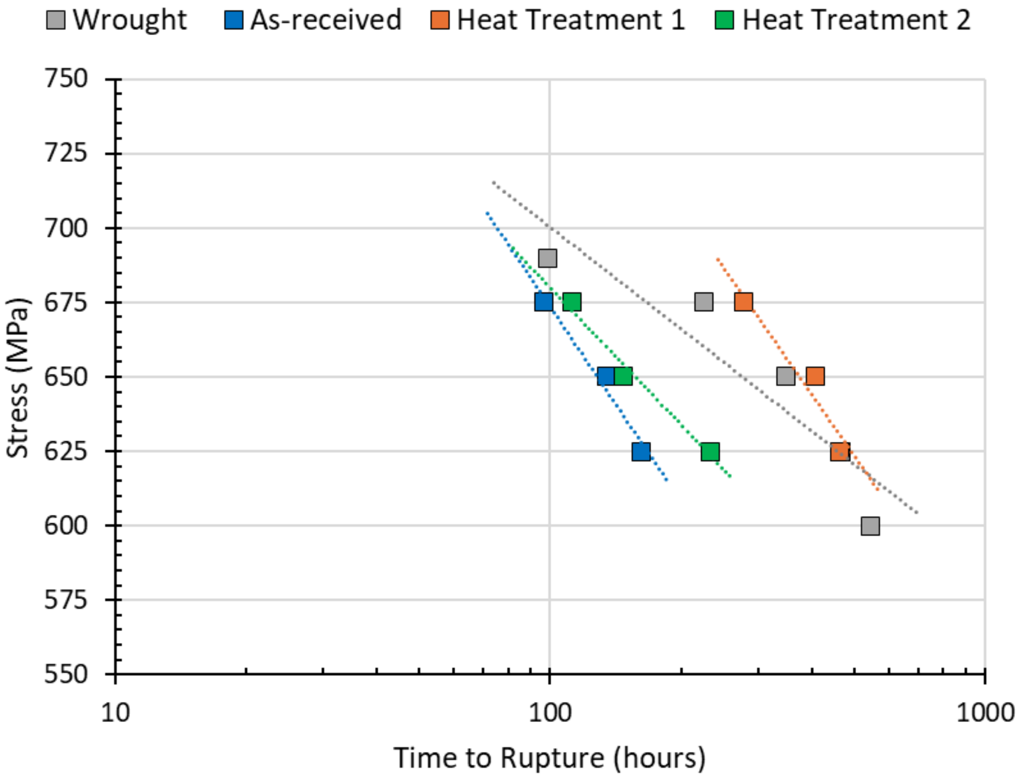

Figure 82: *Graph to show wrought and PBF-LB IN718 creep rupture time at 650°C.*

Alongside the two time to rupture graphs, plots to illustrate the creep rate and creep stages during testing are shown in Figure 83 and Figure 84. Figure 83 represents the wrought material at 650MPa at varying temperatures and Figure 84 represents the wrought and PBF-LB samples at 650°C under an applied stress of 650MPa. Assessment of Figure 83 indicates that as temperature increases, and stress remains the same, the minimum creep rate increases and time to rupture decreases. Furthermore, Figure 84 shows that wrought and HT1 specimens demonstrate a reduced minimum creep rate during the secondary stage of creep, resulting in a longer rupture life compared to AR and HT2. Also, from Figure 84, the wrought material exhibits a higher volume of plastic strain to rupture compared to PBF-LB material; this agrees with the ductile properties seen in other testing and fractographic analyses.

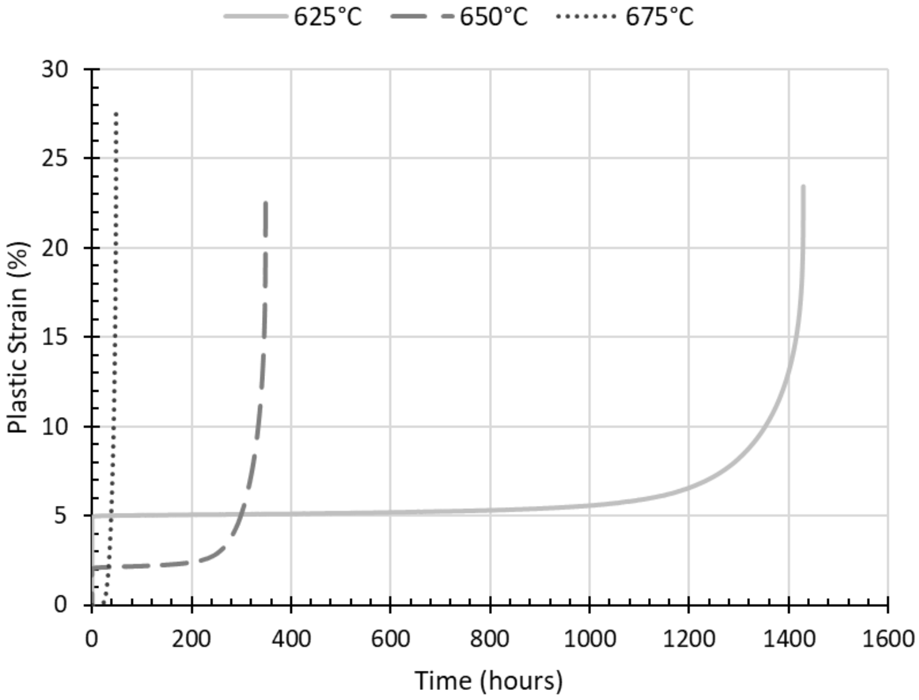

Figure 83: *Graph to show plastic strain against time for wrought IN718 at 650MPa with varying temperature.*

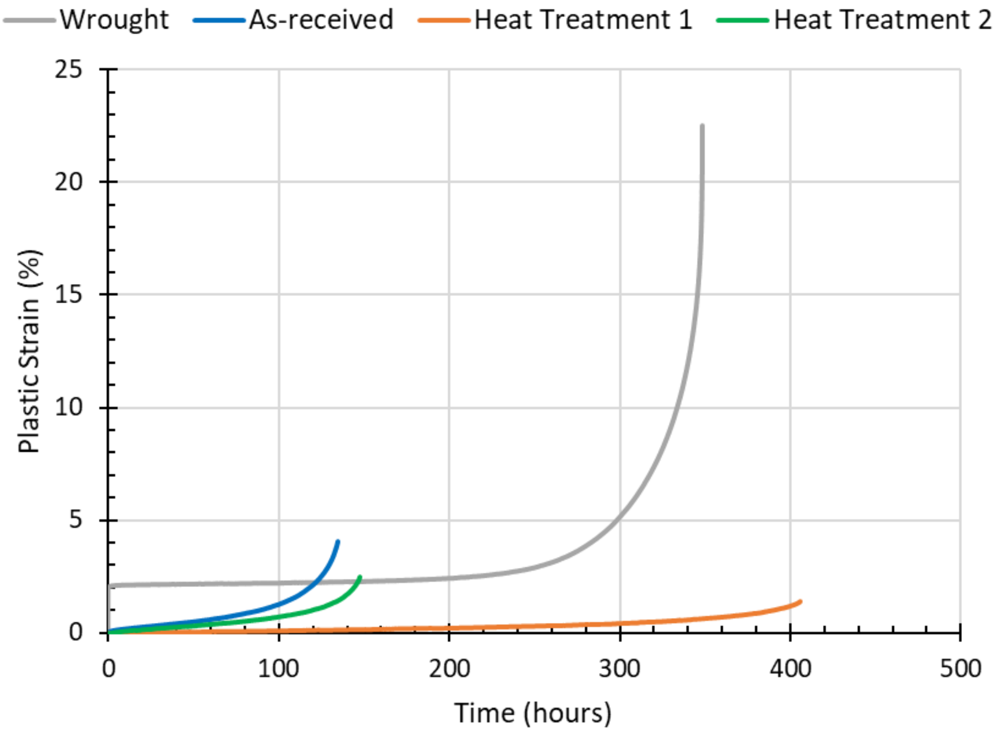

Figure 84: *Graph to show plastic strain against time for wrought and PBF-LB IN718 samples at 650°C and 650MPa.*

Further assessment of the creep data allowed for interpretation of minimum creep rates for tests conducted at 650°C. This data is presented in Figure 85 and Table 26 and shows that AR and HT2 have similar but worse creep resistance compared to wrought and HT1, which exhibit similar and superior resistance to creep.

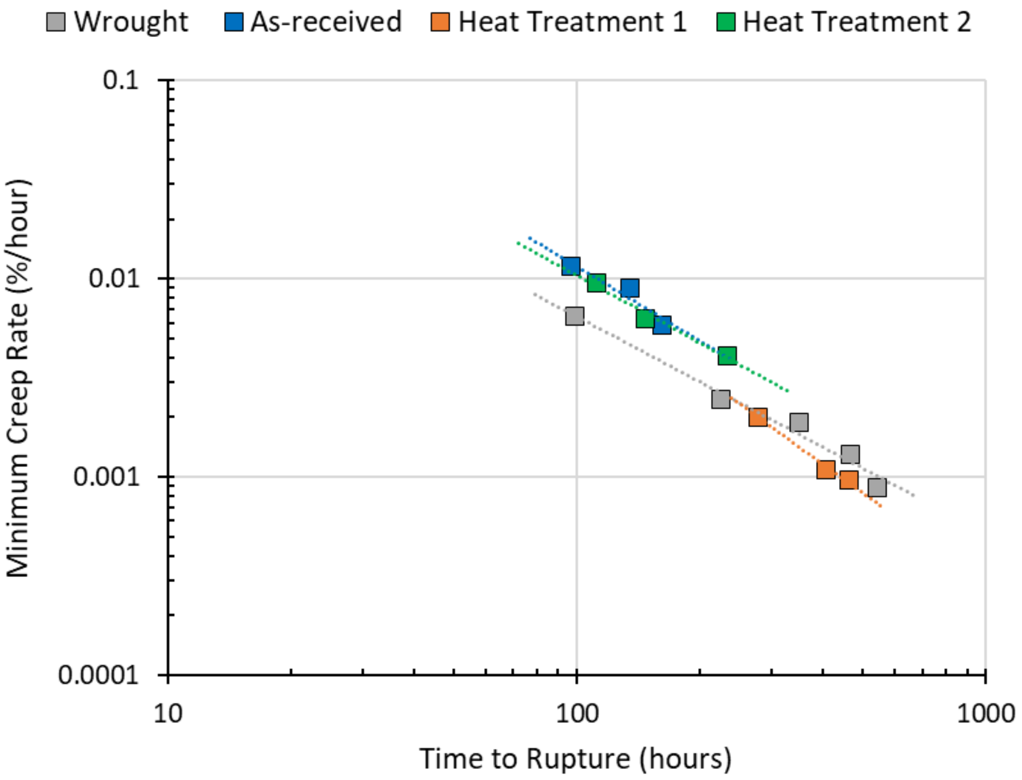

Figure 85: *Graph to show minimum creep rate against time for wrought and additive samples at 650°C with varying stress.*

Table 26 - *Minimum creep rate and time to rupture for 650MPa creep tests.*

	Minimum Creep Rate (%/hour)	**Time to Rupture (hours)**
Wrought	0.00189	348.7
As-received	0.00900	134.8
Heat Treatment 1	0.00109	405.7
Heat Treatment 2	0.00630	147.2

6.2 Constant Load Creep Fractography

Fractographic analysis was conducted on the creep samples post-test to analyse the modes of failure between samples and varying test conditions. Figure 86 shows the fracture surfaces of the wrought and PBF-LB samples tested at 650°C with a constant load of 650MPa. Interpretation of the fractographs indicates that the wrought material is the most ductile compared to the additive samples, with evidence of micro-voids and dimpling. It is also clear that the wrought sample experienced the most necking, with the largest reduction in cross-sectional area. On the other hand, the PBF-LB material shows features attributed to more brittle type failure modes, with less micro-voids and dimpling and more intergranular cracks and secondary cracking following a chessboard pattern.

Alternatively, Figure 87 shows the HT2 samples at 650°C with varying constant loads of 625MPa, 650MPa and 675MPa. The fractographic analysis of these samples still exhibits a chessboard pattern of a brittle nature.

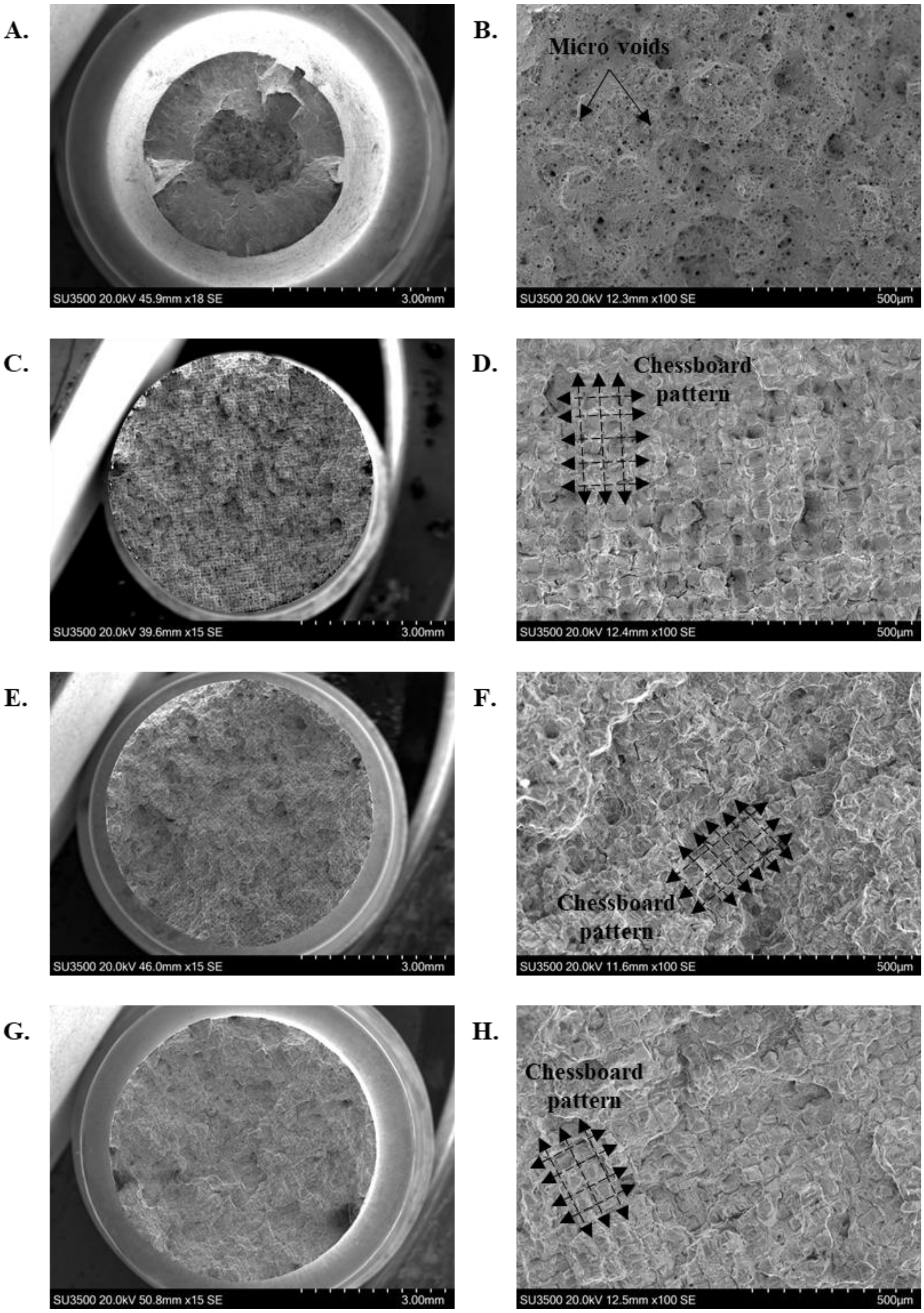

Figure 86: *Fractographic images of creep samples tested at 650°C, 650MPa at low magnification (left column) and higher magnification (right column). A and B are wrought. C and D are AR. E and F are HT1. G and H are HT2.*

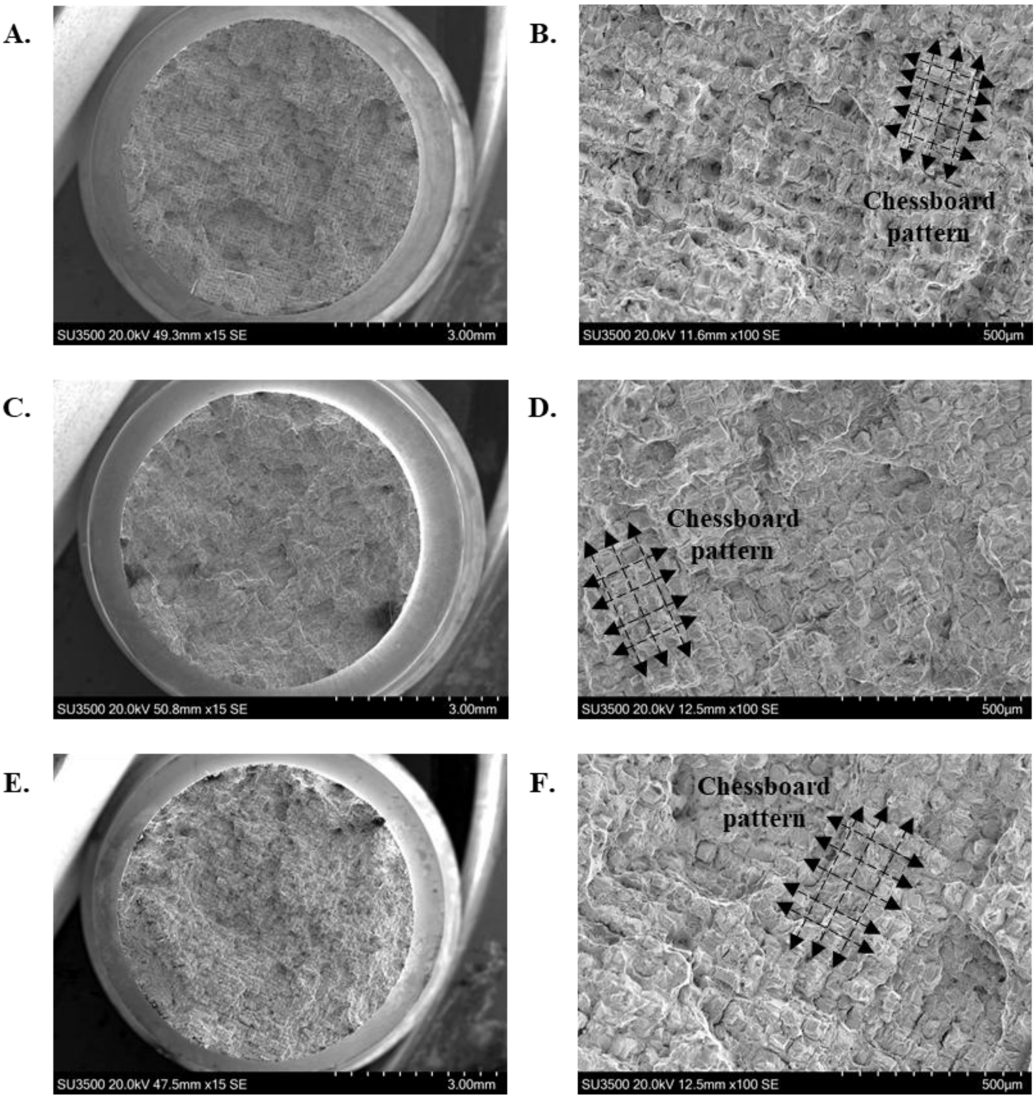

Figure 87: *Fractographic images of HT2 creep samples tested at 650°C, at low magnification (left column) and higher magnification (right column). A and B are at 625MPa. C and D are at 650MPa. E and F are at 675MPa.*

Following fractographic analysis, samples were section in the XZ plane near the fracture surface and etched with Kalling's No.2 Reagent in order to assess the deformation behaviour in the various microstructures post-creep. Representative FEG-SEM micrographs are depicted in Figure 88 for the same samples previously displayed in Figure 86 (wrought and PBF-LB samples tested at 650MPa at 650°C). Overall, all variants displayed notable evidence of creep damage, with cavitation observed along grain boundaries. However, the degree to which the cavities have coalesced vary between sample types. It appears that the AR and HT2 variants display mainly coalesced cavities whereas the wrought and HT1 variants show mainly uncoalesced cavities.

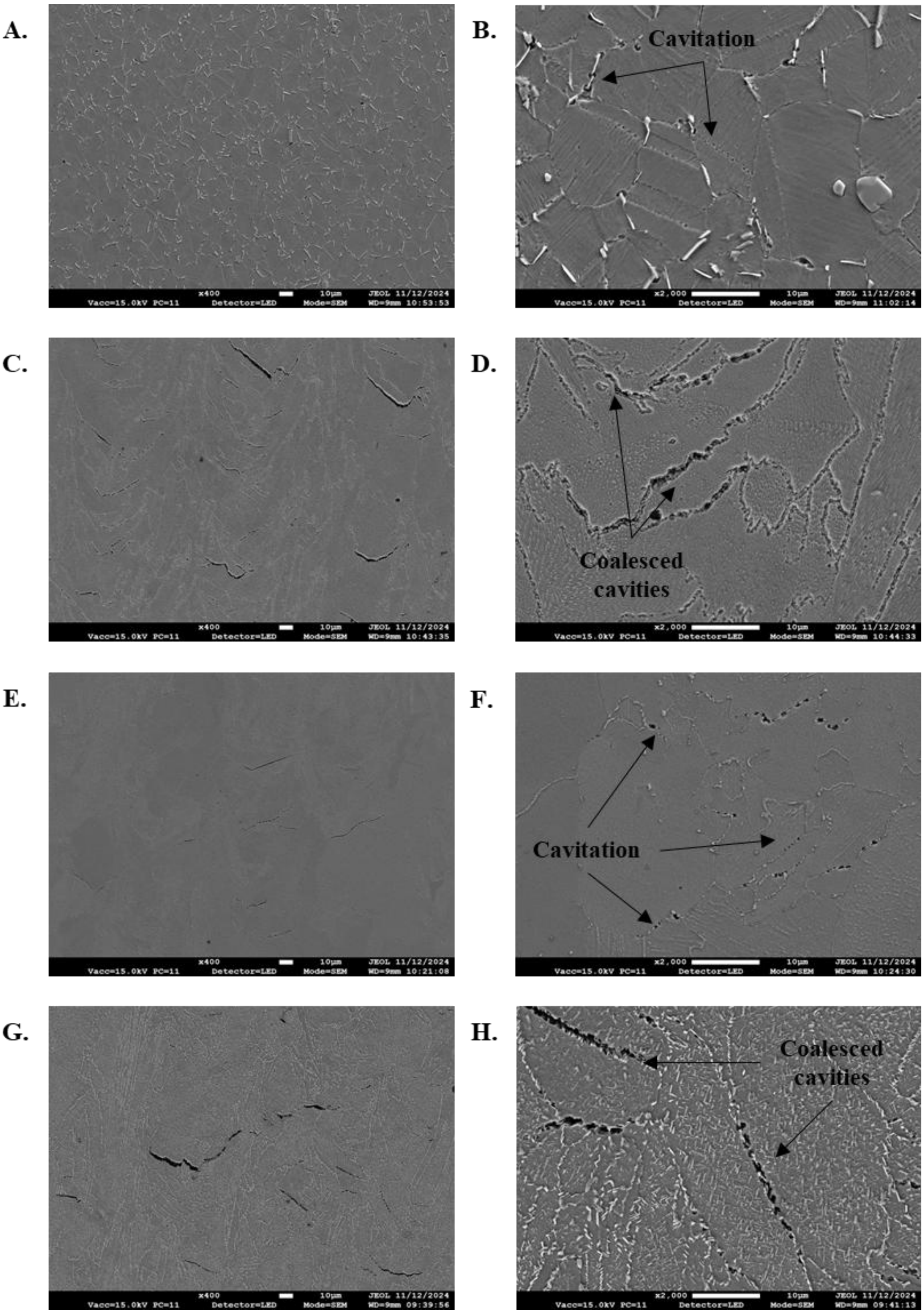

Figure 88: *Kalling's No.2 etched FEG-SEM micrographs of creep samples in XZ plane at lower magnification (left column) and higher magnification (right column). A and B are wrought. C and D are AR. E and F are HT1. G and H are HT2.*

Cavitation analysis of the XZ plane of the respective samples from Figure 87 (HT2 creep samples tested at 625MPa, 650MPa, and 675MPa, at 650°C) are shown in Figure 89. From this it can be seen that the samples display cavitation and coalescence, indicating creep damage. The variation in the magnitude of cavitation and coalescence is not significantly different, which supports the short variation in test time across the samples (162 hours for 675MPa, 135 hours for 650MPa, and 96 hours for 625MPa).

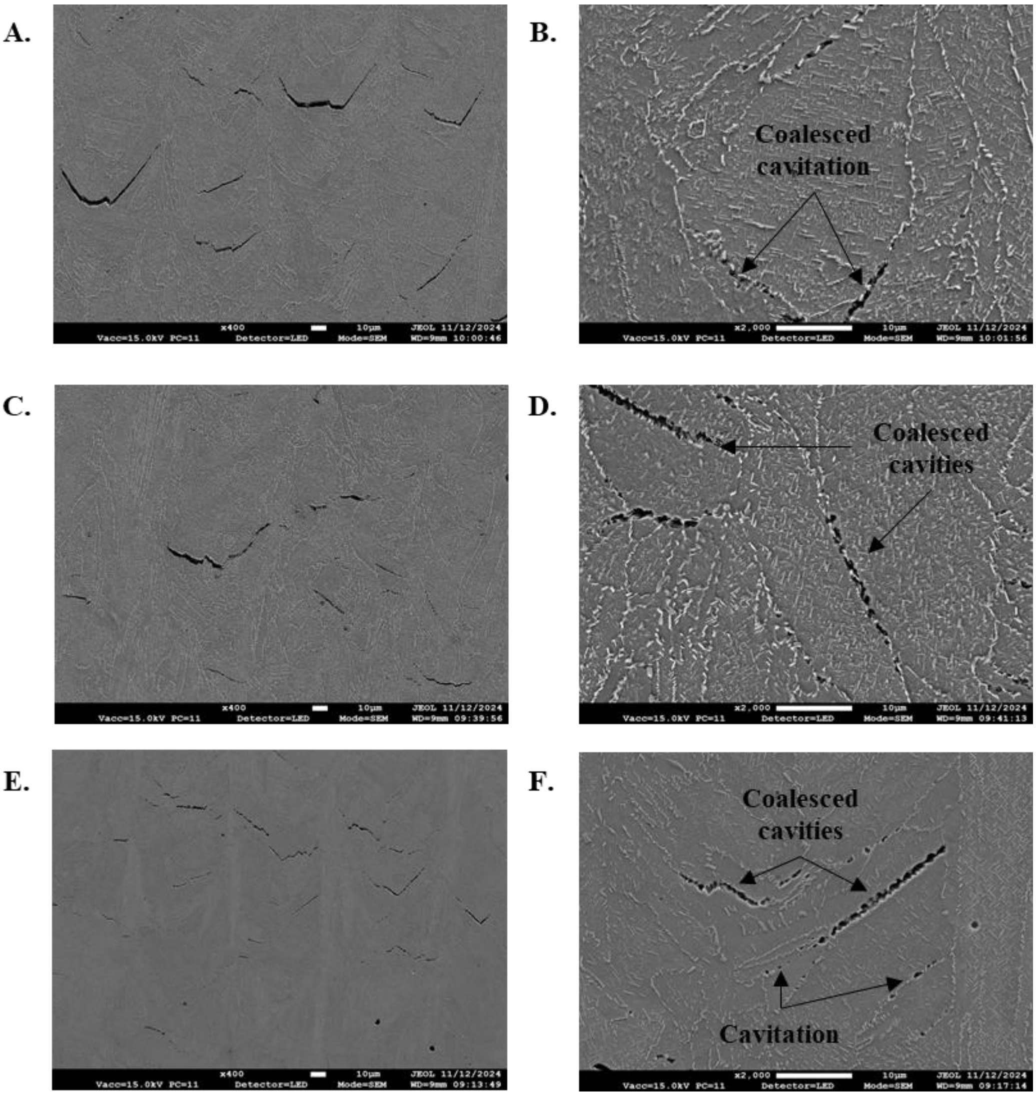

Figure 89: *Kalling's No.2 etched FEG-SEM micrographs of 650°C tested HT2 creep samples in XZ plane at lower magnification (left column) and higher magnification (right column). A and B are at 625MPa. C and D are at 650MPa. E and F are at 675MPa.*

6.3 Constant Load Creep Post-test Microstructural Changes

During cavitation analysis of the tested creep samples, changes in the phases and grain size (compared to untested samples) was observed. Consequently, EBSD and FEG-SEM analysis was employed to investigate further.

Initial EBSD analysis on the wrought samples tested at 650°C with varying stresses (600-690MPa), is reported in Figure 90 with respective grain data presented in Table 27. Rx percentage was calculated by assessing the percentage of grains with GOS less than or equal to 2° [189–191]. Additionally, high angle grain boundaries (HAGBs) were defined as greater than 15°, whereas low angle grain boundaries (LAGBs) were defined as larger than 2° but less than or equal to 15° [192].

The EBSD maps and data analysis shows that post-creep testing there is a reduction in grain area as Rx decreases, which typically aligns with increasing load (625MPa does not follow this trend). There is also a decrease in twin density with an increase in test load (apart from 600MPa, which does not follow this trend).

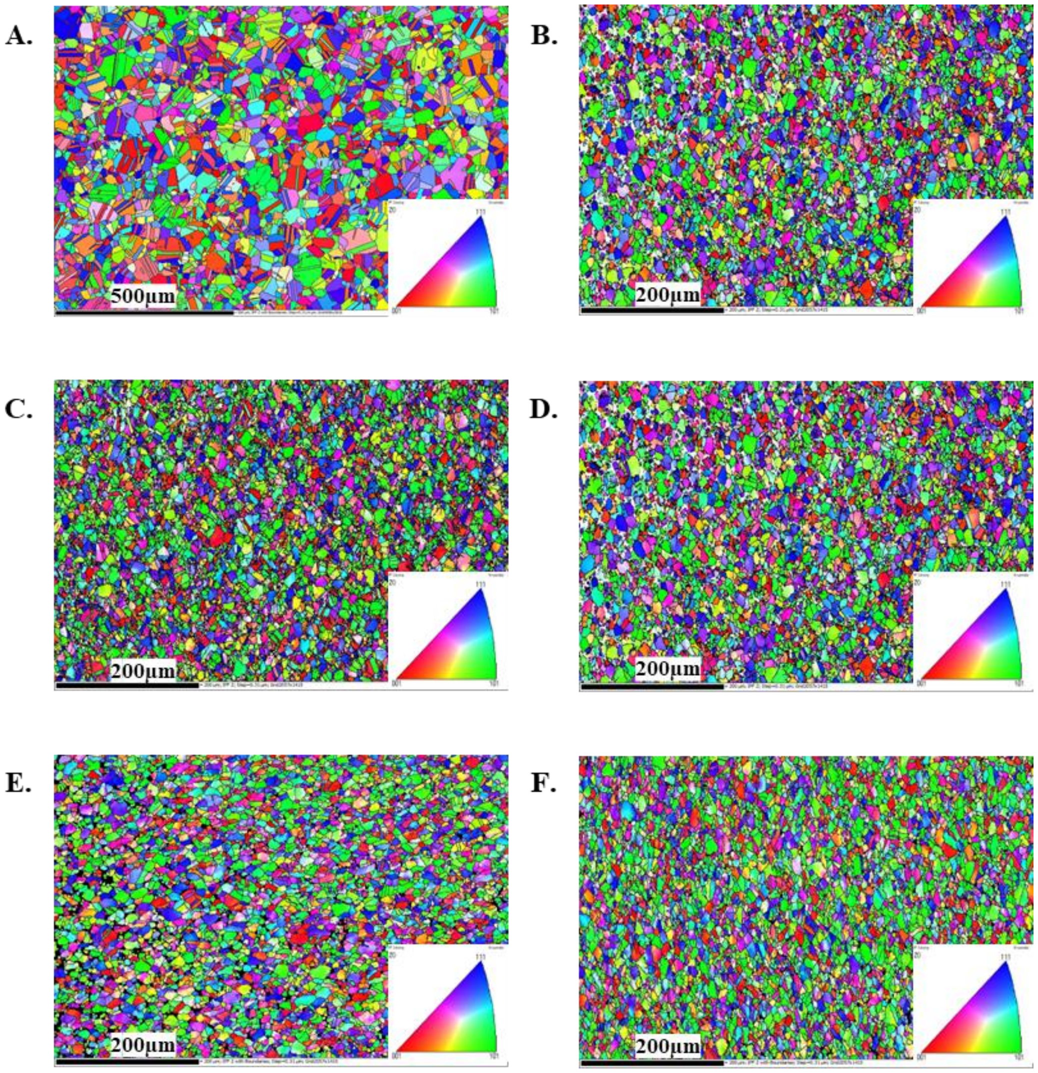

Figure 90: *EBSD map of wrought IN718 A) untested at 100x magnification and B-C) tested at 600MPa, 625MPa, 650MPa, 675MPa, and 690MPa, at 200x magnification, respectively.*

Table 27 *- Data from EBSD IPF maps for wrought IN718 before and after constant load creep testing at 650°C for 600-690MPa.*

Sample (Constant Load)	**With Twins**			**Twin Density (%)**	**Rx (%)**	**HAGBs (%)**	**LAGBs (%)**
	Grain Area (µm²⁾	**Grain Diameter (µm)**	**Aspect Ratio**				
Untested	193	12.5	0.49	51.4	97.9	93.0	7.0
600MPa	44	6.3	0.56	4.32	33.6	21.9	78.1
625MPa	32	5.3	0.54	5.66	19.1	26.0	74.0
650MPa	43	6.2	0.56	4.88	25.6	23.0	77.0
675MPa	37	5.9	0.64	3.56	20.7	22.6	77.4
690MPa	31	5.3	0.56	2.44	17.6	17.4	82.6

Analysis conducted on the PBF-LB variants at 650MPa is shown in Figure 91 with respective grain data reported in Table 28. Rx, HAGBs, and LAGBs, were calculated using the same method as previously described. Comparing the untested wrought and PBF-LB variants it can be seen that the wrought material has the highest Rx and AR has the lowest. For AR and HT1 post-creep analysis shows an increase in LAGBs and decrease in Rx. Alternatively, HT2 post-creep analysis shows a decrease in LAGBs and Rx.

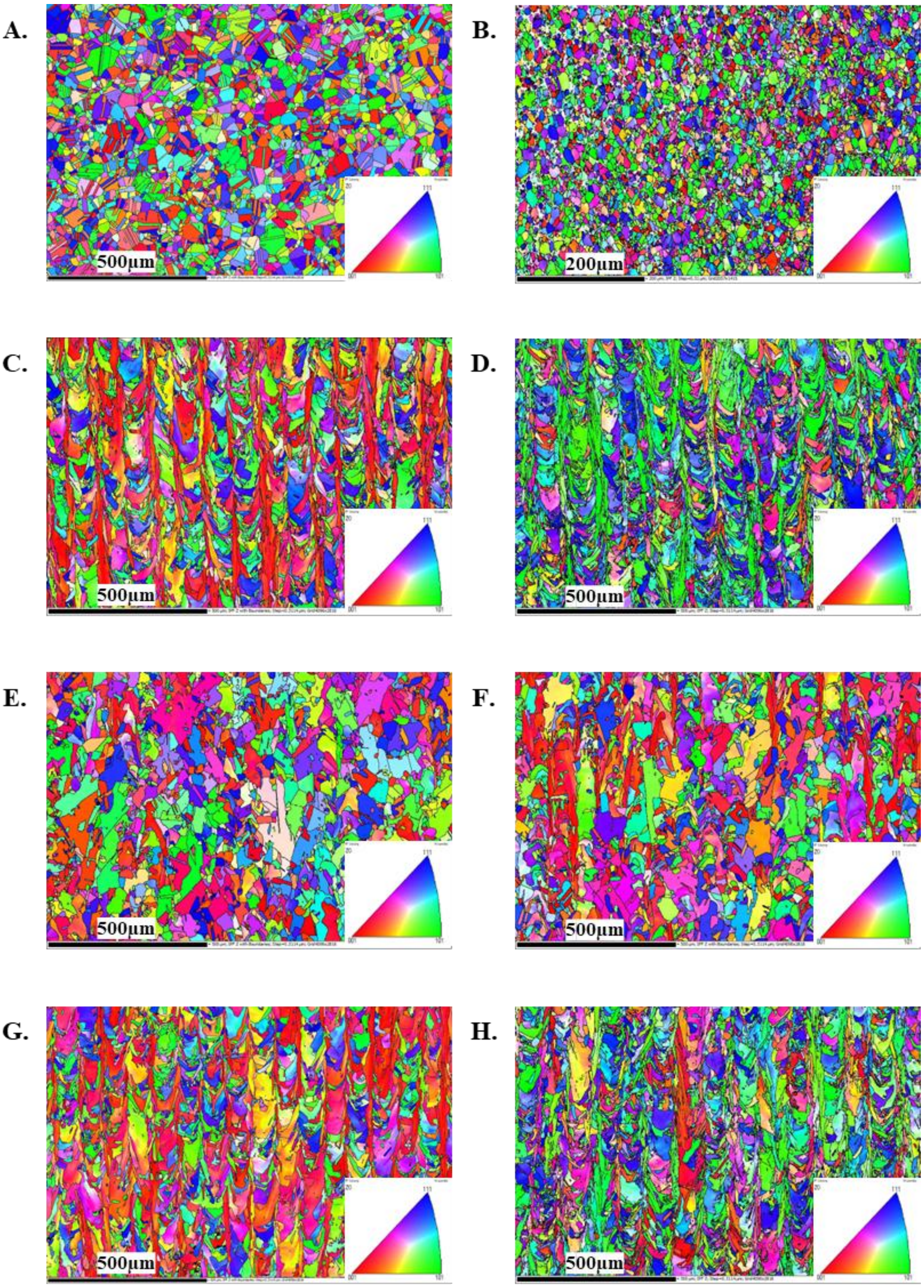

Figure 91: *EBSD map of untested and tested creep samples at 100x magnification, apart from B which is 200x magnification. A, C, E, and G, represent untested wrought, AR, HT1, and HT2, respectively. B, D, F, and G, represent 650MPa, 650°C tested wrought, AR, HT1, and HT2, respectively.*

Table 28 - *Data from EBSD IPFs map for wrought and PBF-LB IN718 before and after constant load creep testing at 650°C, 650MPa.*

Sample (Constant Load)	**With Twins**			**Twin Density (%)**	**Rx (%)**	**HAGBs (%)**	**LAGBs (%)**
	Grain Area (µm²⁾	**Grain Diameter (µm)**	**Aspect Ratio**				
Wrought Untested	193	12.5	0.49	51.4	97.9	93.0	7.0
Wrought Tested	43	6.2	0.56	4.88	25.6	23.0	77.0
AR Untested	195	10.4	0.42	0.5	29.7	49.2	50.8
AR Tested	151	9.1	0.44	0.6	26.3	45.2	54.8
HT1 Untested	293	13.3	0.47	25.3	77.1	60.6	39.4
HT1 Tested	291	13.4	0.47	13.8	67.2	53.8	46.2
HT2 Untested	174	9.8	0.43	0.3	34.0	36.0	64.0
HT2 Tested	167	9.7	0.44	0.6	30.7	49.0	51.0

FEG-SEM analysis of changes to phases during testing are displayed in Figure 92. Quantitatively comparing this to FEG-SEM images in Figure 53 and Figure 59 to Figure 61 prior to testing, it can be seen that the δ in wrought, HT1, and HT2 could possibly have grown. Additionally, the carbides in HT1 and HT2 appear larger. AR appears largely unchanged with a calculated Laves volume fraction of 5.39 ±0.63%. Higher magnification images were not generated due to the inability to quantify γ' and γ''.

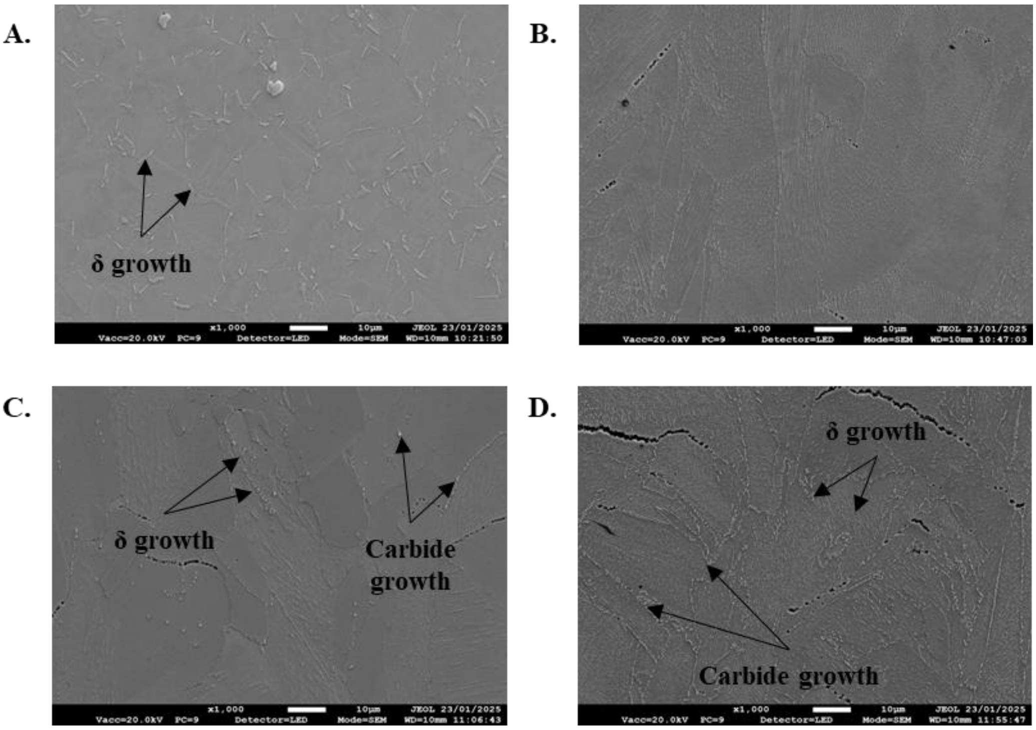

Figure 92: *Post-creep test FEG-SEM micrographs of Kalling's No.2 etched A) wrought, B) AR, C) HT1, and D) HT2, at 1,000x magnification.*

6.4 Small Punch Creep

SPC testing carried out at 650°C on vertical and horizontal PBF-LB variants is shown in Figure 93 and Figure 94, respectively. The data for vertical and horizontal PBF-LB variants are also compared to wrought IN718 tested at 650°C. Wrought data was interrupted prior to full failure due to the prolonged length of test time and non-failure is denoted by arrows, as seen on Figure 93 and Figure 94. For both vertical and horizontal PBF-LB samples, the creep life is far inferior than the wrought specimens.

Focusing on vertical PBF-LB testing, where most data is collated, there appears to be a general trend where HT2 is superior compared to HT1 and AR. At loads 400N and below, AR is inferior to HT1 but when load is increased above 400N, AR becomes superior to HT1. Additionally, at 425N, all vertical PBF-LB variants show a larger decrease in time to rupture for the given load than expected.

Initial data for horizontal PBF-LB SPC testing shows a different trend to vertical PBF-LB, where HT1 appears superior compared to AR and HT2.

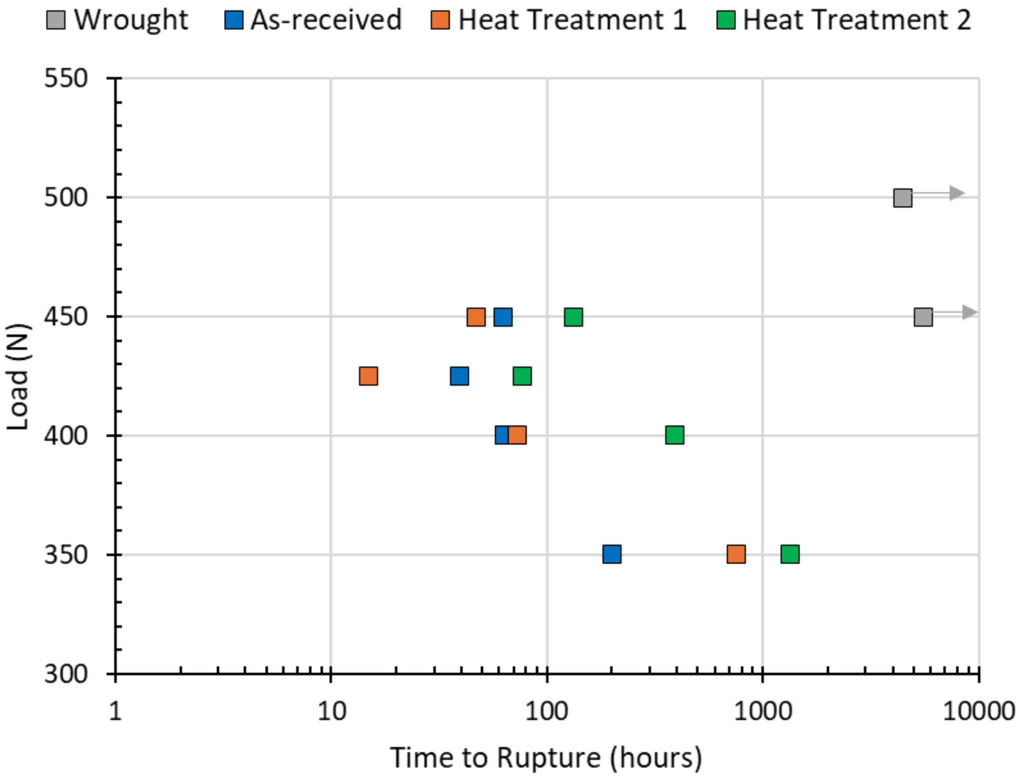

Figure 93: *SPC Load - time to rupture behaviour for vertical PBF-LB and wrought IN718.*

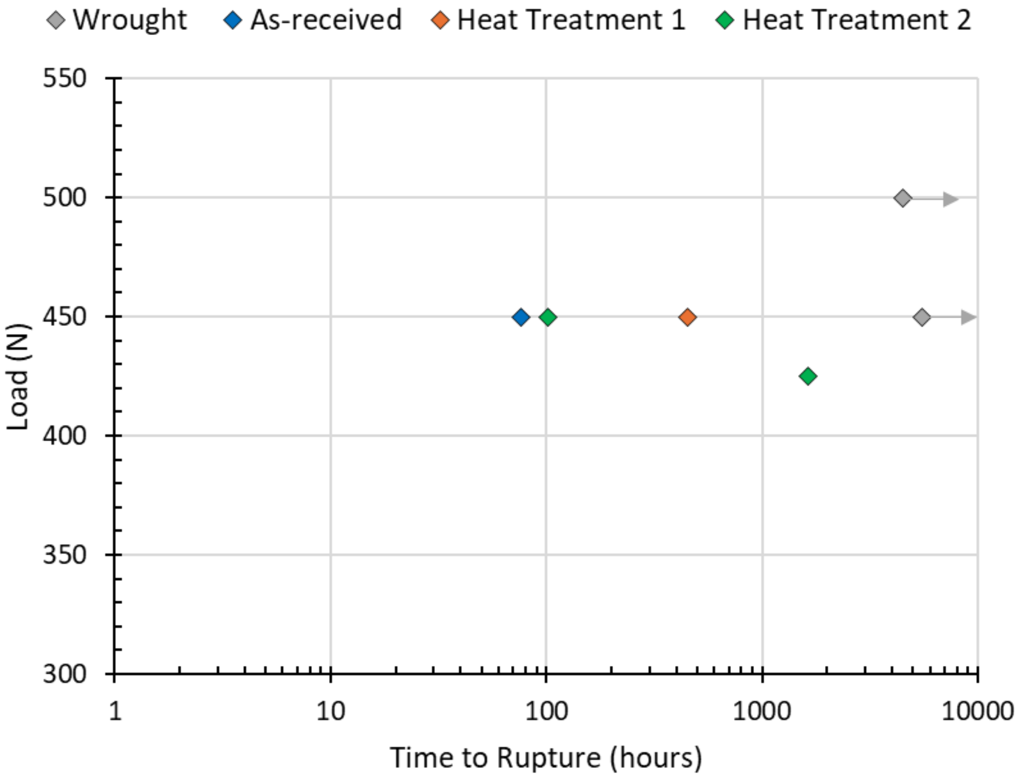

Figure 94: *SPC Load - time to rupture behaviour for horizontal PBF-LB and wrought IN718.*

Comparison of the vertical PBF-LB and wrought IN718 time-displacement curves at 450N are shown in Figure 95 and horizontal PBF-LB and wrought time-displacement curves at 450N are shown in Figure 96. From Figure 95 it can be seen that the wrought material has the lowest displacement rate during the 2^y creep stage compared to the PBF-LB variants. Additionally, the wrought material shows most ductility in the 1^y stage compared to the PBF-LB variants. Horizontal PBF-LB shows the same trends displayed by the vertical PBF-LB samples when compared to wrought but the ordering of PBF-LB failure varies (as mentioned previously).

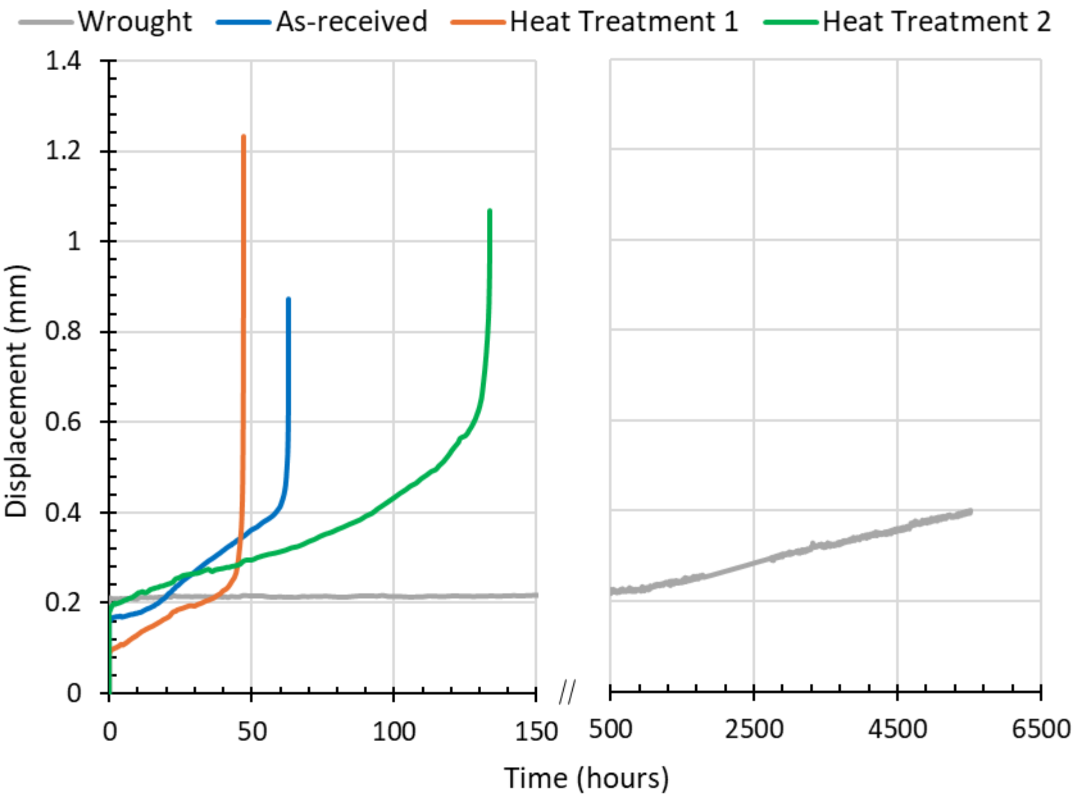

Figure 95: *SPC time - displacement curves for 450N load for vertical PBF-LB and wrought IN718.*

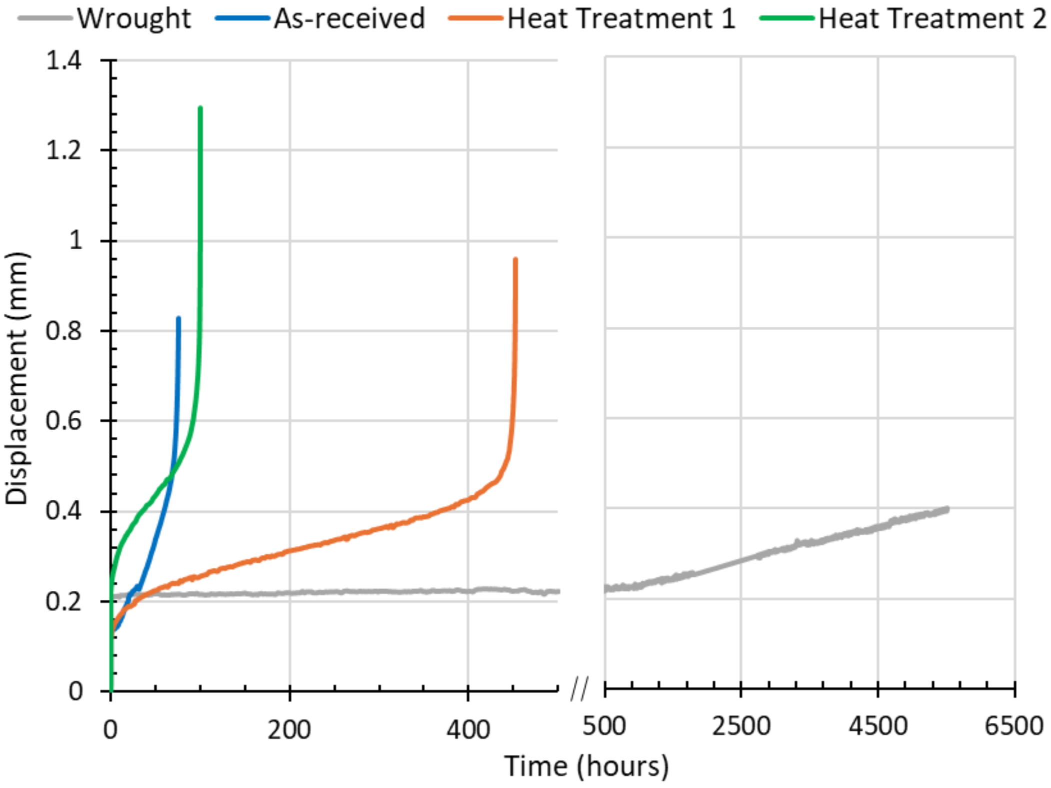

Figure 96: *SPC time-displacement curves for 450N load for horizontal PBF-LB and wrought IN718.*

In addition to load displacement curves, the plots of time to rupture against minimum displacement rate can be seen in Figure 97 and Figure 98 for vertical PBF-LB and horizontal PBF-LB, respectively. These graphs reflect preliminary observations where wrought displays the lowest minimum displacement rate. For vertical PBF-LB, HT2 shows the lowest minimum displacement rate and for horizontal PBF-LB, HT1 displays the lowest minimum displacement rate.

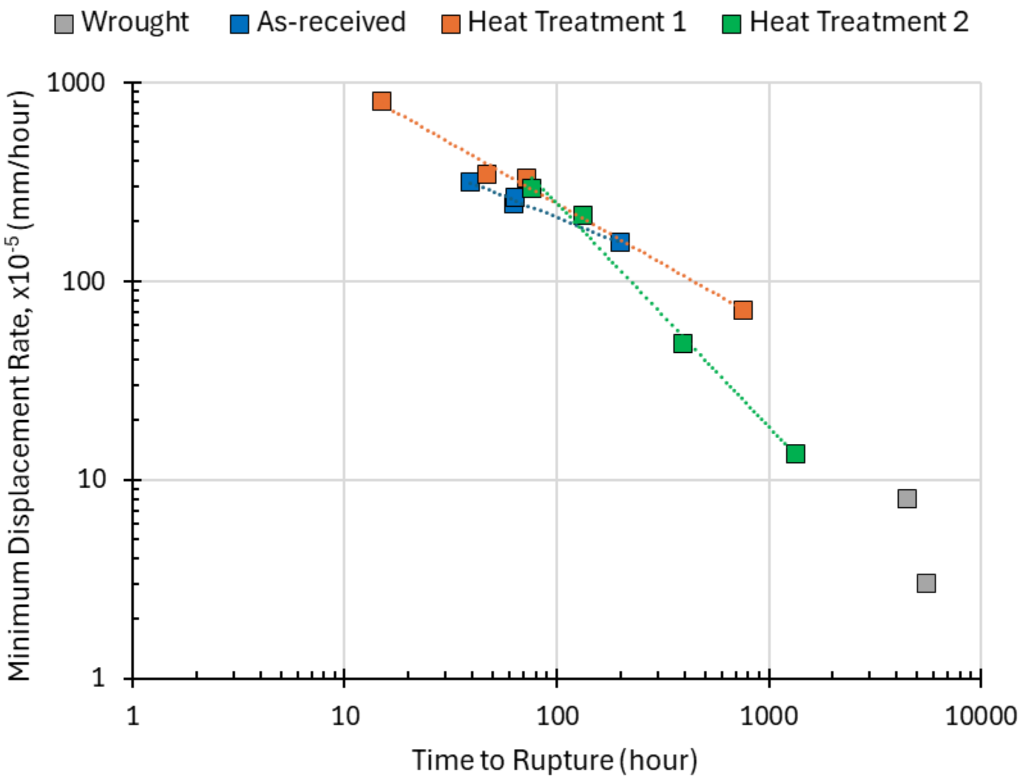

Figure 97: *Minimum displacement rate against time to rupture for vertical PBF-LBand wrought IN718 tested under SPC conditions.*

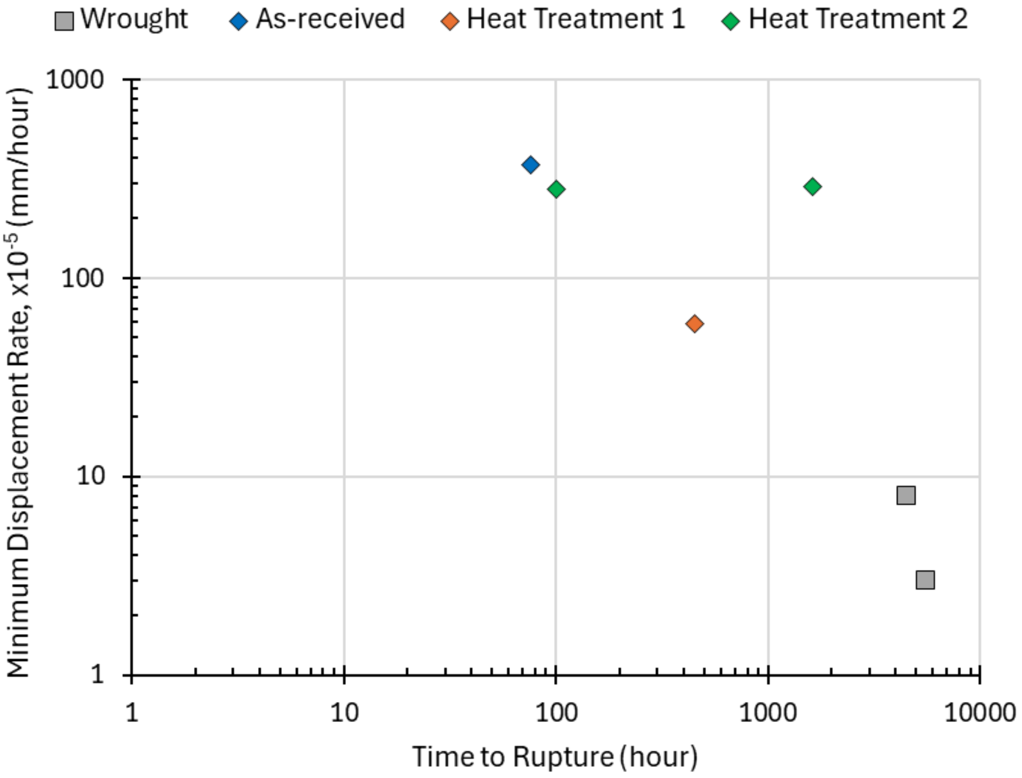

Figure 98: *Minimum displacement rate against time to rupture for horizontal PBF-LB and wrought IN718 tested under SPC conditions.*

6.5 Small Punch Creep Fractography

Post-test fractography was completed on each of the SPC tested samples. Samples tested at the varying loads (450N, 425N, 400N, 350N) for vertical HT2 are shown in Figure 99. The overall fracture surface shows transverse fracture and higher magnification images show the fracture route aligning with microstructural direction.

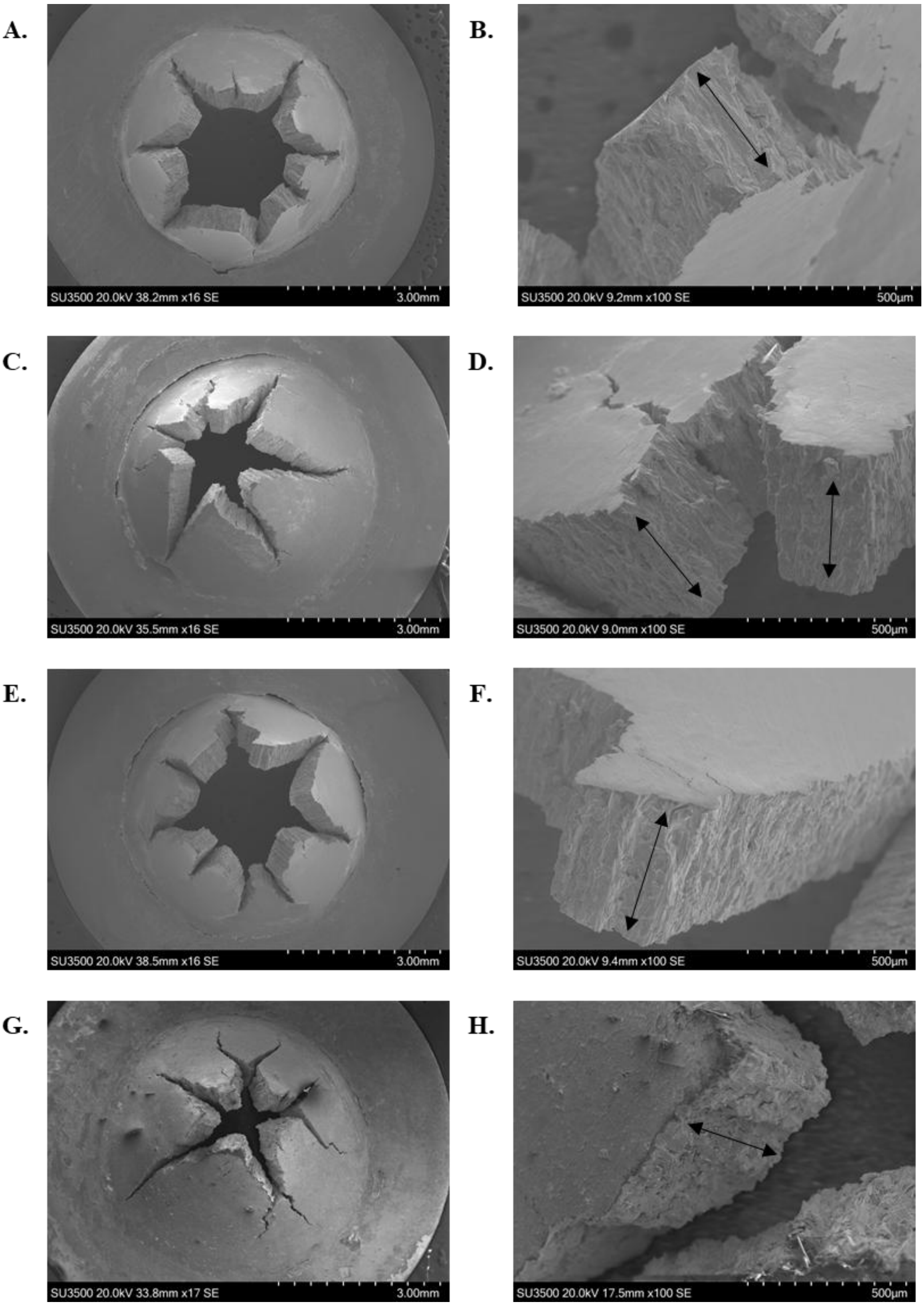

Figure 99: *Low magnification (left column) and 100x magnification (right column) SEM images of vertical HT2 SPC fracture surfaces. A and B represent 450N. C and D represent 425N. E and F represent 400N. G and H represent 350N. Black arrows denote fracture route.*

Similarly, fractographic images for all the variants tested at 450N are presented in Figure 100, Figure 101, and Figure 102, for wrought, vertical, and horizontal PBF-

LB, respectively. Figure 100 shows the wrought variant did not reach failure with limited deformation displayed as minimal stretching rather than any cracking or perforation. Alternatively, Figure 101 (vertical PBF-LB) and Figure 102 (horizontal PBF-LB) shows failure with cracking transverse (for vertical PBF-LB) and longitudinal (for horizontal PBF-LB) across the sample. Higher magnification images for vertical and horizontal PBF-LB shows strong directional fracture routes, particularly for AR and HT2, as denoted by the black arrows in Figure 101 and Figure 102.

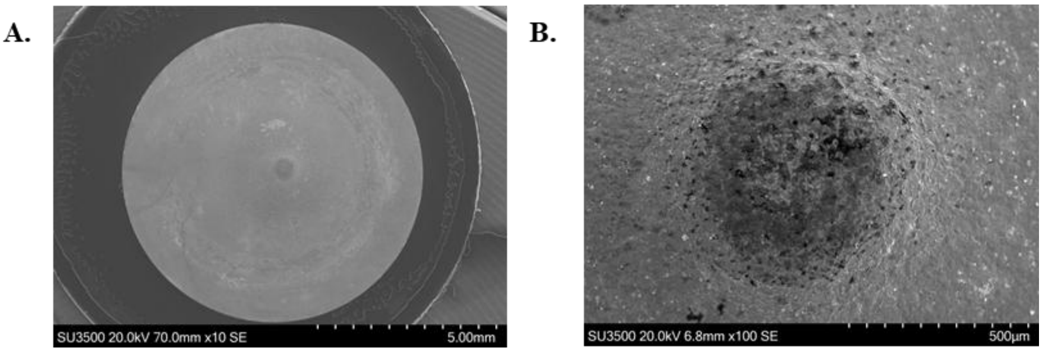

Figure 100: *SEM images of wrought 450N SPC fracture surface at A) low magnification and B) 100x magnification.*

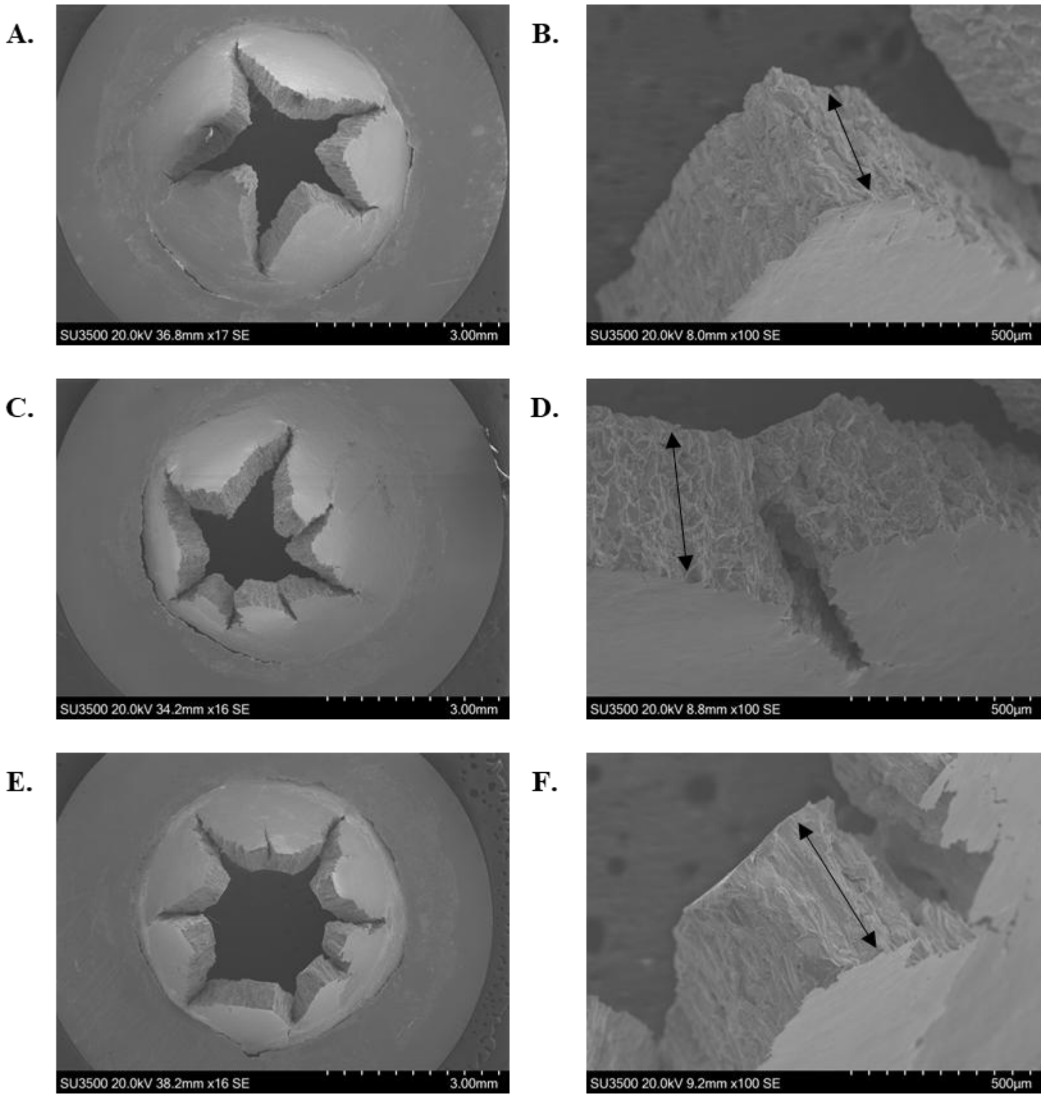

Figure 101: *Low magnification (left column) and 100x magnification (right column) SEM images of vertical 450N SPC fracture surfaces. A and B represent AR. C and D represent HT1. E and F represent HT2. Black arrows denote fracture route.*

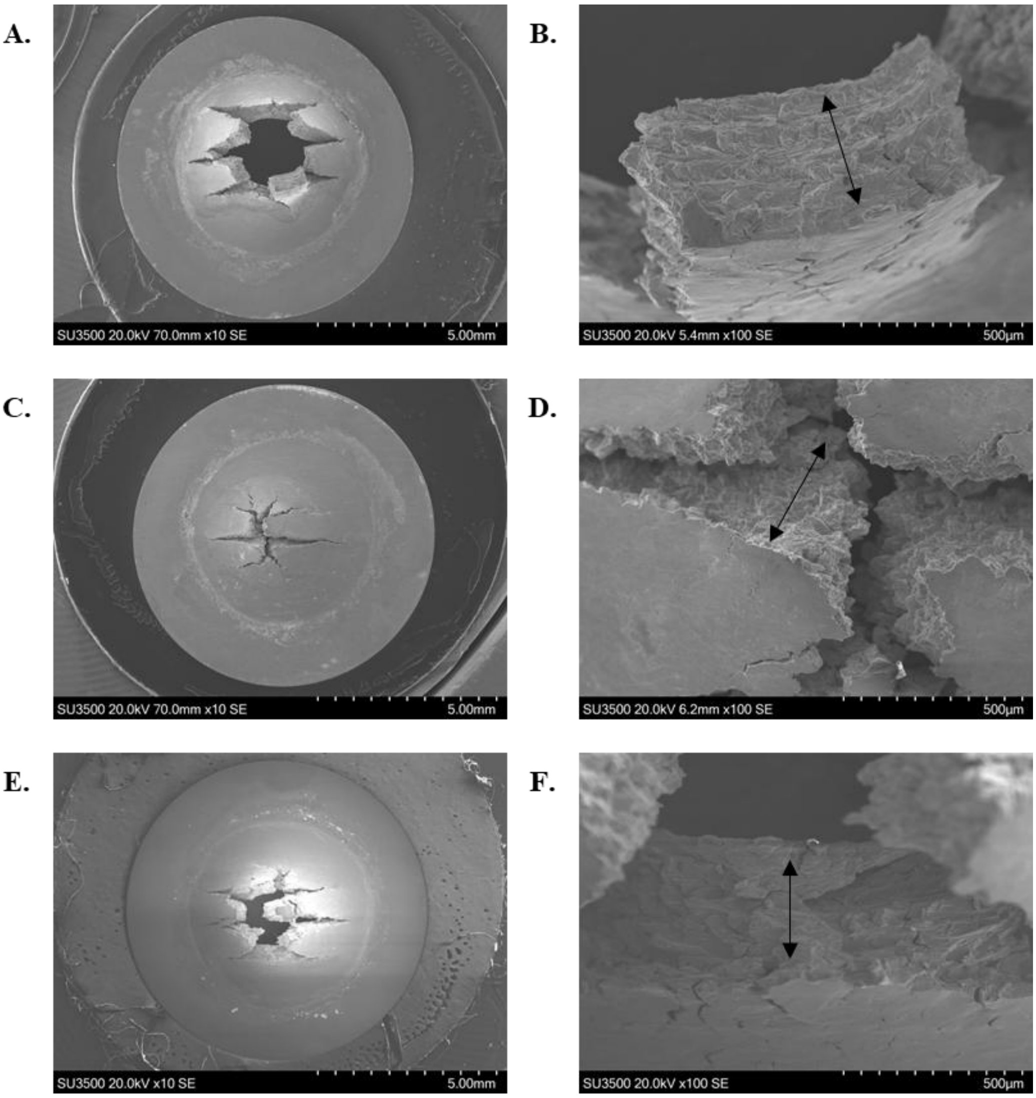

Figure 102: *Low magnification (left column) and 100x magnification (right column) SEM images of horizontal 450N SPC fracture surfaces. A and B represent AR. C and D represent HT1. E and F represent HT2. Black arrows denote fracture route.*

Alongside fractographic images, cavitation analysis was carried out on the SPC samples. Figure 103 shows the degree of cavitation for HT2 at varying loads and Figure 104, Figure 105, and Figure 106, shows the degree of cavitation for the varying samples at 450N for wrought, vertical, and horizontal PBF-LB, respectively. For Figure 103 to Figure 106 it can be seen that the samples with lower minimum creep rates and longer time to rupture display more uncoalesced cavities compared to samples with higher creep rates and shorter time to rupture, where more coalesced cavities can be observed. Observations for wrought 450N SPC in Figure 104 indicates no cavitation, aligning with the non-failure of the sample.

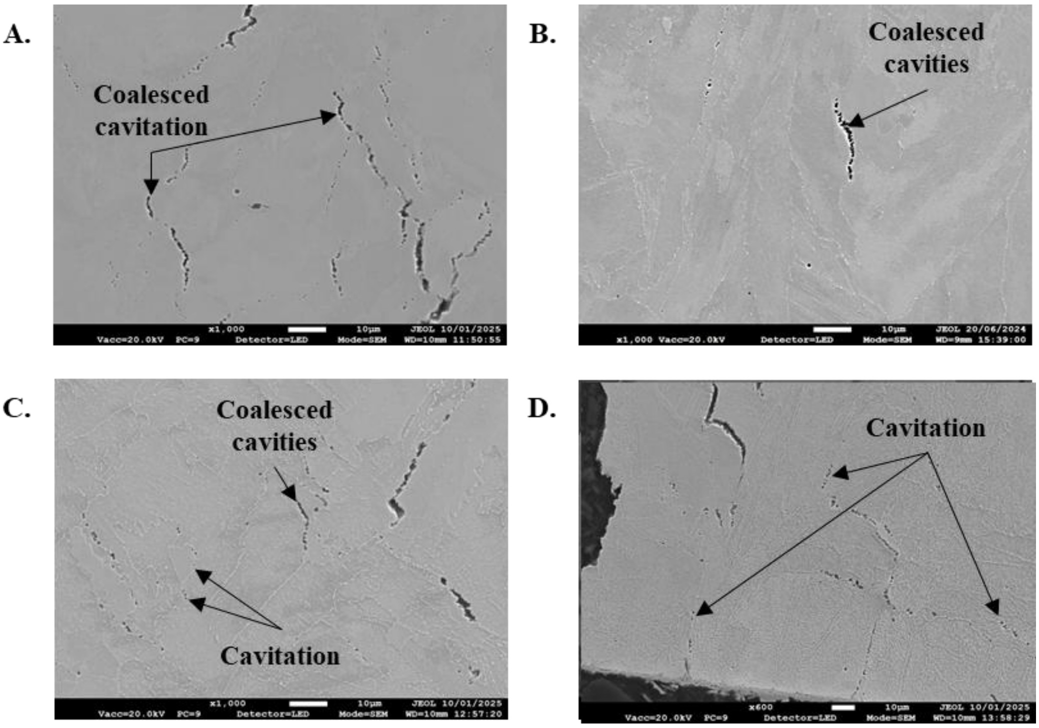

***Figure 103:** FEG-SEM cavitation analysis of vertical HT2 PBF-LB SPC. A represents 450N. B represents 425N. C represents 400N. D represents 350N.*

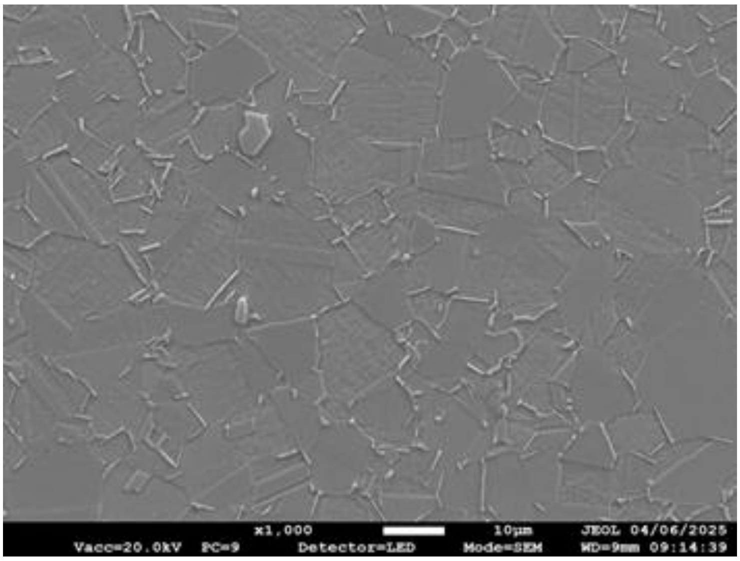

***Figure 104:** FEG-SEM cavitation analysis of wrought 450N SPC.*

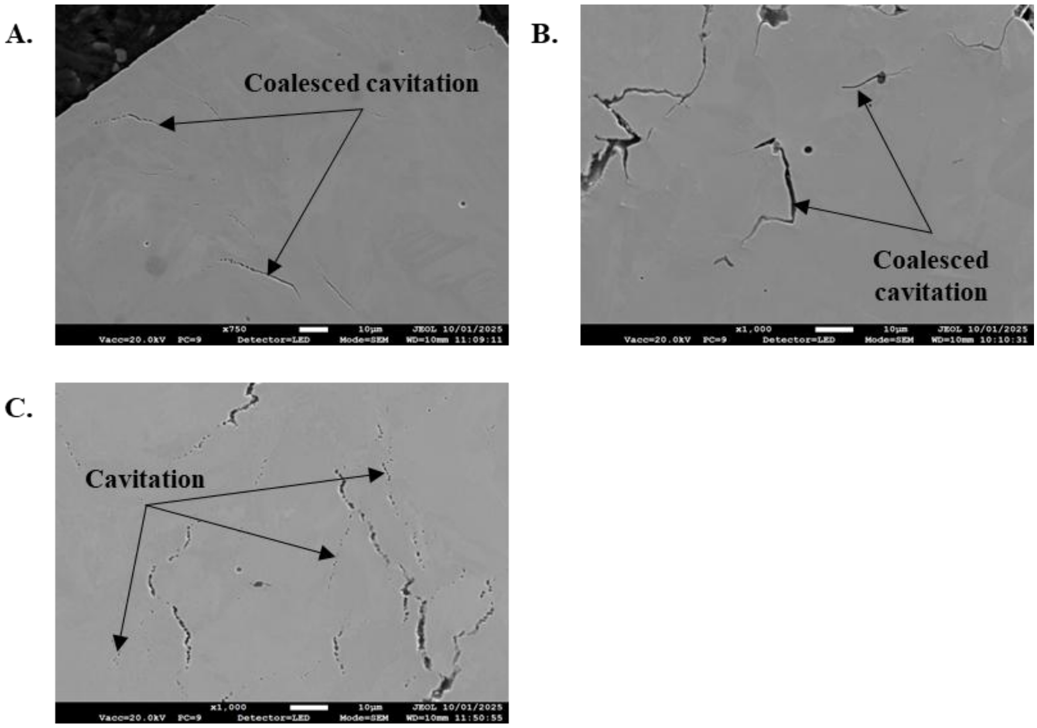

Figure 105: *FEG-SEM cavitation analysis of vertical PBF-LB 450N SPC. A represents AR. B represents HT1. C represents HT2.*

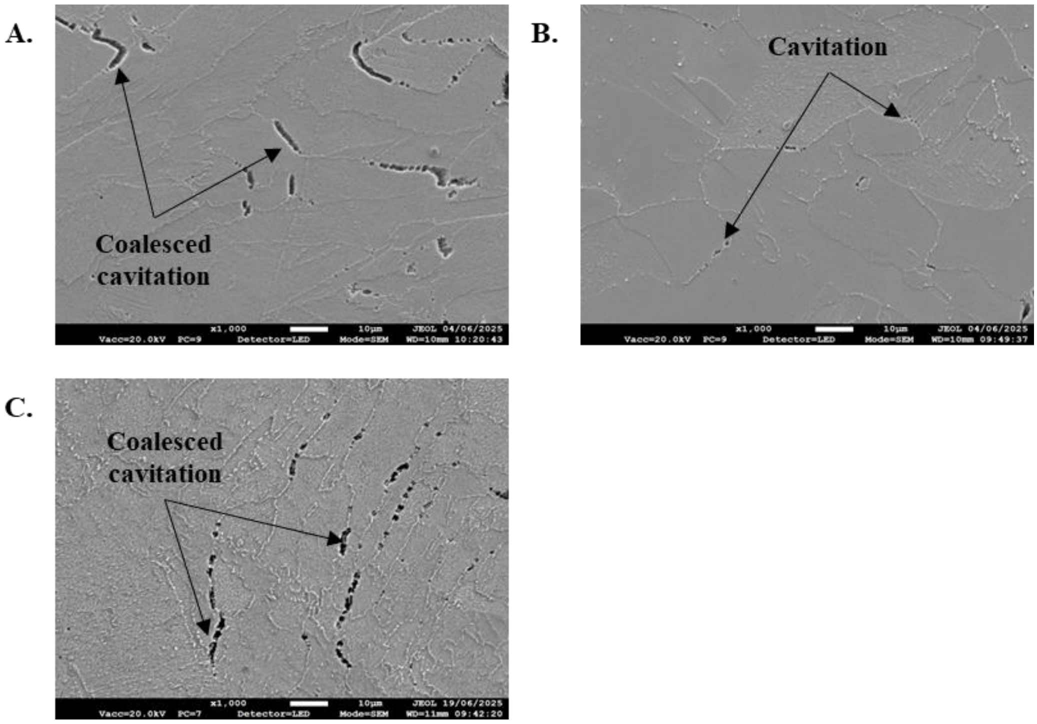

Figure 106: *FEG-SEM cavitation analysis of horizontal 450N PBF-LB SPC. A represents AR. B represents HT1. C represents HT2.*

6.6 Summary

Given that the trend displayed by the horizontal SPC samples aligns with the trend displayed by the traditional constant load creep tests, it would be advised that the correlation be performed on this set of results. However, due to the lack of data this would not be feasible or reliable for correlation.

Omission of the use of the k_{sp} approach was due to the k_{sp} correlation factor, which ranges from 0-1 and is based on the material's ductility and deformation response. Tensile results reported in this thesis for wrought and AM IN718 (with varying HTs) behave like distinct materials with different strength and ductility, therefore, a universal k_{sp} values applicable for all IN718 variants is not suitable. Consequently, k_{sp} must be determined separately for each variant, but cannot be established for this investigation due to lack of sufficient test repeats and stress levels for each sample condition (wrought and AM AR, HT1, and HT2).

Analysis of the SPC cavitation showed cavitation in the failed samples, with degrees of coalescence relating to time to rupture and minimum creep rate. Research suggests that cavitation and microcracking in SPC is initiated at the end of the primary creep staged, rather than at the end of the steady-state creep stage in uniaxial creep testing, and structures with spatially heterogeneous microstructure experience cracking along and normal to the grain boundaries [193]. Therefore the larger grained, heterogenous microstructure displayed by wrought, with no observed cavitation, suggests that there is increased resistance to cracking and cavitation due to grain boundary routes, when compared to the AM variants. Further research by Wang et al. [194] suggested that crack initiated from Laves phases at the grain boundaries and propagated along the grain boundaries. This crack initiation theory could be why cavitation is observed in the AM variants (which have Laves phases present) and not the wrought IN718 variant (where Laves phase is not observed).

7 Results – Strain Control Low Cycle Fatigue

7.1 Strain Control Low Cycle Fatigue

Assessment of the strain amplitude and number of cycles to failure for RT and ET LCF data is shown in Figure 107 and Figure 108, respectively. From these graphs it appears that for a given strain amplitude the different variants behave similarly, but at amplitudes above 0.4%, typically wrought and HT1 appear inferior, reaching fewer cycles than AR and HT2. This graphical trend is also shown in the data tabulated in Table 29 for RT and Table 30 for ET. From this the trends regarding cyclic softening and hardening can be observed. At ET all samples experience cyclic softening and at RT most samples experience cyclic hardening (HT1 and HT2 at 0.5% experience cyclic softening).

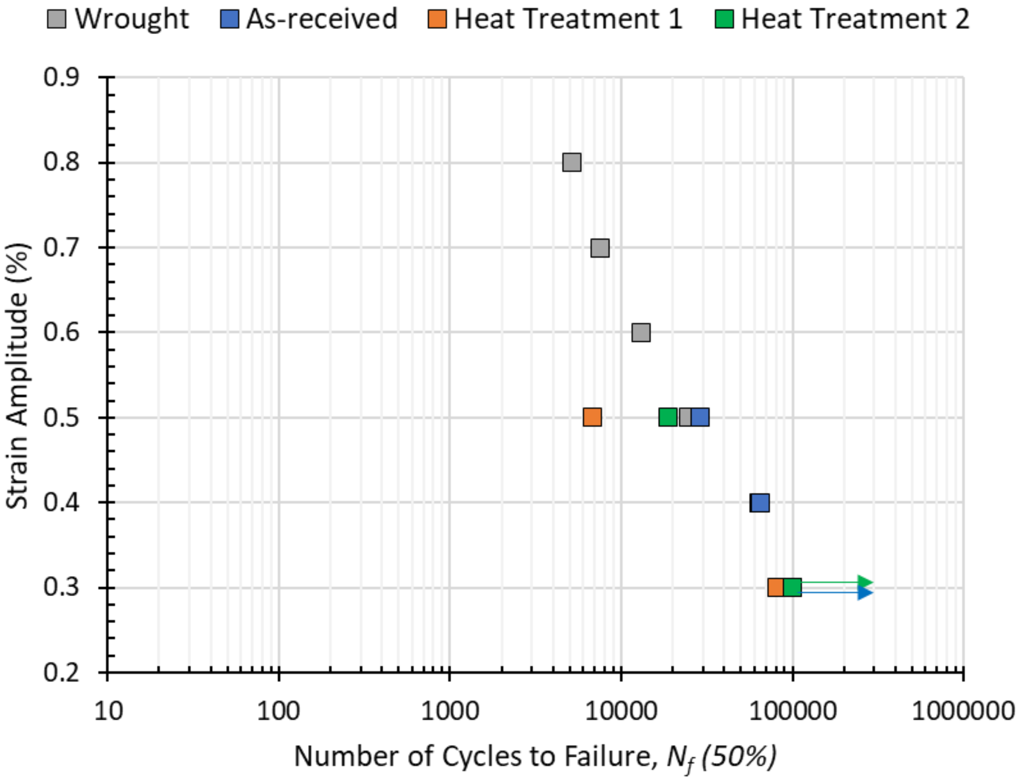

Figure 107: *Graph to show strain amplitude against number of cycles to failure for RT LCF tests.*

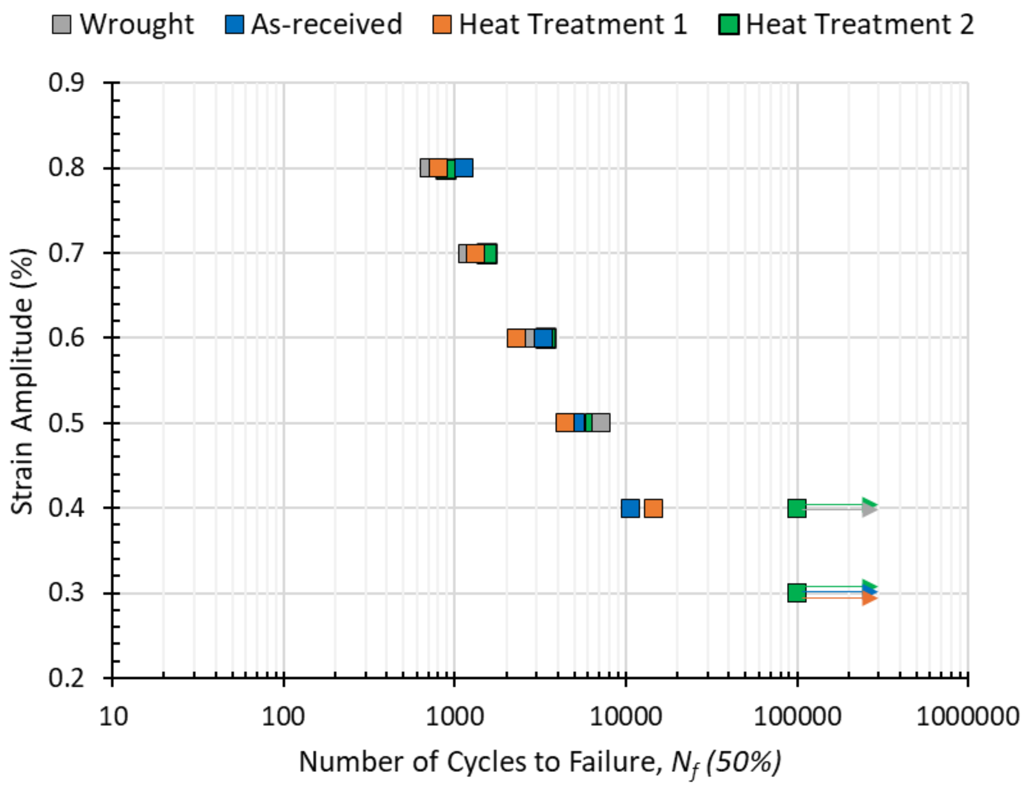

Figure 108: *Graph to show strain amplitude against number of cycles to failure for ET LCF tests.*

Table 29 - *LCF data for all samples at RT.*

Sample Type	Strain Amplitude (%)	N_f (50%)	Stress Maximum (MPa)	Stress Minimum (MPa)	Stress Range (MPa)	Loop Comment
Wrought	0.4	64400	525.2	-533.3	1058.6	Hardening
	0.5	24800	559.7	-574.5	1134.2	Hardening
	0.6	13119	593.4	-613.1	1206.5	Hardening
	0.7	7562	622.4	-642.1	1264.5	Hardening
	0.8	5143	641.2	-663.9	1305.1	Hardening
As-received	0.3	100000	414.8	-503.3	918.1	N/A
	0.4	65200	533.1	-667.3	1200.5	Hardening
	0.5	29000	646.1	-761.5	1407.6	Hardening
Heat Treatment 1	0.3	81058	592.8	-588.5	1181.3	N/A
	0.5	18765	846.6	-887.2	1733.7	Softening
Heat Treatment 2	0.3	18765	624.5	-468.7	1093.2	Hardening
	0.5	100000	846.6	-887.2	1733.7	Softening

Table 30 - LCF data for all samples at ET.

Sample Type	Strain Amplitude (%)	N_f (50%)	Stress Maximum (MPa)	Stress Minimum (MPa)	Stress Range (MPa)	Loop Comment
Wrought	0.4	100000	527.6	-570.2	1097.8	Softening
	0.5	7149	511.5	-521.8	1033.4	Softening
	0.6	2592	511.9	-540.6	1052.5	Softening
	0.7	1189	560.8	-569.9	1130.7	Softening
	0.8	710	579.3	-580.5	1159.8	Softening
As-received	0.3	100000	499.0	-413.5	912.4	Softening
	0.4	10549	593.7	-583.1	1176.8	Softening
	0.5	5101	616.8	-651.2	1268.0	Softening
	0.6	3303	738.4	-793.4	1531.7	Softening
	0.8	1139	653.3	-680.9	1334.2	Softening
Heat Treatment 1	0.3	100000	465.0	-504.5	969.5	Softening
	0.4	14500	621.4	-631.6	1253.0	Softening
	0.5	4416	734.8	-765.1	1499.8	Softening
	0.6	2285	782.8	-820.5	1603.3	Softening
	0.7	1325	810.0	-854.7	1664.7	Softening
	0.8	806	831.7	-891.1	1722.9	Softening
Heat Treatment 2	0.3	478.1	-437.2	915.2	100000	Softening
	0.4	551.6	-601.9	1153.5	100000	Softening
	0.5	656.9	-691.6	1348.5	6600	Softening
	0.6	693.9	-732.1	1426.0	3358	Softening
	0.7	754.5	-791.4	1545.9	1541	Softening
	0.8	767.5	-815.7	1583.2	880	Softening

Although the strain amplitude against number of cycles to failure suggests HT1 is inferior, assessment of the stabilised stress range against number of cycles to failure for RT and ET (Figure 109 and Figure 110, respectively) shows that HT1 is superior in comparison to the other IN718 variants. It can also be seen that the wrought material appears the worst performing when compared to the additive material.

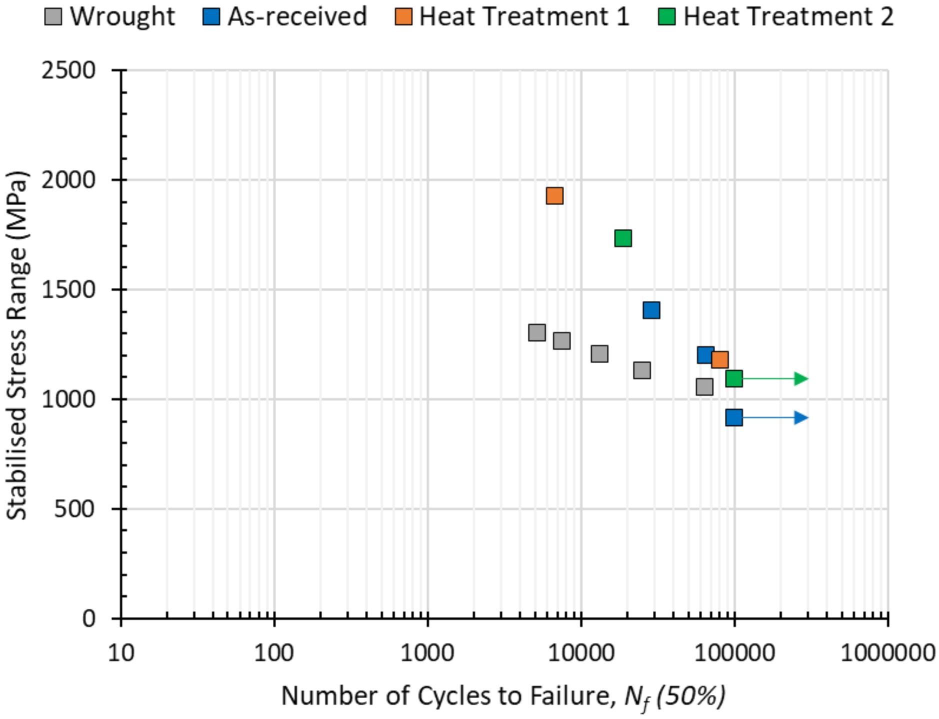

Figure 109: *Graph to show stabilised stress range against number of cycles to failure for RT LCF tests.*

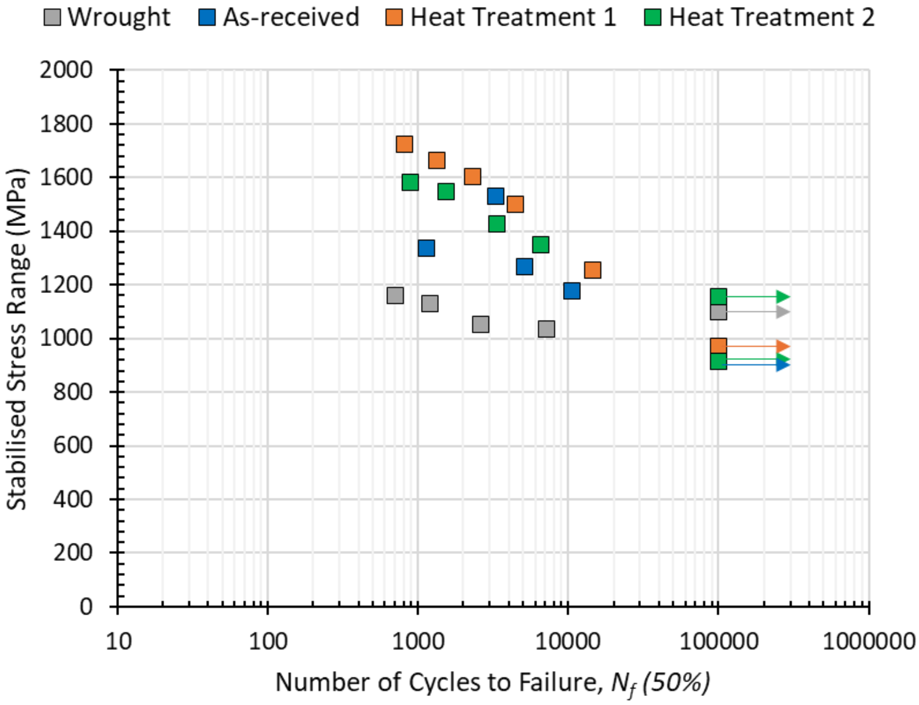

Figure 110: *Graph to show stabilised stress range against number of cycles to failure for ET LCF tests.*

Focussing on the 0.5% strain amplitude tests at RT the first (monotonic) hysteresis loop and stabilised ($N_f/2$) hysteresis loop for the different samples can be seen in Figure 111 and Figure 112, respectively. From these figures it can be seen that the wrought material has the largest plastic stress range. HT1 and HT2 show the least plastic stress range, keeping in the elastic range until reaching the stabilised loop where some plasticity has occurred. Comparing the first and stabilised loop also shows that wrought and AR experience the most cyclic hardening, whereas HT1 and HT2 show little, to no, cyclic hardening. It is also noted that the first loop for the wrought variant appears to show stress drops approaching peak stress, and also an exceed of the defined 0.5% strain amplitude. This material behaviour has been linked to DSA and the test was not void as the strain amplitude of 0.5% was rectified within the following few cycles.

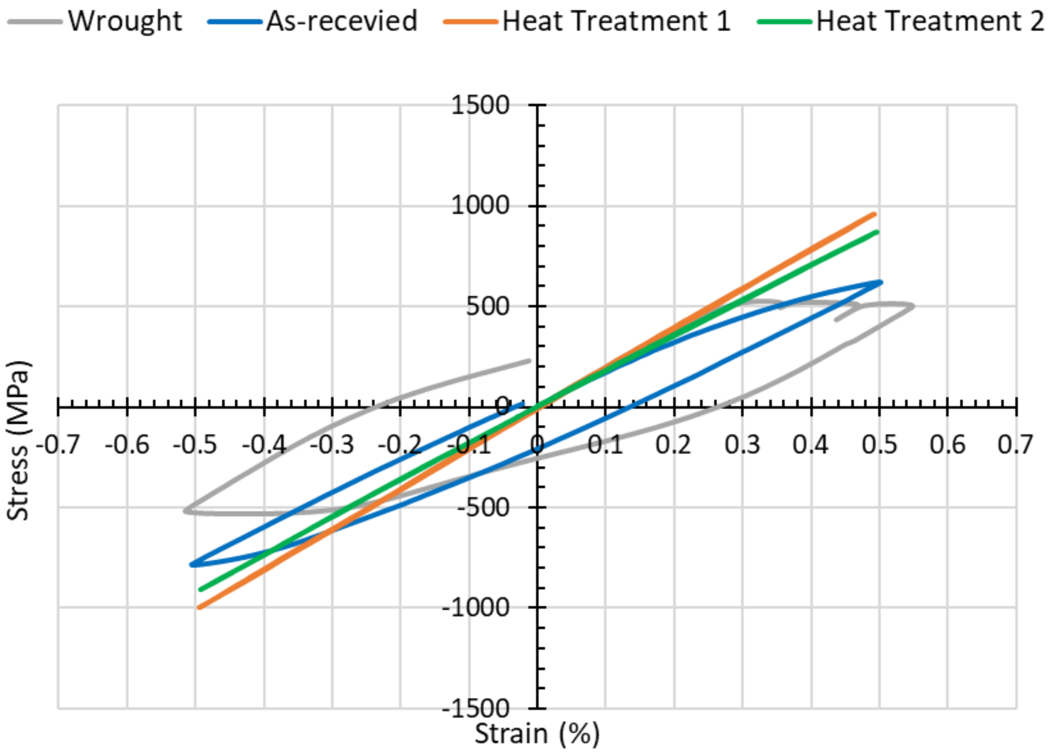

Figure 111: *Graph to show first hysteresis loop for RT LCF tests at 0.5% strain amplitude.*

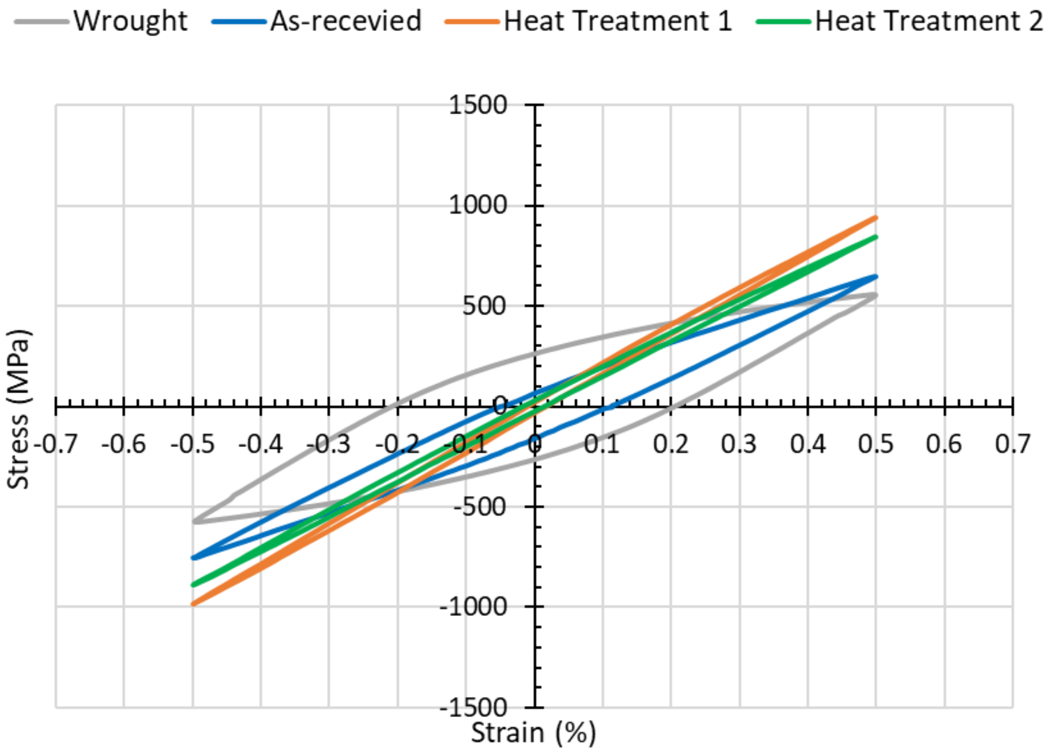

Figure 112: *Graph to show stabilised hysteresis loop for RT LCF tests at 0.5% strain amplitude.*

Similarly, the same hysteresis loop analysis was conducted on the ET samples at 0.5% strain amplitude. The first hysteresis loops are shown in Figure 113 and the stabilised hysteresis loops are shown in Figure 114. Similarly to that at RT, the wrought material exhibits the largest plastic strain range in both the first and stabilised loop. The ET testing suggests a different behaviour than the RT testing as the additive materials, especially HT1 and HT2, show much more plasticity in the stabilised cycle. Also, it shows that all variants undergo cyclic softening. Furthermore, as mentioned for the RT testing, the same behaviour of stress dropping and 'overshooting' the specified strain amplitude is seen on the first cycle of the wrought specimen.

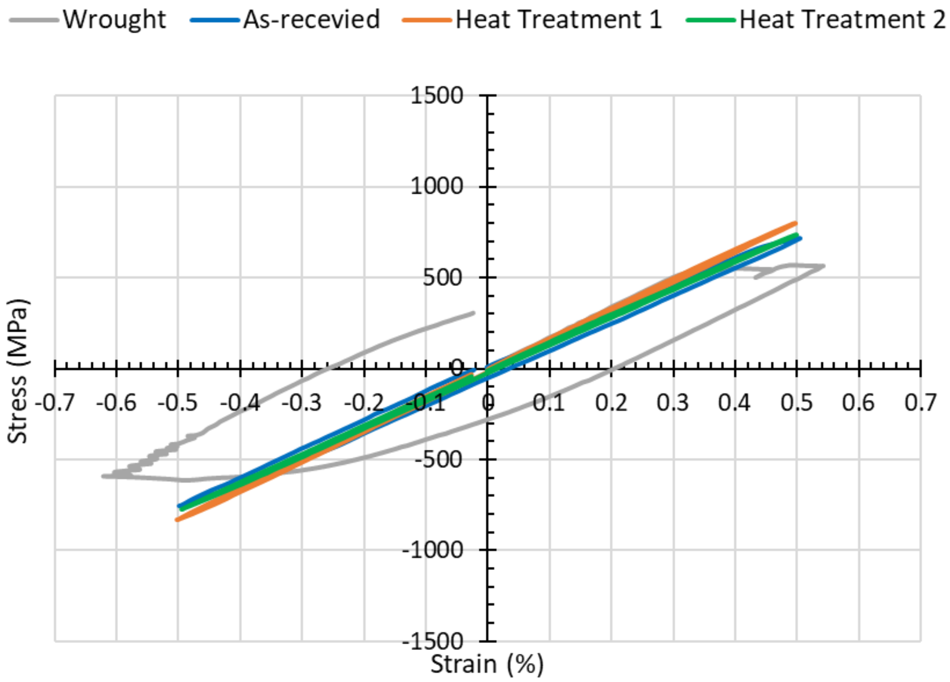

Figure 113: *Graph to show first hysteresis loop for ET LCF tests at 0.5% strain amplitude.*

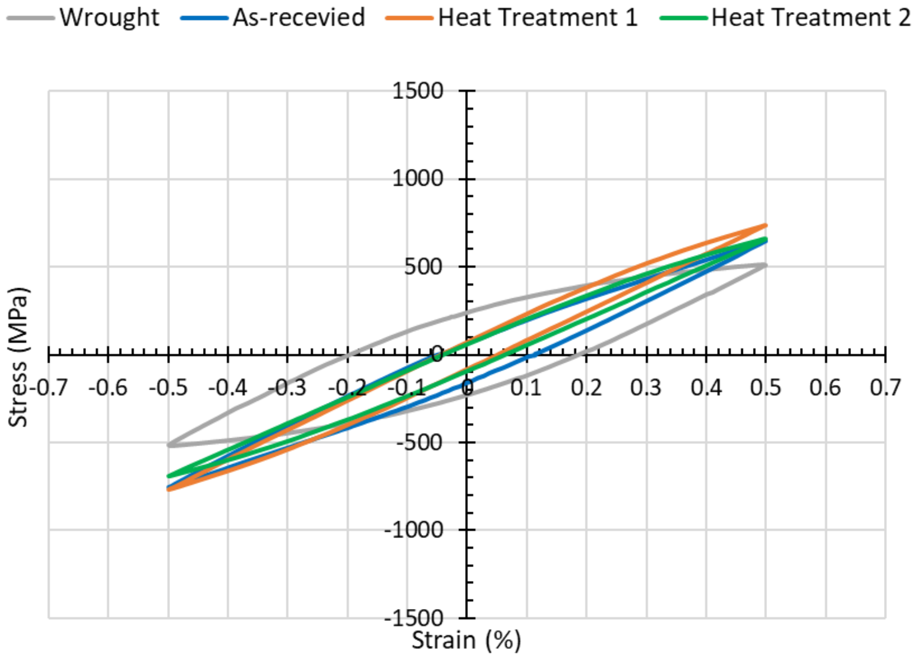

Figure 114: *Graph to show stabilised hysteresis loop for ET LCF tests at 0.5% strain amplitude.*

In addition to the hysteresis loops, assessment of the maximum stress and minimum stress evolution during testing at 0.5% strain amplitude was completed. RT data is shown in Figure 115 and ET data is shown in Figure 116.

Analysis of the RT graph suggests that the HT1 sample accrues the highest stress range with the shortest number of cycles to failure, followed closely by HT2 with a slightly lower stress range but much higher number of cycles to failure. AR and wrought materials show a lower stress range than HT1 and HT2, with AR being higher for both stress range and number of cycles to failure, compared to wrought.

Evaluation of the ET data shows that the HT1 variant behaves similarly to the RT tests, showing the highest stress range but lowest number of fatigue cycles to failure. Overall all samples see a decrease in stress range when increasing to ET. However, the difference in stress range from RT to ET varies for each sample. Additionally, for ET testing the wrought and HT2 samples show a higher number of cycles to failure than the AR.

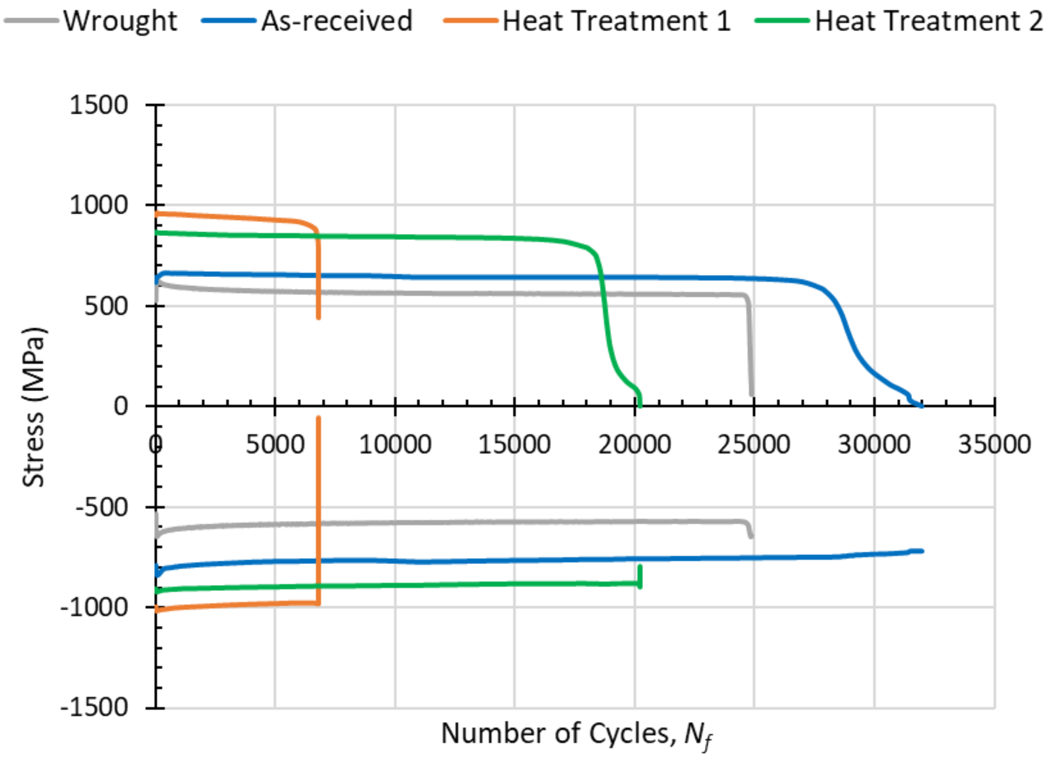

Figure 115: *Graph to show maximum and minimum stress against number of cycles to failure for RT LCF tests at 0.5% strain amplitude.*

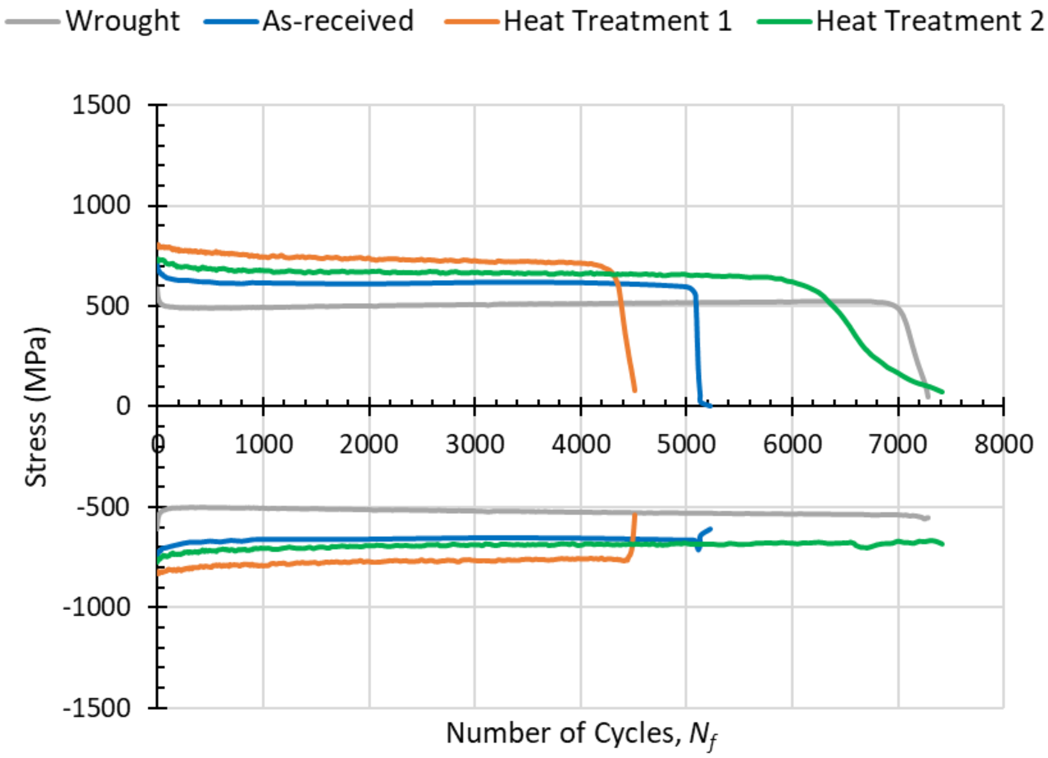

Figure 116: *Graph to show maximum and minimum stress against number of cycles to failure for ET LCF tests at 0.5% strain amplitude.*

7.2 Fractography

Post-test fractographic analysis was conducted on the LCF samples tested at $\varepsilon_{max} = 0.5\%$ to understand the varying modes of failure. An overall, low magnification image was captured for each sample type at each test temperature condition and is shown in Figure 117. All the fracture surfaces exhibit typical fatigue failures with surface or near-subsurface initiation sites, highlighted by red regions, and ductile overload areas, highlighted by the yellow regions. The wrought material at RT and ET shows one clear initiation region whereas the PBF-LB material shows multiple initiation sites. To further support the low magnification fractographs, higher magnification images were taken on the SEM (both SE and BED) and are presented in Figure 118. The higher magnification images show possible major initiation sites for each test.

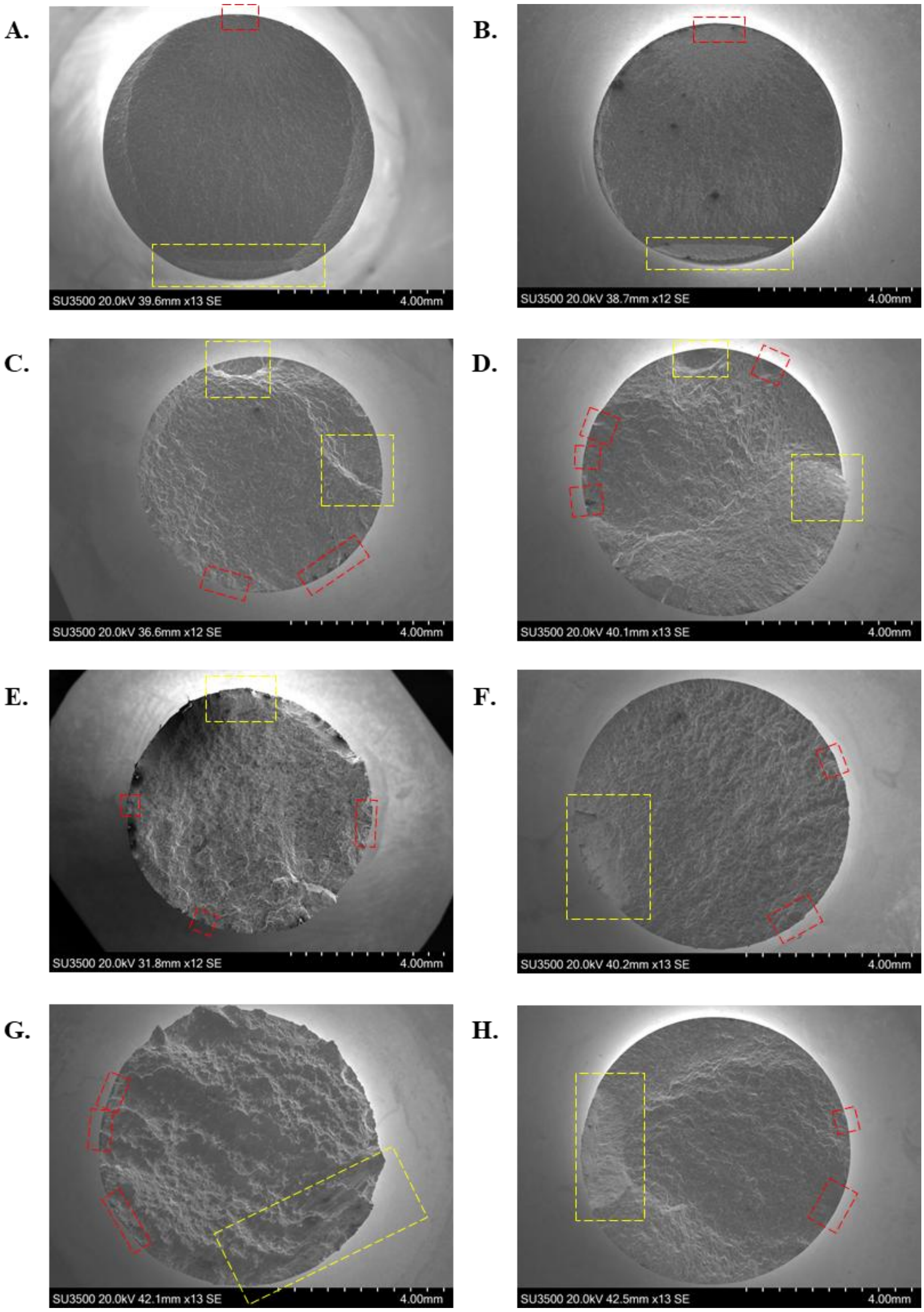

Figure 117: *Low magnification SEM images of LCF fracture surfaces. Left column are RT tests and right column are ET tests. A and B are wrought. C and D are AR. E and F are HT1. G and H are HT2.*

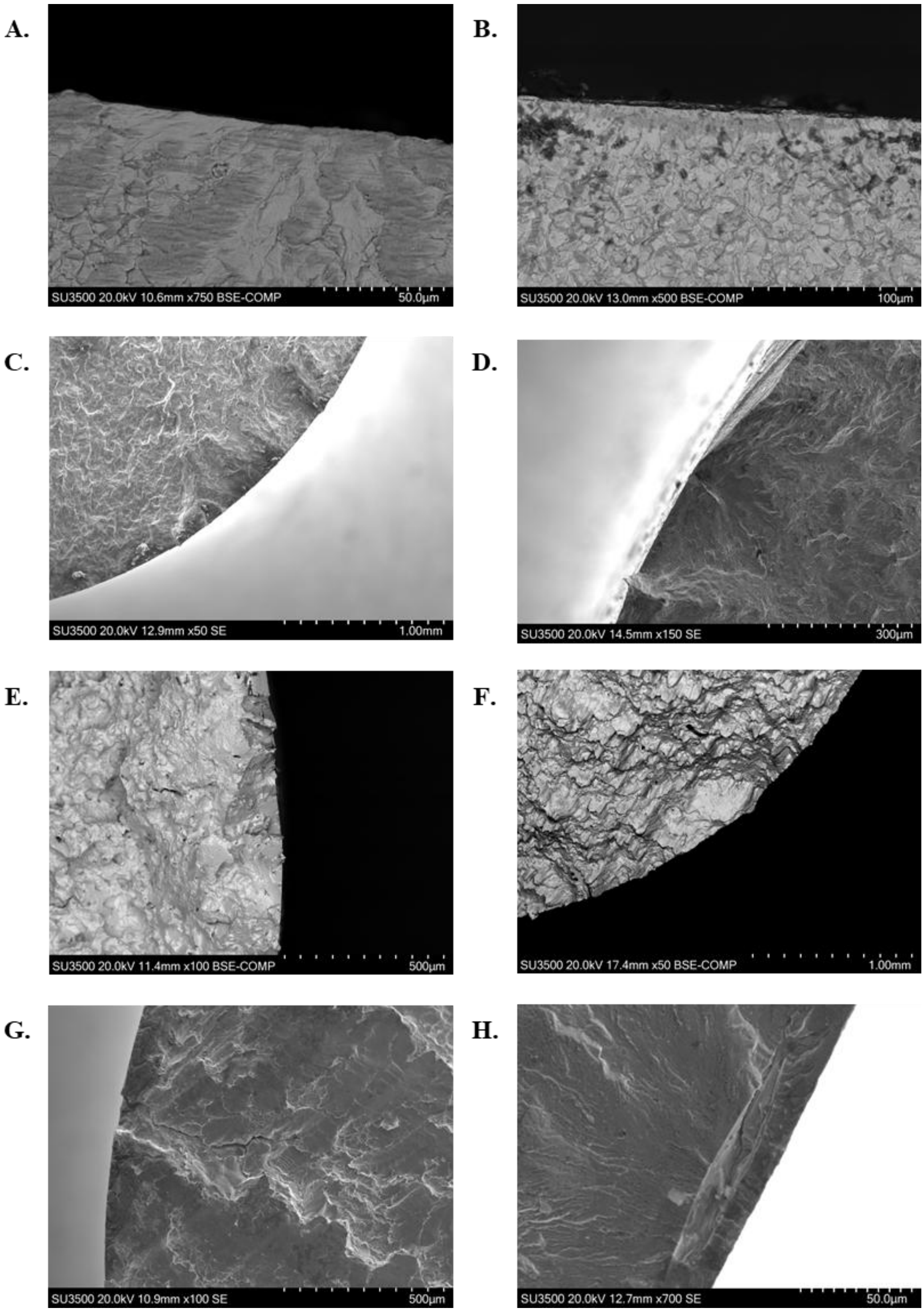

Figure 118: *Higher magnification SEM images of LCF fracture surfaces. Left column are RT tests and right column are ET tests. A and B are wrought. C and D are AR. E and F are HT1. G and H are HT2.*

8 Discussion

8.1 Microstructure

As shown in section 4.2, Table 10, for the PBF-LB samples exhibited very limited porosity, attributed to the fine PSD, roller type used on the FormUp 350, and chessboard scan strategy, meaning fabricated samples are considered near-full density and failure initiations are not linked to porosity or other manufacturing defects such as keyholing or lack of fusion. For the level of this study, optical analysis to assess porosity was suffice, and implementation of standard ASTM B311 [195] was not needed.

Assessing microstructural features it is evident that the PBF-LB process displays different microstructural features to the wrought IN718. The wrought variant displays typical features associated with conventionally manufactured IN718 including a large equiaxed grain size and high twin density with large blocky carbides, and δ, which was promoted via the heat treatment that was implemented. The lack and inability to assess γ' and γ'' in wrought IN718 via FEG-SEM aligns with research conducted by Anbarasan et al. [80] where the precipitation behaviour of γ', γ'', and δ, phases in IN718 via different heat treatment conditions was studied. Using a controlled heating rate of 10°C/min prevented stress development and promoted limited precipitation of γ', γ'', and δ phases. Heating to 980°C and holding for 1 hour caused γ' and γ'' precipitation, with γ'' transforming into stable δ. Using a furnace cooling rate of 5°C/min allowed some γ' and γ'' precipitation, but their low volume fraction rendered them undetectable by XRD, though peak broadening suggested their presence. Alternatively, iced brine quenching (13600°C/min) showed no γ' and γ''.

Overall, the microstructure of wrought IN718 was isotropic, with no texture presented (displaying a low MUD value of 1.20), which is typical for traditionally manufactured IN718.

The typical wrought microstructure is a contrast to the typical additive AR microstructure which displays as anisotropic, with large epitaxially grown columnar grains displayed in the XZ compared to smaller more cuboidal equiaxed grains with 'tracks' of fine grains in the XY plane. This is directly linked to the thermal gradient experienced by the part during fabrication and chessboard scan strategy implemented during manufacturing [196,197]. Even though there is a presence of directional solidification, there is no substantial preferential grain orientation growth, reflected by MUD values below 3.0, indicating no texture [198–200]. It is also shown that the AR AM structure exhibits a large Laves network that is not present in the wrought variant. This network is also attributed to the thermal processing history of the AM sample reflected by the mixture of cellular and columnar Laves phase growth with a minimal observed presence of γ' and γ'' [113].

Initial analysis of the PBF-LB samples showed that there were no microstructural differences between the vertical and horizontal builds for each AM variant. This includes grain characteristics (area, diameter, aspect ratio, twin density), texture, and phase type, quantity, and distribution. There is a slight difference between grain characteristics for vertical and horizontal, XY and XZ planes but this is linked to natural variation within samples. However, it is clear that the vertical XZ plane is consistently larger than the horizontal XZ plane. This is attributed to the assessment region of each sample (middle of the cylindrical bars as per Figure 34) where the vertically built sample would have been from a higher region on the build plate, where grains would be more elongated and columnar compared to lower on the build plate, where it is closer to the thermal sink and a reduced element of grain growth would be expected.

During an assessment of the planes for AR, HT1, and HT2, the reported MUD values from the IPFs were consistently less than 3.0, suggesting there was no texture present. Additionally, all AM variants exhibited fine dispersed oxides present within the microstructure, typically Al or Ti based. These oxides do not appear to be present within the wrought microstructure. Given that the abundance, distribution and sizes appear consistent across all AM variants, it suggests that they are formed during manufacturing and are not influenced by the HT procedure. Presence of oxides and adaption of HTs to strengthen Ni-superalloys via oxide dispersion strengthening has been reported [201–205]. In this research it is implied that the oxides in the AM variants may attribute to varying mechanical properties compared to wrought IN718 but do not contribute to variations between AR, HT1 and HT2 (due to consistency of the oxides between AM variants).

Assessment of the phases confirmed variations between AR, HT1 and HT2. The different microstructures presented are directly linked to the post-manufacturing heat treatment. Given AR did not undergo a heat treatment, melt pool lines are still visible and there is no grain growth or phase precipitation promoted. Alternatively, for HT1 the initial annealing stage of 1065°C for 1 hour provides a stress relief and dissolution of the Laves phase [206], which are presented as discontinuous Laves during FEG-SEM analysis. This section of the heat treatment also promotes homogenisation, recrystallisation and twinning [105] and is evident in microstructural analysis completed as HT1 presents larger more equiaxed grains and higher twin density than AR. Considering the two step aging, the chosen temperatures (760°C, 650°C) that were held for a given length of time (10 hours for both temperatures) act as a γ', γ'' and carbide forming environment. Additionally, 650°C for 10 hours provides the conditions for δ nucleation at γ grain boundaries, with growth occurring at the expense of γ'' [207]. Influence of the implemented two step aging is seen in FEG-SEM analysis where the identification of γ', γ'', carbides, and δ, was confirmed through morphology comparison and EDX [208–210]. This heat treatment was chosen with influence from industry (ASTM AMCoE CMDS) with the aim to improve fatigue performance.

On the other hand, HT2 was implemented with the guidance of industry (ASTM AMCoE) to improve creep performance. Using a lower initial annealing temperature of 955°C for 1 hour still enabled Laves dissolution and stress relief, but the lower temperature enabled rapid precipitation of δ at grain boundaries and inhibited grain growth and recrystallisation [211]. This effect is reflected by the small grain size and low twin density that is consistent with the AR variant. Additionally, the high presence of δ at grain boundaries are notable during FEG-SEM analysis. The quantity (higher) and location (grain boundaries) is as predicted by the heat treatment and a big contrast to HT1 and the non-heat treated variant (AR). Implementation of the two step aging for HT2 (730°C for 8 hours, 635°C for 10 hours) was for γ', γ'' and carbide formation and δ nucleation at γ-grain boundaries at the expense of γ''. The inability to observe γ'' in HT2 during FEG-SEM analysis may be due to the reduced time during the first aging step causing less γ'' to form, overabundance of δ causing Nb depletion and diminished or fine γ'' that cannot be observed on FEG-SEM due to analysis limitations.

Microstructural features discussed in this section directly relate to the varying mechanical properties of the different variants.

8.2 Microhardness

The Vickers microhardness profiles and trends exhibited by the different sample types can be directly linked to the respective microstructure. Low hardness for wrought is likely due to the large grain size compared to the AM samples. Larger grain size means fewer grain boundaries, therefore, less ‘resistance’ when indenting causing a lower hardness value. Consequently, the smaller grain size presented by the AM samples is reflect by an increased hardness value. For AR, HT1, and HT2, the different phase types, quantity, and location, attributes to the variation in hardness between the different AM samples. The presence of carbides and δ is linked to the higher hardness seen in the heat treated samples (HT1, HT2) compared to the non-heat treated sample (AR). Although HT1 and HT2 appear to display similar hardness averages, there is a slight increase for HT2, which is likely due to the increased quantity of carbides and δ along grain boundaries. The increased quantity and location influences the material’s ability to resist pile-up and deformation, hence the increased hardness in HT2 [8,212]. Cao et al. [213], reports an increase in hardness during microhardness testing of different heat treated PBF-LB IN718 samples. Increased hardness was linked to the presence of coherent strain between the matrix and δ, which inhibited the movement of dislocations

Additionally, there is no distinct difference between the vertical and horizontally built PBF-LB samples, which is due to the consistent microstructure between the different build orientations. However, trends between the XY and XZ planes for each build direction for AR, HT1, and HT2, can be observed. For vertical samples, the XY is lower than the XZ, whereas for horizontal samples, the XY is lower or the same compared to the XZ. This is attributed to the larger range in grain size between XY and XZ exhibited by the vertical sample compared to the horizontal sample. However the overall consistency between XY and XZ planes for wrought and PBF-LB samples suggests phase homogeneity throughout the structure.

8.3 Tensile

Interpreting the tensile properties, it is evident that the PBF-LB samples have higher UTS, 0.2% PS, and YS values, but reduced strain to failure when compared to the wrought samples. Superior tensile properties seen in the PBF-LB samples is linked to the microstructural characteristics – grain and phase morphologies. The significantly smaller grain size presented by the PBF-LB material compared to the wrought material leads to an increase in grain boundary area and consequently an increase in tensile properties, but decrease in ductility. Decreased ductility is attributed to the higher presence of Laves and δ phase in PBF-LB samples, compared to wrought.

Similarly, between the different PBF-LB variants, HT1 and HT2 exhibit similar tensile properties (despite the varied heat treatments) which significantly surpass the strength related properties of the non-heat treated PBF-LB variant (AR). The reduction in tensile properties but increased ductility for AR is due to the large, brittle Laves network and lack of γ', γ'', δ and carbides. Furthermore, the increase in strength-based properties, reduction in ductility, and similarity between HT1 and HT2 is likely due to the increased presence of γ', γ'', δ, carbides, and dissolution of Laves phase. Although similar, HT2 (at RT and ET) displays a slightly higher UTS but slightly lower YS, 0.2% PS and strain to failure when compared to HT1. This behaviour is attributed to the increased δ throughout the microstructure, especially at grain boundaries. This is corroborated by research from Choudhary et al. [214] where various heat treatments were applied to tailor the phase composition of PBF-LB IN718. The study found that γ' and γ'' precipitation during double aging significantly enhanced the tensile strength of heat treated PBF-LB IN718, demonstrating an improvement of 23.2%. Additionally, improved properties of the heat treated samples was associated with the dissolved detrimental Laves phases that was present in the non-heat treated condition. However, hardening of the γ matrix and an increased presence of δ at grain boundaries, reduced ductility in the heat treated samples due to pinning effect.

Further assessment of the ET data shows an overall decrease in UTS and Young's modulus when compared to the corresponding samples tested at RT. In addition, when testing at ET, the 0.2% PS and YS increases for wrought and AR samples but decreases for HT1 and HT2 samples. Furthermore, as test temperature increases the strain to failure appears consistent for the wrought variant but decreases for PBF-LB. Alongside the microstructural differences discussed, the variation in ET data compared to RT is also associated with the DSA present during testing.

DSA is a phenomenon observed in several polycrystalline materials including IN718 [215,216]. It is characterised by an increase in strength and decrease in ductility when the material is deformed at intermediate temperatures [216]. This behaviour arises from the interaction between mobile dislocations and diffusing solute atoms, such as carbon, nitrogen and niobium [217]. DSA can be present as different forms:

normal and inverse [218]. The mechanism for normal dynamic strain aging (NDSA) involves solute atoms pinning dislocations, temporarily increasing the material's resistance to further deformation (yield point phenomenon), which can lead to serrated stress-strain curves, otherwise known as the Portevin-Le Chatelier (PLC) effect [219–221]. Alternatively, inverse dynamic strain aging (IDSA) occurs via dislocation unpinning, where solute atoms move away from dislocations as they continue to deform, leading to a decrease in flow stress and increase in strain. As the dislocations are not strongly pinned, the flow stress is decreased due to dislocation motion facilitation by dynamic redistribution of solute atoms. This produces a smoother curve compared to NDSA, with improved ductility due to better accommodation of plastic deformation. Overall, NDSA occurs when critical strain increases with strain rate or decreasing temperature, whereas, for IDSA critical strain increases with temperature or decreasing strain rate [218].

The serrations observed in stress-strain curves during NDSA and IDSA can be categorised into various types based on their appearance and underlying mechanisms, as shown in Figure 119. Type A serrations are typically regular, repeating, well defined drops in stress which are defined by the pinning and unpinning of dislocations by solute atoms. Type B serrations are less regular and pronounced compared to type A due to the more sporadic and less intense pinning and unpinning of dislocations. Type A and type B are usually the most common NDSA serration types seen during tensile testing. Alternatively, the most common IDSA serration type is type C serrations. These are seen to be very irregular, low-amplitude stress drops caused by more diffuse and widespread interaction between dislocations and solute atoms. Alongside common serration types, there are other types such as type D and type E that have been identified. Type D serrations are characterised by a step-like shape on the stress-strain curve, as a result of localised strain bursts. Sometimes, type D serrations can present less step-like (more rounded) behaviour and this could be due to several reasons such as: a gradual stress drop, more dynamic solute diffusion, heterogenous deformation, or interaction with secondary phases. Type E serrations are present as very sporadic and discontinuous stress drops due to irregular interactions between dislocations an solute atoms, caused by heterogenous distribution of solute atoms or varying dislocation densities.

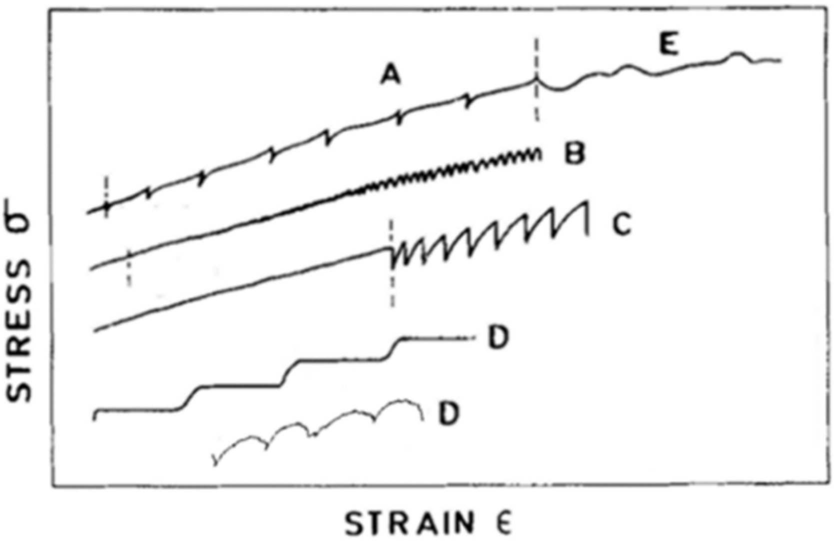

Figure 119: *Schematic of serration types observed during serrated yielding. Adapted from [216].*

Research by Al-lami et al. [222] examined the deformation behaviour of non-heat treated AM IN718 via tensile testing at temperatures of 25, 250, 450, and 650°C with constant strain rates of 10^{-3} and $10^{-4}s^{-1}$. From the tests, they reported serrated flow stress associated with DSA at 250°C and 450°C: 250°C displayed type A at $10^{-3}s^{-1}$ and $10^{-4}s^{-1}$, 450°C displayed type B at $10^{-3}s^{-1}$ and type C at $10^{-4}s^{-1}$. With the utilisation of atom probe tomography (APT) conclusions for the presented DSA types were linked to atom clustering. Serrations at 250°C were linked with increased growth and density of Ti clusters, and an unchanged (compared to room temperature testing) high density of Nb clusters. Alternatively, for 450°C, Ti cluster density was seen to increase again, but Nb cluster density decreased substantially. In addition, the transition from type B to type C serrations at 450°C with a decrease in strain rate was found to align with previous research [217,223,224] which suggests that increased temperature enhances solute diffusion, while lowering strain rates slows dislocation slip, which attributes to stronger solute pinning of dislocations. Consequently, it was inferred that the Ti clustering influenced the DSA at lower strain rates and attributed to the transition to type C serrations. However, further APT research would be needed to confirm this.

For samples tested in this report, it is clear that the wrought material exhibits the most DSA with predominant type B and C serrations, compared to PBF-LB variants where DSA is less severe and exhibited as types D and E. The DSA types observed across the various IN718 samples is indicative of the microstructural homogeneity. The wrought sample exhibits consistent, regularly repeating serrations, whereas the LB-PBF variants display more irregular and sporadic serration patterns. This variation is likely attributed to the greater microstructural uniformity in the wrought material compared to the more heterogeneous nature of the LB-PBF samples.

Mechanical tensile properties exhibited by the tested samples are supported by post-test fractography: the ductile variant (wrought) shows necking with visible reduced cross-sectional area, dimples, and micro voids, whereas the less ductile variants (PBF-LB AR, HT1, HT2) exhibit a flatter fracture surface and a reduced presence of micro voids.

8.4 Small Punch Tensile and Correlation to Uniaxial Tensile Properties

From the SPT results generated in this research, an assessment of maximum force against displacement unveiled several points of interest. Firstly, the AR samples exhibited the greatest anisotropy at RT. This is indicated by the large difference between the vertical and horizontal tests, where the vertically built samples display low ductility but high F_{MAX} and horizontally orientated samples exhibit high ductility and low F_{MAX}. This is due to larger microstructural difference between he XY and XZ plane of the AR. Alternatively, this difference is not as great in the other AM variants, suggesting they are more homogenised.

Secondly, horizontal samples tend to have a lower maximum force and higher ductility compared to vertical counterparts. This is possibly linked to the increased grain boundary pathway for the fracture route compare to vertical samples, as depicted in Figure 40.

Lastly, ET testing reduces maximum force compared to RT testing, which reflects the behaviour seen in the uniaxial tensile tests. This behaviour is seen at ET due to increased dislocation movement and atomic diffusion, causing a drop in resistance.

Assessing the standard force against deflection plots, it can be seen that wrought was the most ductile sample and exhibited the highest F_{MAX}. This makes the wrought material appear superior to PBF-LB. However, it is not until predictions are calculated and account for ductility at F_{MAX} that the wrought material is actually inferior to PBF-

LB in terms of tensile-strength related properties. This reflects the uniaxial data where wrought has the most ductility but reduced tensile-strength properties.

Some other general trends in the force-displacement curves can be seen between the PBF-LB samples. The typical ordering of the ductility and F_{MAX} of the samples aligns with uniaxial tensile results, where HT1 and HT2 appear to have similar properties, where ductility for HT1 and HT2 is lower than the ductility seen for AR, and F_{MAX} is typically higher for HT1 and HT2 compared to AR. However, these trends are not always clear to see within the curves and SPT data until predictions are made, and values d_m and F_{MAX} are considered (e.g. AR vertical at RT).

Further assessment of the force-displacement plots revealed a presence of DSA. This aligns with the DSA displayed in the uniaxial tensile tests. However, the type of DSA seen in SPT is not heavily reported, particularly for IN718, therefore it is assumed that the stress drops seen in SPT reflect the types of DSA seen in uniaxial tensile tests. Especially given that the DSA in SPT presents as repetitive and controlled in wrought but sporadic in the AM variants (as seen in uniaxial tensile). DSA Types B and C for wrought IN718 appear consistent with research on Inconel 625 [225] and Inconel 617 [226].

Post-test fractography analysis exhibited failures that aligned with the collected data, where the most ductile variant (wrought) displayed the least amount of secondary cracking, signifying that the sample ‘stretched’ rather than ‘split/broke’. Alternatively, the least ductile variants (particularly HT2 at 650°C) showed increased secondary cracking.

Following uniaxial tensile and SPT testing, correlation methods were investigated to assess the feasibility and accuracy of mechanical property predictions from SPT, compared to uniaxial tensile results. This assessment is required by industry and research to support the validation and certification of complex or thin components where traditionally sized test specimens would not be applicable. Also, small scale methods reduce waste material and energy, which is an important factor when considering the environment and cost of an AM build.

The UTS and YS prediction methods showed that some general trends and specific samples can be well predicted and aligned with uniaxial results. However, the proposed methods are not fully accurate for all samples and trends. This is likely due to the correlation factors being based on multiple materials rather than IN718 only [135,172]. Additionally, the varying, and often unique, microstructures of the PBF-LB

IN718 samples cannot be applied to the ‘generic’ correlation factors. Consequently, it could be suggested to provide alternative correlation factors for each sample type but this would require a significant amount of additional research and remove the advantage of quick and general formulae that could be used for fast part/material qualification. Additionally, the constants used here were derived from a series of tests at RT, and not ET. Likewise, for the ET correlations it is assumed that there is no DSA present, which may be another reason why the SPT predictions do not fully align with the uniaxial results.

This research does suggest that assessment of vertical SPT to vertical uniaxial tensile is slightly more accurate than comparing horizontal SPT to vertical uniaxial tensile. Particularly for UTS and YS predictions at ET and UTS prediction at RT. Even though vertical SPT to vertical uniaxial tensile is better than horizontal SPT to vertical uniaxial, there is still a maximum percentage difference of 38.6%. On the other hand, horizontal SPT to vertical uniaxial tensile is more accurate for RT YS prediction. This is likely due to the fracture routes between the different planes and orientations, as demonstrated by Figure 40. Additionally, the maximum percentage difference for horizontal SPT to vertical uniaxial tensile is 45.5%.

Overall, most SPT predicted properties follow the same trends exhibited by uniaxial tensile tests. However, to develop a more consistent and accurate method where only one orientation is needed to correlate RT and ET properties, new constants for the equations should be defined or added to account for DSA during ET testing. This would involve further testing completed over a wider range of testing parameters and repeated testing, in order to generate the constants required for accurate correlation.

8.5 Constant Load Creep

Initial constant load creep testing at 650MPa at 625°C, 650°C, and 675°C on wrought IN718 showed that with increasing temperature, there was an increase in the minimum creep rate and a reduction in creep rupture time. This is because at higher temperatures plastic deformation is accelerated due to enhanced dislocation motion and grain boundary weakening causing rapid void formation.

Constant load creep testing displayed results that suggest wrought and HT1 have similar and superior creep resistance properties, compared to inferior properties exhibited by similarly behaving AR and HT2. The resultant creep properties can be linked to the variation in grain size and phases present.

The superior and similar level of creep resistance seen in wrought and HT1 is attributed to different reasons. For the wrought material, attaining the largest grain size (590μm^2) compared to HT1 (465μm^2), AR (196μm^2), and HT2 (179μm^2), enhances creep resistance by reducing the total grain boundary area, thereby limiting creep mechanisms such as Coble and Nabarro-Herring creep. In Coble creep, atomic diffusion along grain boundaries is suppressed with decreased grain boundary area. Whereas, in Nabarro-Herring creep, the increased diffusion distance from larger grains reduces the overall creep rate. Additionally, the larger grain size provides superior ductility, as shown in Figure 84 (and previously discussed in Section 8.3), due the material's ability to experience significantly more plastic strain prior to rupture. This is because at higher temperatures, where dislocation glide and climb are more active, the larger grain size allows for easier dislocation movement across the crystal lattice. Furthermore, the high twin percentage (51.4%) in the wrought IN718 can provide redistribution of stress within the material allowing for accommodation of plastic strain and delay in rupture.

Although HT1 exhibits a larger grain size than AR and HT2, the grain size is still smaller than wrought. Therefore the presence of intra- and inter-granular fine carbides and δ likely contributes to the comparable creep properties of the wrought and HT1 IN718 variants. This is because the carbides and δ phase hinder dislocation movement and impede grain boundary sliding. However, Gao et al. [227] reported that prolonged exposure to high temperatures can result in the interaction of Nb-carbides with environmental elements, particularly oxygen, leading to the formation of brittle niobium oxides at grain boundaries. The presence of these oxides can promote crack initiation and propagation, ultimately reducing creep life. Consequently, at lower applied stress levels, where extended creep life is anticipated, HT1 is expected to exhibit inferior performance compared to the wrought variant. This is attributed to the increased susceptibility of HT1 to form oxides, which may accelerate creep degradation and explain why the trend lines converge in Figure 82 and diverge in Figure 85.

Alternatively, the smaller grain size of AR and HT2 attributes to the inferior creep properties and increased creep rate, compared to wrought and HT1. Additionally, for AR the presence of large, brittle, and incoherent, Laves network acts as an preferential crack initiation and propagation site whilst also facilitating grain boundary sliding and void formation. Also, the lack of γ'' strengthening phase in AR weakens the material and lowers creep resistance. On the other hand, for HT2, the excessive δ phase present causes stress concentration sites, facilitating creep crack initiation, whilst also disrupting grain cohesion and increasing susceptibility to intergranular creep failure. Additionally, the diminished γ'' due to depleted Nb content from excessive δ adversely affects the creep resistance of HT2. Both AR and HT2 reduced creep properties due to microstructural characteristics is reflected by the rapid 1^y and 2^y creep stages in Figure 84 and high creep rate in Figure 85.

For AR and HT2, the faster creep rate and deleterious phase influence can be seen in the post-test cavitation analysis, where AR and HT2 display larger regions of coalesced cavities compared to wrought and HT1, which displays regions of uncoalesced cavitation. Further post-test analysis on the fracture surfaces on the tested samples confirms the more ductile failure of the wrought material through the observation of necking, dimpling and micro voids. Alternatively, the more brittle fractures seen on the PBF-LB samples show flat fractures with little-to-no necking and a fracture morphology resembling a ‘chessboard’ pattern, as seen in the vertical XY EBSD scans (Figure 47). This indicates that the scan strategies implemented, influence cooling rates and resultant dislocation densities and precipitates that influence creep failure mechanism(s) as cavity formation along the grain and thermal morphology of the tested samples resembled the scan-strategy implemented.

Further post-test analysis was completed on wrought and AM IN718 samples via EBSD and FEG-SEM to understand grain and phase change during testing, respectively. Particular assessment of Rx percentage was completed with GOS ≤ 2°, rather than ≤ 5° due to the fine structure of the samples, as demonstrated by the variation in values for the untested samples assessed at ≤ 5° and ≤ 2° e.g AR at ≤ 5° was 80.5% but at ≤ 2° showed 29.7%. The changes to the grain characteristics post-creep test is likely linked to dynamic recrystallisation (DRX). DRX is a mechanism where new grains nucleate and grow during plastic deformation. There are two main types of DRX, continuous dynamic recrystallisation (CDRX) and discontinuous dynamic recrystallisation (DDRX) [192]. CDRX is a gradual process where there is a steady build-up of subgrain boundary misorientation caused by the accumulation of dislocations. The initial gathering of dislocations within the material creates regions of LAGB subgrains. Further accumulation of dislocations at these subgrains causes evolution into HAGBs. Alternatively, DDRX is a more rapid transformation where new grains emerge suddenly through the expansion and migration of HAGBs. Evidence of DDRX can be seen from a large presence of HAGBs and small grains with reduced dislocation density. Both the CDRX and DDRX mechanisms are illustrated in Figure 120.

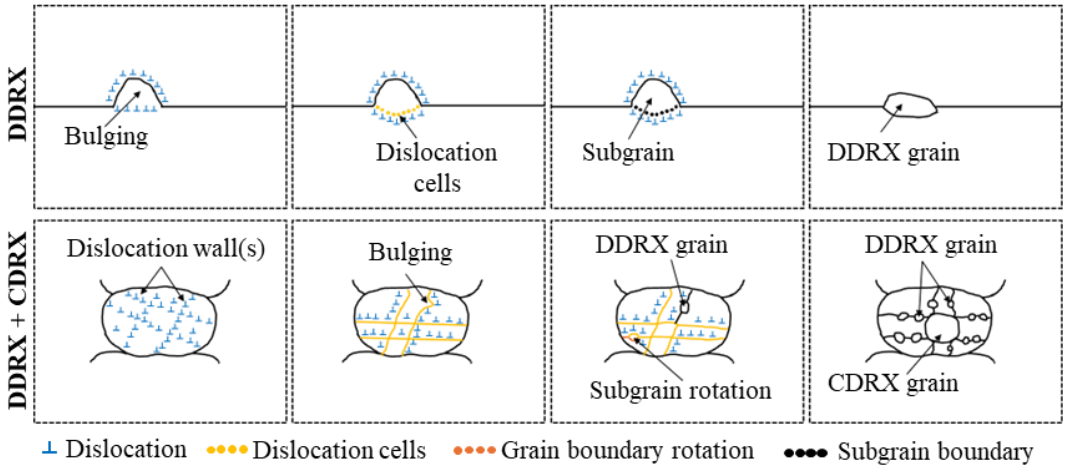

Figure 120: *Schematic to illustrate CDRX and DDRX mechanisms.*

Analysis of the EBSD maps and grain data for wrought IN718 showed that as Rx decreases, grain area decreases, which signifies new, small, and not fully recrystallised grains forming from HAGBs and twin boundaries (TBs). This trend is not followed by the 625MPa test, which could be due to the prolonged length of testing when compared to loads above 625MPa and below 690MPa. Additionally, a decrease in twin density can be seen in the tested samples. Typically as load increases there is a decrease in HAGBs (and increase in LAGBs). This is likely due to HAGBs and TBs acting as nucleation sites for subgrains during DRX. Note that 600MPa does not follow this trend and likely does not due to the extended period of testing time, allowing for more HAGBs and TBs to undergo DRX. It is also noted that the Rx value for untested wrought IN718 samples shows that the material is fully recrystallised, which is a contrast to the least Rxed sample – AR IN718.

The PBF-LB samples show some trends that align with the DRX mechanism. For the AR and HT1 sample, after creep testing there is an increase in LAGBs, decrease in Rx, and reduction in grain size. This is due to the formation of smaller grains during testing and these changes align with the DRX process, as seen in the wrought material. However, the changes are not as drastic for AR and HT1, possibly because of the lower presence of initial HAGBs and TBs in the untested AR and HT1 material compared to the untested wrought material. Alternatively, HT2 shows a decrease in LAGBs and Rx signifying new grains forming with HAGBs, suggesting the onset of DDRX.

The mechanism of DRX has been reported and modelled previously for IN718 [192,228–232]. Research by Jiang et al. [232] investigated how δ phases influenced the hot compression behaviour of IN718. It was found that the δ phase promoted deformation twinning by reducing the stacking fault energy and enhancing stress concentrations, whilst also increasing the DRX grain fraction by 21%, when compared to a δ-free IN718. Alternate research by Hao et al. [192] subjected IN718 specimens with different rolling percentages to creep tests at 660°C and 690MPa. Analysis via EBSD revealed both CDRX and DDRX had occurred, particularly DDRX in the higher rolling percentage. It was found that the coherent twin boundaries tended to transform into incoherent boundaries during creep, making them more susceptible to migration and nucleation for Rx. Consequently, the IN718 sample containing more coherent twin boundaries experienced higher DRX.

Although research regarding DRX has been reported, particularly for conventionally manufactured IN718, the research for this thesis for DRX and phase changes requires further investigation – as discussed in the ‘Future Work’ section.

Alongside the grain characteristic changes, the changes in phases can be observed. Comparing FEG-SEM images of post-test samples to pre-tested samples it is possible that the wrought IN718 experiences δ growth. For HT1 and HT2, there is possible δ growth and presence of enlarged carbides. Possible phase coarsening during testing aligns with some previous research [233,234]. Alternatively, for AR, the phases appear largely unchanged with a calculated Laves volume fraction of 5.39 ±0.63%, compared to untested with a Laves volume fraction of 4.39 ±0.92%. The slight increase seen in the tested AR sample is likely due to sample variation or limitations of analysis via ImageJ where areas of cavitation may appear similar to Laves area, and although these were attempted to be mitigated from calculations, an influence may still be present.

Based on this discussion section, the trend between IN718 variants and their respective creep properties was not as expected, as HT2 was implemented to improve creep performance.

8.6 Small Punch Creep and Correlation of Constant Load Creep to Small Punch Creep

The superiority of the wrought sample displayed by SPC tests suggests that grain size remains one of the most significant influencing factors. However, the trends seen by the vertical PBF-LB variants do not follow this assumption. Consequently, the small scale testing would suggest that the phase type, quantity, and distribution, plays a larger role in creep resistance. For example, HT2 SPC vertical samples were superior to other PBF-LB samples even though HT2 presents a smaller grain size (compared to HT1). This would suggest that the phases, particularly δ and carbides present at grain boundaries have improved creep resistance, providing resistance to grain boundary creep mechanisms. Resistance to creep was also seen in the cavitation analysis where HT2 at 450N presented the most uncoalesced cavities, compared to HT1 and AR where failure appeared via mostly coalesced cavities.

The trends seen in PBF-LB horizontal SPC results show similarity to trends seen in traditional constant load creep testing, where the ordering of time to rupture for a particular load aligns with the ordering presented for the traditional creep tests. This corroborates with theory that horizontal small scale aligns with vertical full-sized tests, as shown in Figure 40. However, due to the lack of data for the horizontal results, a correlation method was not supplied in this thesis.

Variation in the responses of the vertical and horizontal SPC tests compared to uniaxial creep tests is likely due to the failure response during testing. Whilst traditional creep testing is considered uniaxial in the tensile direction. SPC testing is a compressive biaxial mechanism. Although SPC can be an effective tool for analysing creep properties when analysing complex components where traditional samples cannot be obtained. It should be important to consider than the mechanism of failure between SPC and uniaxial creep may not be a direct comparison and will require future work.

8.7 Strain Control Low Cycle Fatigue

An overall assessment of the LCF data suggests that for strain amplitude compared to number of cycles to failure, there is similarity between the different variants and minimal scatter. It is only when stabilised stress range is considered that a clear indication of superiority is seen, where HT1 is typically the best, followed by HT2, AR, and then wrought. However, focussing on the 0.5% strain amplitude tests, the increased stress range for HT1 may not justify the decreased number of cycles to failure (when compared to HT2). Overall, the general trend of best performance does not follow the trend of grain size where AR is the smallest (89μm^2), followed by HT1 (101μm^2), HT2 (166μm^2), and wrought (193μm^2). This is likely due to the influence of secondary phases and precipitates. Given the wrought material appears the most inferior, this would likely be associated with the coarse grain size, providing fewer grain boundaries for dislocation resistance. Alternatively, for the AR, the small grain size although appears to be slightly superior to wrought, it appears to be outweighed by the presence of brittle Laves network, causing deleterious properties compared to HT1 and HT2. Therefore, although HT1 and HT2 consist of grains larger than AR, the combination of δ, γ’, and γ’’ phases result in an improved fatigue performance.

Focussing on the maximum and minimum stress plots for 0.5% strain amplitude tests it indicates that all samples undergo cyclic softening immediately, particularly for the wrought variant. The RT data indicates the HT1 sample experiences the highest stress range and fails in the fewest cycles, followed closely by HT2, which endures slightly less stress but lasts significantly longer. AR and wrought samples exhibit lower stress ranges than HT1 and HT2, with AR outperforming wrought in both stress range and fatigue life. On the other hand, at ET all samples see a decrease in maximum and minimum stress but the difference in this stress range from RT to ET varies between sample type. Wrought and AR only decrease by 101MPa and 139MPa, respectively, compared to HT1 and HT2 which decrease by 428MPa and 385MPa, respectively. Also, at ET the wrought and HT2 materials display a higher number of cycles to failure compared to AR at RT.

Observations of the first and stabilised loops show that the wrought material has a much larger plastic strain range compared to the PBF-LB samples. For RT testing the AR and wrought materials undergo some cyclic hardening, whereas HT1 and HT2 undergo slight cyclic softening. Alternatively, for ET testing, all variants show cyclic softening.

Additionally, the first hysteresis loops for RT and ET testing for wrought shows stress drop(s) approaching the strain amplitude and an ‘overshoot’ where the specified strain amplitude is exceeded. This behaviour is linked to DSA and is rectified by the software during subsequent cycles. DSA behaviours are not noted in any of the PBF-LB samples. This could be due to the type of DSA presented by the wrought variant (type B and C) compared to the PBF-LB variants (type D and E) [235,236]. Additionally, the initial softening of the wrought material, which is not seen (as drastically) in the AM material, aligns with the theory of accumulation of dislocations and formation of slip bands, leading to regions of localised plastic deformation.

The failure of all samples LCF tested were not linked to any singular defects such as gas-pores or lack of fusion, but rather associated with typical surface or near sub-surface features. Wrought material exhibited a singular origin with clear crack propagation and failure regions compared to the PBF-LB samples which exhibited multiple initiation zones with non-uniform crack propagation and failure regions. This is likely due to the inhomogeneous microstructure of the PBF-LB samples, compared to the homogenous microstructure of the wrought IN718. It is also noted that not all micro-features such as striations were available for analysis due to the compressive nature of the R=-1 loading regime.

Overall, it is considered that PBF-LB HT1 would be the preferred choice for components exposed to stress-fatigue, whereas HT2 would be the preferred choice for components exposed to strain-fatigue. This suggests that although the influence of the HT to improve fatigue properties (HT1) was not as extensive as expected, it can still be considered as slightly improved compared to HT2. Overall, implementing the heat treatments improved properties compared to AR and also the wrought IN718 variant.

9 Conclusion

This project evaluated the influence of post-processing HT routes on the microstructural evolution and mechanical behaviour of IN718 fabricated via PBF-LB. The objective was to enhance the alloy's resistance to fatigue (HT1) and creep (HT2). From the investigation, the following conclusions can be drawn:

- PBF-LB samples fabricated utilising a chessboard strategy produced samples with near-full density (≥ 99.8%) with minimal porosity and manufacturing defects, validating the AM process, non-necessity for HIP, and optical porosity analysis at this research level.
- Microstructural assessment confirmed differences between wrought and PBF-LB IN718 samples. Wrought IN718 presented an isotropic structure with equiaxed grains, high twin density (51.4%), large carbides, and fine δ phase. Alternatively, AR PBF-LB IN718 displayed anisotropic features, no texture, and Laves network (4.39%). Minor differences, that were not considered substantial, between vertical and horizontal samples were noted due to varying locations on the build height. Variation from wrought to AR caused an increase in hardness and tensile strength properties but decrease in ductility for the AR samples.
- The HT1 route, involving annealing and two sequential aging steps of 10 hours each, induced pronounced microstructural modifications relative to the AR condition. Notably, there was a large increase in twin density and a twofold increase in average grain size. Alternatively, HT2 which involved a lower annealing temperature and decreased the time and temperature aging cycle, yielded a microstructure resembling that of AR in terms of grain morphology and texture but introduced grain boundary precipitates such as Nb-rich carbides, δ phase, and dissolved Laves phase. These features contributed to an improvement in hardness – HT2 demonstrated a 32% increase compared to AR despite negligible changes in grain size.
- Both HTs significantly enhanced the yield and UTS by roughly 200-500MPa relative to the AR condition, albeit at the expense of ductility.
- ET tensile testing displayed DSA phenomena across all material variants but manifested more consistently and intensely in the wrought (designated as types B and C) than the PBF-LB variants (types D and E). This disparity is attributed to the higher prevalence of secondary precipitates, such as γ'' and δ, which are known to obstruct

dislocation motion and thereby influence the characteristic serrated flow behaviour during deformation. Additionally, DSA was linked to the ‘overshoot’ and serrated yielding observed in wrought LCF testing.

- For a given strain amplitude during LCF testing, all variants showed similar cycles to failure. However, stabilised stress range clearly differentiated performance: HT1 exhibited the highest, followed by HT2, AR, and then wrought. At 0.5% strain amplitude HT2 offered a better balance between stress range and fatigue life than HT1, which experienced much earlier failure despite only a slight increase in stress. Overall, improved fatigue resistance in HT samples was linked to the presence of strengthening phases (γ’, γ’’ and δ) along with reduced grain size compared to wrought. AR presented smaller grains than wrought but the deleterious Laves phase contributed to reduced fatigue performance compared to HT AM variants.
- Creep testing revealed HT1 and wrought material exhibited superior performance compared to AR and HT2. This was primarily associated with coarser grain structure displayed by wrought and HT2, which inhibited grain boundary sliding and voids. Alternatively, inferior creep resistance of AR and HT2 was likely linked to finer grains, and the presence of brittle Laves and δ phase. While both HT1 and wrought displayed similar creep behaviour, wrought exhibited improved ductility due to its ability to activate more slip systems. In contrast, micro-twinning was the dominant deformation mode in PBF-LB materials.
- Post-creep analysis revealed evidence of CDRX and DDRX. Dominance of the DRX mechanism was dictated by material condition. HT2 displayed characteristics associated with DDRX e.g. new HAGBs. Whereas HT1 and AR displayed CDRX characteristics e.g. increased LAGBs and finer grains.
- In summary, the HT1 HT shows considerable promise for enhancing fatigue resistance in PBF-LB IN718. Although HT2 offered modest improvements in hardness and tensile strength, its impact on creep resistance was limited, rendering it less effective overall. Nevertheless, HT2 demonstrated comparable tensile and somewhat similar LCF characteristics to HT1, suggesting possible utility in applications where creep resistance is less critical.
- SPT predicted properties showed some good alignment with uniaxial tensile trends, yet accuracy was limited due to the generalised correlation constant not tailored

for IN718 or AM specific structures. For this research, vertical SPT to vertical uniaxial tensile appeared the most reliable method.

- SPC suggested, based on ordering of creep life, that horizontal SPC would be best to correlate to vertical uniaxial creep results. Given only few tests were conducted for horizontal AM and wrought samples, correlation methods were not implemented. Consequently, future work suggestions are presented for this aspect of the study.

10 Key Findings

This study has comprehensively assessed the high-temperature performance of PBF-LB IN718 subjected to two distinct post-manufacture heat treatments, in comparison with both AR PBF-LB and conventionally wrought material. Key findings and outcomes from this investigation are:

1. Reported and analysed mechanical behaviour at room and elevated temperature of wrought and PBF-LB IN718: Observations in trends for tensile, fatigue, and SPT, have been observed at RT and ET, alongside creep testing at ET and hardness assessment at RT. These assessments have been carried out on wrought and AM IN718 (under different HT conditions). The production of this data will support and aid the scientific and industrial AM community for data generation for standardisation.
2. Shown the influence of varying heat treatment on the microstructural and mechanical properties of PBF-LB IN718 and need for further research: as briefly mentioned, the HTs chosen for implementation for HT1 and HT2 were designed and suggested through ASTM AMCoE following guidelines from AMS5662-5664. Considering that the chosen heat treatments are typically implemented for conventional material, it suggests that the initial microstructure of the additive material has not been considered e.g. maintained grain size, initial residual stresses, and variation in elemental segregation. Although the effect of the heat treatment has acted as it would for a conventional material (δ growth, grain growth at 1065°C, etc), it is considered that mechanical outcomes may not be as predicted due to the 'starting' additive microstructure. Consequently, this highlights the need for heat treatments specific for additive material, where the initial microstructure is considered.
3. Proved that if optimised parameters (machine and powder) are used then HIP is not needed: Given that no failures were singularly caused by internal defects such as gas porosity, LoF, and keyholing. This adds to the additive community discussion as to whether HIP is or is not needed for AM components if parameters are optimised for low porosity. Particularly because these samples did not undergo any HIP or stress-relieving.
4. Small scale testing provides an effective option for testing complex components where full size mechanical testing is not feasible. For this project, SPC

and SPT results showed similar trends in terms of ordering of superiority and properties (e.g. DSA presence and ductility). However, the correlation between SPT and SPC generated results with uniaxial properties did not appear to be reliable to the degree that would be necessary for industrial application. Consequently, further research into IN718 AM specific constants for empirical correlation and further testing on more samples is suggested.

5. Provided insight into some final areas for improvement with regards to standardising and best practices: 1) etching methods specifically for AM structures for grain and phase analysis 2) 2D porosity analysis procedures specific for AM 3) phase quantification procedures and limits for fine constituents 4) limits for grain characteristics e.g. GOS 5) AM specific HT routes 6) novel techniques such as SPC and SPT for trends or correlation 7) practices for formatting and reporting data for universal collaboration and understanding.

11 Future Work

Although research within this thesis provides some discussion and data to inform gaps within the additive manufacturing landscape, some specific improvements for this PhD project, if extra time and expenses were available, include:

- Testing horizontally built samples uniaxially to support small scale results and provide a comparison to the vertical data presented in this work. This will help generate correlation constants for small scale testing and provided a basis to assess whether build orientation influences mechanical properties or is influenced differently by heat treatments compared to vertically built samples.
- Conducting transmission electron microscopy and x-ray diffraction analysis to confirm the small phases such as γ’, γ’’, and δ, rather than rely on previous literature and EDX that might not show significant/accurate chemical differences for more robust conclusions.
- Including possible analysis such as neutron diffraction to quantify phases by volume percentage as it would also allow for specific phase quantities rather than qualitative analysis. This will aid the understanding of the influence of HTs on the phase quantities to support HT selection for AM IN718 and provide a more quantitative comparison to link to the mechanical properties presented by different microstructures with different phase quantities.
- Utilise this data for larger research into different heat treatments for additive components in order to fully understand process-structure-property relationships, the need (or not) for HIP, and machine-to-machine variation.
- Complete in-situ creep testing, monitoring or interrupted creep tests to assess the mechanism of DRX in more detail. This would enable analysis of the mechanism at different stages in order to understand how it evolves during creep exposure.

12 References

[1] Vafadar A, Guzzomi F, Rassau A, Hayward K. Advances in Metal Additive Manufacturing: A Review of Common Processes, Industrial Applications, and Current Challenges. Applied Sciences 2021;11. https://doi.org/10.3390/app11031213.

[2] Bhatia A, Sehgal AK. Additive manufacturing materials, methods and applications: A review. Mater Today Proc 2023;81:1060–7. https://doi.org/10.1016/J.MATPR.2021.04.379.

[3] Nabavi SF, Dalir H, Farshidianfar A. A comprehensive review of recent advances in laser powder bed fusion characteristics modeling: metallurgical and defects. The International Journal of Advanced Manufacturing Technology 2024;132:2233–69. https://doi.org/10.1007/s00170-024-13491-1.

[4] Chaudhari SB, Wakchaure VD. A Comprehensive Review on the High-Temperature Behavior of Additively Manufactured Inconel 718. In: Mallaiah M, Thapliyal S, Bose SC, editors. Recent Advances in Additive Manufacturing, Springer Singapore; 2024, p. 439–524. https://doi.org/10.1007/978-981-97-6016-9_34.

[5] Jiang C-P, Masrurotin, Wibisono AT, Macek W, Ramezani M. Enhancing Internal Cooling Channel Design in Inconel 718 Turbine Blades via Laser Powder Bed Fusion: A Comprehensive Review of Surface Topography Enhancements. International Journal of Precision Engineering and Manufacturing 2024;26:487–511. https://doi.org/10.1007/s12541-024-01177-3.

[6] Goulmy JP, Kaminski M, Leroy FH, Kanoute P. A probabilistic model to consider scale and gradient effects in the prediction of the fatigue life of Inconel 718 for turbine disk application. Eng Fract Mech 2025;320. https://doi.org/10.1016/j.engfracmech.2025.111086.

[7] Hamdi H, Abedi HR. Thermal stability of Ni-based superalloys fabricated through additive manufacturing: A review. Journal of Materials Research and Technology 2024;30:4424–76. https://doi.org/10.1016/j.jmrt.2024.04.161.

[8] Tucho WM, Ohm BA, Canizalez SAP, Egeland A, Mildt MB, Nedreberg ML, et al. Effects of δ Phase and Annealing Twins on Mechanical Properties and Impact Toughness of L-PBF Inconel 718. Journal of Manufacturing and Materials Processing 2024;8. https://doi.org/10.3390/jmmp8040135.

[9] Volpato GM, Tetzlaff U, Fredel MC. A comprehensive literature review on laser powder bed fusion of Inconel superalloys. Addit Manuf 2022;55. https://doi.org/10.1016/J.ADDMA.2022.102871.

[10] Ajay P, Dabhade V V. Heat treatments of Inconel 718 nickel-based superalloy: A Review. Metals and Materials International 2025;31:1204–31. https://doi.org/10.1007/s12540-024-01812-8.

[11] Teixeira Ó, Silva FJG, Atzeni E. Residual stresses and heat treatments of Inconel 718 parts manufactured via metal laser beam powder bed fusion: an overview. The International Journal of Advanced Manufacturing Technology 2021;113:3139–62. https://doi.org/10.1007/s00170-021-06835-8.

[12] Ran R, Wang Y, Zhang Y, Fang F, Xia Y, Zhang W, et al. Two-stage annealing treatment to uniformly refine the microstructure, tailor δ precipitates and improve tensile properties of Inconel 718 alloy. J Alloys Compd 2022;927. https://doi.org/10.1016/j.jallcom.2022.166820.

[13] Fayed EM, Saadati M, Shahriari D, Brailovski V, Jahazi M, Medraj M. Effect of homogenization and solution treatments time on the elevated-temperature mechanical behavior of Inconel 718 fabricated by laser powder bed fusion. Sci Rep 2021;11. https://doi.org/10.1038/s41598-021-81618-5.

[14] Xu L, Chai Z, Peng B, Zhou W, Chen X. Effect of heat treatment on microstructures and mechanical properties of Inconel 718 additively manufactured using gradient laser power. Materials Science and Engineering: A 2023;868. https://doi.org/10.1016/j.msea.2023.144754.

[15] Lerda S, Bassini E, Marchese G, Biamino S, Ugues D. Rapid L-PBF printing of IN718 coupled with HIP-quench: A novel approach to manufacture and heat treatment of a nickel-based alloy. Journal of Materials Research and Technology 2024;30:6983–94. https://doi.org/10.1016/j.jmrt.2024.05.128.

[16] Lam MC, Koumpias A, Haselhuhn AS, Wessman A, Tin S. An additively manufactured IN718 strengthened by CSL boundaries with high-temperature tensile and short-term creep resistance up to 800°C. Materials Science and Engineering: A 2025;922. https://doi.org/10.1016/j.msea.2024.147654.

[17] Rezaei A, Rezaeian A, Kermanpur A, Badrossamay M, Foroozmehr E, Marashi M, et al. Microstructural and mechanical anisotropy of selective laser melted IN718 superalloy at room and high temperatures using small punch test. Mater Charact 2020;162. https://doi.org/10.1016/J.MATCHAR.2020.110200.

[18] Wang X, Xu L, Zhao L, Han Y, Liu Z. Defect-based additive manufactured creep performance evaluation via small punch test. Int J Mech Sci 2024;279. https://doi.org/10.1016/j.ijmecsci.2024.109565.

[19] Balaji D, Ranga J, Bhuvaneswari V, Arulmurugan B, Rajeshkumar L, Manimohan MP, et al. Additive Manufacturing for Aerospace from Inception to Certification. J Nanomater 2022. https://doi.org/10.1155/2022/7226852.

[20] Venturi F, Taylor R. Additive Manufacturing in the Context of Repeatability and Reliability. J Mater Eng Perform 2023. https://doi.org/10.1007/s11665-023-07897-3.

[21] Srinivasan D. Challenges in Qualifying Additive Manufacturing for Turbine Components: A Review. Transactions of the Indian Institute of Metals 2021;74:1107–28. https://doi.org/10.1007/s12666-021-02199-5.

[22] Frazier WE. Metal Additive Manufacturing: A Review. J Mater Eng Perform 2014;23. https://doi.org/10.1007/s11665-014-0958-z.

[23] Wohlers Associates. What is Additive Manufacturing? 2022. https://wohlersassociates.com/terminology-and-definitions/additive-manufacturing/ (accessed September 22, 2022).

[24] Hosseini E, Popovich VA. A review of mechanical properties of additively manufactured Inconel 718. Addit Manuf 2019;30:100877. https://doi.org/10.1016/J.ADDMA.2019.100877.

[25] Bandyopadhyay A, Zhang Y, Bose S. Recent developments in metal additive manufacturing. Curr Opin Chem Eng 2020;28:96–104. https://doi.org/10.1016/J.COCHE.2020.03.001.

[26] ASTM International. ISO/ASTM 52900: Additive manufacturing - General principles - Fundamentals and vocabulary 2021:1–14.

[27] Wohlers Associates. The Seven AM Processes 2022. https://wohlersassociates.com/terminology-and-definitions/the-seven-am-processes/ (accessed September 22, 2022).

[28] de Pastre MA, Quinsat Y, Lartigue C. Effects of additive manufacturing processes on part defects and properties: a classification review. International Journal on Interactive Design and Manufacturing (IJIDeM) 2022;16:1471–96. https://doi.org/10.1007/S12008-022-00839-8.

[29] Bandyopadhyay A, Traxel KD, Lang M, Juhasz M, Eliaz N, Bose S. Alloy design via additive manufacturing: Advantages, challenges, applications and perspectives. Materials Today 2022;52:207–24. https://doi.org/10.1016/J.MATTOD.2021.11.026.

[30] Ramesh Kumar S, Srinivas V, Jagan Reddy G, Raghavender Rao M, Raghu T. 3D Printing of Fuel Injector in IN718 Alloy for Missile Applications. Transactions of the Indian National Academy of Engineering 2021 6:4 2021;6:1099–109. https://doi.org/10.1007/S41403-021-00253-8.

[31] Salmi M. Additive Manufacturing Processes in Medical Applications. Materials 2021;14:191. https://doi.org/10.3390/ma14010191.

[32] Yadroitsev I, Yadroitsava I, Du Plessis A. Basics of Laser Powder Bed Fusion. Fundamentals of Laser Powder Bed Fusion of Metals 2021:15–28. https://doi.org/https://doi.org/10.1016/B978-0-12-824090-8.00024-X.

[33] Brennan M, Keist JS, Palmer TA. Defects in Metal Additive Manufacturing Processes. In: Bourell D, Frazier W, Seifi M, editors. Additive Manufacturing Processes, vol. 24, ASM International; 2020, p. 277–86. https://doi.org/10.31399/asm.hb.v24.a0006557.

[34] Deloitte. Challenges of Additive Manufacturing: Why companies don’t use Additive Manufacturing in serial production 2019.

[35] Wohlers T, Mostow N, Campbell I, Diegel O, Kowen J, Fidan, et al. Wohlers Report 2022. Washington, DC: Wohlers Associates; 2022.

[36] Blakey-Milner B, Gradl P, Snedden G, Brooks M, Pitot J, Lopez E, et al. Metal additive manufacturing in aerospace: A review 2021. https://doi.org/10.1016/j.matdes.2021.110008.

[37] Dordlofva C. A Design for Qualification Framework for the Development of Additive Manufacturing Components-A Case Study from the Space Industry 2020. https://doi.org/10.3390/aerospace7030025.

[38] EWI. What Is Powder Bed Fusion? 2022. https://ewi.org/capabilities/additive-manufacturing/what-is-powder-bed-fusion/ (accessed July 11, 2022).

[39] Park JH, Bang GB, Lee KA, Son Y, Song YH, Lee BS, et al. Effect of Preheating Temperature on Microstructural and Mechanical Properties of Inconel 718 Fabricated by Selective Laser Melting. Metals and Materials International 2022;28:2836–48. https://doi.org/10.1007/S12540-022-01169-W/FIGURES/13.

[40] Stephanie Hendrixson. AM 101: Powder Bed Fusion (PBF) 2022. https://www.additivemanufacturing.media/articles/am-101-powder-bed-fusion-pbf (accessed July 11, 2022).

[41] TWI Ltd. What Is Powder Bed Fusion? Process Definition and Advantages 2022. https://www.twi-global.com/technical-knowledge/faqs/what-is-powder-bed-fusion (accessed July 11, 2022).

[42] Tang H, Qian M, Liu N, Zhang X, Yang G, Wang J. Effect of Powder Reuse Times on Additive Manufacturing of Ti-6Al-4V by Selective Electron Beam Melting. The Journal of the Minerals, Metals and Mining Society 2015;67. https://doi.org/10.1007/s11837-015-1300-4.

[43] Wang L, Yu A, Li E, Shen H, Zhou Z. Effects of spreader geometry on powder spreading process in powder bed additive manufacturing. Powder Technol 2021;384:211–22. https://doi.org/10.1016/j.powtec.2021.02.022.

[44] Williams N, Whittaker P, Craxford J. LEAP 71 successfully tests innovative AI-designed Aerospike engine. Ionvar Communications Ltd 2025.

[45] Zhao Y, Aoyagi K, Daino Y, Yamanaka K, Chiba A. Significance of powder feedstock characteristics in defect suppression of additively manufactured Inconel 718. Addit Manuf 2020;34:101277. https://doi.org/10.1016/J.ADDMA.2020.101277.

[46] Popovich A, Sufiiarov V. Metal Powder Additive Manufacturing. New Trends in 3D Printing, InTech; 2016, p. 215–36. https://doi.org/10.5772/63337.

[47] Dunkley JJ. Metal Powder Atomisation Methods for Modern Manufacturing. Johnson Matthey Technology Review 2019;63:226–32. https://doi.org/10.1595/205651319X15583434137356.

[48] Popov V V., Grilli ML, Koptyug A, Jaworska L, Katz-Demyanetz A, Klobčar D, et al. Powder Bed Fusion Additive Manufacturing Using Critical Raw Materials: A Review. Materials 2021;14. https://doi.org/10.3390/ma14040909.

[49] Ruan G, Liu C, Qu H, Guo C, Li G, Li X, et al. A comparative study on laser powder bed fusion of IN718 powders produced by gas atomization and plasma rotating electrode process. Materials Science and Engineering: A 2022;850. https://doi.org/10.1016/J.MSEA.2022.143589.

[50] Wu Z, Yarasi SR, Mostafaei A, Rollett AD. Powder Characterization for Metal Additive Manufacturing. Additive Manufacturing Processes, vol. 24, ASM International; 2020, p. 172–9. https://doi.org/10.31399/asm.hb.v24.a0006568.

[51] Vock S, Klöden B, Kirchner A, Weißgärber T, Kieback B. Powders for powder bed fusion: a review. Progress in Additive Manufacturing 2019;4:383–97. https://doi.org/10.1007/S40964-019-00078-6/TABLES/3.

[52] ASTM International. ASTM B213-20: Standard Test Methods for Flow Rate of Metal Powders Using the Hall Flowmeter Funnel 2020:1–4. https://doi.org/10.1520/B0213-20.

[53] ASTM International. ASTM B527-22: Standard Test Method for Tap Density of Metal Powders and Compounds 2023:1–4. https://doi.org/10.1520/B0527-22.

[54] Moghimian P, Poirié T, Habibnejad-Korayem M, Zavala JA, Kroeger J, Marion F, et al. Metal powders in additive manufacturing: A review on reusability and recyclability of common titanium, nickel and aluminum alloys. Addit Manuf 2021;43:102017. https://doi.org/10.1016/J.ADDMA.2021.102017.

[55] Kirka MM. Additive Manufacturing of Nickel-Base Superalloys. In: Bourell D, Frazier W, Kuhn H, Seifi M, editors. Additive Manufacturing Processes, vol. 24, ASM International; 2020, p. 339–45. https://doi.org/10.31399/asm.hb.v24.a0006582.

[56] Yi F, Zhou Q, Wang C, Yan Z, Liu B. Effect of powder reuse on powder characteristics and properties of Inconel 718 parts produced by selective laser melting. Journal of Materials Research and Technology 2021;13:524–33. https://doi.org/10.1016/j.jmrt.2021.04.091.

[57] Soltani-Tehrani A, Shamsaei N, Surya AV, Mallory J, Ramakrishnan R. Powder Reuse Effects on the Tensile Behavior of Additively Manufactured Inconel 718 Parts. Solid Freeform Fabrication 2021: Proceedings of the 32nd Annual International Solid Freeform Fabrication Symposium – An Additive Manufacturing Conference Reviewed Paper, University of Texas at Austin; 2021. https://doi.org/10.26153/TSW/17617.

[58] Paccou E, Mokhtari M, Keller C, Nguejio J, Lefebvre W, Sauvage X, et al. Investigations of powder reusing on microstructure and mechanical properties

of Inconel 718 obtained by additive manufacturing. Materials Science and Engineering: A 2021;828. https://doi.org/10.1016/j.msea.2021.142113.

[59] Srinivasan D, Ananth K. Recent Advances in Alloy Development for Metal Additive Manufacturing in Gas Turbine/Aerospace Applications: A Review. Journal of the Indian Institute of Science 2022 102:1 2022;102:311–49. https://doi.org/10.1007/S41745-022-00290-4.

[60] Cooke S, Ahmadi K, Willerth S, Herring R. Metal additive manufacturing: Technology, metallurgy and modelling. J Manuf Process 2020;57:978–1003. https://doi.org/10.1016/J.JMAPRO.2020.07.025.

[61] Sanchez S, Smith P, Xu Z, Gaspard G, Hyde CJ, Wits WW, et al. Powder Bed Fusion of nickel-based superalloys: A review. Int J Mach Tools Manuf 2021;165. https://doi.org/10.1016/J.IJMACHTOOLS.2021.103729.

[62] Catchpole-Smith S, Aboulkhair N, Parry L, Tuck C, Ashcroft IA, Clare A. Fractal scan strategies for selective laser melting of ‘unweldable’ nickel superalloys. Addit Manuf 2017;15:113–22. https://doi.org/10.1016/J.ADDMA.2017.02.002.

[63] Bhadeshia HKDH. Nickel Based Superalloys. University of Cambridge n.d. https://www.phase-trans.msm.cam.ac.uk/2003/Superalloys/superalloys.html (accessed September 27, 2022).

[64] Callister WD, Rethwisch DG. Materials Science and Engineering. vol. 9. 9th ed. Singapore: John Wiley & Sons; 2015.

[65] Pollock TM, Tin S. Nickel-Based Superalloys for Advanced Turbine Engines: Chemistry, Microstructure and Properties. Journal of Propulsion and Power 2006;22:361–74. https://doi.org/10.2514/1.18239.

[66] Jena AK, Chaturvedi MC. The role of alloying elements in the design of nickel-base superalloys. J Mater Sci 1984;19:3121–39. https://doi.org/10.1007/BF00549796.

[67] Sashank SS, Rajakumar S, Karthikeyan R, Nagaraju DS. Weldability, Mechanical Properties and Microstructure of Nickel Based Super Alloys: a review n.d. https://doi.org/10.1051/e3sconf/202018401040.

[68] Nezhadfar PD, Johnson AS, Shamsaei N. Fatigue behavior and microstructural evolution of additively manufactured Inconel 718 under cyclic loading at elevated temperature. Int J Fatigue 2020;136. https://doi.org/10.1016/j.ijfatigue.2020.105598.

[69] Wu Y, Li C, Xia X, Liang H, Qi Q, Liu Y. Precipitate Coarsening and its Effects on the Hot Deformation Behaviour of the Recently Developed y’ strengthened Superalloys. Journal of Materials Science & Technology 2021;67:95–104.

[70] Barker JF. The Initial Years of Alloy 718 - A G.E. Perspective. The Minerals, Metals & Materials Society 1989:269–77.

[71] Qi H, Azer M, Ritter A. Studies of Standard Heat Treatment Effects on Microstructure and Mechanical Properties of Laser Net Shape Manufactured INCONEL 718. The Minerals, Metals & Materials Society and ASM International 2009 2009;40A. https://doi.org/10.1007/s11661-009-9949-3.

[72] Radha CH, Shna K, Rao KP. The formation and control of Laves phase in superalloy 718 welds. JOURNAL OF MATE RIALS SCIENCE 1997;32:1977–84.

[73] Special Metals INCONEL® Alloy 718 n.d. https://www.matweb.com/search/DataSheet.aspx?MatGUID=94950a2d209040a09b89952d45086134&ckck=1 (accessed February 21, 2023).

[74] Xu J, Ma T, Peng RL, Hosseini S. Effect of post-processes on the microstructure and mechanical properties of laser powder bed fused IN718 superalloy. Addit Manuf 2021;48:102416. https://doi.org/10.1016/J.ADDMA.2021.102416.

[75] DuPont JN, Lippold JC, Kiser SD. Welding Metallurgy and Weldability of Nickel-Base Alloys. New Jersey: John Wiley & Sons Inc. ; 2009.

[76] Radavich JF. Superalloy 718 - Metallurgy and Applications: The Physical Metallurgy of Cast and Wrought Alloy 718. The Minerals, Metals & Materials Society 1989:229–40.

[77] Sjöberg G. Casting Superalloys for Structural Applications. The Minerals, Metals & Materials Society 2010:117–30.

[78] Maj P, Adamczyk-Cieslak B, Slesik M, Mizera J, Pieja T, Sieniawski J, et al. The Precipitation Processes and Mechanical Properties of Aged Inconel 718 Alloy After Annealing. Archives of Metallurgy and Materials 2017;62:1695–702. https://doi.org/10.1515/amm-2017-0259.

[79] Bryndza G, Tchuindjang JT, Chen F, Habraken AM, Sepúlveda H, Tuninetti V, et al. Review of the Microstructural Impact on Creep Mechanisms and Performance for Laser Powder Bed Fusion Inconel 718. Materials 2025;18. https://doi.org/10.3390/ma18020276.

[80] Anbarasan N, Gupta BK, Prakash S, Muthukumar P, Oyyaravelu R, Kumar RJF, et al. Effect of Heat Treatment on the Microstructure and Mechanical Properties of Inconel 718. Mater Today Proc 2018;5:7716–24. https://doi.org/10.1016/j.matpr.2017.11.448.

[81] Rao GA, Kumar M, Srinivas M, Sarma DS. Effect of standard heat treatment on the microstructure and mechanical properties of hot isostatically pressed superalloy inconel 718. Materials Science and Engineering: A 2003;355:114–25. https://doi.org/10.1016/S0921-5093(03)00079-0.

[82] Kasperovich G, Gussone J, Requena G, Schell N, Stark A, Haubrich J. Tailoring the strength of inconel 718: Insights into LPBF parameters and heat treatment synergy. Mater Des 2025;250. https://doi.org/10.1016/j.matdes.2025.113627.

[83] Wu H, Zhuang X, Nie Y, Li Y, Jiang L. Effect of heat treatment on mechanical property and microstructure of a powder metallurgy nickel-based superalloy. Materials Science and Engineering: A 2019;754:29–37. https://doi.org/10.1016/j.msea.2019.03.064.

[84] Wu S, Peng HZ, Gao X, Hodgson PD, Song HY, Zhu YM, et al. Improving creep property of additively manufactured Inconel 718 through specifically-designed post heat treatments. Materials Science & Engineering A 2022;857. https://doi.org/10.1016/j.msea.2022.144047.

[85] Rezaie A, Vahdat SE. Study of Effects of Temperature and Pressure in HIP Process on Mechanical Properties of Nickel-based Superalloys. Mater Today Proc 2017;4:152–6. https://doi.org/10.1016/J.MATPR.2017.01.008.

[86] Schirra JJ, Caless RH, Hatala RW. The Effect of Laves Phase on the Mechanical Properties of Wrought and Cast + HIP Inconel 718. Superalloys 718, 625 and Various Derivatives (1991), TMS; 1991, p. 375–88. https://doi.org/10.7449/1991/Superalloys_1991_375_388.

[87] Paturi UMR, B. VD, Reddy NS. Progress of machinability on the machining of Inconel 718: A comprehensive review on the perception of cleaner machining. Clean Eng Technol 2021;5:100323. https://doi.org/10.1016/J.CLET.2021.100323.

[88] Pinheiro C, Kondo MY, Amaral SS, Callisaya ES, De Souza JVC, De Sampaio Alves MC, et al. Effect of machining parameters on turning process of Inconel 718. Materials and Manufacturing Processes 2021;36:1421–37. https://doi.org/10.1080/10426914.2021.1914839.

[89] Guo D, Wang D, Wu S, Qi H, Saetang V. Investigation on turning of Inconel 718 using differently coated microtextured tools. Proceedings of the Institution of Mechanical Engineers, Part E: Journal of Process Mechanical Engineering 2023;239:754–64. https://doi.org/10.1177/09544089231191720.

[90] Liu X, Lin X, Jia X, Li Y, Shao C. Influence of tool nose angle on cutting performance in hot machining of Inconel 718. Journal of Engineering and Applied Science 2024;71. https://doi.org/10.1186/s44147-024-00423-9.

[91] Cobbinah PV, Nzeukou RA, Onawale OT, Matizamhuka WR. Laser Powder Bed Fusion of Potential Superalloys: A Review. Metals - Open Access Metallurgy Journal 2020;11:58. https://doi.org/10.3390/met11010058.

[92] Gor M, Soni H, Wankhede V, Sahlot P, Grzelak K, Szachgluchowicz I, et al. A Critical Review on Effect of Process Parameters on Mechanical and Microstructural Properties of Powder-Bed Fusion Additive Manufacturing of SS316l. Materials 2021;14. https://doi.org/10.3390/ma14216527.

[93] Al-Lami J, Dessolier T, Rogers SR, Pirzada T, Pham M. Dislocation Distribution, Crystallographic Texture Evolution, and Plastic Inhomogeneity of Inconel 718 Fabricated by Laser Powder Bed Fusion. Adv Eng Mater 2024. https://doi.org/10.1002/adem.202400524.

[94] Pereira JC, Aranzabe J, Taboada MC, Ruiz N, Rodriguez PP. Analysis of Microstructure and Mechanical Properties in As-Built/As-Cast and Heat-Treated Conditions for IN718 Alloy Obtained by Selective Laser Melting and Investment Casting Processes. Crystals 2021;11. https://doi.org/10.3390/CRYST11101196.

[95] Gokcekaya O, Ishimoto T, Hibino S, Yasutomi J, Narushima T, Nakano T. Unique crystallographic texture formation in Inconel 718 by laser powder bed fusion and its effect on mechanical anisotropy. Acta Mater 2021;212:116876. https://doi.org/10.1016/J.ACTAMAT.2021.116876.

[96] Popovich VA, Borisov E V., Popovich AA, Sufiiarov VS, Masaylo D V., Alzina L. Functionally graded Inconel 718 processed by additive manufacturing: Crystallographic texture, anisotropy of microstructure and mechanical properties. Mater Des 2017;114:441–9. https://doi.org/10.1016/J.MATDES.2016.10.075.

[97] Thanumoorthy RS, Sekar P, Bontha S, Balan ASS. A study on the effect of process parameters and scan strategies on microstructure and mechanical properties of laser directed energy deposited IN718. J Mater Process Technol 2023;319. https://doi.org/10.1016/J.JMATPROTEC.2023.118096.

[98] Ghorbanpour S, Sahu S, Deshmukh K, Borisov E, Riemslag T, Reinton E, et al. Effect of microstructure induced anisotropy on fatigue behaviour of functionally graded Inconel 718 fabricated by additive manufacturing. Mater Charact 2021;179:111350. https://doi.org/10.1016/J.MATCHAR.2021.111350.

[99] Yu CH, Peng RL, Lee TL, Luzin V, Lundgren JE, Moverare J. Anisotropic behaviours of LPBF Hastelloy X under slow strain rate tensile testing at elevated temperature. Materials Science and Engineering: A 2022;844:143174. https://doi.org/10.1016/J.MSEA.2022.143174.

[100] Pitrmuc Z, Šimota J, Beránek L, Mikeš P, Andronov V, Sommer J, et al. Mechanical and Microstructural Anisotropy of Laser Powder Bed Fusion 316L Stainless Steel. Materials 2022;15. https://doi.org/10.3390/MA15020551.

[101] Dzugan J, Seifi M, Rund M, Podany P, Grylls R, Lewandowski JJ. The Use of Miniature Specimens to Determine Local Properties and Fracture Behavior of LPBF-Processed Inconel 718 in as-Deposited and Post-Treated States. Materials 2022;15. https://doi.org/10.3390/MA15134724.

[102] Tabatabaeian A, Ghasemi AR, Shokrieh MM, Marzbanrad B, Baraheni M, Fotouhi M. Residual Stress in Engineering Materials: A Review. Adv Eng Mater 2022;24. https://doi.org/10.1002/ADEM.202100786.

[103] Dutton B, Vesga W, Waller J, James S, Seifi M. Metal Additive Manufacturing Defect Formation and Nondestructive Evaluation Detectability. In: Shamsaei N, Daniewicz S, Hrabe N, Beretta S, Waller J, Seifi M, editors. Structural Integrity of Additive Manufactured Parts, 100 Barr Harbor Drive,

PO Box C700, West Conshohocken, PA 19428-2959: ASTM International; 2020, p. 1–50. https://doi.org/10.1520/STP162020180136.

[104] Deng D, Peng RL, Söderberg H, Moverare J. On the formation of microstructural gradients in a nickel-base superalloy during electron beam melting. Mater Des 2018;160:251–61. https://doi.org/10.1016/J.MATDES.2018.09.006.

[105] Gruber K, Dziedzic R, Kuźnicka B, Madejski B, Malicki M. Impact of high temperature stress relieving on final properties of Inconel 718 processed by laser powder bed fusion. Materials Science and Engineering: A 2021;813:141111. https://doi.org/10.1016/J.MSEA.2021.141111.

[106] Chang SH. In situ TEM observation of γ′, γ″ and δ precipitations on Inconel 718 superalloy through HIP treatment. J Alloys Compd 2009;486:716–21. https://doi.org/10.1016/J.JALLCOM.2009.07.046.

[107] Tillmann W, Schaak C, Nellesen J, Schaper M, Aydinöz ME, Hoyer KP. Hot isostatic pressing of IN718 components manufactured by selective laser melting. Addit Manuf 2017;13:93–102. https://doi.org/10.1016/J.ADDMA.2016.11.006.

[108] Bernal D, Chamorro X, Hurtado I, Lopez-Galilea I, Bürger D, Weber S, et al. Integration of Hot Isostatic Pressing and Heat Treatment for Advanced Modified γ-TiAl TNM Alloys. Materials 2022, Vol 15, Page 4211 2022;15. https://doi.org/10.3390/MA15124211.

[109] Fayed EM, Brailovski V, Jahazi M, Medraj M. Stability of the microstructure and elevated-temperature mechanical properties of additively manufactured Inconel 718 superalloy subjected to long-term in-service thermal cycling. Materials Science and Engineering: A 2022;838:142790. https://doi.org/10.1016/J.MSEA.2022.142790.

[110] Gruber K, Stopyra W, Kobiela K, Madejski B, Malicki M, Kurzynowski T. Mechanical properties of Inconel 718 additively manufactured by laser powder bed fusion after industrial high-temperature heat treatment. J Manuf Process 2022;73:642–59. https://doi.org/10.1016/J.JMAPRO.2021.11.053.

[111] Liu H, Cheng W, Sun Y, Ma R, Wang Y, Bai J, et al. Effects of Process Parameters and Heat Treatment on Microstructure and Mechanical Characteristics of Laser Powder Bed Fusion Alloy Inconel 718. Coatings 2023;13. https://doi.org/10.3390/coatings13010189.

[112] Zhang D, Niu W, Cao X, Liu Z. Effect of standard heat treatment on the microstructure and mechanical properties of selective laser melting manufactured Inconel 718 superalloy. Materials Science and Engineering: A 2015;644:32–40. https://doi.org/10.1016/J.MSEA.2015.06.021.

[113] Tajyar A, Brooks N, Holtham N, Rowe R, Newell DJ, Palazotto AN, et al. Effects of a modified heat-treatment on microstructure and mechanical properties of additively manufactured Inconel 718. Materials Science and

Engineering: A 2022;838:142770. https://doi.org/10.1016/J.MSEA.2022.142770.

[114] Heo S, Lim Y, Kwak N, Jeon C, Choi M, Jo I. Impact of Heat Treatment and Building Direction on Tensile Properties and Fracture Mechanism of Inconel 718 Produced by SLM Process. Metals (Basel) 2024;14. https://doi.org/10.3390/met14040440.

[115] Li N, Wang C, Li C. Microstructures and High-Temperature Mechanical Properties of Inconel 718 Superalloy Fabricated via Laser Powder Bed Fusion. Materials 2024;17. https://doi.org/10.3390/ma17153735.

[116] Lee S, Shao S, Wells DN, Zetek M, Kepka M, Shamsaei N. Fatigue behavior and modeling of additively manufactured IN718: The effect of surface treatments and surface measurement techniques. J Mater Process Technol 2022;302:117475. https://doi.org/10.1016/J.JMATPROTEC.2021.117475.

[117] AMAZE. Additive Manufacturing Aiming towards Zero Waste and Efficient Production of High-Tech Metal Products. Manufacturing Technology Centre 2017.

[118] Xu J, Wu Z, Niu J, Song Y, Liang C, Yang K, et al. Effect of Laser Energy Density on the Microstructure and Microhardness of Inconel 718 Alloy Fabricated by Selective Laser Melting. Crystals (Basel) 2022;12. https://doi.org/10.3390/cryst12091243.

[119] Gockel J, Sheridan L, Koerper B, Whip B. The influence of additive manufacturing processing parameters on surface roughness and fatigue life. Int J Fatigue 2019;124:380–8. https://doi.org/10.1016/J.IJFATIGUE.2019.03.025.

[120] ASTM International. ASTM E8/E8M-21: Standard Test Methods for Tension Testing of Metallic Materials 2022.

[121] Kim C, Park J, Joo Y, Kong B, Hong HU, Shin JH, et al. Effects of Specimen Orientation and Heat Treatment on Microstructure and Crack Propagation Path of the IN718 Alloy Built by the Additive Manufacturing Process. Metals and Materials International 2022. https://doi.org/10.1007/S12540-022-01322-5/FIGURES/13.

[122] Sun SH, Koizumi Y, Saito T, Yamanaka K, Li YP, Cui Y, et al. Electron beam additive manufacturing of Inconel 718 alloy rods: Impact of build direction on microstructure and high-temperature tensile properties. Addit Manuf 2018;23:457–70. https://doi.org/10.1016/J.ADDMA.2018.08.017.

[123] Mostafaei A, Ghiaasiaan R, Ho I-T, Strayer S, Chang K-C, Shamsaei N, et al. Additive Manufacturing of Nickel-based superalloys: a state-of-the-art review on process-structure-defect-property relationship. Prog Mater Sci 2023. https://doi.org/10.1016/J.PMATSCI.2023.101108.

[124] Dzugan J, Seifi M, Rzepa S, Prochazka R, Rund M, Podany P, et al. Mechanical properties characterisation of metallic components produced by

additive manufacturing using miniaturised specimens. Https://DoiOrg/101080/1745275920222161400 2023;18. https://doi.org/10.1080/17452759.2022.2161400.

[125] Bathais C, André P. Fatigue of Materials and Structures: Fundamentals. John Wiley & Sons, Inc.; 2010.

[126] Igwemezie V, Mehmanparast A, Kolios A. Materials selection for XL wind turbine support structures: A corrosion-fatigue perspective. Marine Structures 2018;61:381–97. https://doi.org/10.1016/j.marstruc.2018.06.008.

[127] Konečná R, Kunz L, Nicoletto G, Bača A. Long fatigue crack growth in Inconel 718 produced by selective laser melting. Int J Fatigue 2016;92:499–506. https://doi.org/10.1016/J.IJFATIGUE.2016.03.012.

[128] Xu Z, Hyde CJ, Tuck C, Clare AT. Creep behaviour of inconel 718 processed by laser powder bed fusion. J Mater Process Technol 2018;256:13–24. https://doi.org/10.1016/J.JMATPROTEC.2018.01.040.

[129] Kuo Y-L, Horikawa S, Kakehi K. Effects of build direction and heat treatment on creep properties of Ni-base superalloy built up by additive manufacturing. Scr Mater 2017;129:74–8. https://doi.org/10.1016/j.scriptamat.2016.10.035.

[130] Wu S, Song HY, Peng HZ, Hodgson PD, Wang H, Wu XH, et al. A microstructure-based creep model for additively manufactured nickel-based superalloys. Acta Mater 2022;224. https://doi.org/10.1016/J.ACTAMAT.2021.117528.

[131] Reed R, Tang T. Using PIP testing to Navigate the Additive Alloy Design Space. 2022.

[132] Weaver JS, Pathak S, Reichardt A, Vo HT, Maloy SA, Hosemann P, et al. Spherical nanoindentation of proton irradiated 304 stainless steel: A comparison of small scale mechanical test techniques for measuring irradiation hardening. Journal of Nuclear Materials 2017;493:368–79. https://doi.org/10.1016/J.JNUCMAT.2017.06.031.

[133] BSI Standards Publication. BS EN 10371: Metallic materials - Small punch test method 2021:1–60.

[134] ASTM International. ASTM E3205: Standard Test Method for Small Punch Testing of Metallic Materials 2020:1–12. https://doi.org/10.1520/E3205-20.

[135] Torres J, Gordon AP. Mechanics of the small punch test: a review and qualification of additive manufacturing materials. Journal of Materials Science 2021 56:18 2021;56:10707–44. https://doi.org/10.1007/S10853-021-05929-8.

[136] Torres J, Gordon AP. Expedited Optimization of AM Materials Using Miniaturized Testing. Minerals, Metals and Materials Series 2020:97–113. https://doi.org/10.1007/978-3-030-36296-6_10/COVER.

[137] Lancaster RJ, Jeffs SP, Haigh BJ, Barnard NC. Derivation of material properties using small punch and shear punch test methods. Mater Des 2022;215. https://doi.org/10.1016/J.MATDES.2022.110473.

[138] Hyde TH, Sun W. A novel, high-sensitivity, small specimen creep test. Journal of Strain Analysis for Engineering Design 2009;44:171–85. https://doi.org/10.1243/03093247JSA502.

[139] Kazakeviciute J, Rouse JP, De Focatiis DSA, Hyde CJ. The development of a novel technique for small ring specimen tensile testing. Theoretical and Applied Fracture Mechanics 2019;99:131–9. https://doi.org/10.1016/j.tafmec.2018.11.016.

[140] Rouse JP, Simonelli M, Hyde CJ. On the use of small ring testing for the characterisation of elastic and yield material property variation in additively manufactured materials. Addit Manuf 2020;36. https://doi.org/10.1016/j.addma.2020.101589.

[141] Wen C, Xu T, Guan K. Correlation Factor Study of Small Punch Creep Test and Its Life Prediction. Materials 2016;9. https://doi.org/10.3390/ma9100796.

[142] Jeffs SP, Lancaster RJ, Garcia TE. Creep lifing methodologies applied to a single crystal superalloy by use of small scale test techniques. Materials Science and Engineering: A 2015;636:529–35. https://doi.org/10.1016/j.msea.2015.03.119.

[143] Williams T, Evans M, Harrison W. An Investigation into the Correlation of Small Punch and Uniaxial Creep Data for Waspaloy. Metallurgical and Materials Transactions A 2021;52:3460–74. https://doi.org/10.1007/s11661-021-06318-1.

[144] Bruchhausen M, Altstadt E, Austin T, Dymacek P, Holmström S, Jeffs S, et al. European standard on small punch testing of metallic materials. Ubiquity Proceedings, 2018, p. 11. https://doi.org/10.5334/uproc.11.

[145] Blagoeva DT, Hurst RC. Application of the CEN (European Committee for Standardization) small punch creep testing code of practice to a representative repair welded P91 pipe. Materials Science and Engineering: A 2009;510–511:219–23. https://doi.org/10.1016/j.msea.2008.05.058.

[146] Peng J, Gao M, Zhang H, Geng X, Liu X, Pan H. Small punch creep test reveals the differences of high-temperature creep behaviours for laser powder bed fusion and Rolled Inconel 718 alloys. Materials Science and Engineering: A 2023;886. https://doi.org/10.1016/j.msea.2023.145698.

[147] Davies SJ, Jeffs SP, Coleman MP, Lancaster RJ. Effects of heat treatment on microstructure and creep properties of a laser powder bed fused nickel superalloy. Mater Des 2018;159:39–46. https://doi.org/10.1016/j.matdes.2018.08.039.

[148] ISO. ISO 14577: Metallic materials — Instrumented indentation test for hardness and materials parameters 2015:1–46.

[149] ASTM Interational. ASTM E2546: Practice for Instrumented Indentation Testing 2015:1–24. https://doi.org/10.1520/E2546-15.

[150] Ye C, Chen J, Xu M, Wei X, Lu H. Multi-scale simulation of nanoindentation on cast Inconel 718 and NbC precipitate for mechanical properties prediction. Materials Science and Engineering: A 2016;662:385–94. https://doi.org/10.1016/j.msea.2016.03.081.

[151] Wang F, Li G, Liu M, Wang D, Yan D, Fan J. Acquisition of heterogeneous constitutive relationship of Ni60 laser cladding layer based on nano-indentation experiment. Mater Today Commun 2023;34. https://doi.org/10.1016/j.mtcomm.2022.105049.

[152] Dao M, Chollacoop N, Van Vliet KJ, Venkatesh TA, Suresh S. Computational modeling of the forward and reverse problems in instrumented sharp indentation. Acta Mater 2001;49:3899–918. https://doi.org/10.1016/S1359-6454(01)00295-6.

[153] Rossi E, Wheeler JM, Sebastiani M. High-speed nanoindentation mapping: A review of recent advances and applications. Curr Opin Solid State Mater Sci 2023;27. https://doi.org/10.1016/j.cossms.2023.101107.

[154] Liu Z, Lang L, Mohammed SMAK, Chen D, He B, Zou Y. Small-depth nanoindentation studies of an additively manufactured titanium alloy: Anisotropic nanomechanical properties and correlation with microscopic mechanical behaviour. Materialia (Oxf) 2023;30. https://doi.org/10.1016/j.mtla.2023.101802.

[155] Tang YT, Campbell JE, Burley M, Dean J, Reed RC, Clyne TW. Profilometry-based indentation plastometry to obtain stress-strain curves from anisotropic superalloy components made by additive manufacturing. Materialia (Oxf) 2021;15. https://doi.org/10.1016/J.MTLA.2021.101017.

[156] Clyne TW, Campbell JE, Burley M, Dean J. Profilometry-Based Inverse Finite Element Method Indentation Plastometry. Adv Eng Mater 2021;23:2100437. https://doi.org/10.1002/ADEM.202100437.

[157] Burley M, Campbell JE, Reiff-Musgrove R, Dean J, Clyne TW. The Effect of Residual Stresses on Stress–Strain Curves Obtained via Profilometry-Based Inverse Finite Element Method Indentation Plastometry. Adv Eng Mater 2021;23. https://doi.org/10.1002/ADEM.202001478.

[158] Godec D, Gonzalez-Gutierrez J, Nordin A, Pei E, Ureña Alcázar J. A Guide to Additive Manufacturing 2022. https://doi.org/10.1007/978-3-031-05863-9.

[159] Hatami S. Variation of fatigue strength of parts manufactured by laser powder bed fusion. Powder Metallurgy 2022;65:259–64. https://doi.org/10.1080/00325899.2021.2010932.

[160] Gradl PR, Tinker DC, Ivester J, Skinner SW, Teasley T, Bili JL. Geometric feature reproducibility for laser powder bed fusion (L-PBF) additive

manufacturing with Inconel 718. Addit Manuf 2021;47. https://doi.org/10.1016/J.ADDMA.2021.102305.

[161] Jamshid M, Huff R, Enrique P, Diegel O, Lin Ng J, Kowen J, et al. Wohlers Report 2025: 3D Printing and Additive Manufacturing Global State of the Industry . 30th ed. Washington DC: Wohlers Associates Powered by ASTM; 2025.

[162] Chen Z, Han C, Gao M, Kandukuri SY, Zhou K. A review on qualification and certification for metal additive manufacturing. Virtual Phys Prototyp 2022;17:382–405. https://doi.org/10.1080/17452759.2021.2018938.

[163] Wang Y, Guo W, Xu C, Zhang Y, Ji Q, Feng X, et al. Defects, microstructure, and properties in laser powder bed fusion IN718: Power density effects and feature maps. J Manuf Process 2025;135:240–52. https://doi.org/10.1016/j.jmapro.2025.01.054.

[164] Stopka KS, Desrosiers A, Nicodemus T, Krutz N, Andreaco A, Sangid MD. Intentionally seeding pores in additively manufactured alloy 718: Process parameters, microstructure, defects, and fatigue. Addit Manuf 2023;66. https://doi.org/10.1016/J.ADDMA.2023.103450.

[165] Shamsaei N, Yadollahi A, Bian L, Thompson SM. An overview of Direct Laser Deposition for additive manufacturing; Part II: Mechanical behavior, process parameter optimization and control. Addit Manuf 2015;8:12–35. https://doi.org/https://doi.org/10.1016/j.addma.2015.07.002.

[166] Wang X, Gong X, Chou K. Review on powder-bed laser additive manufacturing of Inconel 718 parts. Proc IMechE Part B: J Engineering Manufacture 2017;231:1890–903. https://doi.org/10.1177/0954405415619883.

[167] Choudhary S, Gaur V. Improved properties of additively prepared Inconel 718 alloy post-processed with a new heat treatment. Materials Science and Engineering: A 2024;911. https://doi.org/10.1016/j.msea.2024.146930.

[168] Zhao Y, Li K, Gargani M, Xiong W. A comparative analysis of Inconel 718 made by additive manufacturing and suction casting: Microstructure evolution in homogenization. Addit Manuf 2020;36. https://doi.org/10.1016/j.addma.2020.101404.

[169] Jiang R, Mostafaei A, Pauza J, Kantzos C, Rollett AD. Varied heat treatments and properties of laser powder bed printed Inconel 718. Materials Science and Engineering: A 2019;755:170–80. https://doi.org/10.1016/J.MSEA.2019.03.103.

[170] Yong CK, Gibbons GJ, Wong CC, West G. A Critical Review of the Material Characteristics of Additive Manufactured IN718 for High-Temperature Application. Metals 2020;10. https://doi.org/10.3390/MET10121576.

[171] Mostafaei A, Ghiaasiaan R, Ho IT, Strayer S, Chang KC, Shamsaei N, et al. Additive manufacturing of nickel-based superalloys: A state-of-the-art review

on process-structure-defect-property relationship. Prog Mater Sci 2023;136. https://doi.org/10.1016/J.PMATSCI.2023.101108.

[172] Leclerc N, Khosravani A, Hashemi S, Miracle DB, Kalidindi SR. Correlation of Measured Load-Displacement Curves in Small Punch Tests with Tensile Stress-Strain Curves. Acta Mater 2021;204:116501. https://doi.org/10.1016/j.actamat.2020.116501.

[173] Courtright ZS, Leclerc NP, Kim HN, Kalidindi SR. Critical Comparison of Spherical Microindentation, Small Punch Test, and Uniaxial Tensile Testing for Selective Laser Melted Inconel 718. Applied Sciences 2021;11. https://doi.org/10.3390/APP11031061.

[174] Wilkinson MD, Dumontier M, Aalbersberg IjJ, Appleton G, Axton M, Baak A, et al. The FAIR Guiding Principles for scientific data management and stewardship. Sci Data 2016;3. https://doi.org/10.1038/sdata.2016.18.

[175] Bjarsch T, Drechsler K, Schilp J. Ontologies for FAIR Data in Additive Manufacturing: A Use Case-Based Evaluation. Adv Eng Mater 2025;27. https://doi.org/10.1002/adem.202401528.

[176] SAE International. AMS2774G: Heat Treatment Wrought Nickel Alloy and Cobalt Alloy Parts 2020.

[177] SAE International. AMS5664G: Nickel Alloy, Corrosion- and Heat-Resistant, Bars, Forgings, Extrusions, Rings, and Stock for Forgings and Rings 52.5Ni - 19Cr - 3.0Mo - 5.1Cb (Nb) - 0.90Ti - 0.50Al - 18Fe Consumable Electrode or Vacuum Induction Melted 1950 °F (1066 °C) Solution Heat Treated, Precipitation Hardenable 2022.

[178] SAE International. AMS5662P: Nickel Alloy, Corrosion- and Heat-Resistant, Bars, Forgings, Rings, and Stock for Forgings and Rings 52.5Ni - 19Cr - 3.0Mo - 5.1Cb (Nb) - 0.90Ti - 0.50Al - 18Fe Consumable Electrode or Vacuum Induction Melted 1775 °F (968 °C) Solution Heat Treated, Precipitation-Hardenable 2022.

[179] ASTM International. ASTM B822-20: Test Method for Particle Size Distribution of Metal Powders and Related Compounds by Light Scattering 2020. https://doi.org/10.1520/B0822-20.

[180] ASTM International. ASTM B527-22: Standard Test Method for Tap Density of Metal Powders and Compounds 2023.

[181] ASTM International. ASTM B417-22: Test Method for Apparent Density of Non-Free-Flowing Metal Powders Using the Carney Funnel 2022. https://doi.org/10.1520/B0417-22.

[182] BSI. BS ISO 13067:2020 Microbeam analysis. Electron backscatter diffraction. Measurement of average grain size 2020.

[183] ASTM International. ASTM E92-12 Standard Test Methods for Vickers Hardness and Knoop Hardness of Metallic Materials. Book of Standards 2023;03.01.

[184] ASTM International. ASTM E21-20: Standard Test Methods for Elevated Temperature Tension Tests of Metallic Materials 2021.

[185] BSI Standards Publication. BS EN 7270: Metallic materials - Constant amplitude strain controlled axial fatigue - Method of test 2006:1–24.

[186] BSI Standards Publication. BS ISO 12106: Metallic materials - Fatigue testing - Axial-strain-controlled method 2017:1–38.

[187] ASTM International. ASTM E606/E606M-21: Standard Test Method for Strain-Controlled Fatigue Testing 2021:1–16. https://doi.org/10.1520/E0606_E0606M-21.

[188] ASTM International. ASTM E139-11: Standard Test Methods for Conducting Creep, Creep-Rupture, and Stress-Rupture Tests of Metallic Materials 2018:1–14.

[189] Zhang H, Zhang K, Zhou H, Lu Z, Zhao C, Yang X. Effect of strain rate on microstructure evolution of a nickel-based superalloy during hot deformation. Mater Des 2015;80:51–62. https://doi.org/10.1016/j.matdes.2015.05.004.

[190] Newell DJ, O'Hara RP, Cobb GR, Palazotto AN, Kirka MM, Burggraf LW, et al. Mitigation of scan strategy effects and material anisotropy through supersolvus annealing in LPBF IN718. Materials Science and Engineering: A 2019;764. https://doi.org/10.1016/j.msea.2019.138230.

[191] Serrano-Munoz I, Agudo Jácome L, Thompsom S, Schneider J. On the transferability of post-processing heat treatments designed for PBF-LB IN718 alloys to directed energy deposition specimens. The International Journal of Advanced Manufacturing Technology 2025;137:3949–65. https://doi.org/10.1007/s00170-025-15386-1.

[192] Hao D, Wang Q, Ma H, Wu D, Kang J, Dong H, et al. The influence of grain boundary character distribution on the high-temperature creep behavior and damage mechanism of Inconel 718. Mater Des 2024;248. https://doi.org/10.1016/j.matdes.2024.113525.

[193] Wang LY, Wang YC, Zhou ZJ, Wan HY, Li CP, Chen GF, et al. Small punch creep performance of heterogeneous microstructure dominated Inconel 718 fabricated by selective laser melting. Mater Des 2020;195. https://doi.org/10.1016/j.matdes.2020.109042.

[194] Wang LY, Zhou ZJ, Li CP, Chen GF, Zhang GP. Comparative investigation of small punch creep resistance of Inconel 718 fabricated by selective laser melting. Materials Science and Engineering: A 2019;745:31–8. https://doi.org/10.1016/j.msea.2018.12.083.

[195] ASTM International. ASTM B311-17: Standard Test Method for Density of Powder Metallurgy (PM) Materials Containing Less Than Two Percent Porosity. ASTM International 2017:1–5.

[196] Pant P, Salvemini F, Proper S, Luzin V, Simonsson K, Sjöström S, et al. A study of the influence of novel scan strategies on residual stress and microstructure of L-shaped LPBF IN718 samples. Mater Des 2022;214. https://doi.org/10.1016/j.matdes.2022.110386.

[197] Schröder J, Evans A, Polatidis E, Čapek J, Mohr G, Serrano-Munoz I, et al. Understanding the impact of texture on the micromechanical anisotropy of laser powder bed fused Inconel 718. J Mater Sci 2022;57:15036–58. https://doi.org/10.1007/s10853-022-07499-9.

[198] Cheng M, Xiao X, Luo G, Song L. Integrated control of molten pool morphology and solidification texture by adjusting pulse duration in laser additive manufacturing of Inconel 718. Opt Laser Technol 2021;142. https://doi.org/10.1016/j.optlastec.2021.107137.

[199] Chen J, Yao Z, Wang F, Chi Y, Wang Z, Tofil S, et al. Grain refinement and Laves phase dispersion by high-intensity ultrasonic vibration in laser cladding of Inconel 718. Journal of Materials Research and Technology 2024;30:8563–75. https://doi.org/10.1016/j.jmrt.2024.05.229.

[200] Fayed EM, Saadati M, Shahriari D, Brailovski V, Jahazi M, Medraj M. Optimization of the Post-Process Heat Treatment of Inconel 718 Superalloy Fabricated by Laser Powder Bed Fusion Process. Metals (Basel) 2021;11. https://doi.org/10.3390/met11010144.

[201] Obana M, Prasad K, Ito A, Torizuka S. The possible role of nano sized precipitates on the mechanical properties of additively manufactured IN 718 superalloy. Materials Science and Engineering: A 2021;826. https://doi.org/10.1016/j.msea.2021.141972.

[202] Yu H, Hayashi S, Kakehi K, Kuo Y-L. Study of Formed Oxides in IN718 Alloy during the Fabrication by Selective Laser Melting and Electron Beam Melting. Metals (Basel) 2018;9. https://doi.org/10.3390/met9010019.

[203] Lee H, Jung JE, Kang D-S, Jeong HW, Yun DW, Choe J, et al. Oxide dispersion strengthened IN718 owing to powder reuse in selective laser melting. Materials Science and Engineering: A 2022;832. https://doi.org/10.1016/j.msea.2021.142369.

[204] Yalcin MY, Gokbayrak AA, Duygulu O, Derin B, Poplawsky JD, El-Atwani O, et al. Laser powder bed fusion of oxide dispersion-strengthened IN718 alloys: A complementary study on microstructure and mechanical properties. Materials Science and Engineering: A 2024;903. https://doi.org/10.1016/j.msea.2024.146663.

[205] Hu H, Pan Y, Hu L, Du D, Wang S, Wen J-F, et al. Microstructure instability of additively manufactured alloy 718 fabricated by laser powder bed fusion

during thermal exposure at 600–1000 °C. J Alloys Compd 2025;1010. https://doi.org/10.1016/j.jallcom.2024.177316.

[206] Li X, Shi JJ, Wang CH, Cao GH, Russell AM, Zhou ZJ, et al. Effect of heat treatment on microstructure evolution of Inconel 718 alloy fabricated by selective laser melting. J Alloys Compd 2018;764:639–49. https://doi.org/10.1016/j.jallcom.2018.06.112.

[207] Reed RC. The Superalloys: Fundamentals and Applications . Cambridge University Press; 2006.

[208] Ferreri NC, Vogel SC, Knezevic M. Determining volume fractions of γ, γ′, γ″, δ, and MC-carbide phases in Inconel 718 as a function of its processing history using an advanced neutron diffraction procedure. Materials Science and Engineering: A 2020;781. https://doi.org/10.1016/j.msea.2020.139228.

[209] Meng G, Gong Y, Zhang J, Zhao J. Effect of heat treatment on microstructure, precipitation behavior and mechanical properties of Inconel 718 fabricated by laser direct energy deposition. Materials Science and Engineering A 2024;898. https://doi.org/10.1016/j.msea.2024.146396.

[210] Liu X, Hu R, Zou H, Zhou M, Gao Z, Zhang K, et al. Tailoring the microstructure and deformation mechanisms of an additively manufactured nickel-based superalloy by post-aging heat treatment. Vacuum 2024;225. https://doi.org/10.1016/j.vacuum.2024.113238.

[211] Yeh A, Kuo C, Wei C, Nguyen H, Bor H. Aging Effects on the gamma’ and gamma’’ Precipitates of Inconel 718 Superalloy. 7th International Symposium on Superalloy 718 and Derivatives (2010), John Wiley & Sons, Inc.; 2010, p. 679–88. https://doi.org/10.7449/2010/Superalloys_2010_679_688.

[212] Li P, Zhou J, Gong Y, Meng X, Lu J. Effect of post-heat treatment on the microstructure and mechanical properties of laser metal deposition Inconel 718. Journal of Mechanical Science and Technology 2021;35:2871–8. https://doi.org/10.1007/s12206-021-0610-4.

[213] Cao Y, Bai P, Liu F, Hou X, Guo Y. Effect of the Solution Temperature on the Precipitates and Grain Evolution of IN718 Fabricated by Laser Additive Manufacturing. Materials 2020;13. https://doi.org/10.3390/MA13020340.

[214] Choudhary S, Pandey A, Gaur V. Role of microstructural phases in enhanced mechanical properties of additively manufactured IN718 alloy. Materials Science and Engineering: A 2023;862. https://doi.org/10.1016/j.msea.2022.144484.

[215] Schwink Ch, Nortmann A. The present experimental knowledge of dynamic strain ageing in binary f.c.c. solid solutions. Materials Science and Engineering: A 1997;234–236:1–7. https://doi.org/10.1016/S0921-5093(97)00139-1.

[216] Rowlands BS, Rae C, Galindo-Nava E. The Portevin-Le Chatelier effect in nickel-base superalloys: Origins, consequences and comparison to strain

ageing in other alloy systems. Prog Mater Sci 2023;132. https://doi.org/10.1016/j.pmatsci.2022.101038.

[217] Nalawade S, Mahadevan S, Singh JB, Ramaswamy K, Verma A. Serrated Yielding in Alloy 718. Superalloy 718 and Derivatives, Wiley; 2010, p. 808–23. https://doi.org/10.1002/9781118495223.ch62.

[218] Max B, Viguier B, Andrieu E, Cloue JM. A Re-examination of the Portevin-Le Chatelier Effect in Alloy 718 in Connection with Oxidation-Assisted Intergranular Cracking. Metallurgical and Materials Transactions A 2014;45A:5431–41. https://doi.org/10.1007/s11661-014-2508-6.

[219] Tang L, Xu L, Li Y, Tan J, Li C, Li J, et al. The influence of additive manufacturing on Portevin-Le Châtelier (PLC) effect in Ni–Co-based superalloy. Journal of Materials Research and Technology 2024;30:9318–24. https://doi.org/10.1016/J.JMRT.2024.05.261.

[220] Jiang Y, Zou T, Liu M, Wang Q, Pei Y, Zhang H, et al. Tensile Deformation Behaviors and Microstructure Evolution Under Various Temperatures for MAR-M247 Nickel-Based Superalloy. Adv Eng Mater 2024;26. https://doi.org/10.1002/adem.202302056.

[221] Yilmaz A. The Portevin-Le Chatelier effect: A review of experimental findings. Sci Technol Adv Mater 2011;12:63001–17. https://doi.org/10.1088/1468-6996/12/6/063001.

[222] Al-Lami J, Theska F, Ahuactzin-Garcia E, Primig S, Davies C, Pham M-S. On the origin of thermal dependence of 3D printed Inconel 718: Roles of atom clustering. Appl Mater Today 2024;40. https://doi.org/10.1016/j.apmt.2024.102414.

[223] Nalawade SA, Sundararaman M, Kishore R, Shah JG. The influence of aging on the serrated yielding phenomena in a nickel-base superalloy. Scr Mater 2008;59:991–4. https://doi.org/10.1016/j.scriptamat.2008.07.004.

[224] Brechtl J, Chen S, Lee C, Shi Y, Feng R, Xie X, et al. A Review of the Serrated-Flow Phenomenon and Its Role in the Deformation Behavior of High-Entropy Alloys. Metals (Basel) 2020;10. https://doi.org/10.3390/met10081101.

[225] Shi S, Shu H, Li C, Wei Y, Yang S. Small punch investigation of the dynamic strain aging behaviour and intermediate temperature embrittlement of Inconel 625. Mater Today Commun 2023;35. https://doi.org/10.1016/j.mtcomm.2023.106368.

[226] Yang S, Xue L, Lu W, Ling X. Experimental study on the mechanical strength and dynamic strain aging of Inconel 617 using small punch test. J Alloys Compd 2019;815. https://doi.org/10.1016/j.jallcom.2019.152447.

[227] Gao M, Wei RP. Grain Boundary Niobium Carbides in Inconel 718. Scr Mater 1997;37:1843–9. https://doi.org/10.1016/S1359-6462(97)00373-4.

[228] Hao D, Jin W, Ma H, Wang Q, You B, Wu D, et al. Microstructure evolution and creep behavior of Inconel 718 alloy subjected rolling process. Mater Charact 2025;223. https://doi.org/10.1016/j.matchar.2025.114888.

[229] Pradeep K, Buzolin RH, Domankova M, Godor F, Stanojevic A, Poletti MC. Dynamic recrystallisation in Inconel®718 at creep conditions. Materials Science and Engineering: A 2024;893. https://doi.org/10.1016/j.msea.2024.146146.

[230] Huang L, Qi F, Hua P, Yu L, Liu F, Sun W, et al. Discontinuous Dynamic Recrystallization of Inconel 718 Superalloy During the Superplastic Deformation. Metallurgical and Materials Transactions A 2015;46:4276–85. https://doi.org/10.1007/s11661-015-3031-0.

[231] Sankar A, M M, McCarthy T, Pasco J, Ejera SK, Aranas C. Grain disintegration and dynamic recrystallization during impact tests of additively manufactured nickel-based alloy 718. Journal of Materials Research and Technology 2024;33:4844–57. https://doi.org/10.1016/j.jmrt.2024.10.157.

[232] Jiang W, Lu J, Guan H, Wang M, Cheng X, Liu L, et al. Study of pre-precipitated δ phase promoting deformation twinning and recrystallization behavior of Inconel 718 superalloy during hot compression. Mater Des 2023;226. https://doi.org/10.1016/j.matdes.2023.111693.

[233] Chen K, Dong J, Yao Z. Creep Failure and Damage Mechanism of Inconel 718 Alloy at 800–900 °C. Metals and Materials International 2019;27:970–84. https://doi.org/10.1007/s12540-019-00447-4.

[234] Wang Q, Ge S, Wu D, Ma H, Kang J, Liu M, et al. Evolution of microstructural characteristics during creep behavior of Inconel 718 alloy. Materials Science and Engineering: A 2022;857. https://doi.org/10.1016/j.msea.2022.143859.

[235] Huron ES. Serrated Yielding in a Nickel-Base Superalloy. The Minerals, Metals, & Materials Society (TMS): Superalloys 1992:675–84.

[236] Segersäll M, Moverare J, Leidermark D, Simonsson K. Low-Cycle Fatigue Behaviour of a Ni-Based Single-Crystal Superalloy. Adv Mat Res 2014;891–892:416–21. https://doi.org/10.4028/www.scientific.net/AMR.891-892.416.